2012

Design of electron dual foil scattering systems for Elekta Infinity radiotherapy accelerators

Justin Deloy LeBlanc
Louisiana State University and Agricultural and Mechanical College

DESIGN OF ELECTRON DUAL FOIL SCATTERING SYSTEMS FOR ELEKTA INFINITY RADIOTHERAPY ACCELERATORS

A Thesis

Submitted to the Graduate Faculty of the
Louisiana State University and
Agricultural and Mechanical College
in partial fulfillment of the
requirements for the Degree of
Master of Science

in

The Department of Physics and Astronomy

by
Justin Deloy LeBlanc
B.S., Rhodes College, 2009
August 2012

Acknowledgements

I would like to thank the members of my committee Dr. Kenneth Hogstrom, Dr. Bobby Carver, Dr. Jonas Fontenot, and Dr. Gregory Guzik.

I would like to express a tremendous amount of gratitude to my advisor, Dr. Hogstrom, for the amount of time and effort he invested into this project. Without his insight, expertise, and dedication, I could not have completed this project.

I would also like to express my sincerest appreciation to Dr. Bobby Carver for his encouragement throughout the duration of this project, which to no small degree facilitated my perseverance through the frustrations that accompany research.

I would like to thank each member of my cohort, but in particular, I would like to thank Guy Harris for his assistance with Monte Carlo simulations; Garrett Pitcher for his assistance with taking measurements; and Nels Knutson for listening to me complain—a lot.

I would like to thank Ms. Susan Hammond and Ms. Yvonne Thomas for all of their administrative assistance over the past few years.

I would like to thank Elekta Inc. for their funding support for this project, and I would like to thank Dr. Michael Price for allowing me to use his laptop throughout the past year.

Portions of this research were conducted with high performance computational resources provided by Louisiana State University (http://www.hpc.lsu.edu).

Table of Contents

List of Tables

List of Figures

Abstract

Purpose: To design a dual foil scattering system within Elekta Infinity radiotherapy accelerator constraints that results in clinical electron beams that meet flatness criteria of ±3% (±4%) along its principal axes (diagonal axes) for the 25x25cm^2 applicator and most probable surface energies of 7-20 MeV (1 MeV increments).

Methods: An analytical electron dual scattering foil system simulator was commissioned and verified using Monte Carlo (MC) simulations. Verification required comparing analytical simulator with MC-calculated electron fluence profiles for identical geometries: (1) only primary foil and (2) both primary and secondary foils in the beam. Also, simulator-calculated bremsstrahlung dose was validated by comparison to measured data. Measured dose profiles, with and without 25x25cm^2 applicator, and simulator profiles were used to estimate objective profiles. Objective profiles ("ideal" profiles), which if achieved should produce uniform beams, were determined for current Elekta beam energies. Objective profiles were then interpolated for beam energies of 7-20 MeV in 1-MeV increments. Then, the simulator was used to design a new dual scattering foil system (5 primary and 3 secondary foils) such that the simulator's design profiles closely matched the objective profiles. Design profiles were compared with MC-calculated dose profiles, after which the initial objective profiles were modified, and a second design optimization was performed. MC dose calculations were used to evaluate the modified dual scattering foil design.

Results: For all design energies (7-20 MeV), the modified dual scattering foil design produced MC dose profiles that were within the flatness criteria of ±3% along the principal axes, except for 8 MeV (3.2% maximum deviation). Along the diagonal axes, the modified designs produced MC dose profiles within the flatness criteria of ±4% except at 7, 8, and 17

MeV (maximum deviation of 5.1% at 8 MeV).

Conclusions: The dual scattering foil system simulator and present methodology should be capable of designing electron dual scattering foil systems provided a validated MC model of the accelerator produces accurate dose calculations (1% accuracy in beam's umbra). Results of this study did not prove the hypothesis, believed due to the need for a greater number of iterations and more optimal primary foil thickness selections.

Chapter 1 Introduction

1.1 Clinical Utilization of Electron Beam Therapy

Due to characteristically high surface dose, relatively uniform dose plateau (surface to depth of 90% dose, R_{90}), and steep distal dose fall-off with depth (90%-10%, R_{90-10}), electron beams can be utilized in radiotherapy to irradiate superficial targets while minimizing dose to underlying critical structures. Use of energies up to 20 MeV allows for the treatment of disease within approximately 6 cm of the surface whilst sparing deeper normal tissues (Hogstrom 2004).

Tapley (1976), Vaeth and Meyer (1991), and Hogstrom (2004) enumerate a number of instances for which electron beam thereapy may be utilized. It is particularly useful in treatment of cancer of the skin, such as eyelids, nose, ear, scalp, and lips, as well as more widely spread diseases of limbs or total skin (e.g., melanoma, lymphoma, and mycosis fungoides). Electron beam therapy is also used to treat disease of the upper respiratory and digestive tract (e.g., floor of mouth, soft palate, retromolar trigone, and salivary glands), post-mastectomy chestwall, and post-lumpectomy tumor bed and lymph nodes. It is sometimes used to treat diseases of the retina or orbit, as well as spine (e.g., craniospinal irradiation) and paraspinal muscles. Electron beam therapy may also be used in intracavitary irradiation of the cervix or intraoperatively to treat the pancreas of other abdominal structures.

1.2 Modern Electron Beam Accelerators

The widespread proliferation of electron radiotherapy has been made possible by the development of the modern clinical linear accelerator (LINAC). Modern LINACs produce therapeutic electron beams by virtue of several key components. Electrons are thermonically emitted from a filament (e.g., electron gun) and are injected into an accelerator chamber. The electrons are then accelerated by one of two methods. Accelerators that utilize the standing wave accomplish this by use of a klystron. Conversely, LINACs, such as Elekta's *Infinity*, implement the traveling wave method by use of a magnetron.

The accelerated electron beam exits the linear accelerator approximately as a monoenergetic, monodirectional pencil beam and enters the treatment head (illustrated in Figure 1(a)), which performs four main purposes:

1. Redirect: The length of the accelerator cavity required for particle acceleration is relatively long (approximately 1-2 meters), and the beams created are horizontal. Therefore, the beam must be redirected from its axis of travel parallel to the patient treatment couch to one perpendicular to it. This is accomplished by using an achromatic bending magnet to change the particles' trajectory by either 90˚ or 270˚ (depending on manufacturer) with respect to the accelerating chamber. Elekta utilizes a slalom-type, achromatic bending magnet to bend its beam just over 90˚ and to refocus the particles into a point.

2. Broaden and Flatten: After the electron beam has been redirected, it is then necessary to broaden the beam to as large as 30x30cm^2 to enable clinical use. This is achieved by use of a thin high-Z foil placed near the exit window. After passing through this

foil, the beam is broadened, but has a non-uniform fluence, and, in fact, is nearly Gaussian. Clinical beams are desired to be as uniform as possible, so Bjarngard (1975) first demonstrated the use of a Gaussian-shaped secondary foil (consisting of stacked disks) to scatter the more intense central portion of the beam radially outward, thereby increasing uniformity. This has become the convention, and all non-scanning type electron beams utilize dual foil scattering systems. An illustration of the dual scattering foil system is included in Figure 1(b).

3. Collimate: Because treatment volumes vary from patient to patient and from procedure to procedure, it is necessary to be able to collimate the electron beam to an arbitrary shape. Electron treatment heads incorporate a variety of collimation systems, but the most common are electron applicators, typically ranging in field sizes (defined at isocenter) from 6x6cm^2 up to 25x25cm^2,depending on manufacturer. Electron fields can be further customized by use of Cerrobend—a metal alloy with a low melting point, used to shape fields specifically for individual patient targets. Pre-collimation of the beam upstream of the applicators by the x-ray collimators reduces radiation leakage outside the field. For special procedures, such as intraoperative or intracavitary, specialized applicators are used.

4. Monitor: Modern linear accelerator heads typically contain two parallel plate, segmented ionization chambers. These chambers monitor the flatness and symmetry of the beam in orthogonal directions, as well as output. If either of these chambers detect significant changes in any of these three parameters, interlocks will automatically shut off the beam.

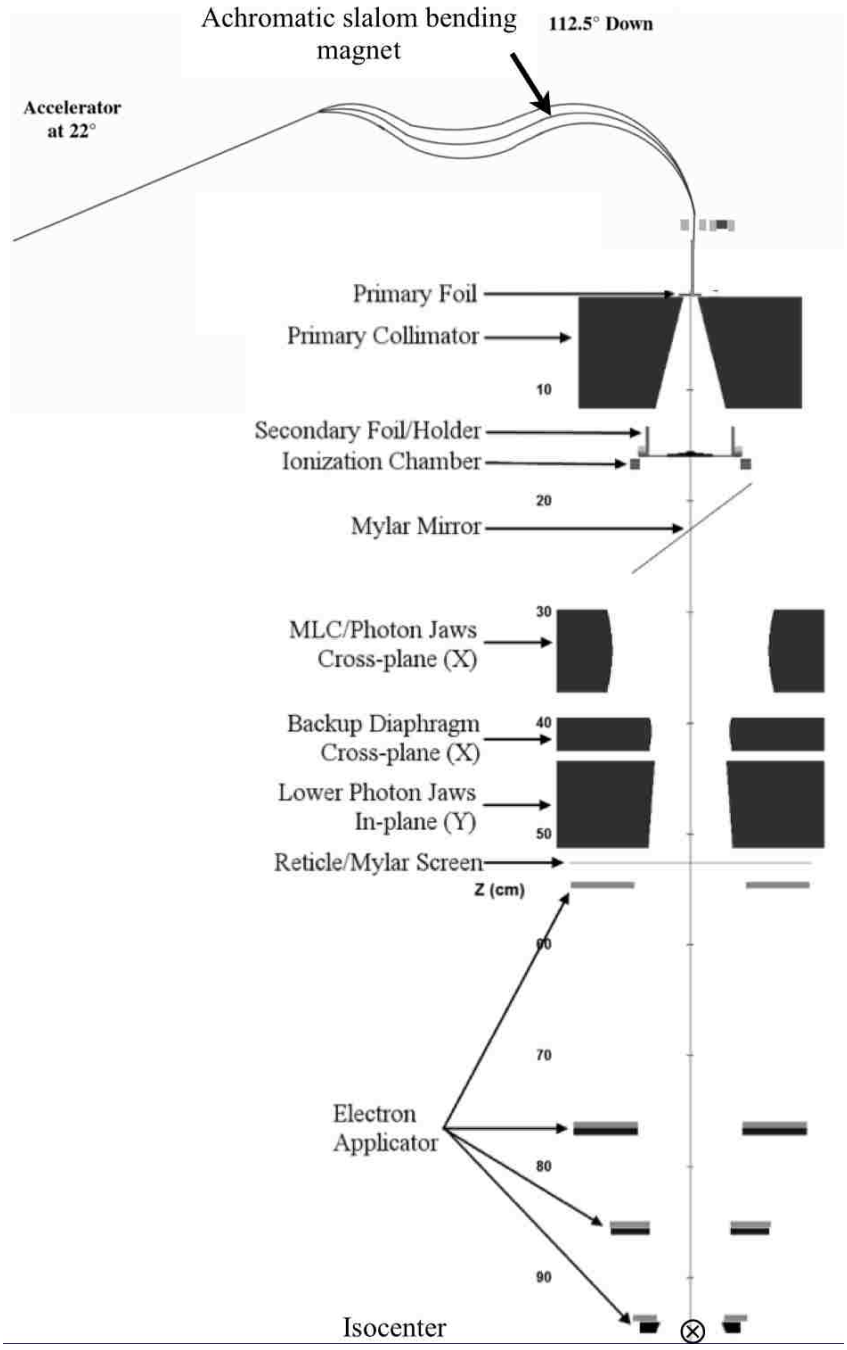

(a)

Figure 1: Illustration of (a) the Elekta Infinity treatment head, depicting beam components from the exit window to the primary x-ray collimators (figure adapted from Harris 2012) and (b) the dual foil scattering system system (figure adapted from Karzmark *et al*. 1993).

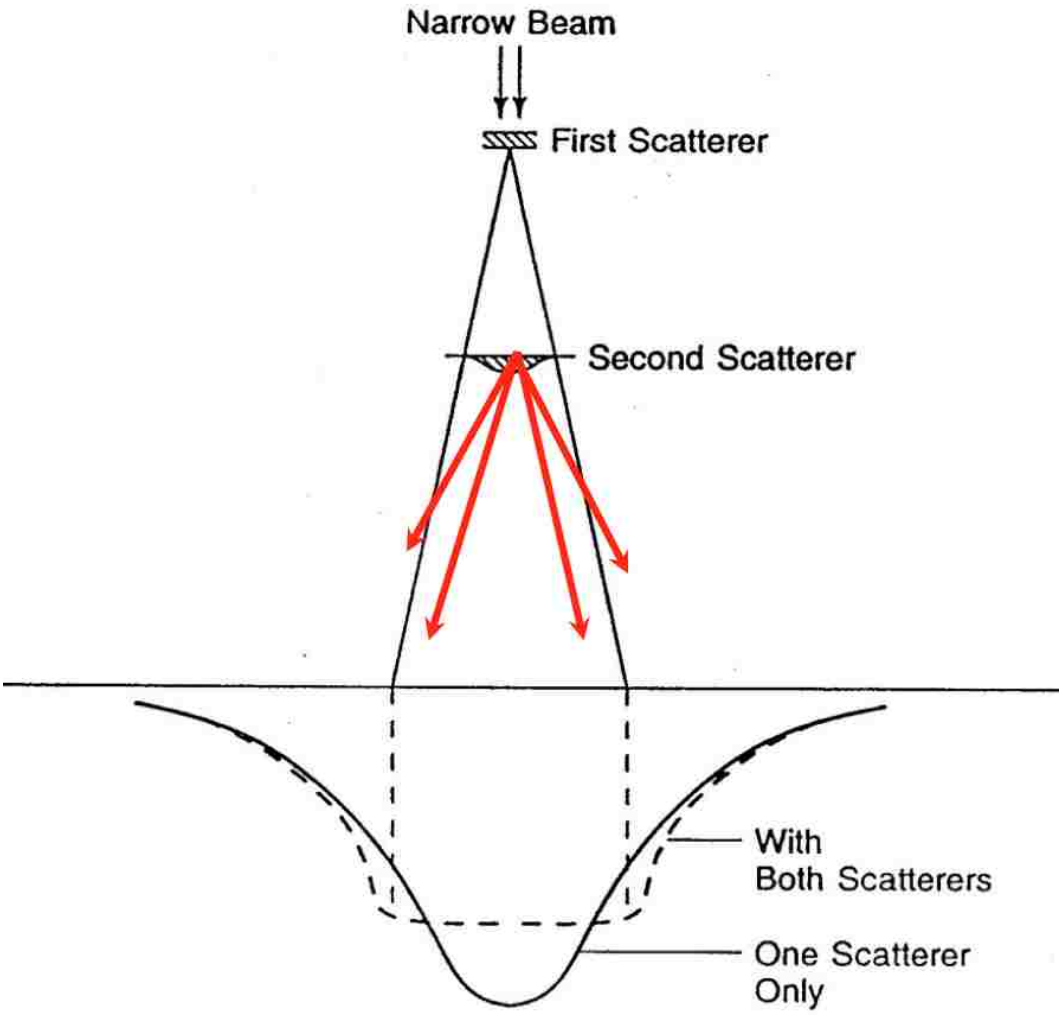

Figure 1 (continued): Illustration of (a) the Elekta Infinity treatment head, depicting beam components from the exit window to the primary x-ray collimators (figure adapted from Harris 2012) and (b) the dual foil scattering system (figure adapted from Karzmark *et al*. 1993).

1.3 Elekta Electron Beams

1.3.1 Uniqueness of Utilization of Elekta at MBPCC

Clinical electron beams are typically specified by the shape of the central axis depth dose curve and cross-field profiles along the principal axes and diagonals. Prior to the installation of Elekta Infinity accelerators at Mary Bird Perkins Cancer Center (MBPCC),

several unique specifications were laid out. Instead of beam energies being specified in terms of nominal most probable surface energies, MBPCC required that electron beam energies be tuned to specified R_{90} values, so the electron beams were tuned such that the resulting R_{90} produced were 2, 2.5, 3, 3.5, 4, 5, and 6 cm.

In the American Association of Physicists in Medicine's Task Group 25, Khan *et al*. (1991) recommended that the variation in the cross-field and diagonal dose profiles normalized to central axis should be within ±5% over the clinically relevant range. Clinically relevant range refers to 2cm inside the 50% off-axis ratio (OAR) along the principal axes, and $2\sqrt{2}$ cm inside the 25% OAR along the diagonals. Prior to commissioning, MBPCC stated its own more stringent flatness requirements: ±3% along the principal axes and ±4% along the diagonals. Figure 2 shows diagrams depicting MBPCC's flatness specifications, as well as the clinically relevant range over which dose is evaluated for flatness along both the principal axes and the diagonals.

These unique specifications were made with the philosophy that multiple Elekta Infinity accelerators may be matched. MBPCC is currently installing its 5^{th} machine, and with matched electron beams a single set of commissioning data may be utilized for planning (dose calculations), monitor unit calculations, and quality assurance.

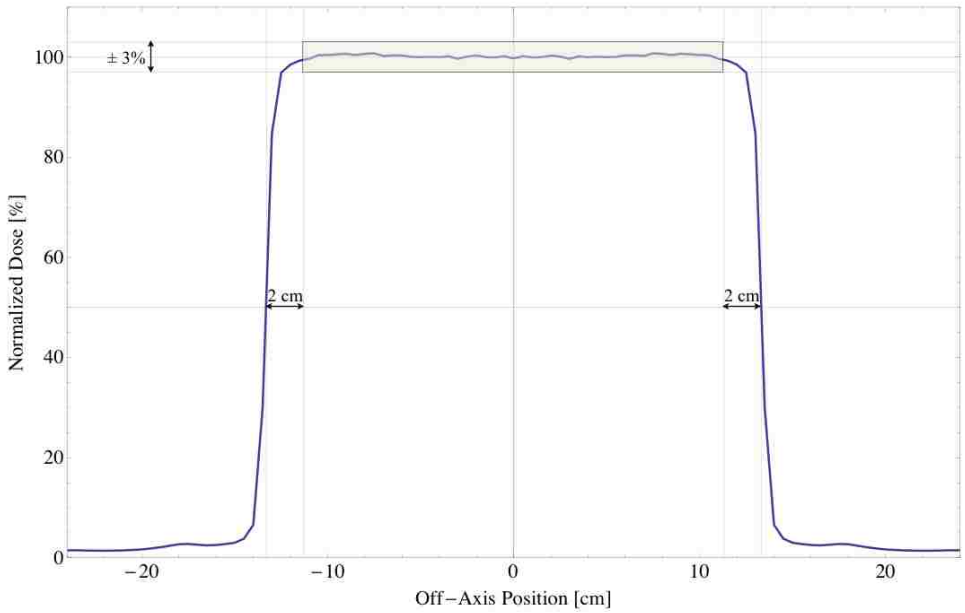

(a)

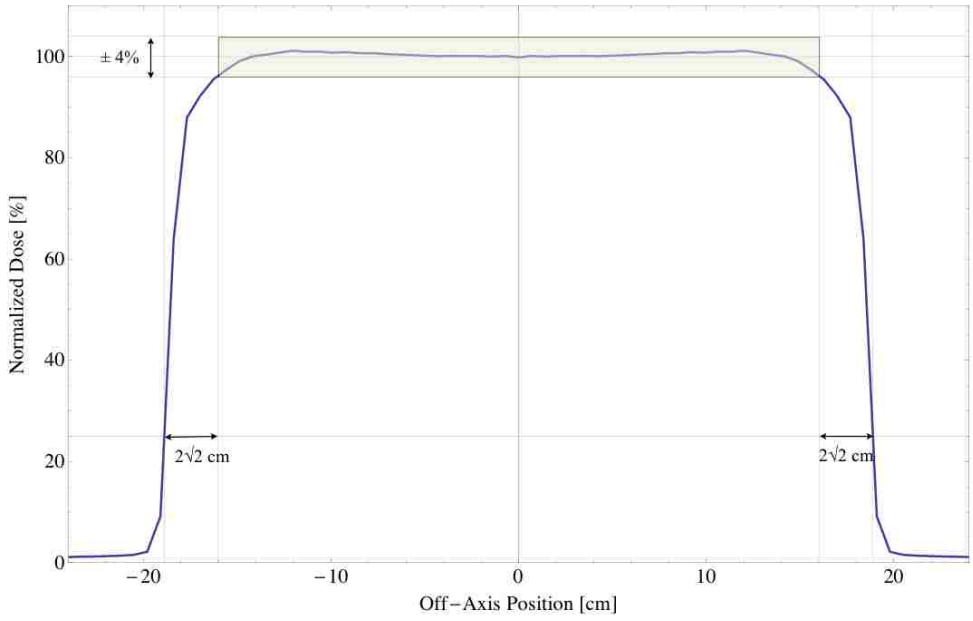

(b)

Figure 2: Diagrams depicting MBPCC's flatness specifications for (a) principal axes with collimator edge at 50% dose and (b) diagonals with corner of collimator edge at 25% dose. The shaded box in each diagram corresponds to the region over which the profile flatness is evaluated.

1.3.2 MBPCC Issues with Elekta Electron Beams

In order to achieve the flatness of the MBPCC specified beams, (whose energies and R_{90} values differ from Elekta's standard ones), Elekta had to modify their dual foil scattering system and to send factory engineers to assist in beam turning for essentially each installation. Additionally, Elekta's electron beam applicators are heavy and awkward for radiotherapists to mount and dismount as compared to their competitors.

As a result, MBPCC has an agreement with Elekta to assist them in the design of (1) a new dual foil scattering system that has equal or greater beam uniformity and greater energy robustness (i.e., capable of producing flat beams at a number of different energies) and (2) a new collimating system whose applicators are lighter, are easier to handle, and produces leakage below IEC requirements as much as reasonably achievable.

1.4 Dual Scattering Foil System Design Goal

1.4.1 Project Overview

MBPCC currently has two projects running in parallel: One to design the dual scattering foil system (the subject of this study) and one to redesign the electron collimating system. Because the electron collimating and dual foil scattering foil systems have some interdependence, they are typically designed simultaneously. This was the case for the Varian linear accelerators' electron beams, whose collimating and dual foil systems were redesigned (Klein *et al*. 1995), but for different reasons—namely (1) its previous scattering foil designs provided insufficiently flattened beams, particularly along the diagonals (Klein *et al*. 1995), and (2) its previous collimating system having had significant leakage (Keys *et al.* 1984). Redesign of that system was successful, as was reported by Klein

et al (1995), who, along with Shiu *et al*. (1994), reported details of the dose characteristics of the new electron beams.

1.4.2 Goals of Present Work

The goal of the present work is to develop a process that will allow the design of a new dual scattering foil system based on the general constraints of the present Elekta machine, such as the number of possible options for primary and secondary foil combinations. (The method put forth is not only applicable to the Elekta Infinity and could be used for other accelerators if its respective constraints were taken into account.) Furthermore, the present study will utilize the existing applicators and x-ray jaw settings (the latter with slight modifications) to develop a design process that can be used to finalize the design once the new electron collimation design is completed. As mentioned before, there is a parallel project, separate from the work of this thesis, by another graduate student to design a new collimation system using the existing dual foil scattering system.

1.5 Strategy of Dual Scattering Foil System Design

The dual scattering foil system was designed in the present work using analytical calculations, Monte Carlo calculations, and measurements. The analytical calculation was used to design a dual foil system to a predefined objective profile that considered the desired beam uniformity and the physics not modeled or not accurately modeled by the analytical calculation. The Monte Carlo calculation, which should agree with measured data, was used for the final dose calculation. When Monte Carlo calculations disagree with measurement, then such differences *should* be accounted for in the design process.

Configuring the Monte Carlo calculation for Elekta electron beams and comparing results with measurements was the subject of another student's MS thesis (Harris 2012).

Components contributing to the dose in an electron beam include that from (1) the primary electron beam, (2) x-ray production in the dual foil system, (3) electrons scattered from the x-ray jaws, (4) electrons scattered from the electron applicator, and (5) attenuation and production of x-rays in the electron applicator (Lax *et al*. 1980). All of these are included in the Monte Carlo calculation; only the major ones (1 and 2 above) are included in the analytical calculation.

The analytical calculation used in the current work was an enhancement to the model presented by Green (1991). Green's model transported only the primary electron beam using Fermi Eyges theory (Green 1991; Grusell 1994). It required an energy- and Z-dependent correction factor (K-factor ranged from 0.39 to 1.01) to the ICRU Report 35 (ICRU 1984) calculation of scattering power. Although it did not model any of the above effects other than the primary electrons , it had excellent agreement with measured data for the Siemens electron beams without electron collimation. It modified its objective profile so that with the addition of collimation, a flat beam was produced, attributing that difference to collimator scatter from the Siemens x-ray jaws.

Green's model was improved by Kainz *et al*. (2005), whose primary modification was using the Gaussian term of the Moliere method for calculation of scattering powers. It agreed well with Monte Carlo calculations so long as the initial energy spread was not too large (<50%) (Kainz et al 2004).

The analytical calculation used in the present study was modified to (1) include an off-axis bremsstrahlung component from the dual foil system, (2) use the reduced-Gaussian calculation of scattering powers, (3) use the mean electron rather than the most probable energy in its calculations (the latter used by Green), and (4) include an improved method for calculation of the magnitude of the bremsstrahlung dose component (discussed in Chapter 2). Preliminary Monte Carlo calculations revealed that scatter from the Elekta x-ray collimators has a small impact on the shape of the beam's off-axis profile (<1.5%). Moreover, the magnitude of this impact varies little with either jaw positions or energy (cf. Appendix A). Therefore, collimator scatter and applicator attenuation of the bremsstrahlung dose component were not modeled.

1.6 Hypothesis

A dual foil scattering foil system within the constraints of the Elekta Infinity radiotherapy linear accelerator can be designed such that clinical beams meet flatness criteria of ±3% (±4%) along its principal axes (diagonal axes) for the 25x25cm^2 applicator and most probable surface energies of 7-20 MeV.

1.7 Specific Aims

Aim 1 — Commissioning of Analytical Code: The analytical dual scattering foil system simulator developed at MBPCC will be commissioned for the MBPCC Elekta Infinity electron beams, and its accuracy will be assessed by comparing its calculations with (1) comparable Monte Carlo simulations for the off-axis dose profile along the major axes (at a depth of 1 or 2 cm) for the primary foil without and with the secondary foil in the absence

of the x-ray jaws and electron applicators and (2) measured central-axis x-ray dose at a depth of R_p+2cm.

Aim 2 — Initial Design of Elekta Scattering Foil System: The analytical electron dual scattering foil system simulator will be used to design three secondary foils (Gaussian-shaped, Aluminum) and five primary foils (each a multiple of a single uniform Tantalum thickness) from which a combination of the two sets will be selected for beams spaced in 1-MeV increments from 7 to 20 MeV (most probably energy at isocenter). The optimal design will closely match at each energy the calculated profile with an objective profile, which if met, should result in the Monte Carlo calculating an off-axis dose profile that results in a uniform beam, i.e., within ±3% (±4%) of central axis dose over the specified range (2 cm inside the edge of a 25x25cm^2 applicator at isocenter).

Aim 3 — Use of Monte Carlo Dose Calculation for Refinement of Design of Electron Dual Scattering Foil System and Resulting Dose Calculation: The results of Aim 2 will be compared with Monte Carlo dose calculations, after which the objective profiles used in Aim 2 will be modified such that a second optimization should provide more uniform beams. The Monte Carlo dose calculations with the revised design of electron dual scattering foil system will be used to test the hypothesis.

Chapter 2 Aim 1 — Commissioning of Analytical Code

Aim 1: The analytical dual scattering foil system simulator developed at MBPCC will be commissioned for the MBPCC Elekta Infinity electron beams, and its accuracy will be assessed by comparing its calculations with (1) comparable Monte Carlo simulations for the off-axis dose profile along the major axes (at a depth of 1 or 2 cm) for the primary foil without and with the secondary foil in the absence of the x-ray jaws and electron applicators and (2) measured central-axis x-ray dose at a depth of R_p+2cm.

The methodology used in this study for design of new dual scattering foils for electron beams consisted of multiple steps: (1) initial dual foil designs using an analytical dual scattering foil system simulator to give desired off-axis profiles, (2) comparison of Monte Carlo calculations with the analytical calculations, (3) modification of the desired off-axis profiles (objective profiles) for the analytical simulator based on comparison of its results with those from Monte Carlo calculations, (4) refinement of the dual scattering foil designs using the analytical simulator with the modified off-axis profiles, and (5) final Monte Carlo calculations for the refined dual scattering foil designs. Prior to this iterative process, both the analytical and Monte Carlo simulators were commissioned and validated for the radiotherapy machine for which the dual foil scattering system was designed, in this case the Elekta Infinity.

In the present section the analytical and Monte Carlo simulators will be described and their commissioning data for the Elekta machine will be provided. Then, results of idealized calculations for the analytical code will be compared equivalent ones using the Monte Carlo simulator. The Monte Carlo simulator has been validated for the current MBPCC Elekta

electron beams by comparison of calculated with measured dose distributions, percent depth dose and off-axis ratios by Harris (2012). The off-axis ratios calculated by Monte Carlo, which can be used to evaluate beam flatness and symmetry, were compared with data measured for the 25x25 cm^2 applicator as part of this study (cf. sections 3.1.1 and 3.2.1).

2.1 Methods

2.1.1 Analytical Dual Foil Scattering System Simulator

The analytical dual scattering foil system simulator used in this project was developed by Medical Physics staff at Mary Bird Perkins Cancer Center (Carver *et al.,* 2012). The physics of the simulator is based on the MS thesis of Allen Green (1991) with the following modifications: (1) scattering powers were calculated according to the reduced Gaussian distribution from ICRU Report 35 (1984) in which $\theta^2_{Reduced\ Gaussian} = \theta^2_{Molière\ Gaussian}(1 - \frac{1.330}{B})$, (2) scattering powers were evaluated using the mean energy of the electron as it traverses the foil, (3) calculation of central-axis bremsstrahlung dose was modified to include additional dependence on the effect of multiple scattering of the electrons in the primary scattering foil, and (4) calculated off-axis dependence profiles now include the component of bremsstrahlung dose.

2.1.1.a Analytical Calculation of Electron Planar Fluence

The geometry of the dual foil scattering system simulator is illustrated in Figure 3. The central z-axis corresponds to the mean direction of the electron beam incident on the primary scattering foil. The primary scattering foil, the base of the secondary scattering foil,

and the plane of calculation are all perpendicular to the z-axis, located at given by $z = 0$, $z = z_1$, and $z = z_2$, respectively. The vector $\vec{\rho}$ corresponds to the position of a given pencil beam in the plane perpendicular to central axis at z_1. The mean direction of the pencil beam comes from the primary foil, projecting at z_2 to $\frac{z_2}{z_1}\rho$.

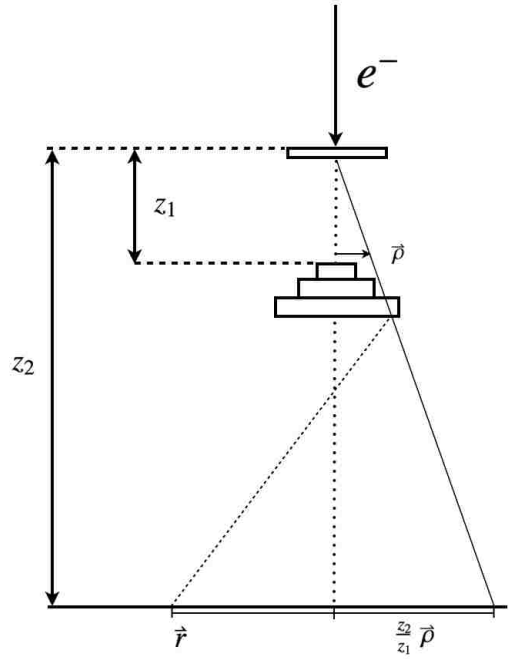

Figure 3: Illustration depicting the variables within the analytical code.

The planar fluence at z_2 per incident electron, according to Green (1991) and Kainz et *al*. (2005), is given by

$$\Phi_p(z_2,\vec{r}) = \int_0^{2\pi} \int_0^{\rho max} \Phi_p(z_1,\vec{\rho})\, \Phi_p(z_2 - z_1,\vec{r},\vec{\rho})\, \rho\, d\rho\, d\Theta \qquad (1)$$

where $\Phi_p(z_2,\vec{r})$ is the convolution of $\Phi_p(z_1,\vec{\rho})$, the electron planar fluence distribution at z_1 per incident electron, and $\Phi_p(z_2 - z_1,\vec{r},\vec{\rho})$, the planar fluence at location $\vec{r}$ in the plane z_2, per incident electron at location $\vec{\rho}$ in the plane z_1. $\Phi_p(z_1,\vec{\rho})$ is assumed to be Gaussian:

$$\Phi_p(z_1,\vec{\rho}) = \frac{1}{\pi \overline{r_1^2}} exp\left(-\frac{\vec{\rho}^2}{\overline{r_1^2}}\right), \quad (2)$$

where $\overline{r_1^2}$ is the mean square at the plane z_1 of an electron beam originating at $z = 0$, which is composed of the scattering components along the electrons' path. The spread contributed by each of these components—the exit window, the primary scattering foil, and the air gap between the primary and secondary foil—result in

$$\overline{r_1^2} = (T_{EW} t_{EW}) z_1^2 + (T_{prim} t_{prim}) z_1^2 + \frac{1}{3} T_{air} z_1^3, \quad (3)$$

where T_{EW}, T_{prim}, and T_{air} are the linear scattering powers of the exit window, primary foil, and air respectively; and t_{EW} and t_{prim} are the thicknesses of the exit window and the primary foil, respectively. The scattering kernel from $(\vec{\rho}, z_1)$ to $(\vec{r}, z_2)$ is given by

$$\Phi_p(\vec{\rho}, z_1; \vec{r}, z_2) = \frac{1}{\pi \overline{r_2^2}} exp\left(-\frac{(\vec{r} - \left(\frac{z_2}{z_1}\right)\vec{\rho})^2}{\overline{r_2^2}}\right), \quad (4)$$

where $\overline{r_2^2}$ is the mean square radius z_2 of an electron pencil beam originating at z_1, given by

$$\overline{r_2^2}(\rho) = T_{sec} t_{sec}(\rho) * (z_2 - z_1)^2 + \frac{1}{3} T_{air} (z_2 - z_1)^3 + \frac{1}{3} T_{air} z_1 (z_2 - z_1)^2. \quad (5)$$

Note that $\overline{r_2^2}$ is a function of ρ because the thickness of the secondary foil varies with ρ.

2.1.1.b Calculation of Bremsstrahlung Dose Component

Within the analytical code, bremsstrahlung dose along central axis is calculated using a similar rationale as Green (1991), but modified to include the impact of multiple coulomb scatter in the primary foil.

Central axis photon dose is assumed to be proportional to (1) the total radiative energy loss (TREL) per incident electron and (2) how that energy is spread laterally, both of which vary with energy. Central-axis electron dose is assumed to be proportional to the

electron fluence on central axis, $\Phi_p(z_2, \vec{r} = 0)$. Thus, bremsstrahlung dose, D_x, at a depth of $R_p + 2$cm as a percentage of maximum central axis dose is estimated by

$$D_x(\%) = \frac{D_x}{D_x + D_e} \approx \frac{D_x}{D_e} = K(E)\left[\frac{TREL/\sqrt{T_{pri}\, t_{pri}}}{\Phi_p(z_2, \vec{r} = 0)}\right] \times 100\% \qquad (6)$$

where D_e is the electron dose; $k(E)$ is an energy dependent proportionality constant obtained from fits to measured data; Φ_{SSD} is the planar fluence per incident electron (given by eq 1); TREL is the total radiative energy loss as calculated from ICRU (1984) radiative stopping powers for the relevant materials; and T_{pri} and t_{pri} are the scattering power and the thickness of the primary foil, respectively. This modification to Green's (1991) photon dose calculation was necessary because there was insufficient data for the Elekta machine to do empirical modeling as done by Green. The constant $K(E)$ was found by performing fits of $\frac{D_x(\%)}{E_{p,i}}$ as a function of $\frac{TREL/\sqrt{T_{pri}\, t_{pri}}}{\Phi_p(z_2, \vec{r}=0)}$. It was found that $\frac{D_x(\%)}{E_{p,i}}$ is described by a second-order polynomial of $\frac{TREL/\sqrt{T_{pri}\, t_{pri}}}{\Phi_p(z_2, \vec{r}=0)}$:

$$D_x(\%) = E_{p,i}\left[k_1\left(\frac{TREL/\sqrt{T_{pri}\, t_{pri}}}{\Phi_p(z_2, \vec{r} = 0)}\right)^2 + k_2\frac{TREL/\sqrt{T_{pri}\, t_{pri}}}{\Phi_p(z_2, \vec{r} = 0)} + k_3\right], \qquad (7)$$

where $k_1 = -2 * 10^{-10}$, $k_2 = 1.1 * 10^{-5}$, and $k_3 = .1121$ as determined by a second order polynomial fit.

Off-axis profiles for the bremsstrahlung component were accounted for using the method put forth by Shiu (1988). Photons were assumed to emanate from a virtual point source 90 cm above isocenter; therefore, (1) central-axis photon dose was assumed to vary by inverse-square and (2) off-axis profiles measured for the MBPCC Elekta Infinity at a

depth of R_p+2cm were back-projected along fan lines diverging from the virtual source to the depth of calculation.

Off-axis dose profiles are generated by adding the electron and photon (bremsstrahlung) dose components. The electron off-axis profile is constructed from the electron fluence off-axis profiles, assuming the two are identical. The photon off-axis profile is added to it weighting it by D_x(%). The resulting off-axis profile is renormalized to 100% on central axis. This is illustrated in Figure 4, which shows an example of the difference between primary electron fluence profiles with and without bremsstrahlung dose included for the 20 MeV beam. The measured bremsstrahlung dose off-axis profile (magnified x10) is also included. The difference in the off-axis profiles illustrates the need to consider bremsstrahlung dose in designing a dual scattering foil system, particularly at the higher energies were D_x can be significant.

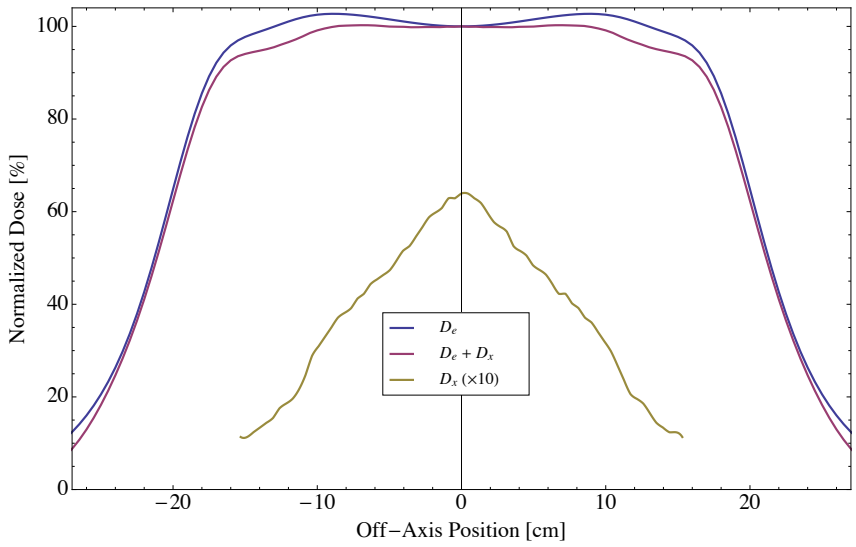

Figure 4: Design simulations with and without photon dose for 20 MeV at a calculation plane at 102cm. Plots of off-axis electron dose (D_e) and the measured bremsstrahlung dose (D_x magnified ×10 for visibility), and total dose (D_e+D_x) for 20 MeV ($E_{p,0}$=20.50MeV).

2.1.1.c Dual Scattering Foil System Simulator

From the graphical user interface (GUI), the user has the ability to change nearly all calculation parameters. Most relevant to this study are those having to with the foil characteristics, such as material composition, central axis thickness, and width (in the case of the secondary foil). The primary foil pane, shown in Figure 5, enables the user to specify the material composition of the foil, as well as its thickness. The thickness may also be varied by use of a slider-bar, and the effects on the resulting off-axis profile are displayed in real-time. Additionally, the option to calculate the off-axis profile with secondary foils absent from the beam is also available.

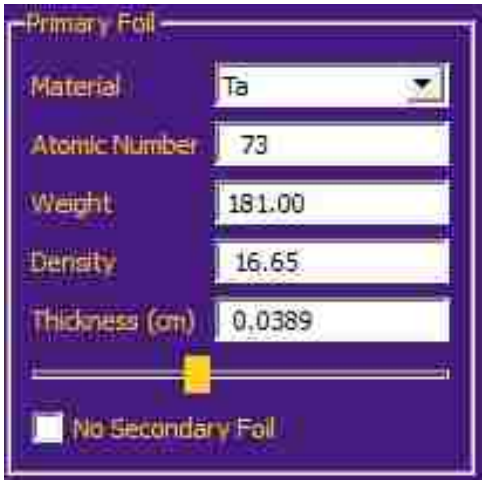

Figure 5: Screenshot of the analytical simulator's graphical user interface (GUI) primary foil parameter pane.

The secondary foil pane (see Figure 6) has a much robust set of options due to the secondary foil's increased complexity. The user has the option to select a user-specified secondary foil file in which the foil's material composition and geometry are hard-coded by the user. In this way, one is able to input into the code a preexisting foil design or a non-standard trial design. Alternatively, the user has the option to choose the program to select a design based on a Gaussian shape. In this case, the user specifies the material, overall

thickness of the foil, the width of the Gaussian, and the number of segments with which to approximate the distribution. The analytical code then determines the thickness of each individual layer based on the number of segments specified and approximates the shape of the Gaussian by intersecting the edge of each descending segment with that of the true Gaussian. Both the thickness and the width of the Gaussian secondary foil may be varied by use of slider-bars, and the resulting impact on the predicted primary electron fluence distribution is indicated in real-time, thereby allowing for rapid optimization of foil parameters.

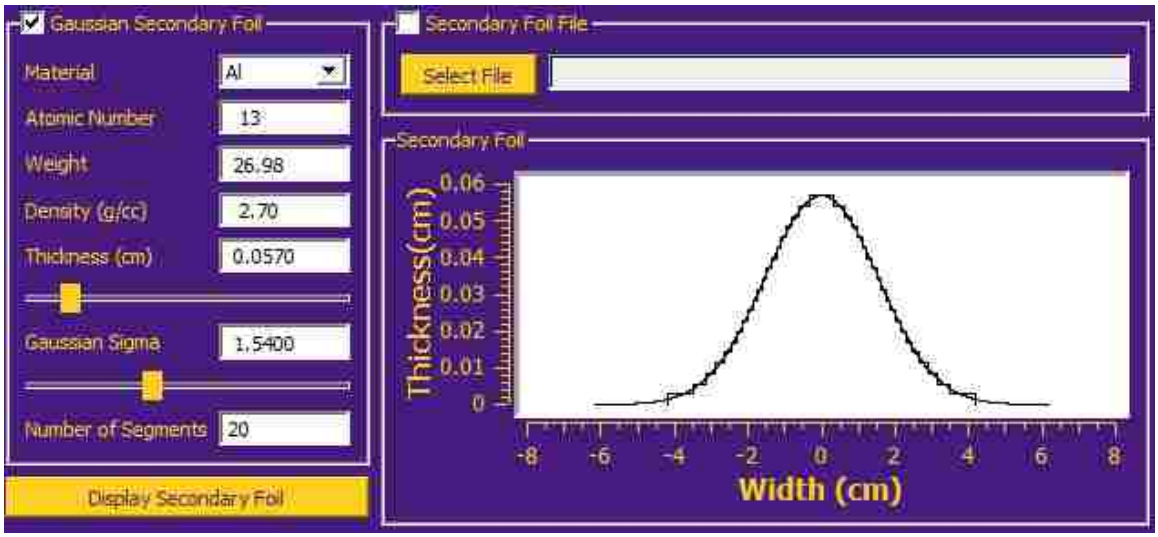

Figure 6: Screenshot of the analytical simulator's GUI secondary foil parameter pane.

In the simulation settings pane (Figure 7) the user has the ability to alter the separation between the primary and secondary foils, the calculation depth, and the thickness of the accelerator exit window (currently constrained to be nickel). Moreover, the option to forward-calculate energy (not shown) provides the versatility for accelerator energy to be specified in terms of either most probable energy at the surface, $E_{p,0}$, or incident monochromatic energy incident on the accelerator end window.

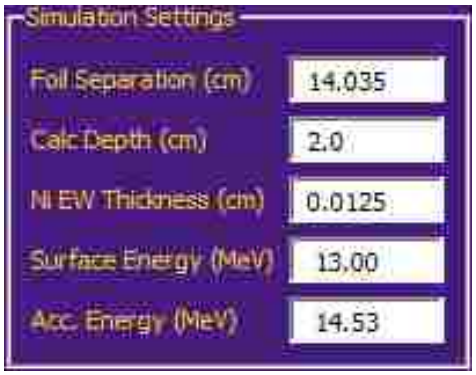

Figure 7: Screenshot of the analytical simulator's GUI simulation settings pane.

In the profile pane (Figure 8) the user can see the real-time display of relative off-axis fluence or dose profile for a given dual scattering foil combination. This pane is also where the bremsstrahlung dose is displayed. Here the user has the option to exclude or include x-ray dose. If x-ray dose is included, the user must specify which measured off-axis bremsstrahlung dose profile to use for the calculation. Finally, the user has the option to display a comparison plot along with the calculated profile. If this option is chosen, the analytical simulator automatically calculated the deviation between the two profiles within a user-specified range. (indicated by the vertical red lines in the

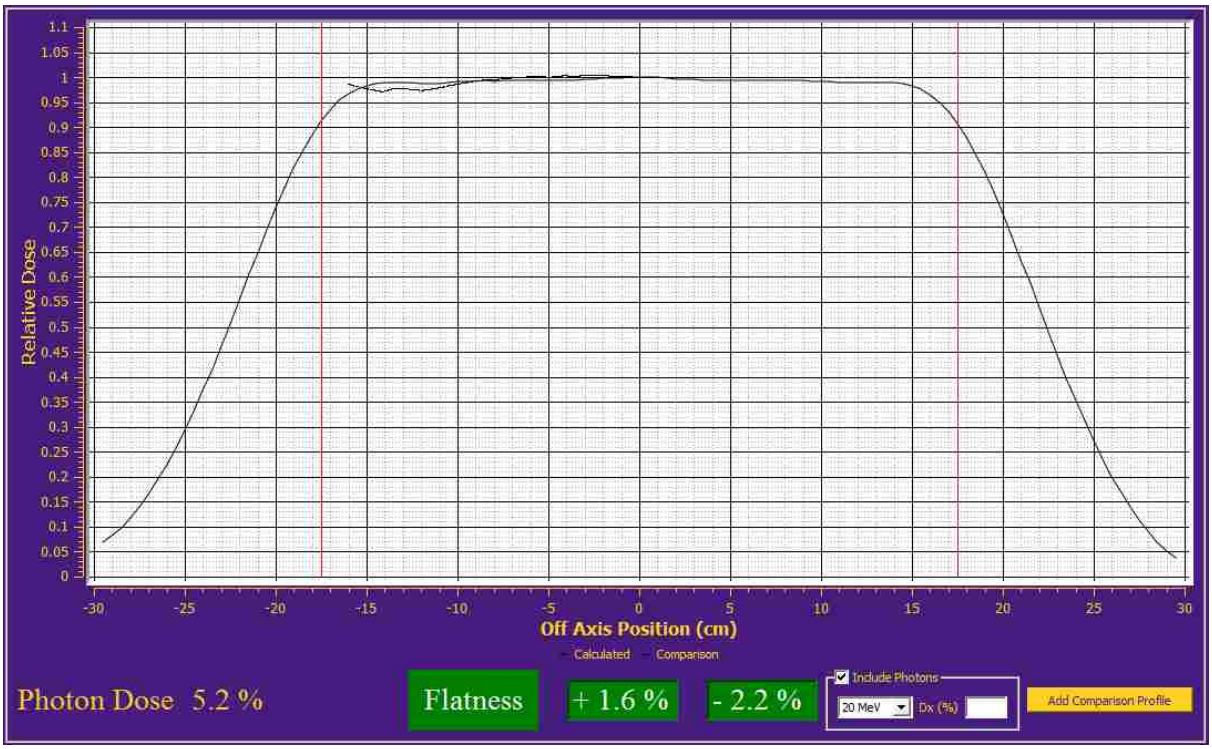

Figure 8: Screenshot of the analytical simulator GUI profile pane.

2.1.2 EGSnrc Monte Carlo Simulator

The EGSnrc Monte Carlo package is an electron and photon transport modeling utility that contains the physics necessary to simulate electron and x-ray beams generated by radiotherapy electron accelerators (Kawrakow *et al.* 2011). BEAMnrc, which is built on EGSnrc, is accompanied by pre-coded component modules, thereby making the geometric construction of an accelerator significantly simpler. The model used in the current work was developed by Guy Harris as a part of his Master's thesis (2012). Geometrically, the inputs to the EGSnrc model consist of all relevant machine components, and may include: exit window, primary foil, primary collimator, secondary foil, ion chamber, mirror (for optical distance indicator), x-ray collimation (jaws and multi-leaf collimator), electron applicators, and collimating insert. Harris determined beam characteristics, including incident Gaussian energy spectra, initial angular divergence of the beam (0˚), and Gaussian

focal spot size (2mm×1mm FWHM) that allowed for the matching with clinical data. The identical input files was used in the present study with the expectation of spot size for which 1mm×1mm FWHM was used.

EGSnrc may be used to generate phasespaces at desired spatial locations. These phasespaces contain relevant information about radiation transported by the code, such as particle type, energy, position, and direction. For the validation of the analytical code, phasespaces were scored in air at 101cm for the beam energy of 7MeV and at 102cm for all beam energies greater than or equal to 9MeV. Phasespaces were then analyzed using BEAMDP, which is a component program of the EGSnrc software package. BEAMDP allows for the derivation of phasespaces' electron fluence profiles, which were then directly comparable to the analytical simulator's output, once normalized.

All Monte Carlo simulations were calculated using *Tezpur*, one of Louisiana State University's High-Performance Computing (HPC) clusters. *Tezpur* runs Red Hat Enterprise Linux 4 and is comprised of 360 compute nodes, each containing two 2.66GHz Dual Core Xeon 64-bit processors.

2.1.3 Validation of Analytical Simulator

2.1.3.a Validation of Primary Electron Fluence (Primary Foil Only)

As a first step, the analytical simulator's ability to accurately calculate scattering powers and energy losses through the primary foil was validated. This validation consisted of comparisons between Monte Carlo and analytical simulator calculations performed containing only the 0.0125 cm thick nickel exit window and various thicknesses of a Ta primary foil in the beam (see Figure 9 for schematic). Without the secondary foil and with

the bremsstrahlung dose profile component turned off, the analytical simulator predicts the primary electron fluence distribution as a strict Gaussian at the calculation plane (101 or 102). Monte Carlo simulations provided a method by which to determine the reasonableness of this inherent assumption. In order to make the Monte Carlo parameters congruent with the calculations of the analytical simulator for these tests, the incident electron beam was modeled with zero angular spread, zero radial spread, and the incident energy being monoenergetic. A total number of 2 billion histories were run to ensure adequate statistical precision at each pixel. From the resulting phasespaces file, the off-axis electron fluence distribution was extracted and normalized to 100% on central-axis for comparison with the result of analytical simulations.

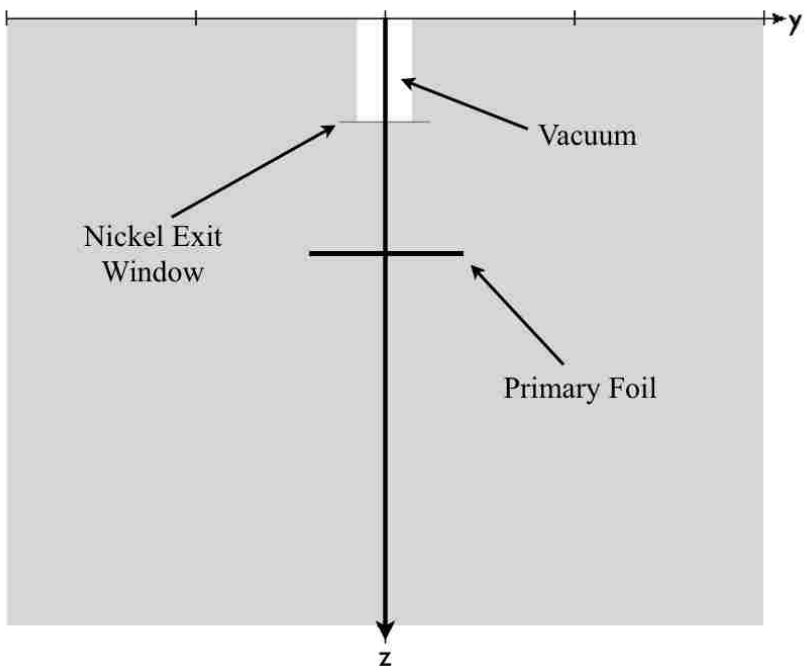

Figure 9: Schematic depicting the accelerator geometry used in the first order validation of primary foil scattering powers.

Comparisons were performed for the range of energies offered by the Elekta Infinity at Mary Bird Perkins Cancer Center accelerator. The energies for which these comparisons performed and Ta thicknesses used may be found in Table 1.

Table 1: List of primary foil thicknesses evaluated in first-order validation of analytical code.

$E_{nominal}$ [MeV]	$E_{p,0}$ [MeV]	Primary Foil Thickness [cm of Ta]
7	7.15	0.0069
9	8.66	0.0138
10	9.92	0.0069
11	11.28	0.01035
13	13.13	0.0138
16	16.22	0.0069
20	20.5	0.0138

2.1.3.b Validation of Primary Electron Fluence (Primary and Secondary Foil)

A more rigorous validation of the overall analytical code was subsequently performed, which consisted of including the exit window, primary foil, and secondary foil in both the Monte Carlo and analytical simulator calculations (see Figure 10 for schematic). For the analytical simulator calculations, the current secondary scattering foils were hard-coded into input files containing the shape and material compositions readable by the analytical code. Figure 11 shows diagrams of the three secondary foils currently utilized in the Elekta Infinity accelerator at MBPCC Baton Rouge. Each foil is made entirely of aluminum, except for a small 0.005 cm thick tantalum disk that sits atop the secondary foil used for the 7 and 9 MeV beams.

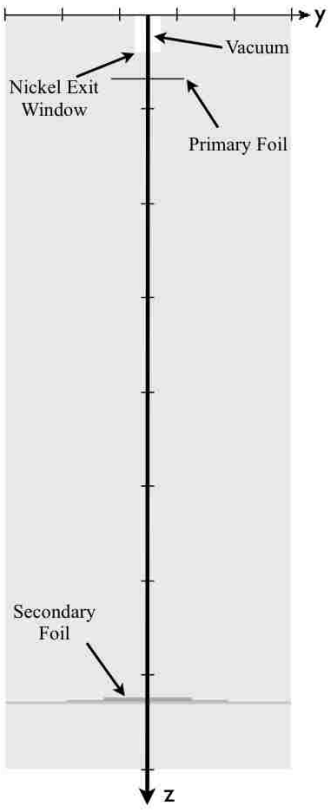

Figure 10: Schematic depicting the accelerator geometry used in the validation of the fluence calculation when both primary and secondary foils are included.

Monte Carlo simulations of 2 billion histories were performed with a monoenergetic incident electron pencil beam having zero radial or angular spread. In these simulations the only beam elements modeled in the Monte Carlo were the nickel exit window, the tantalum primary foils, and the secondary foils. The secondary foil holder, which is comprised of steel and aluminum, were not included in the model because these are not taken into account within the analytical code. Phasespaces were scored at 102 cm for all energies except for 7 MeV, for which a phasespace was scored at 101 cm, per recommendations by Khan *et al.* (1991). From the resulting phasespaces file, the off-axis electron fluence distribution was extracted and normalized to 100% on central-axis for comparison with the result of analytical simulations. Agreement between the Monte Carlo and analytical

simulator calculation was evaluated across the entire range of the Monte Carlo data (±24.5cm), but the region of particular interest is that of ±17.6 cm from central axis. This is because that distance corresponds to the span of the diagonal of a $25\times25cm^2$ applicator field.

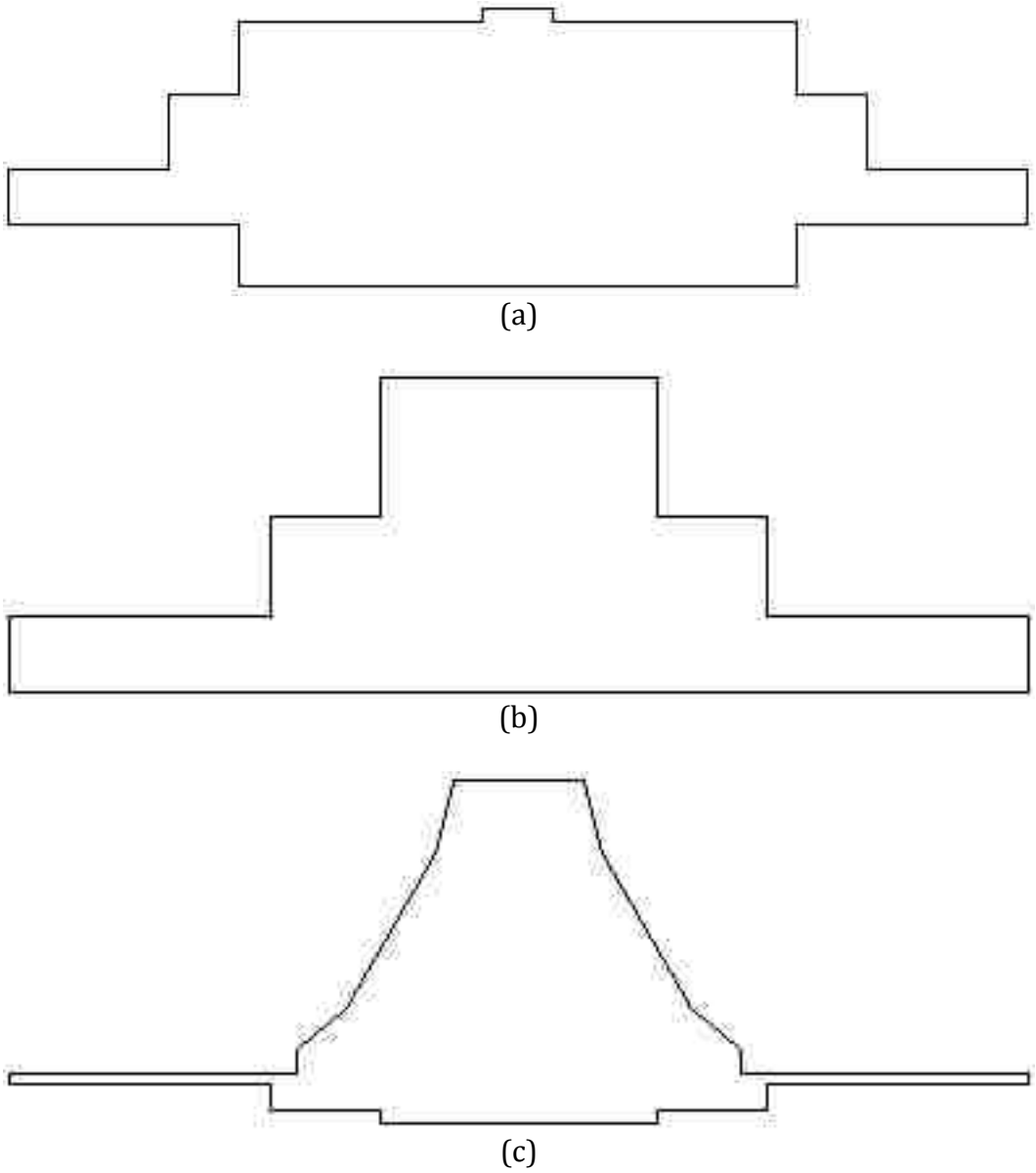

Figure 11: Diagrams depicting the secondary foil used for (a) 7 and 9 MeV, (b) 10, 11, and 13 MeV, and (c) 16 and 20 MeV.

2.1.4 Validation of Analytical Simulator Calculation of Bremsstrahlung Dose

The analytical code's calculation of central-axis bremsstrahlung dose component (D_x) was validated by comparison to measured clinical data. Agreement between the two would provide a high degree of confidence that the analytical code will accurately predict bremsstrahlung dose during the foil design process. Clinical measurements were taken from commissioning data for the Elekta Infinity accelerator located at Mary Bird Perkins Cancer Center in Baton Rouge, LA. Depth dose measurements were available for each of the beam energies, wherein which photon dose contamination percentages could easily be obtained for each of the required depths (R_p+2cm).

2.2 Results

2.2.1 Analytical Code vs. Monte Carlo — A First Order Validation

Across the entire energy range used at Mary Bird Perkins Cancer Center (7-20 MeV), the analytical code's predicted primary electron fluence per incident electron agreed extremely well with Monte Carlo simulations over ranges that are clinically relevant. Plots of data obtained from Monte Carlo simulations and analytical code executions may be found in Figure 12. At 7, 11, and 13 MeV, agreement was essentially within 1.6% within 20 cm of central-axis. The analytical simulator slightly over-predicted Monte Carlo calculations at 9 MeV and under-predicted Monte Carlo calculations at 10, 16, and 20 MeV, being greatest at the higher energies. Within ±24 cm of central axis, the greatest deviation between all Monte Carlo simulations and analytical calculations of primary electron fluence was 4.2% at 16 MeV. Table 2 shows a list of nominal energies with the associated maximum deviation between Monte Carlo and analytical predictions.

The principal cause for the deviations witnessed between the Monte Carlo and analytical prediction of electron fluence at particularly large off-axis positions is likely due the analytical simulator modeling multiple Coulomb scattering as a Gaussian, whereas the Monte Carlo uses full Moliere scattering theory. However, it is expected that this level of accuracy should be acceptable for design of dual scattering foil systems, as is demonstrated in this study.

Table 2: Table of nominal energies and the maximum deviation between Monte Carlo simulations and analytical calculations (i.e., Φ_{MC}-Φ_{DS}) within ±24 cm of central axis, expressed as a percent of fluence on central axis.

Nominal Energy [MeV]	Maximum Deviation Between Monte Carlo and Analytical Code
7	−1.6% at r = 16.5 cm
9	−2.5% at r = 18.5 cm
10	3.2% at r = 24.5 cm
11	2.6% at r = 24.5 cm
13	2.7% at r = 23.5 cm
16	4.4% at r = 18.5 cm
20	4.1% at r = 21.5 cm

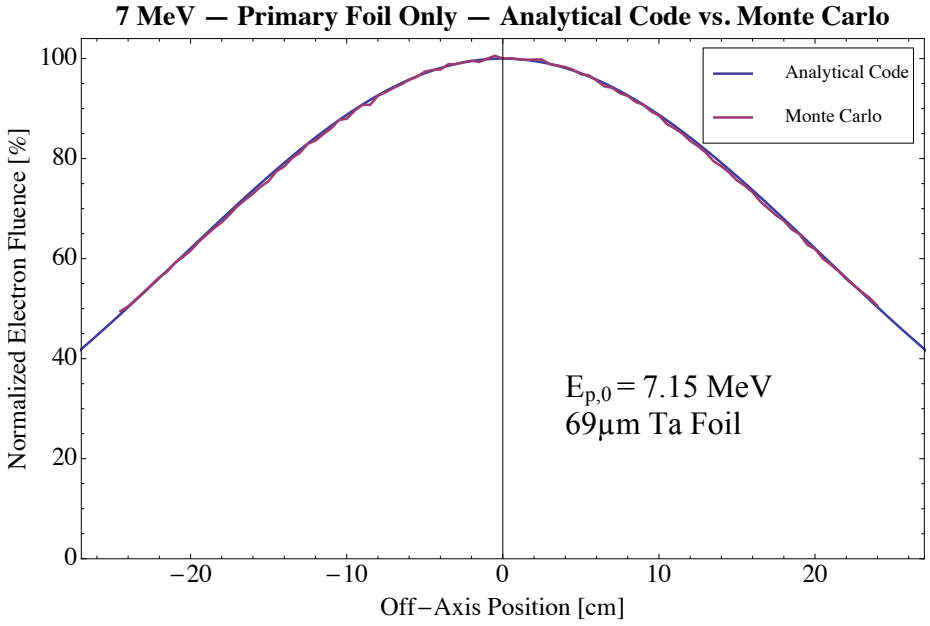

(a)

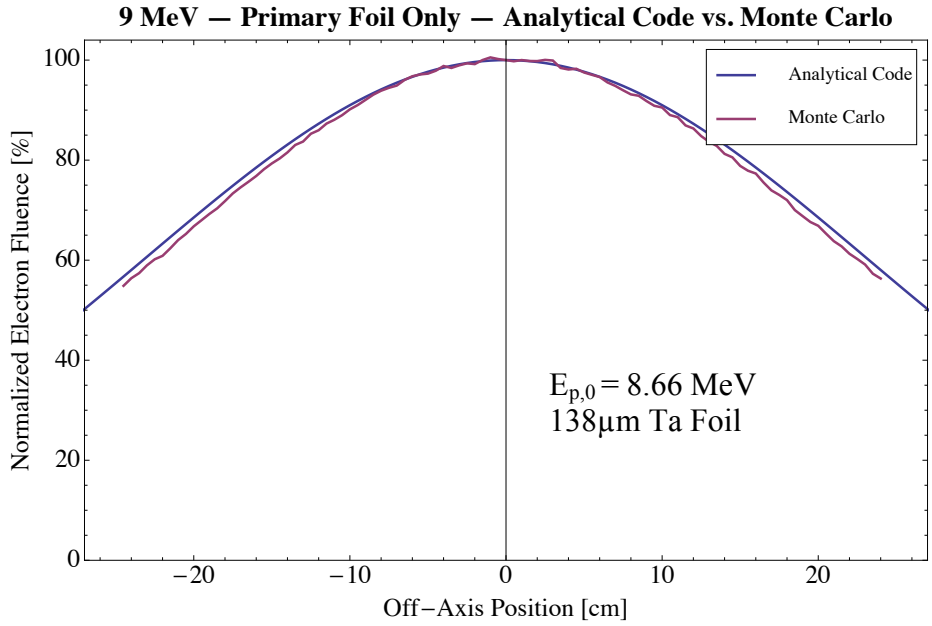

(b)

Figure 12: Plots comparing off-axis relative electron planar fluence profiles calculated by the analytical simulator with those from Monte Carlo simulations with only the Tantalum primary foil in the beam for (a) 7 MeV, (b) 9 MeV, (c) 10 MeV, (d) 11 MeV, (e) 13 MeV, (f) 16 MeV, and (g) 20 MeV.

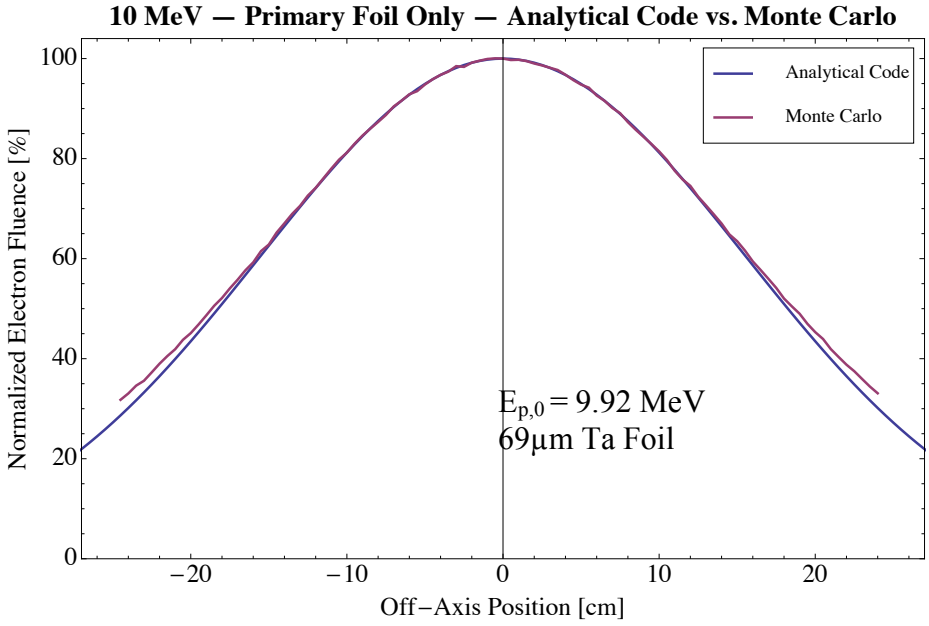

(c)

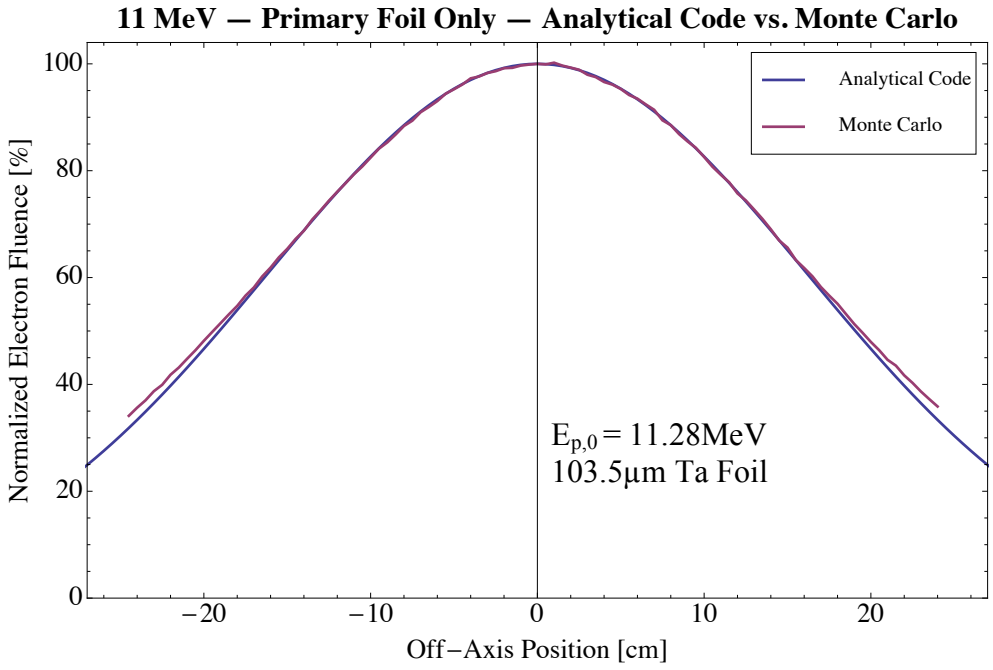

(d)

Figure 12 (continued): Plots comparing off-axis relative electron planar fluence profiles calculated by the analytical simulator with those from Monte Carlo simulations with only the Tantalum primary foil in the beam for (a) 7 MeV, (b) 9 MeV, (c) 10 MeV, (d) 11 MeV, (e) 13 MeV, (f) 16 MeV, and (g) 20 MeV.

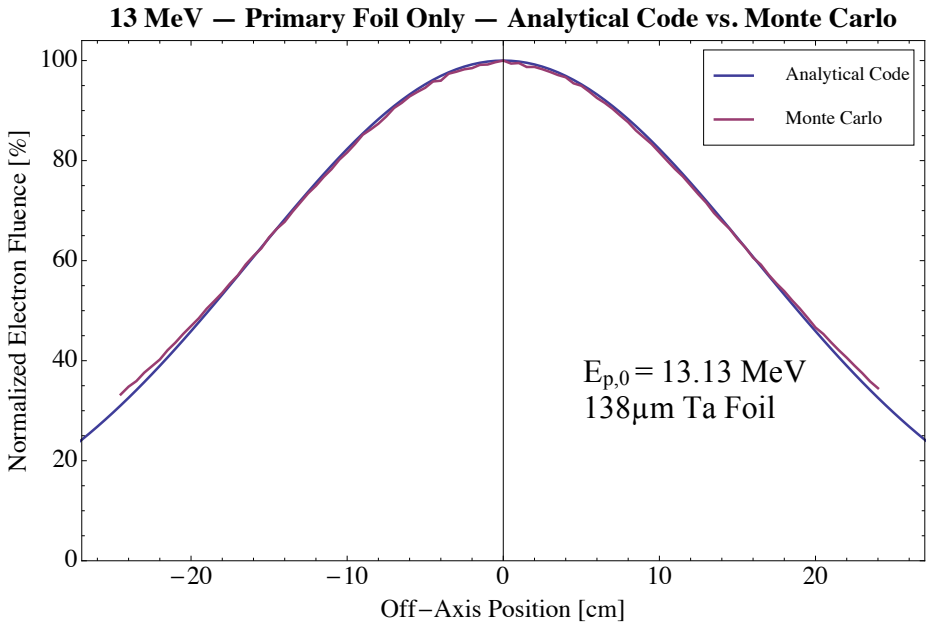

(e)

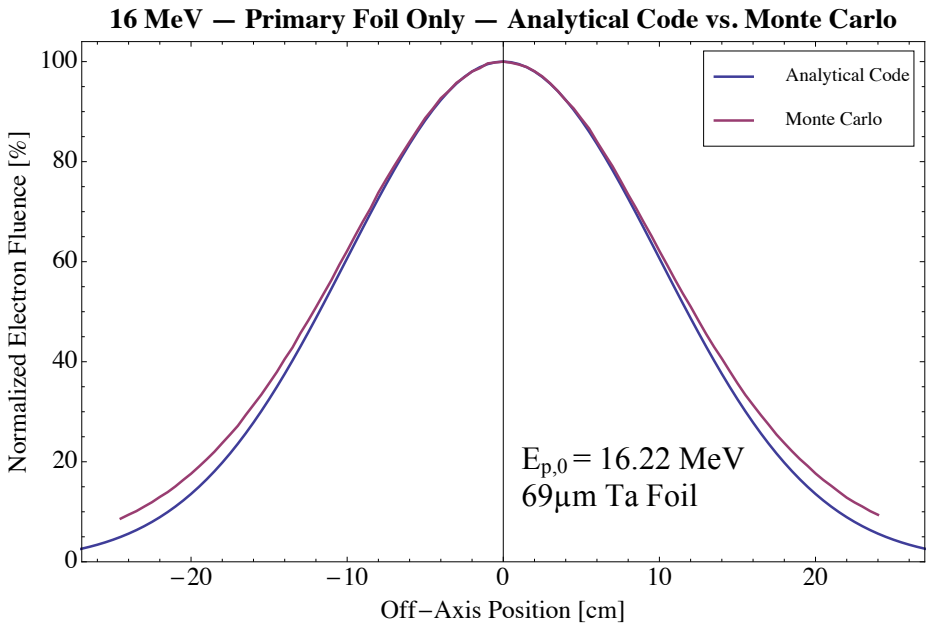

(f)

Figure 12 (continued): Plots comparing off-axis relative electron planar fluence profiles calculated by the analytical simulator with those from Monte Carlo simulations with only the Tantalum primary foil in the beam for (a) 7 MeV, (b) 9 MeV, (c) 10 MeV, (d) 11 MeV, (e) 13 MeV, (f) 16 MeV, and (g) 20 MeV.

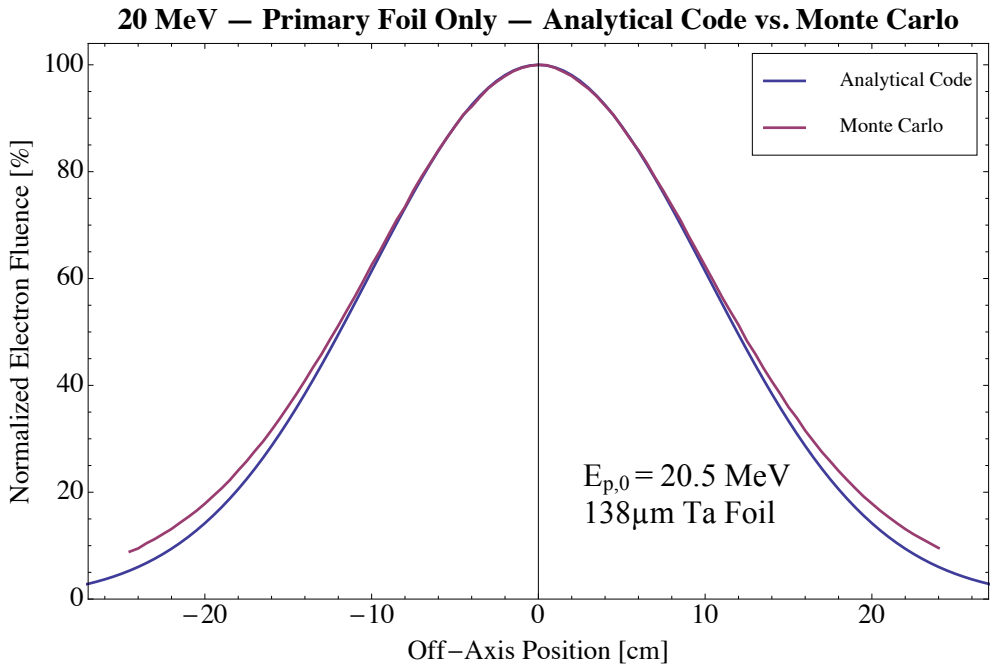

(g)

Figure 12 (continued): Plots comparing off-axis relative electron planar fluence profiles calculated by the analytical simulator with those from Monte Carlo simulations with only the Tantalum primary foil in the beam for (a) 7 MeV, (b) 9 MeV, (c) 10 MeV, (d) 11 MeV, (e) 13 MeV, (f) 16 MeV, and (g) 20 MeV.

2.2.2 Analytical Code vs. Monte Carlo: Validation of Primary and Secondary Foil Calculations

Comparisons between the Monte Carlo and analytical calculations that only include primary and secondary foils revealed a varying degree of agreement. For all energies, the analytical and Monte Carlo simulations matched well within about ±10 cm from central axis, with only the case of 9 MeV exceeding 1.5% with a deviation between the two calculations of 2.1%. Figure 13 shows a comparison plot between the two calculations for 7 and 9 MeV, which share a common secondary foil. At 7 and 9 MeV, the analytical simulator consistently over-predicted the Monte Carlo simulation by a maximum of 4.2% and 4.4% respectively, up until ±17.6cm, after which the two deviate by about 4-5%.

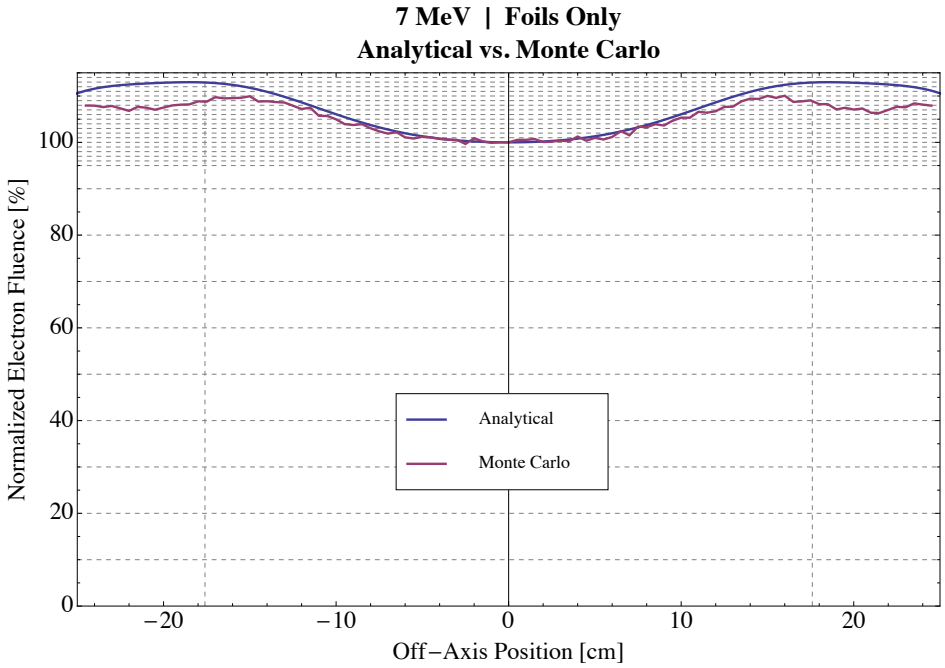

(a)

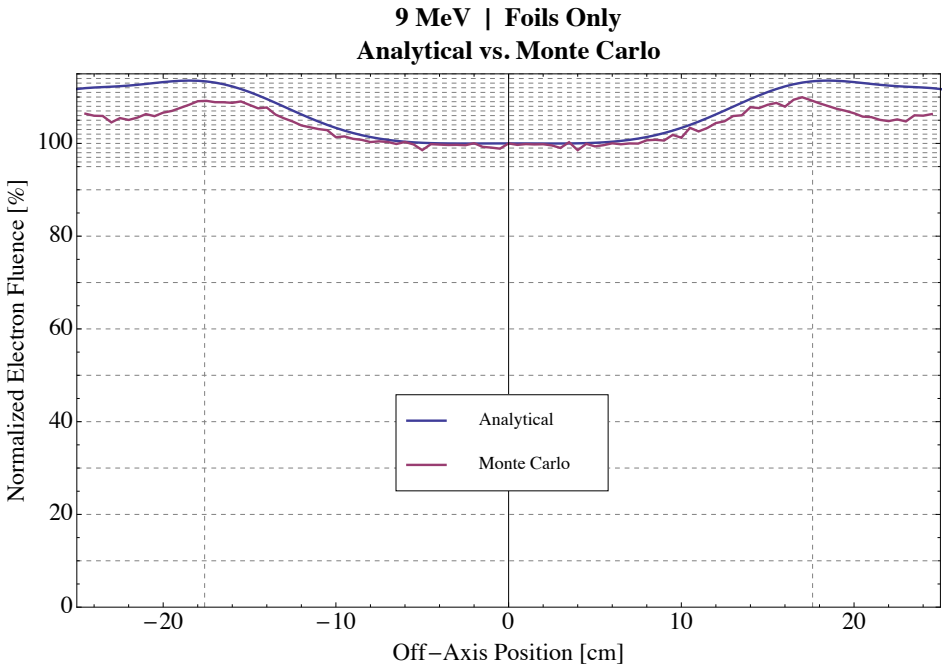

(b)

Figure 13: Plot comparing Monte Carlo with analytical simulator calculations of a monoenergetic pencil beam with only the nickel exit window, primary foil, and secondary foil in the beam for (a) 7 MeV ($E_{p,i}$ = 7.89 MeV) and (b) 9 MeV ($E_{p,i}$ = 9.53 MeV).

Figure 14 shows a comparison between Monte Carlo and analytical simulator calculations for the energies of 10, 11, and 13 MeV, which share a common secondary foil. The Monte Carlo and analytical simulator calculations agree well over the entire range of the data (±24.5cm) with the analytical simulator slightly under-predicting the Monte Carlo calculation with disagreement between the two never exceeding 2.4%. The greatest deviations between the two being 1.7%, 1.8%, and 2.4%, respectively. Within the off-axis distance of ±17.6 cm, however, the greatest deviations are less, i.e., 1.3%, 1.6%, and 1.4%.

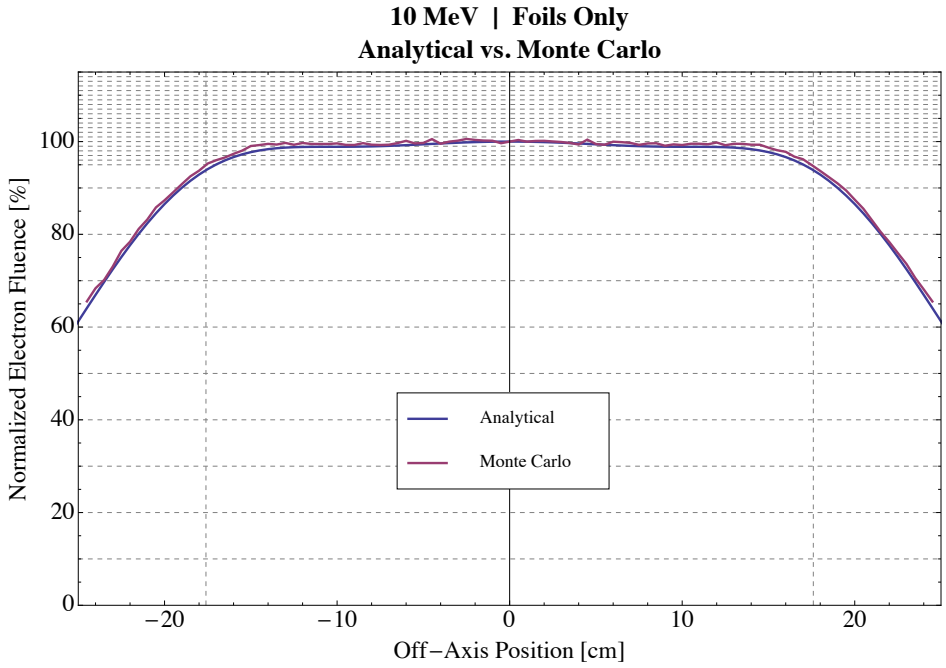

(a)

Figure 14: Plot comparing Monte Carlo with analytical simulator calculations of a monoenergetic pencil beam with only the nickel exit window, primary foil, and secondary foil in the beam for (a) 10 MeV ($E_{p,i}$ = 10.63 MeV), (b) 11 MeV ($E_{p,i}$ = 12.06 MeV), and (c) 13 MeV ($E_{p,i}$ = 13.98 MeV).

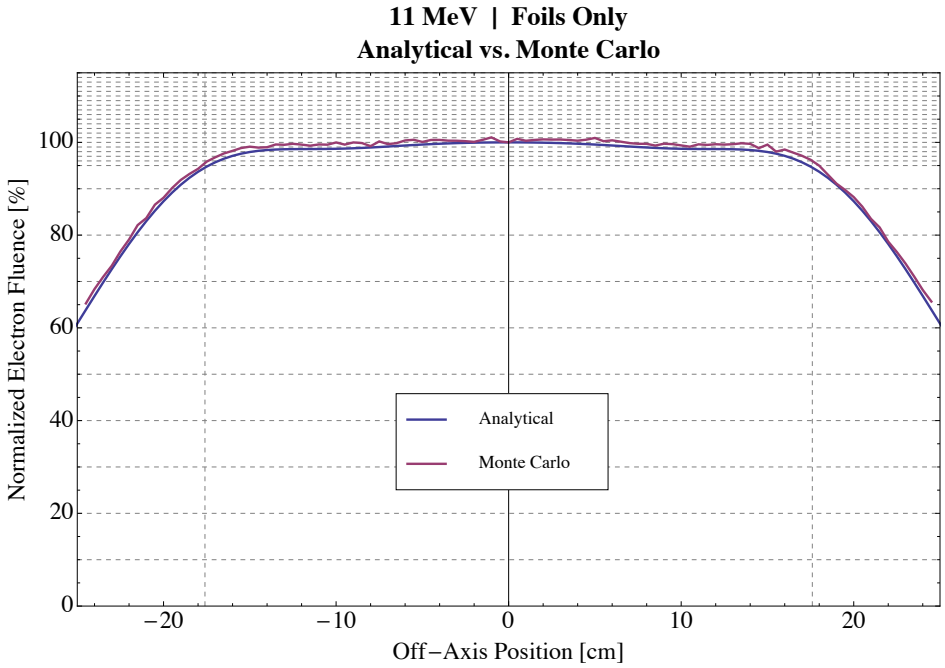

(b)

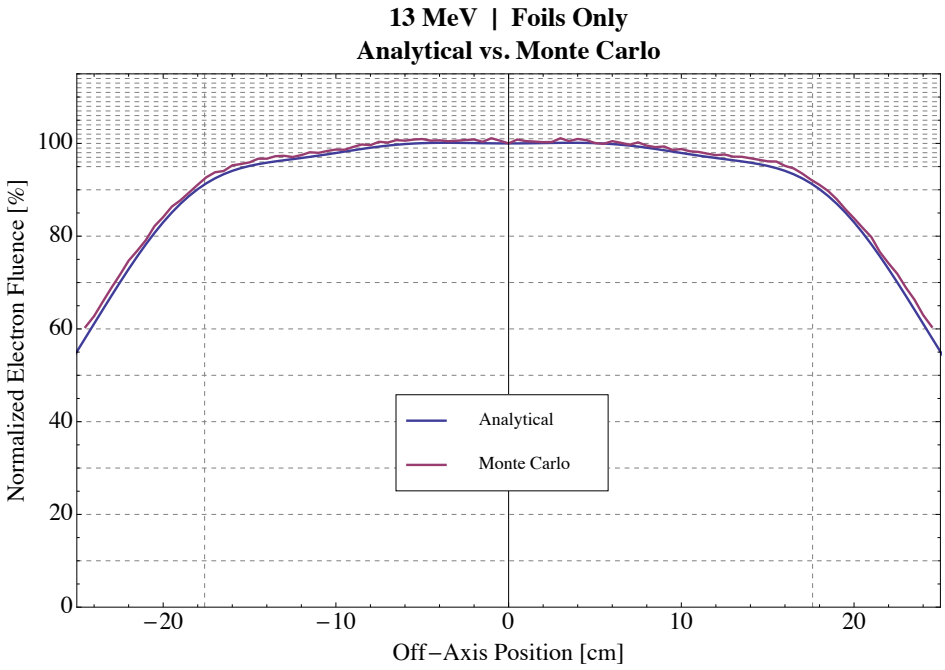

(c)

Figure 14 (continued): Plot comparing Monte Carlo with analytical simulator calculations of a monoenergetic pencil beam with only the nickel exit window, primary foil, and secondary foil in the beam for (a) 10 MeV ($E_{p,i}$ = 10.63 MeV), (b) 11 MeV ($E_{p,i}$ = 12.06 MeV), and (c) 13 MeV ($E_{p,i}$ = 13.98 MeV).

Figure 15 shows a comparison between Monte Carlo and analytical simulator calculations for the two highest energies, 16 and 20 MeV, which share a common secondary foil. Within ±12cm, the analytical simulator calculations agree with Monte Carlo calculations to within 1.1% at 16 MeV and 1.3% at 20 MeV. However, particularly high deviations occur in the fluence fall-off regions (>12cm) region. This is most likely explained by the fact that the analytical simulator under-predicts the scatter caused by the primary foil in this region (c.f. Figure 12(f)). This under-prediction causes the analytical code to also under-predict the width of the fluence profile after it passes through the secondary foil. The under-predictions are not prohibitive, however, because they occur in the dose-fall off regions, which typitcally doe

Computation times between the two methods differed by approximately 7 orders of magnitude (10^7). Typical computation times for Monte Carlo simulations of fluence after passing through both primary and secondary foils took approximately 5-6 hours when using 20 nodes (80 processors). In contrast, the fluence profile calculation times were on the order of milliseconds when using the analytical simulator on a standard personal computer.

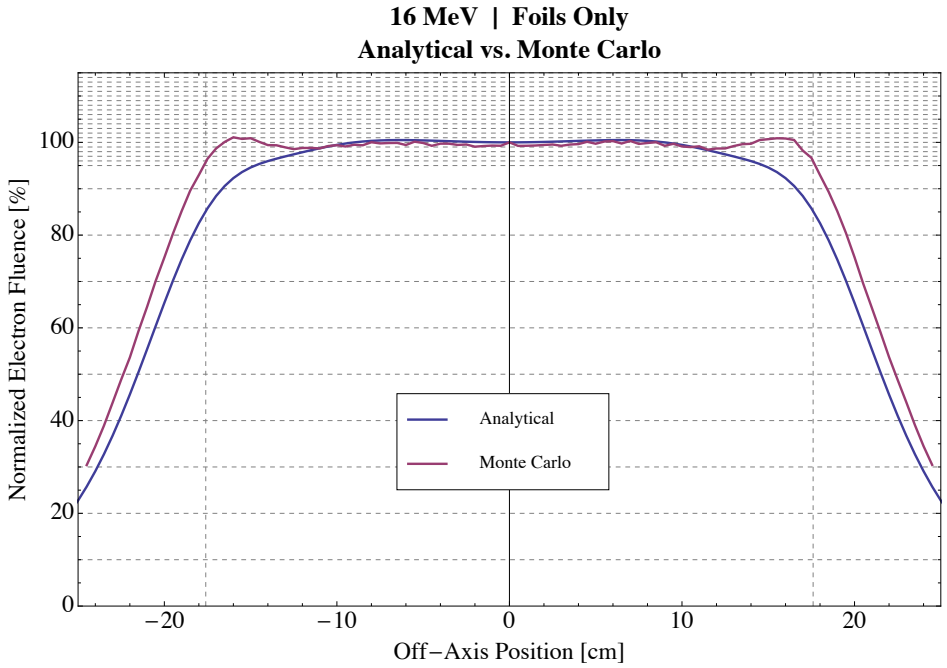

(a)

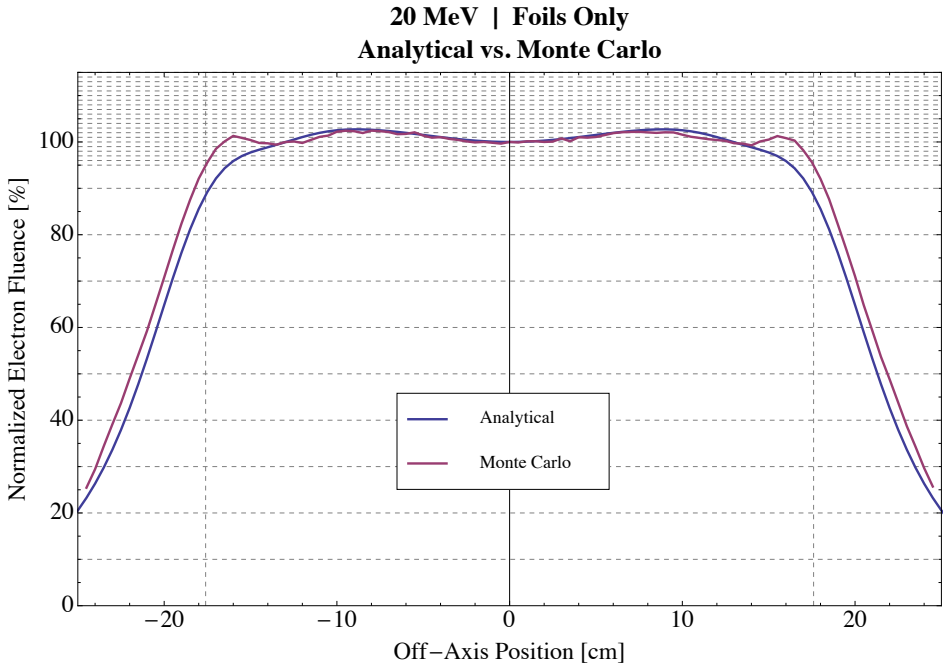

(b)

Figure 15: Plot comparing Monte Carlo with analytical simulator calculations of a monoenergetic pencil beam with only the nickel exit window, primary foil, and secondary foil in the beam for (a) 16 MeV ($E_{p,i}$ = 17.43 MeV), and (b) 20 MeV ($E_{p,i}$ = 21.80 MeV).

2.2.3 Bremsstrahlung Dose Calculation Verification

The analytical simulator's central axis bremsstrahlung dose estimates were compared to those measured during the commissioning of the Elekta Infinity accelerator at MBPCC in Baton Rouge. For all energies but one, the deviation between the calculated and measured x-ray contamination dose was ±0.2%. At 9 MeV there was a 0.4% difference. The results for all seven beam energies are listed in Table 3. It should be noted that percent difference comparisons were normalized to 100% dose (i.e., global—as opposed to local—percent difference).

Table 3: Comparison of clinically measured x-ray dose component with that calculated by the analytical simulator at the specified beam energies and depths.

$E_{nominal}$ [MeV]	$E_{p,0}$ [MeV]	R_p+2 [cm]	Clinical D_x [%]	Calculated D_x [%]
7	7.15	5.5	1.3	1.5
9	8.66	6.2	2.0	1.6
10	9.92	6.9	1.8	1.8
11	11.28	7.6	2.1	2.1
13	13.13	8.5	2.7	2.8
16	16.22	10.0	3.5	3.6
20	20.50	12.1	5.2	5.2

Chapter 3 Aim 2—Initial Design of Electron Dual Scattering Foil System

Aim 2: The analytical electron dual scattering foil system simulator will be used to design three secondary foils (Gaussian-shaped, Aluminum) and five primary foils (each a multiple of a single uniform Tantalum thickness) from which a combination of the two sets will be selected for beams spaced in 1-MeV increments from 7 to 20 MeV (most probably energy at isocenter). The optimal design will closely match at each energy the calculated profile with an objective profile, which if met, should result in the Monte Carlo calculating an off-axis dose profile that results in a uniform beam, i.e., within ±3% (±4%) of central axis dose over the specified range (2 cm inside the edge of a 25x25cm^2 applicator at isocenter).

Because the simulator does not account for the influence of the primary x-ray collimators (i.e., x-ray jaws and back-up MLC diaphragms) or the electron applicator on electron scatter (neither loss of side-scatter equilibrium near the edge of the collimator nor scatter off the collimator), it was necessary to independently determine by measurement the influence of electron scatter to the off-axis profiles. These measured data were then used to modify the objective profile from unity, so that the simulator's objective profile plus the net effect of increased dose from collimator scatter less the loss of dose due to loss of side-scatter equilibrium should produce a uniform off-axis profile. Such objective profiles were subsequently used to perform the design process, which optimized the secondary foils and the thickness of primary foil to give uniform dose over a wide range of energies for each secondary foil. Once completed, the resulting off-axis ratios (OARs) were calculated using a Monte Carlo code that modeled the Elekta electron beams with the designed scattering foils.

3.1 Methods

3.1.1 Off-Axis Profile Measurements

Measurements acquired using the Elekta Infinity accelerator located at Mary Bird Perkins Cancer Center in Baton Rouge provided ample data so as to determine the impact of collimation (loss of side scatter equilibrium and collimator scatter) on the off-axis profile. Comparisons between open field measurements (jaws at 40x40cm^2) and measurements taken when the jaws were set to their respective settings for 25×25cm^2 applicator (cf. Figure 16) revealed that the jaws caused little scatter contribution within clinically relevant off-axis radial distances (approximately ±11.5cm).

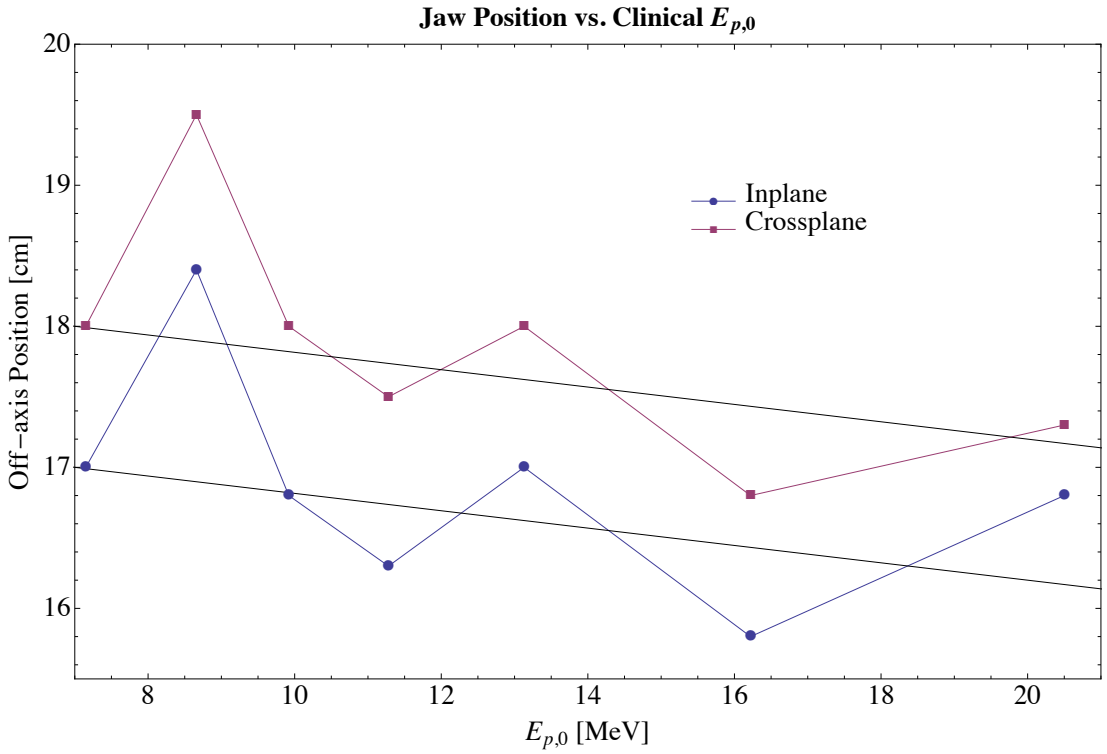

Figure 16: Jaw positions for MBPCC Elekta electron beams as a function of clinical $E_{p,0}$ for the 25×25cm^2 applicator.

Cross-plane and in-plane off-axis profiles were measured for a variety of beam configurations, summarized in Table 4. Under the columns labeled “With Applicator” are

lists of the various applicator sizes measured, the depths at which profiles were measured, and the corresponding energies for which they were measured. The measurements corresponding to 10x10 cm^2, 20x20 cm^2, and 25×25 cm^2 under "Jaws Only" refer to data acquired without the applicator, but with the primary collimation jaws in the position to which they would be set if the applicator were attached. Also, in the case of no applicator, the jaws were set to the largest field size possible (i.e., 40x40cm^2). This setting will thenceforth be referred to as "open field."

Table 4: Table of profiles measured. Each field corresponds to the energies at which that specific beam configuration was measured. Elekta applicator field sizes are defined 5 cm above isocenter (i.e., 95cm SSD). X-ray field sizes are defined at isocenter. For example: for a 25x25cm^2 applicator, cross-plane profiles were taken at a depth of 1cm for 7 and 9 MeV.

		With Applicator		Jaws Only	
	Applicator	**d = 1 cm**	**d = 2 cm**	**d = 1 cm**	**d = 2 cm**
Cross-Plane	**40x40**	–	–	7, 9*	9, 10, 11, 13, 16, 20
	25x25	7, 9*, 13*, 20*	9, 10, 11, 13, 16, 20	7, 9*, 13*, 20*	9, 10, 11, 13, 16, 20
	20x20	7	13, 20	7	13, 20
	10x10	7	13, 20	7	13, 20
In-Plane	**40x40**	–	–	7, 9*	9, 10, 11, 13, 16, 20
	25x25	7, 9*, 13*, 20*	9, 10, 11, 13, 16, 20	7, 9*, 13*, 20*	9, 10, 11, 13, 16, 20
	20x20	7	13, 20	7	13, 20
	10x10	7	13, 20	7	13, 20

*Data not presented

Comparisons between measured open field off-axis profiles and those taken with the jaws only would show the influence of the x-ray collimators, i.e., its impact on side-scatter equilibrium near the x-ray jaw edges and electrons that scatter off of the primary collimators. Similarly, comparisons between measurements taken with the applicators in place and those taken with jaws only show the impact that applicator scatter makes to the off-axis profile.

Measurements were taken using an MCU-controlled 40x44x64cm^3 two-dimensional scanning water tank (Scanditronix Wellhöfer AB RFA 20-SERVO, Uppsala, Sweeden) and OmniPro (v. 6.2) software package. Two PTW N31011 (Freiburg, Germany) 0.125cm^3

cylindrical ion chambers (air cavity diameter ≈ 5.5mm) were used—one that was scanned throughout the electron field and one that was fixed and served as an in-field reference chamber, placed approximately 3 cm above the water in the corner of a $10x10cm^2$ field. Readings were taken as a ratio between the two, both in dose rate mode. This normalization to the reference chamber removed the effect of any fluctuations in the beam rate.

The tank was positioned such that the water surface from the vertical beam was at a source to surface distance (SSD) of 100cm. Before taking data, the field ion chamber was shifted to a depth of 0.14cm (0.5 times the cavity radius) and "zeroed," making the effective point of measurement coincident with the water surface. A step size of 2mm was chosen, and data were acquired at a rate of 5mm/s. In order to verify that acquiring data at this speed would not create "lag" problems, initial scans were repeated with the ion chamber moving in the opposite direction of the first. These scans produced identical results, confirming that acquiring data at this rate would have a negligible "lag" effect on the data.

For quality assurance purposes, the initial water level in the tank was marked before scans were taken, and throughout the data acquisition period, water level was monitored. After approximately half of the scans had been taken, it was necessary to adjust the "zero" position of the detector by no more than 1mm. Also, percent depth dose scans were taken at each of the energies before data collection began. Depth dose scans were also performed after all data had been acquired. The two depth dose scans for each of the energies were compared, and their agreement (<1mm) verified that neither the beams nor measuring apparatus had undergone any significant changes throughout the data acquisition process.

3.1.2 Determination of Objective Profiles

The objective profile is defined as that off-axis ratio which is the design goal of the electron dual scatter foil system simulator. Objective profiles were determined by first comparing the analytical simulator's off-axis relative dose (electron plus x-ray) calculation with what was measured. The simulator utilized the current Elekta foil geometries for which measurements were made. The assumption was then made that if a new dual foil combination were calculated, then the off-axis ratio of the measured profile value to that calculated would be the same as determined for the current dual foil scattering foils at each off-axis position inside the penumbra (i.e., 2 cm inside field edge defined by 50% OAR).

From these calculated profiles the following steps were performed to create the objective profiles for each of the beam energies.

- Step 1: The off-axis positions at which the maximum deviation of the average measured profile, taken with the 25x25cm^2 applicator, from 100% dose were determined. These off-axis positions are indicated by the vertical lines in the example shown in Figure 17, which correspond to ±8.4cm.
- Step 2: Between the two positions (e.g., ±8.4cm), the amount of the deviation from 100% dose was subtracted from the design simulation profile. The result is shown by the gold curve in Figure 17.

- Step 3: The design simulation profile was increased by 5% at ±18 cm off-axis because current diagonal profiles for the 25x25cm^2 applicator ($12.5\sqrt{2} \approx 18$ cm off-axis) are approximately 4-5% too low in the corners as MBPCC clinical

commissioning data showed the off-axis ratios to be approximately 0.95 at all energies.

- Step 4: A scaling factor was determined for the point of maximum deviation that was found in Step 1. In the example of 13 MeV, at the off-axis position of ±8.4 cm the difference between the design simulation and the design simulation minus the scatter contribution corresponds to a scaling factor of approximately 0.98.
- Step 5: For off-axis positions located in between ±18 cm and the position of maximum deviation found in Step 1, scaling factors were determined by linear interpolation between the two known scaling factors: 1.05 at ±18cm and 0.98 at ±8.4. For example, at an off-axis position of ±10cm, the scaling factor was .995. The resulting objective profile was combined with the objective profile from Step 2 (the gold curve in Figure 18).

For this study, the goal is to design foils that produce flat profiles for all energies from 7-20 MeV, not simply the current MBPCC Elekta electron energies. Hence, it was necessary to determine the objective profiles for intermediate energies. This was accomplished by linearly interpolating (or slightly extrapolating in the case of $E_{p,0}$ = 7 MeV) between the objective profiles determined by the above method. Objective profiles were then obtained for most probable energies at the surface ranging from 7-20 MeV. As will be seen in the results, 9 MeV beam data were not used because of its abnormal x-ray jaw settings.

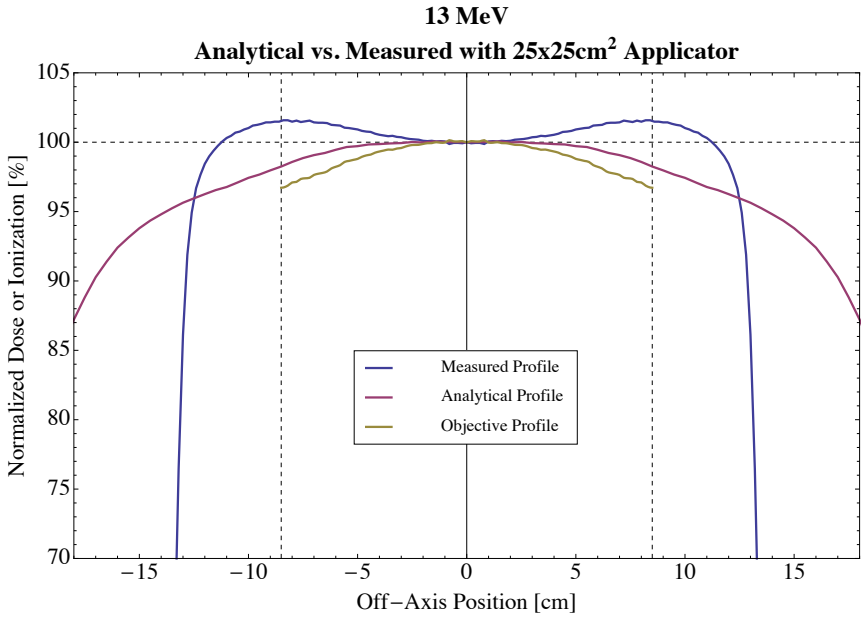

Figure 17: Illustration depicting how the scatter component was accounted for during the development of objective profile for the Elekta 13 MeV beam. The dashed vertical lines indicate the off-axis position at which the average of the measured profiles reach maximum deviation from 100% dose (horizontal dashed line). The gold curve is the objective profile, which was determined by the analytical simulator profile with the estimated scatter component subtracted.

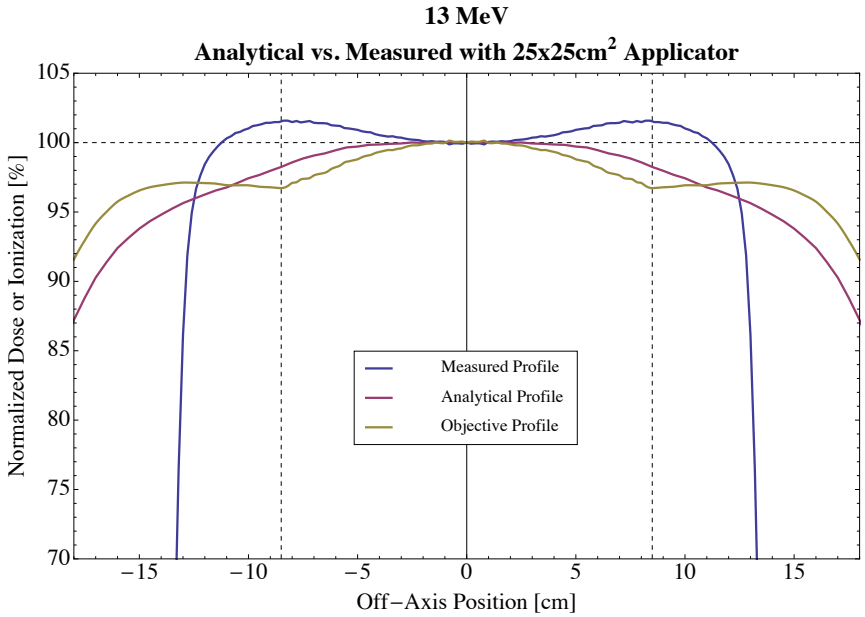

Figure 18: Illustration depicting the completion of the objective profile (gold line). At ±18cm the objective profile is assumed 5% greater than the analytical calculation. Between ±(8.4cm and 18cm) the ratio of the analytical calculation to the objective profile is forced to be linear.

3.1.3 Design Constraints

Elekta Infinity accelerators are presently constrained to having five primary and three secondary foils. Hence, the current design process was limited to the 15 possible combinations of five primary foil thicknesses (multiples of a constant foil thickness) and three secondary foils for each of the energies (most probable energies at the surface of 7-20 MeV) for which the dual foil system was being designed. The design goal was set to get each energy's off-axis profile to be within ±3% of central axis dose everywhere within 18 cm of central axis.

3.1.4 Design Procedure

The dual foil scattering systems were designed according to the following procedure, for which the case of 13 MeV will be used to exemplify the process. It should be noted that the "number of primary foils" presented here refer to 34.5μm thick Ta foil primary foil layers. It was not until later in the design process that it was decided to switch to 30μm layers. However, this switch was irrelevant to the initial steps of the design procedure.

- Step 1: At each of the design energies, a secondary foil was optimized so as to produce the best possible design profile for each of the primary foil thicknesses. This optimization refers to achieving the smallest possible deviation from the objective profile while maintaining the lowest possible D_x. For instance, for 13 MeV a secondary foil was optimized for the case of 3 primary foil layers (103.5μm), 4 primary foil layers (138μm), etc. If it were possible to get a perfect agreement for 13

MeV with 5 primary foil layers, but D_x=5%, this solution would be discarded, as D_x would be too great.

- Step 2: Each of the designs in Step 1 was then tested for energy versatility. That is, each secondary foil design for a given energy and primary foil thickness combination was simulated at other nearby design energies (±1 Mev, ±2 MeV, etc.). At energy and primary foil thickness (number of layers) combination, maximum deviations above and below the objective profile ($\Delta_{max}{}^{+}$ and $\Delta_{max}{}^{-}$, respectively) and bremsstrahlung dose (D_x) were calculated. These data were recorded for each simulation so long as $\Delta_{max}{}^{+}$ and $\Delta_{max}{}^{-}$ did not exceed 10%.
- Step 3: After data were generated for each of the design energies, composite tables of the most versatile foils were generated. These tables indicated the sigma and central-axis thickness of the secondary foil and the number of primary foil thickness layers that produced the best possible agreement for each of the design energies. An example is presented in Table 7. The parameters for the foils referred to in Table 5 and Table 6 are highlighted in green. From these data, it was possible to determine a first-order estimation of the optimal secondary foil thickness and sigma ranges. For instance, for the presented in Table 7, it was clear that the optimal sigma and thickness of the secondary foil for these energies would likely fall in the ranges of approximately 1.41-1.5 cm and 0.14-0.18cm, respectively. Table 5 and Table 6 show data for the example of the secondary foils designed for 13 MeV with 138μm and 103.5μm thick Ta primary foils, respectively. These designs were simulated at energies of 7-12 MeV and 14-20 MeV, and the aforementioned recorded parameters are shown. Note that at some of the energies (e.g., 9 MeV and 7 MeV) it was possible

to get reasonable agreement between design profiles and objective profiles by use of two different primary foil thicknesses for the same secondary foil design. Moreover, notice that it was possible to achieve nearly the same agreement with the objective profile by varying the secondary scattering foil parameters.

- Step 4: After data were generated for each of the design energies, composite tables of the most versatile foils were generated. These tables indicated the sigma and central-axis thickness of the secondary foil and the number of primary foil thickness layers that produced the best possible agreement for each of the design energies. An example is presented in Table 7. The parameters for the foils referred to in Table 5 and Table 6 are highlighted in green. From these data, it was possible to determine a first-order estimation of the optimal secondary foil thickness and sigma ranges. For instance, for the data presented in Table 7, it was clear that the optimal sigma and thickness of the secondary foil for these energies would likely fall in the ranges of approximately of 1.41-1.5cm and 0.14-0.18cm, respectively.

Table 5: Table of data summarizing energy versatility of secondary foil optimized for 13 MeV with 4 Ta primary foil layers (138μm thick), as indicated by the row highlighted in green.

Energy [MeV]	Number of Primary Foils	Δ_{max}^{+} [%]	Δ_{max}^{-} [%]	D_x [%]
7	3	2.6	0.1	1.3
7	2	1.5	2.6	1.2
8	3	2.6	0.4	1.5
9	4	4.1	0.	1.8
9	3	3.0	4.5	1.6
10	2	2.4	0.3	1.7
11	3	2.8	1.1	2.1
12	4	3.3	0.1	2.5
13	4	2.2	2.3	2.7
14	4	1.1	6.9	2.9
15	6	0	4.9	3.5

Table 6: Table of data summarizing energy versatility of secondary foil optimized for 13 MeV with 3 Ta primary foil layers (103.5μm thickness), as indicated by the row highlighted in green.

Energy [MeV]	Number of Primary Foils	Δ_{max}^{+} [%]	Δ_{max}^{-} [%]	D_x [%]
8	4.7	0	1.4	2
9	4.6	2.9	1.5	2
10	1.3	6.1	1.6	1
11	2.7	2.2	2.0	2
12	4.1	0.1	2.3	3
13	2.4	1.8	2.5	3
14	3.1	0.2	2.9	4
15	0	6.2	3.1	4
16	1.5	4.2	3.7	6

Table 7: Table summarizing scattering foil system parameters optimized for a subset of the design energies.

Energy [MeV]	Number of Primary Foils	σ [cm]	Δt [cm]
10	2	1.5	0.1578
11	3	1.495	0.1476
12	3	1.4065	0.1776
12	4	1.525	0.147
13	3	1.302	0.1534
13	4	1.43	0.136
14	3	1.3	0.2074
14	4	1.43	0.1828

- Step 5: The most versatile foil from Step 3 falling within the ranges determined by Step 4 was then selected. For the example case, this would be the secondary foil designed for 12 MeV with 4 primary foils (indicated by green row in Table 8).

- Step 6: Then, for each of the design energies, the worst primary foil combinations were discarded to minimize $\Delta_{max}{}^{+}$, $\Delta_{max}{}^{-}$, and/or D_x. The rows highlighted in red in Table 8 illustrate this process.
- Step 7: From the remaining design data, the energy with the maximum deviation from the objective profile was identified. The secondary foil thickness and sigma were then altered to reduce this deviation. Table 9 shows the same data as Table 8 with the most poorly performing combinations removed. The energy with the maximum deviation from the objective profile is highlighted in red.

Table 8: Table summarizing design data for the secondary foil designed for 12 MeV with 4 primary foil layers, indicated by row highlighted in green. This represents the design selected in Step 4, which is the most versatile secondary foil design from Step 2 that falls within the ranges determined in Step 3. The best energy-primary foil combination was selected with each combination that was discarded in Step 5 being highlighted in red.

Energy [MeV]	Number of Primary Foils	$\Delta_{max}{}^{+}$ [%]	$\Delta_{max}{}^{-}$ [%]	D_x [%]
7	3	1.3	3.1	1.4
7	4	1.9	0.9	1.5
7	6	3.	0.1	1.7
8	4	2.2	2.4	1.7
8	6	2.8	0	1.9
9	4	2.9	5.1	1.8
9	6	3.8	1.1	2.1
10	2	1.8	2.8	1.7
11	3	2.2	3.7	2.1
11	4	4.1	0	2.3
12	4	2.5	1.5	2.5
13	4	1.5	4.8	2.7
14	6	2.4	0.8	3.3

Table 9: Table summarizing best design data after poorly performing combinations were purged (Step 5, cf. Table 8). The design energy with the greatest deviation is highlighted in red.

Energy [MeV]	Number of Primary Foils	Δ_{max}^{+} [%]	Δ_{max}^{-} [%]	D_x [%]
7	4	1.9	0.9	1.5
8	4	2.2	2.4	1.7
9	6	3.8	1.1	2.1
10	2	1.8	2.8	1.7
11	3	2.2	3.7	2.1
12	4	2.5	1.5	2.5
13	4	1.5	4.8	2.7
14	6	2.4	0.8	3.3

- Step 7: The altered secondary foil from Step 6 was then evaluated at each of the design energies. Then, again the greatest deviation was identified, and the secondary foil parameters were adjusted to reduce the deviations. This was performed iteratively until it was not possible to reduce the deviation at any given energy without adversely affecting the agreement at another design energy. During Step 7, the number of primary foils remained unchanged.
- Step 8: These designs were then evaluated with slightly different thicknesses of the primary foil (multiples of 30μm), and the design profiles improved. Thus, Step 7 was performed again so as to ensure that the best possible agreement at each design energy was achieved.

3.2 Results

3.2.1 Measurements of Off-Axis Profiles

Measurements taken with the jaws fully open (40x40cm^2) and no applicator compared with measurements taken with the jaws at their respective positions for the 25x25cm^2 applicator, but with no applicator, indicated that the jaws have little effect on the off-axis ratios, especially for the smaller applicator sizes' settings. Figure 19 shows representative examples of measurements taken with open field compared with measurements taken with the jaws set to the appropriate settings for a 25x25cm^2 applicator for 7, 13 and 20 MeV. As can be seen, the jaws' presence in the field does not serve to increase the off-axis ratios. The greatest deviation was for 7 MeV in the crossplane direction from 10-16 cm off-axis, which is attributed to loss of side-scatter equilibrium. Maximum difference values over the clinically-relevant range (2 cm inside the 50% dose point for a profile measured with the 25x25cm^2 applicator in place) for all energies for the 25x25cm^2 applicator setting may be found in Table 10. Plots of the data for all energies are included in Appendix C. The same comparisons of measurements for 7, 13, and 20 MeV were also done for both 20x20cm^2 and 10x10cm^2 applicator settings and are included in Appendix D and Appendix E, respectively. The results were similar to those for the 25x25cm^2 applicator settings, showing no significant increase in the off-axis ratios attributable to the jaws.

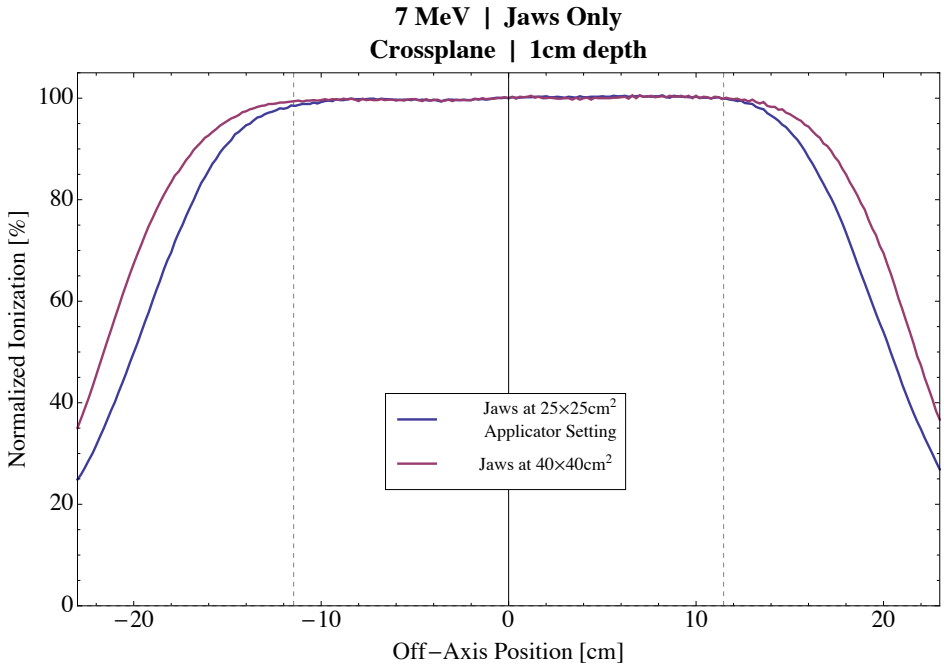

(a)

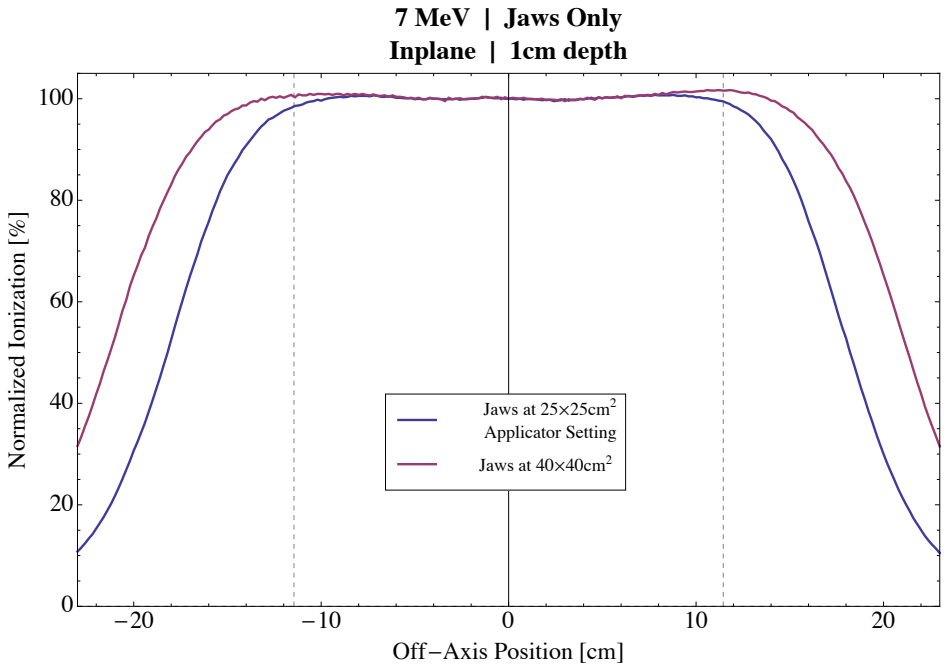

(b)

Figure 19: Plots showing crossplane and inplane comparisons between measurements taken with the jaws at 40x40cm^2 settings and that taken with the jaws at the appropriate settings for a 25x25cm^2 applicator for (a,b) 7 MeV, (c,d) 13 MeV, and (e,f) 20 MeV. The vertical lines delimit the range over which flatness and symmetry are determined clinically for a 25x25cm^2 applicator.

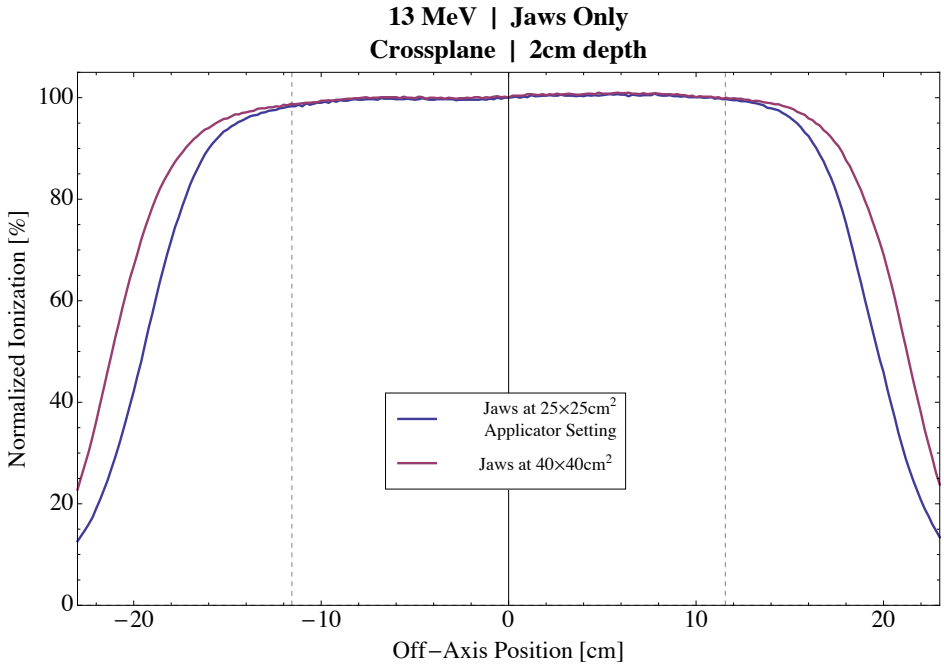

(c)

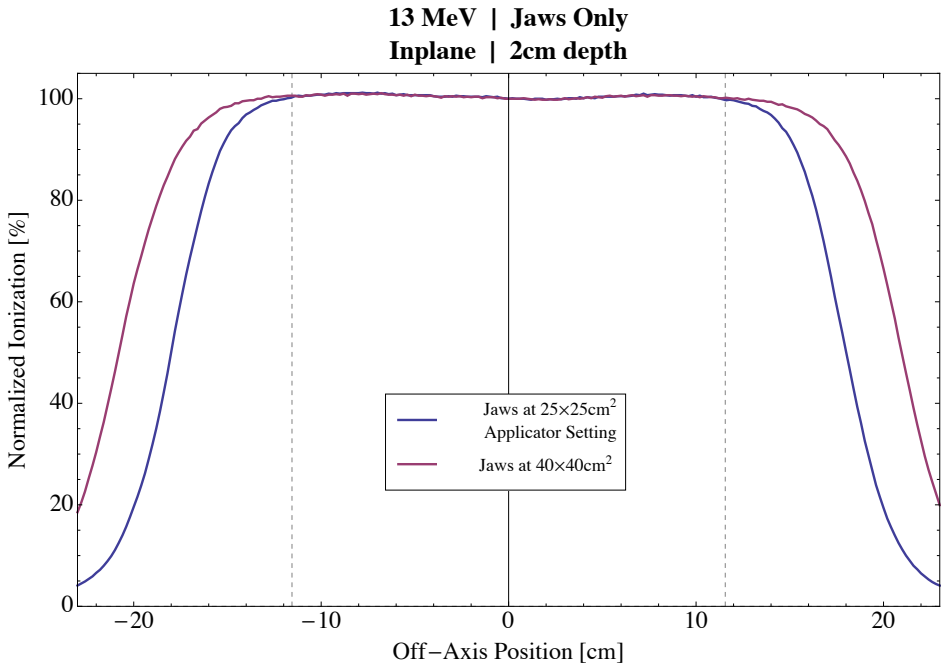

(d)

Figure 19 (continued): Plots showing crossplane and inplane comparisons between measurements taken with the jaws at 40x40cm^2 settings and that taken with the jaws at the appropriate settings for a 25x25cm^2 applicator for (a,b) 7 MeV, (c,d) 13 MeV, and (e,f) 20 MeV. The vertical lines delimit the range over which flatness and symmetry are determined clinically for a 25x25cm^2 applicator.

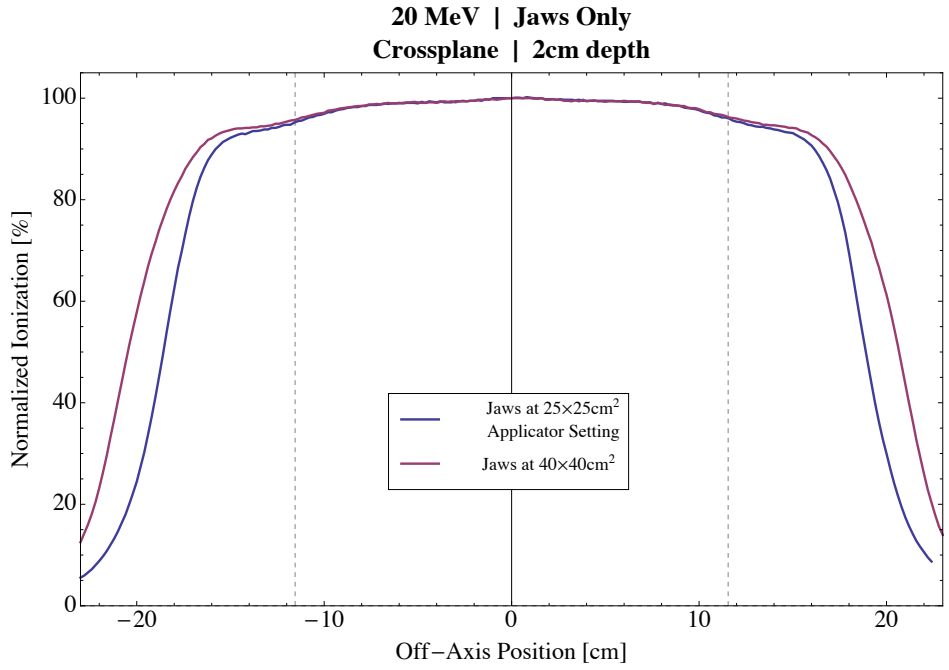

(e)

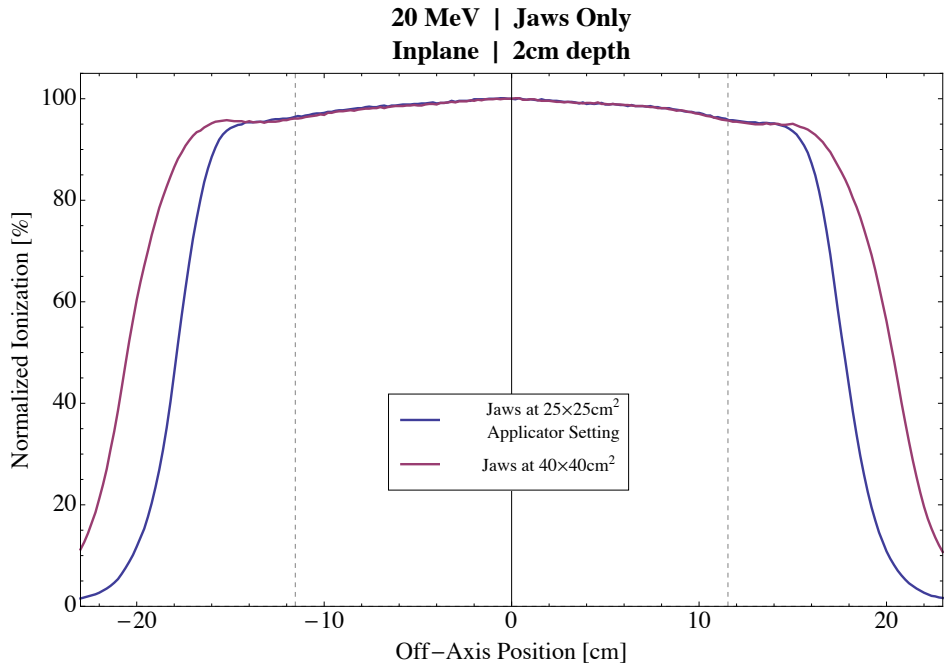

(f)

Figure 19 (continued): Plots showing crossplane and inplane comparisons between measurements taken with the jaws at 40x40cm^2 settings and that taken with the jaws at the appropriate settings for a 25x25cm^2 applicator for (a,b) 7 MeV, (c,d) 13 MeV, and (e,f) 20 MeV. The vertical lines delimit the range over which flatness and symmetry are determined clinically for a 25x25cm^2 applicator.

Table 10: Table of maximum percent differences between open field measurements and measurements taken with the jaws at the settings for 25x25cm^2 applicator over the clinically relevant range (2 cm inside the 50% dose point for a profile measured with the 25x25cm^2 applicator in place).

Nominal Energy [MeV]	$E_{p,0}$ [MeV]	Inplane Difference [%]	Crossplane Difference [%]
7	7.15	2.2	0.9
9	8.66	0.7	0.5
10	9.92	1.5	0.7
11	11.28	1.6	0.6
13	13.13	0.5	0.7
16	16.22	0.5	0.8
20	20.5	0.5	0.6

Measured data with the applicators in place revealed that the greatest impact of collimator scatter on the off-axis profiles originated from the applicators themselves, most significant for the largest applicator sizes. When compared with data taken with an open field, the 25×25cm^2 applicator contributes, on average, just over 1% to the off-axis at its maximum deviation. Representative plots for 7, 13, and 20 MeV are shown in Figure 20. Such comparison plots for all energies are shown in Appendix F. Table 11 shows the calculated mean maximum deviation between open field measurements (jaws at 40x40cm^2) and measurements taken with a 25×25cm^2 applicator in place for all energies.

Table 11: List of maxima of average deviations between measurements taken with 25×25cm^2 applicator in place and open field measurements and their respective off-axis positions.

Nominal Energy [MeV]	Off−Axis Position [cm]	$(\overline{\Delta})_{max}$
7	±8.4	0.9%
9	±8.6	1.2%
10	±8.2	0.9%
11	±9.4	1.2%
13	±8.4	1.1%
16	±8.0	1.1%
20	±10.8	1.5%

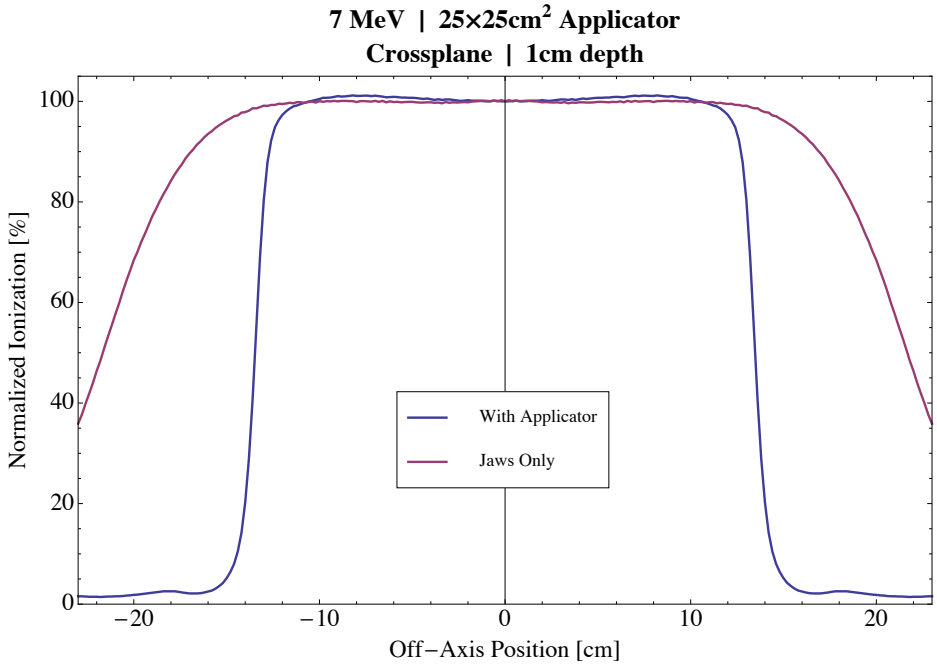

(a)

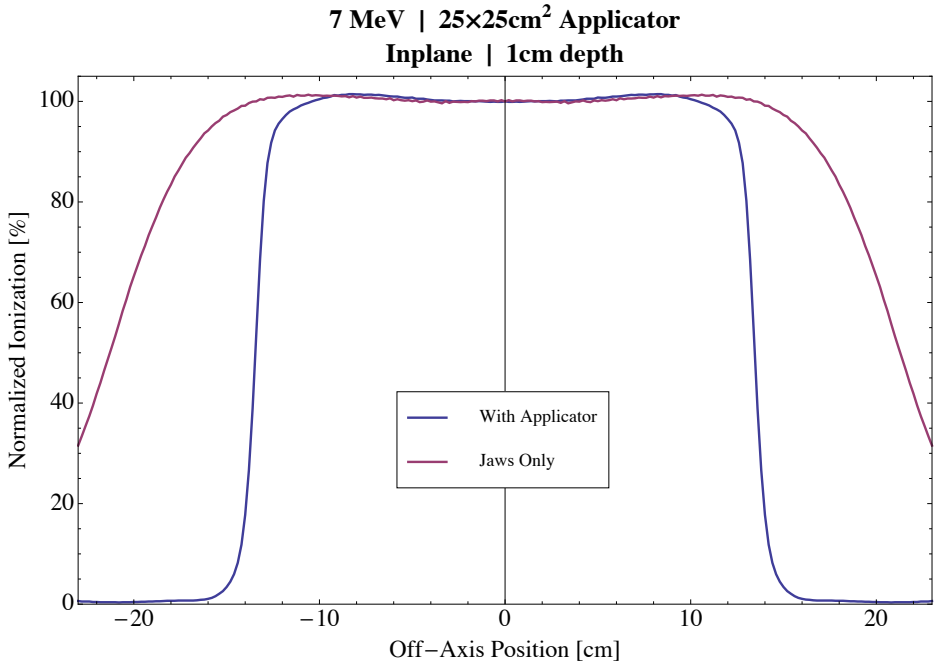

(b)

Figure 20: Plots showing crossplane and inplane comparisons between measurements taken with the jaws at 40x40cm^2 settings and that taken with the 25×25cm^2 applicator in place for (a,b) 7 Mev, (c,d) 13 MeV, and (e,f) 20 MeV.

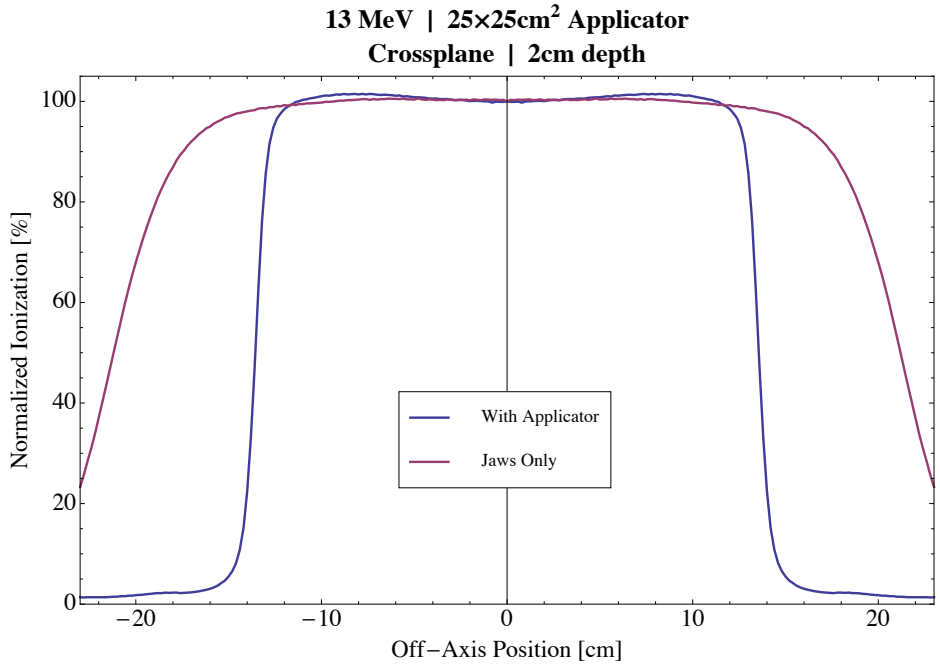

(c)

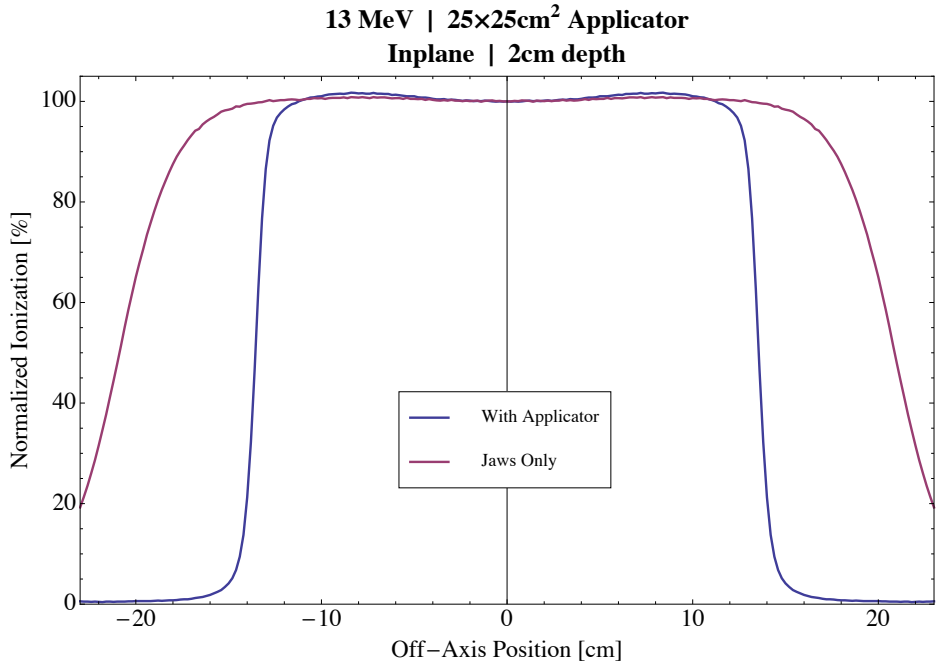

(d)

Figure 20 (continued): Plots showing crossplane and inplane comparisons between measurements taken with the jaws at 40x40cm^2 settings and that taken with the 25×25cm^2 applicator in place for (a,b) 7 Mev, (c,d) 13 MeV, and (e,f) 20 MeV.

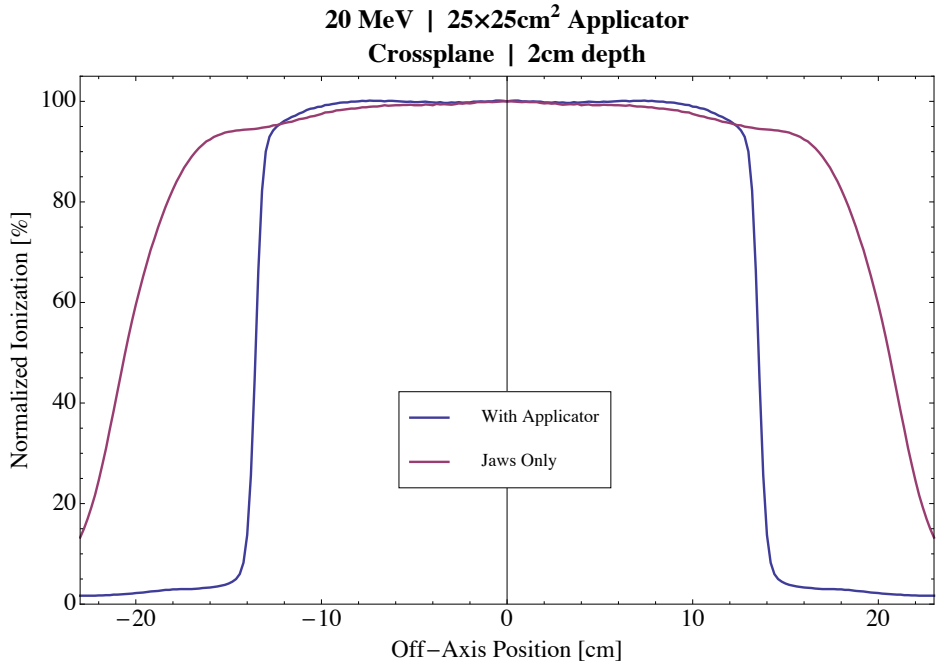

(e)

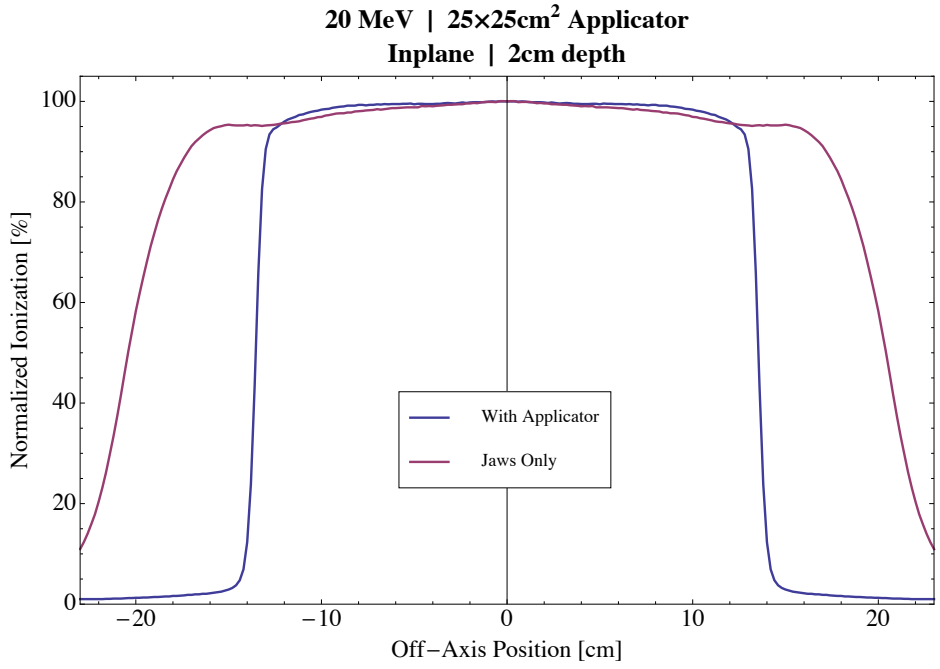

(f)

Figure 20 (continued): Plots showing crossplane and inplane comparisons between measurements taken with the jaws at 40x40cm^2 settings and that taken with the 25x25cm^2 applicator in place for (a,b) 7 Mev, (c,d) 13 MeV, and (e,f) 20 MeV.

Data measured with the 10x10cm^2 applicator in place were compared to measurements taken with an open field, and there was no increase of off-axis relative dose due to scatter contributed by collimation system for 7, 13, or 20 MeV. Data measured with the 20x20cm^2 applicator in place were also compared to open field measurements. An increase in off-axis ratios was seen in a couple of instances. A representative case for each of these comparisons is presented in Figure 21. The increase for the 20x20cm^2 applicator was no greater than that present in the case of the 25x25cm^2 applicator. Moreover, the off-axis locations are nearly the same. Thus, since the aim in this study was to design dual scattering foil systems that produce clinically flat beams for a 25x25cm^2 applicator, it was assumed that doing so would also produce clinically flat beams for each of the applicator sizes. Plots at 7, 13, and 20 MeV comparing open field measurements with the profiles measured with 20x20cm^2 and 10x10cm^2 applicator in place can be found in Appendix G and Appendix H, respectively.

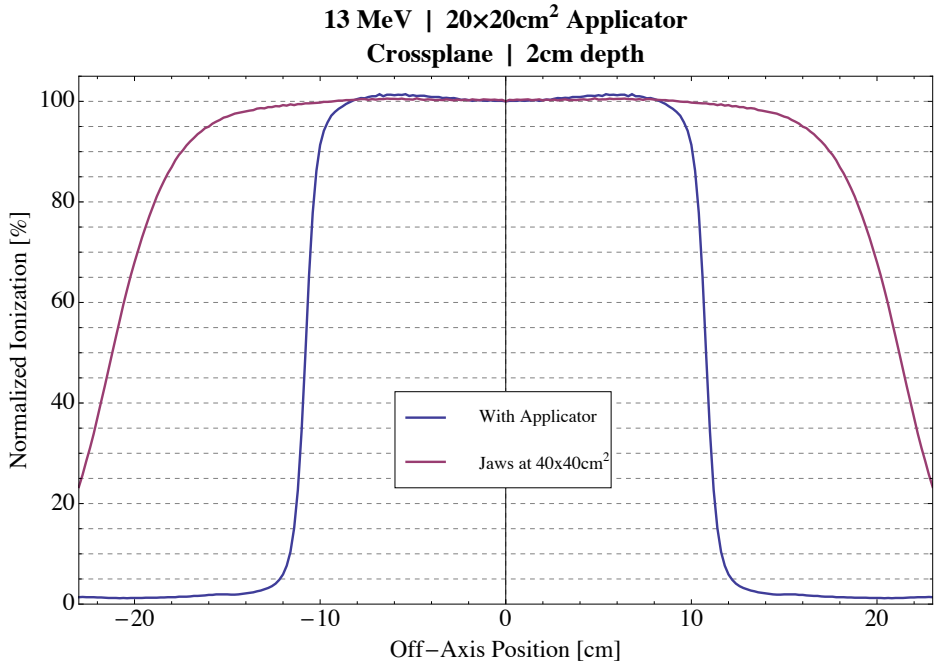

(a)

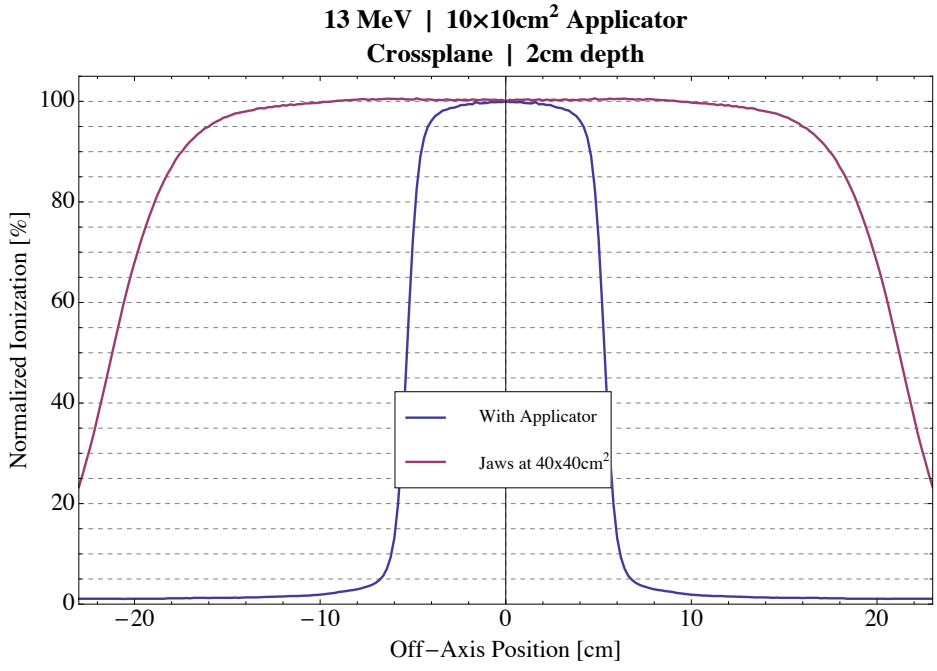

(b)

Figure 21: Plots showing crossplane profile comparisons between open field measurements and measurements taken with the (a) 20x20cm^2 and (b) 10x10cm^2 applicator in place for 13 MeV.

3.2.2 Objective Profiles

Objective profiles for each of the design energies (7-20 MeV, 1-MeV increments) were obtained by linear interpolation from initial ones determined using existing MBPCC Elekta Infinity electron beams. These initial objective profiles, as explained in section 3.1.2 and illustrated in Figure 18, were created using measured 25x25cm^2 data and analytical simulator profiles. Plots comparing the design simulator's prediction of the off-axis dose profile with the measured profile and the resulting objective profile for the current nominal energies (7, 9, 10, 11, 13, 16, and 20 MeV) are shown in Figure 22.

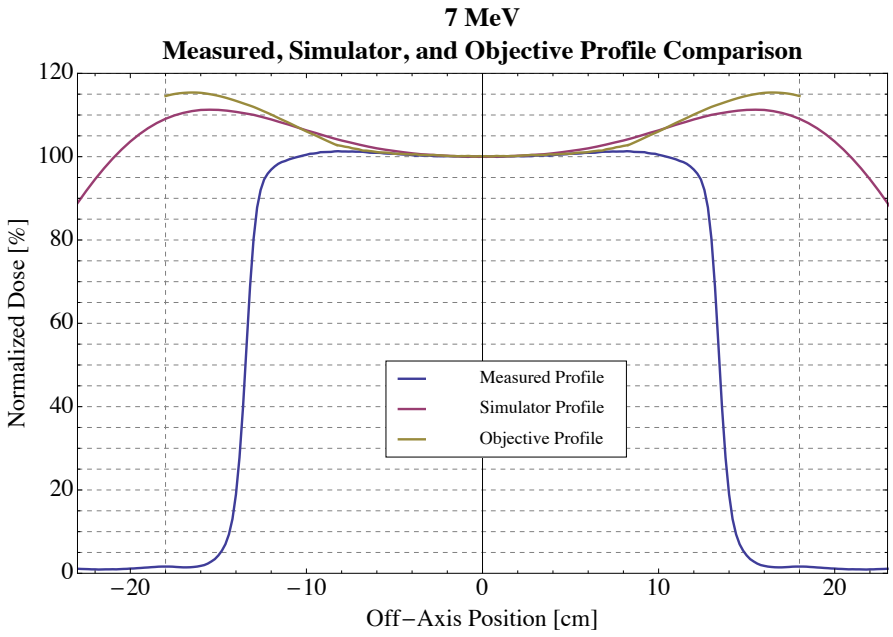

(a)

Figure 22: Plot comparing the measured profile (25x25cm^2), design simulator's calculated profile, and the resulting objective profile for nominal energies of (a) 7 MeV, (b) 9 MeV, (c) 10 MeV, (d) 11 MeV, (e) 13 MeV, (f) 16 MeV, and (g) 20 MeV.

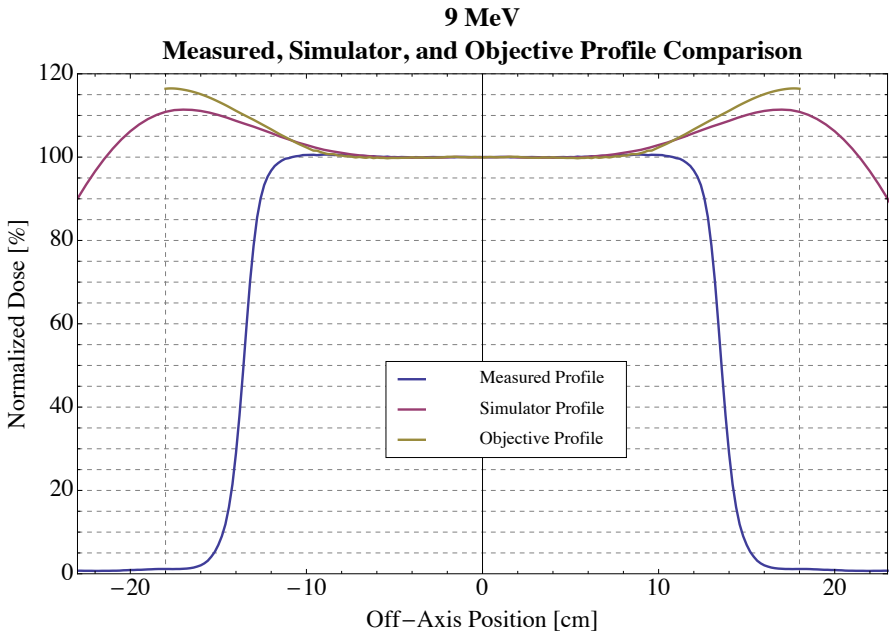

(b)

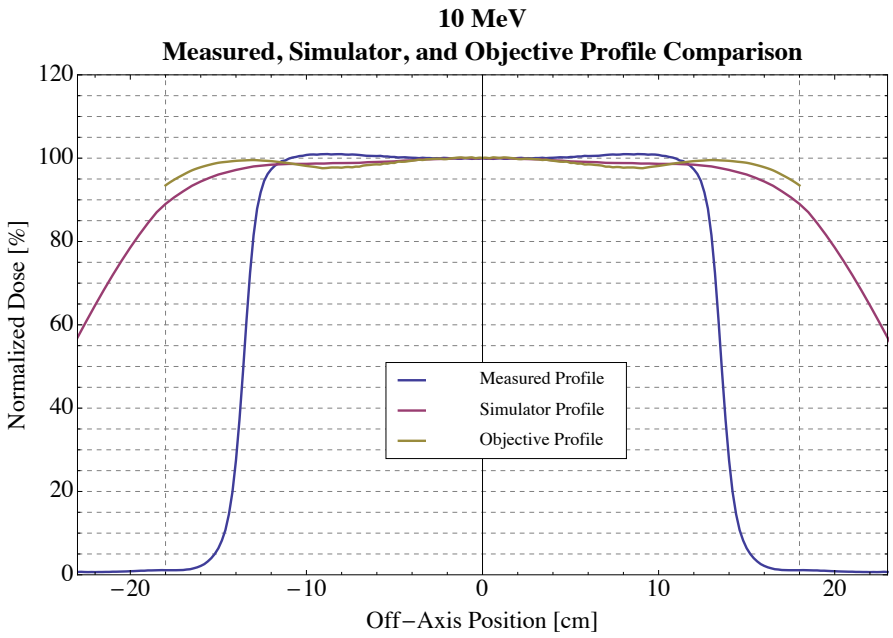

(c)

Figure 22 (continued): Plot comparing the measured profile (25x25cm^2), design simulator's calculated profile, and the resulting objective profile for nominal energies of (a) 7 MeV, (b) 9 MeV, (c) 10 MeV, (d) 11 MeV, (e) 13 MeV, (f) 16 MeV, and (g) 20 MeV.

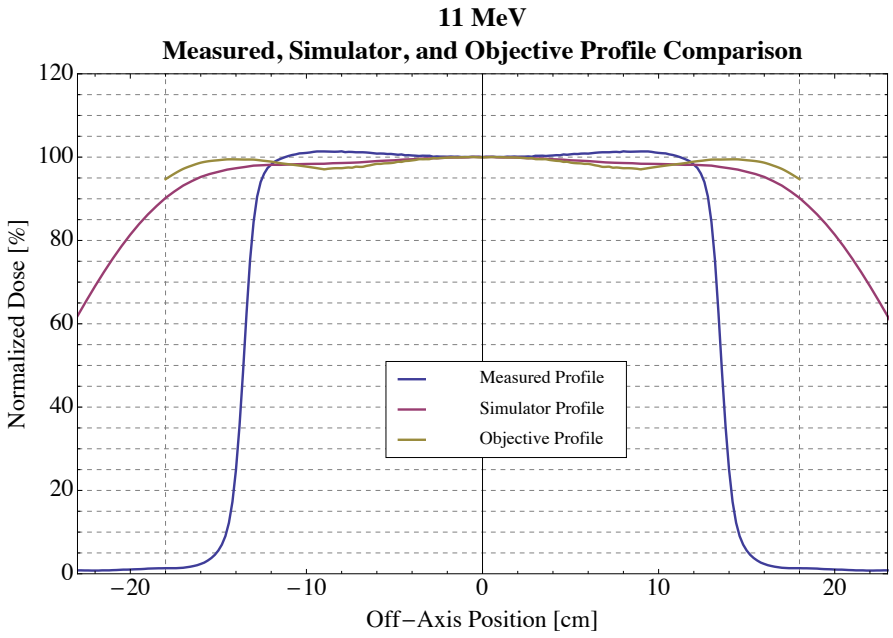

(d)

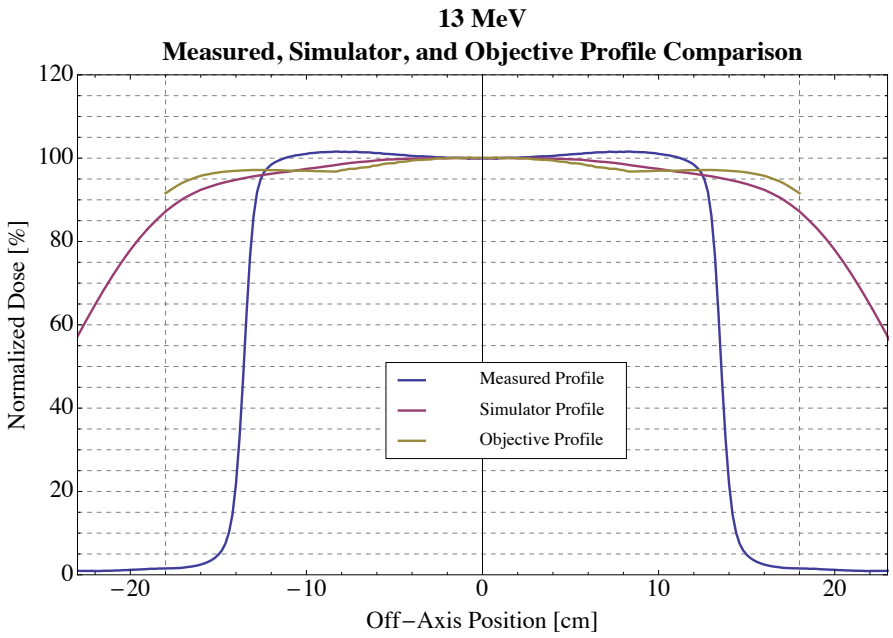

(e)

Figure 22 (continued): Plot comparing the measured profile (25x25cm^2), design simulator's calculated profile, and the resulting objective profile for nominal energies of (a) 7 MeV, (b) 9 MeV, (c) 10 MeV, (d) 11 MeV, (e) 13 MeV, (f) 16 MeV, and (g) 20 MeV.

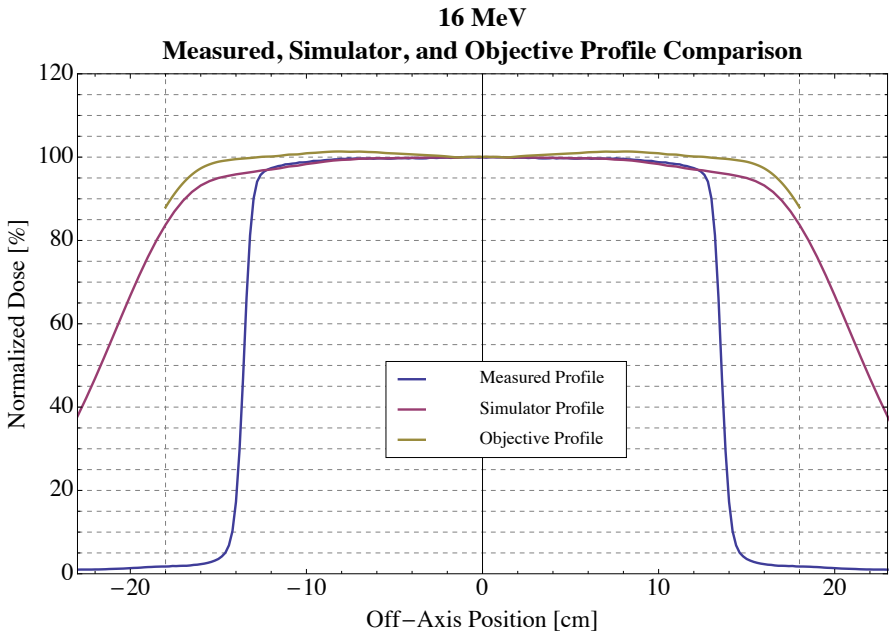

(f)

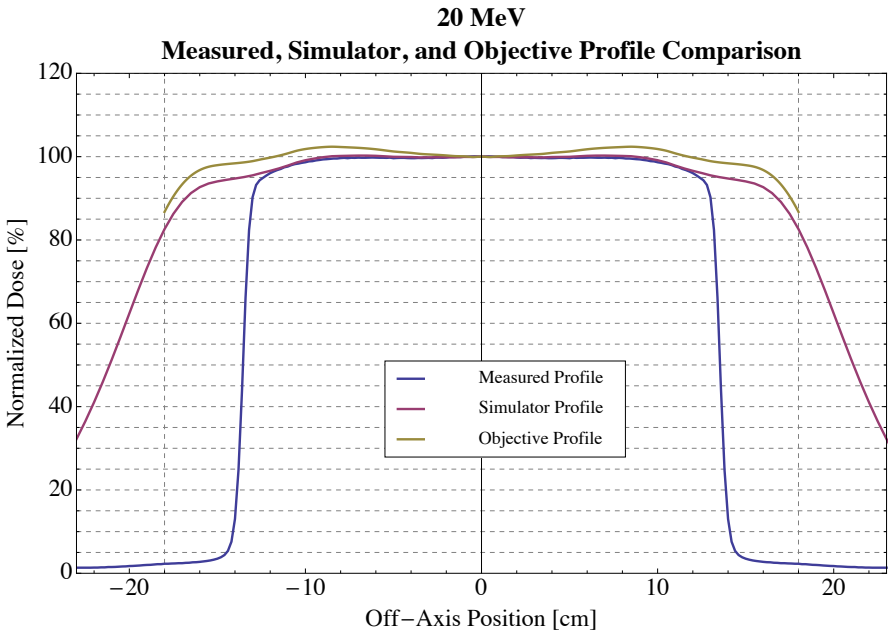

(g)

Figure 22 (continued): Plot comparing the measured profile (25x25cm^2), design simulator's calculated profile, and the resulting objective profile for nominal energies of (a) 7 MeV, (b) 9 MeV, (c) 10 MeV, (d) 11 MeV, (e) 13 MeV, (f) 16 MeV, and (g) 20 MeV.

Plots of all of the initial objective profiles plotted in Figure 22 are compared in Figure 23. Note the similarities of the curves that shared the same secondary foil (#1—7 and 9 MeV; #2—10, 11, and 13 MeV; and #3—16 and 20 MeV). Also, it should be noted that the initial objective profile obtained for the nominal energy of 9 MeV was not utilized in the interpolation process, as its off-axis profile did not follow the trend of the empirical objective profiles at 7 and 10 MeV. This attributed to the irregularity of the x-ray collimator settings at 9 MeV, as illustrated earlier in Figure 16.

Objective profiles utilized in the design process were generated by linear interpolation between the objective profiles in Figure 23 (excluding 9 MeV). At the design energy of 7 MeV it was necessary to extrapolate slightly because the nominal energy of 7 MeV is slightly below the lowest beam energy ($E_{p,0}$=7.15 MeV). The resulting objective profiles from 7-20 MeV (1-MeV increments) are plotted in Figure 24.

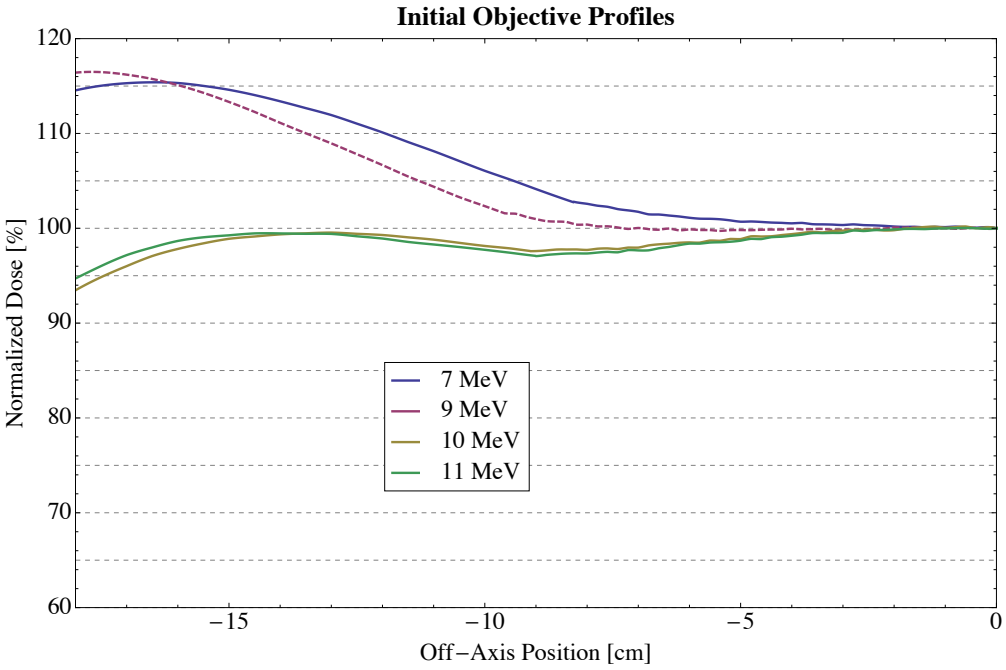

(a)

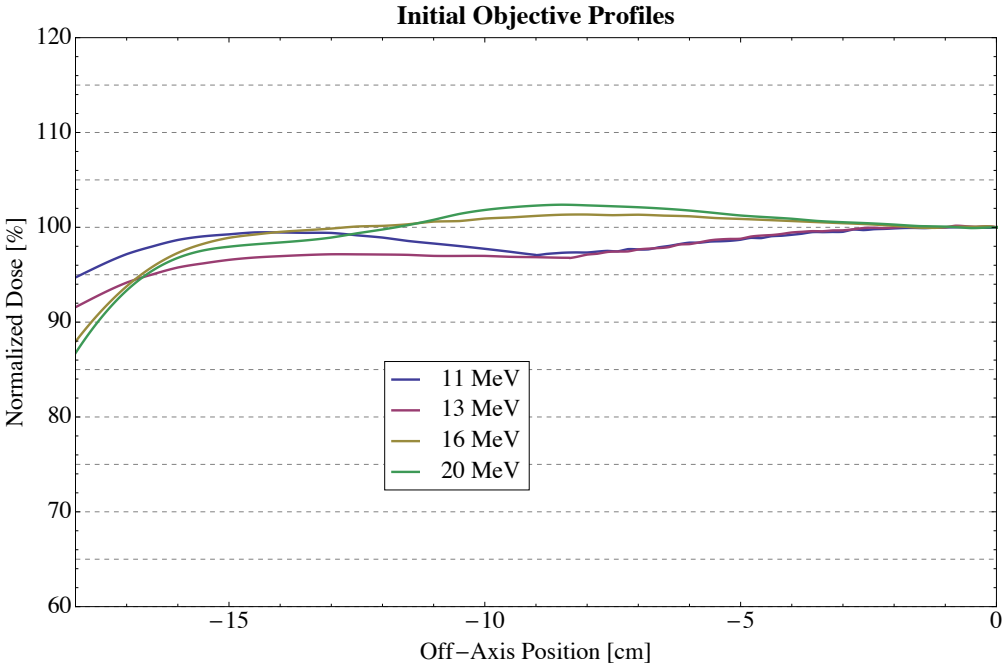

(b)

Figure 23: Plot of initial objective profiles for (a) 7, 9, 10, and 11 MeV and (b) 11, 13, 16, and 20 MeV. The 11 MeV profile is included in both plots as a means of reference. The 9 MeV profile is dashed to indicate that it was not used in the interpolation process for the objective profiles used in the design process.

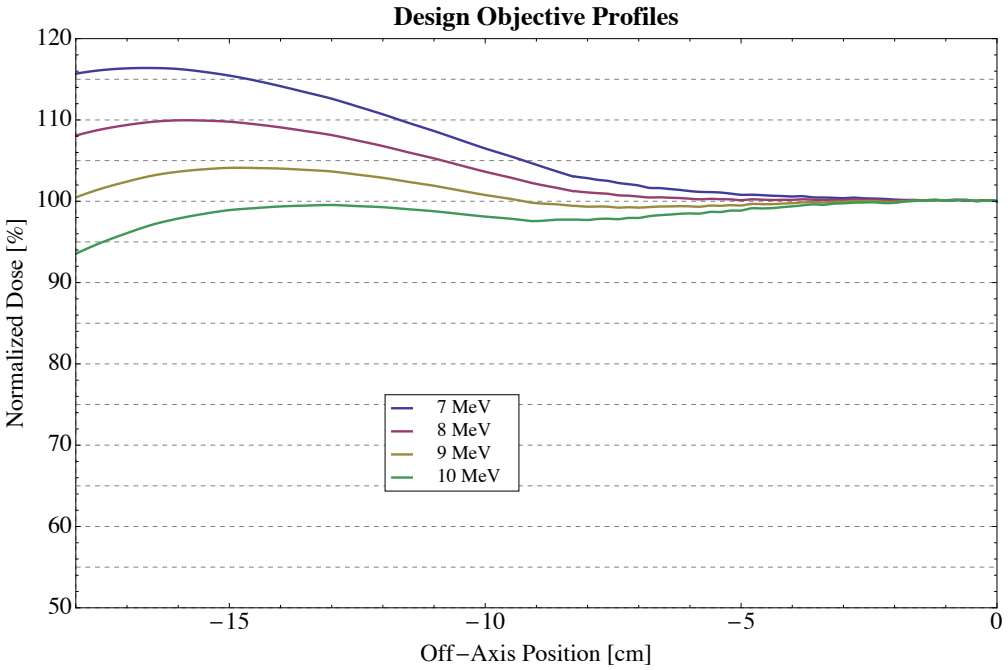

(a)

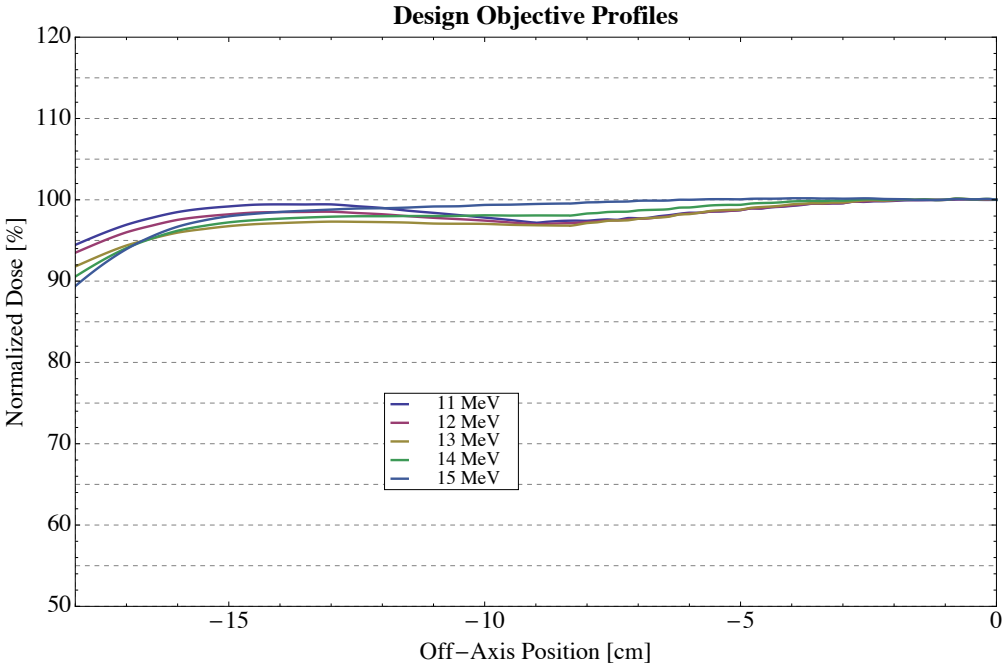

(b)

Figure 24: Interpolated objective profiles utilized in the design process for (a) 7-10 MeV, (b) 11-15 MeV, and (c) 16-20 MeV.

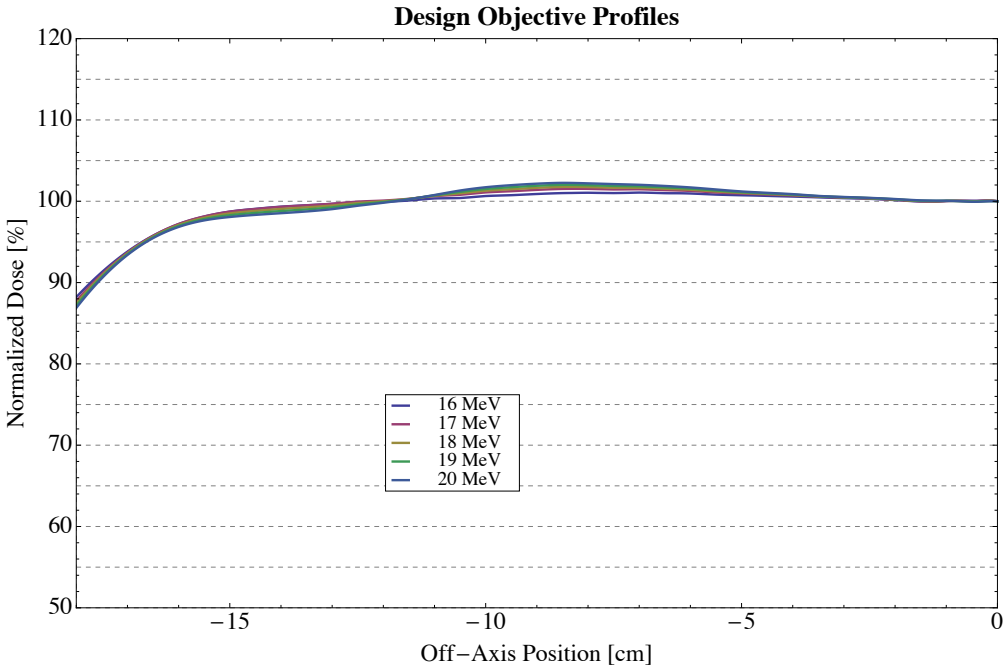

(c)

Figure 24 (continued): Interpolated objective profiles utilized in the design process for (a) 7-10 MeV, (b) 11-15 MeV, and (c) 16-20 MeV.

3.2.3 Foil Designs

The resulting objective profiles (cf. Figure 24) were used as the design goals for each of the design energies. Design profiles were determined with the analytical simulator using the iterative, multi-energy design procedure specified in section 3.1.4. These results are shown for each of the secondary foil designs in Figure 25, Figure 26, and Figure 27. Additionally, a summary of the primary and secondary foil combination used, as well as maximum deviations and central axis photon dose percentage, for each design energy may be found in Table 12. Agreement between the objective profile and the resulting design simulator profiles was consistently within the goal of ±3% over the range of ±18 cm, with the exception of two cases cases (18 MeV and 17 MeV), where the design for each was 4.4% below and 3.3% above, respectively.

Figure 25 shows the agreement between simulation design profiles and objective profiles for the secondary foil designed for most probable energies at the surface of 16-20 MeV. The secondary foil is a Gaussian-shaped aluminum pyramid having a thickness of 0.3614 cm along central axis and a sigma of 1.12 cm (note the simulator approximated the Gaussian using 10 stacked disks of equal thickness). Only half-field profiles are shown as the profiles are radially symmetric. "Number of primary foils" corresponds to the number of 30μm thick tantalum foil layers used in the primary foil; $\Delta_{max}{}^{+}$ and $\Delta_{max}{}^{-}$ refer to the design profiles maximum deviation in percent above and below the objective profile, respectively; and D_x is the design simulator's prediction of the bremsstrahlung (x-ray) dose in percent of maximum central axis dose.

20 MeV	
Number of Primary Foils	6
Secondary Foil Thickness [cm]	0.36140
Secondary Foil Sigma [cm]	1.12
Δ_{max}^{+}	1.
Δ_{max}^{-}	−2.8
D_x [%]	5.2

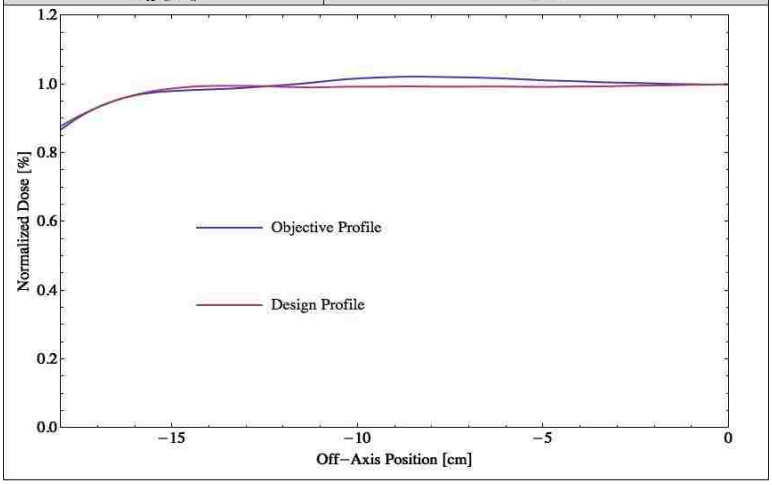

(a)

19 MeV	
Number of Primary Foils	5
Secondary Foil Thickness [cm]	0.36140
Secondary Foil Sigma [cm]	1.12
Δ_{max}^{+}	0.
Δ_{max}^{-}	−2.9
D_x [%]	4.7

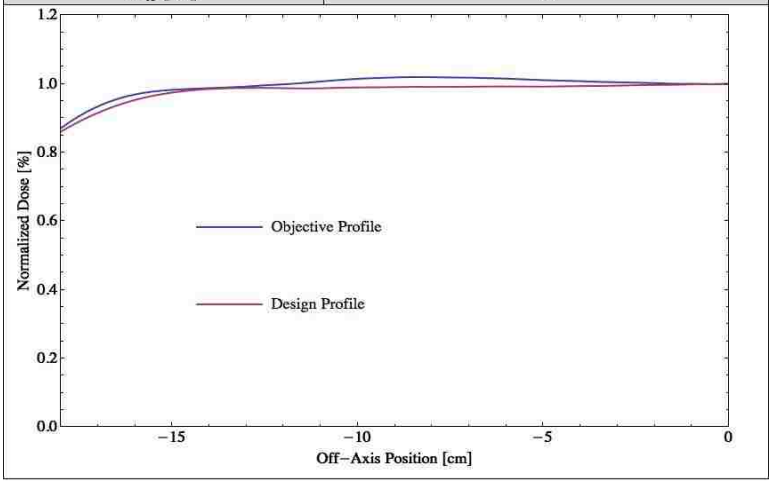

(b)

Figure 25: Comparison of normalized dose [%] versus off-axis position [cm] for the objective and design profiles for design energies of (a) 20 MeV, (b) 19 MeV, (c) 18 MeV, (d) 17 MeV, and (e) 16 MeV. The Al secondary foil parameters are identified; the number of 30μm Ta primary foils varies. The maximum differences above (Δ_{max}^{+}) and below (Δ_{max}^{-}) the objective profile and D_x are indicated.

19 MeV	
Number of Primary Foils	5
Secondary Foil Thickness [cm]	0.36140
Secondary Foil Sigma [cm]	1.12
Δ_{max}^{+}	0.
Δ_{max}^{-}	−2.9
D_x [%]	4.7

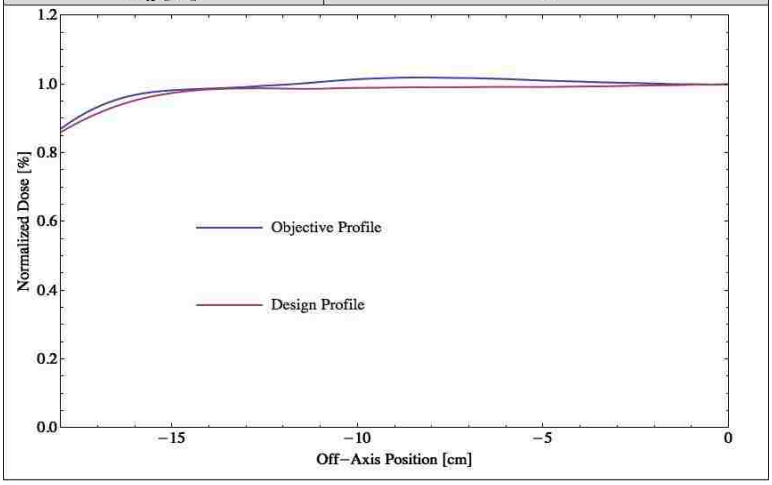

(c)

17 MeV	
Number of Primary Foils	4
Secondary Foil Thickness [cm]	0.36140
Secondary Foil Sigma [cm]	1.12
Δ_{max}^{+}	3.3
Δ_{max}^{-}	−1.2
D_x [%]	4.0

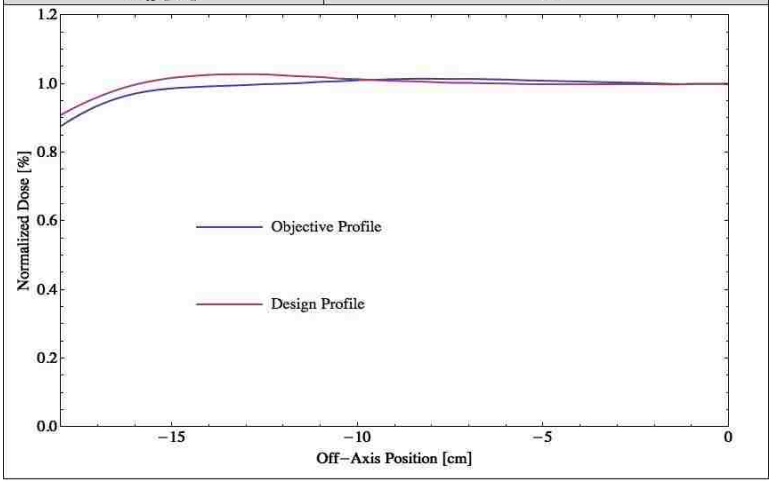

(d)

Figure 25 (continued): Comparison of normalized dose [%] versus off-axis position [cm] for the objective and design profiles for design energies of (a) 20 MeV, (b) 19 MeV, (c) 18 MeV, (d) 17 MeV, and (e) 16 MeV. The Al secondary foil parameters are identified; the number of 30μm Ta primary foils varies. The maximum differences above (Δ_{max}^{+}) and below (Δ_{max}^{-}) the objective profile and D_x are indicated.

16 MeV	
Number of Primary Foils	3
Secondary Foil Thickness [cm]	0.36140
Secondary Foil Sigma [cm]	1.12
$\Delta_{max}{}^{+}$	0.6
$\Delta_{max}{}^{-}$	−2.2
D_x [%]	3.6

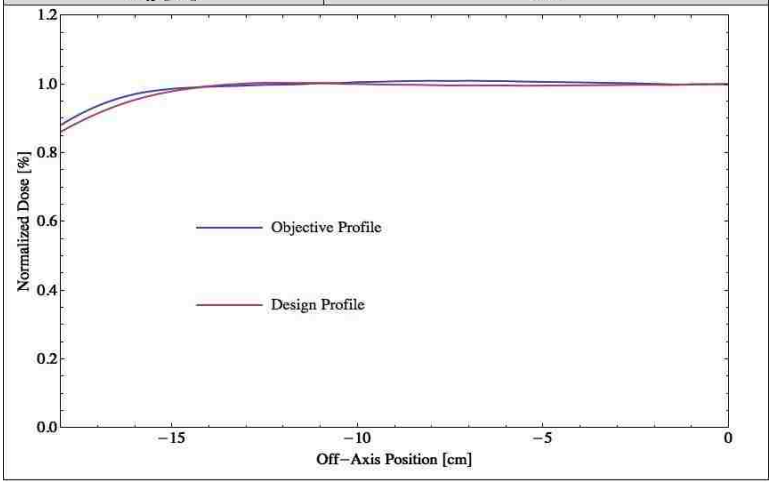

(e)

Figure 25 (continued): Comparison of normalized dose [%] versus off-axis position [cm] for the objective and design profiles for design energies of (a) 20 MeV, (b) 19 MeV, (c) 18 MeV, (d) 17 MeV, and (e) 16 MeV. The Al secondary foil parameters are identified; the number of 30μm Ta primary foils varies. The maximum differences above ($\Delta_{max}{}^{+}$) and below ($\Delta_{max}{}^{-}$) the objective profile and D_x are indicated.

Figure 26 shows the agreement between simulation design profiles and objective profiles for the secondary foil designed for most probable energies at the surface 7-13 MeV. The secondary foil is a Gaussian-shaped aluminum pyramid (approximated by 10 stacked disks of equal thickness) having a thickness of 0.1241 cm along central axis and a sigma of 1.52 cm. Each design profile was within the ±3% goal, with the maximum deviation reaching only 2.7% for 11 MeV.

7 MeV	
Number of Primary Foils	4
Secondary Foil Thickness [cm]	0.12410
Secondary Foil Sigma [cm]	1.52
Δ_{max}^{+}	1.5
Δ_{max}^{-}	−2.7
D_x [%]	1.4

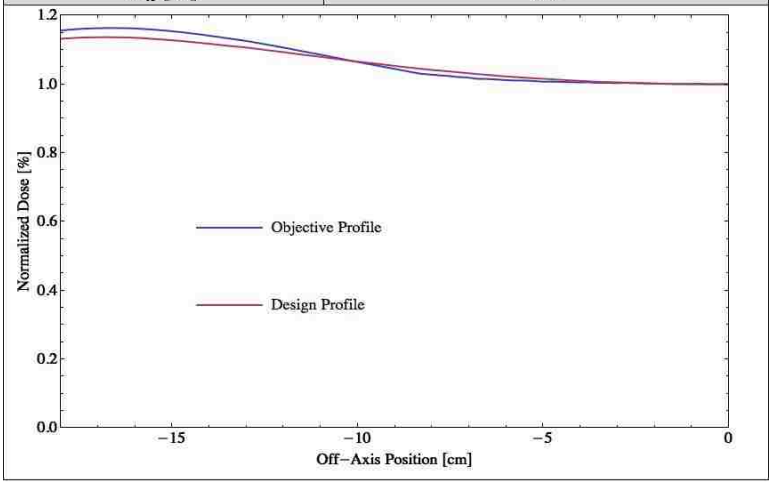

(a)

8 MeV	
Number of Primary Foils	3
Secondary Foil Thickness [cm]	0.12410
Secondary Foil Sigma [cm]	1.52
Δ_{max}^{+}	1.5
Δ_{max}^{-}	−2.4
D_x [%]	1.4

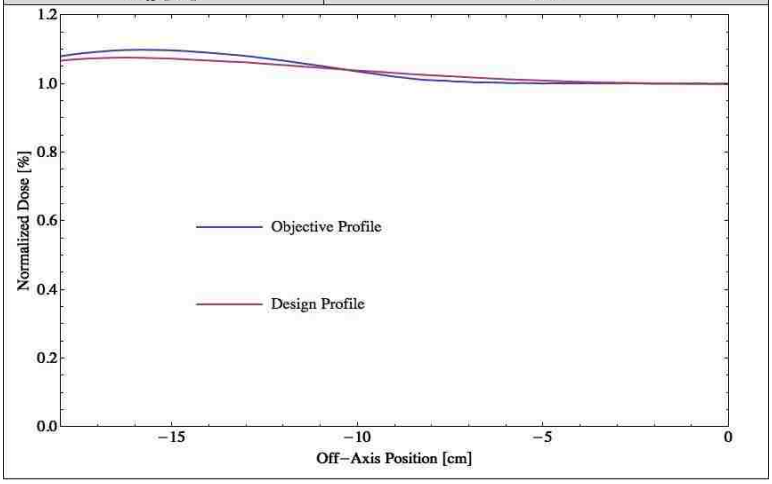

(b)

Figure 26: Comparison of normalized dose [%] versus off-axis position [cm] for the objective and design profiles for design energies of (a) 7 MeV, (b) 8 MeV, (c) 9 MeV, (d) 10 MeV, (e) 11 MeV, (f) 12 MeV, and (g) 13 MeV. The Al secondary foil parameters are identified; the number of 30μm Ta primary foils varies. The maximum differences above (Δ_{max}^{+}) and below (Δ_{max}^{-}) the objective profile and D_x are indicated.

9 MeV	
Number of Primary Foils	3
Secondary Foil Thickness [cm]	0.12410
Secondary Foil Sigma [cm]	1.52
Δ_{max}^{+}	1.8
Δ_{max}^{-}	−1.6
D_x [%]	1.6

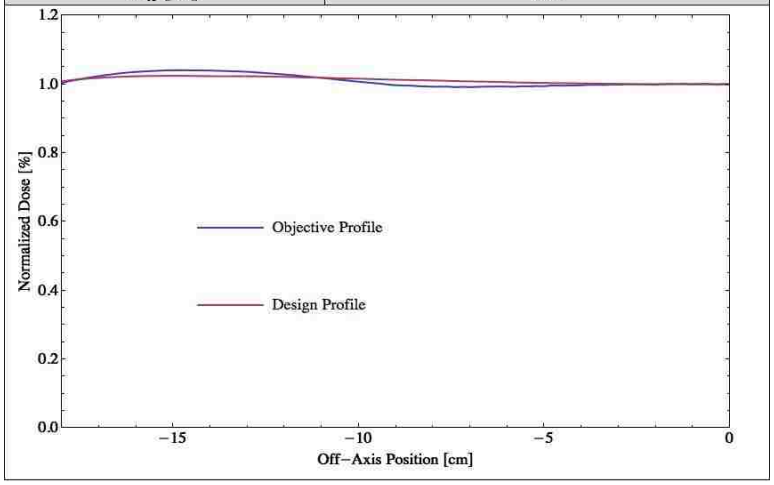

(c)

10 MeV	
Number of Primary Foils	3
Secondary Foil Thickness [cm]	0.12410
Secondary Foil Sigma [cm]	1.52
Δ_{max}^{+}	2.3
Δ_{max}^{-}	−1.1
D_x [%]	1.8

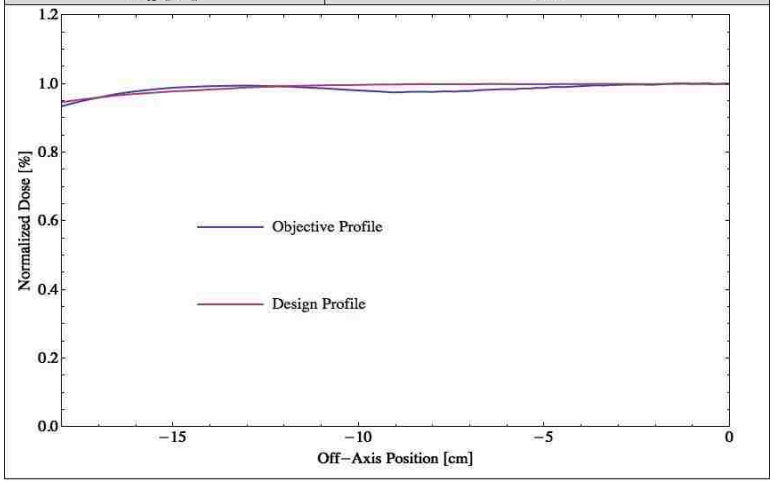

(d)

Figure 26 (continued): Comparison of normalized dose [%] versus off-axis position [cm] for the objective and design profiles for design energies of (a) 7 MeV, (b) 8 MeV, (c) 9 MeV, (d) 10 MeV, (e) 11 MeV, (f) 12 MeV, and (g) 13 MeV. The Al secondary foil parameters are identified; the number of 30μm Ta primary foils varies. The maximum differences above (Δ_{max}^{+}) and below (Δ_{max}^{-}) the objective profile and D_x are indicated.

11 MeV	
Number of Primary Foils	4
Secondary Foil Thickness [cm]	0.12410
Secondary Foil Sigma [cm]	1.52
Δ_{max}^{+}	2.6
Δ_{max}^{-}	−1.7
D_x [%]	2.1

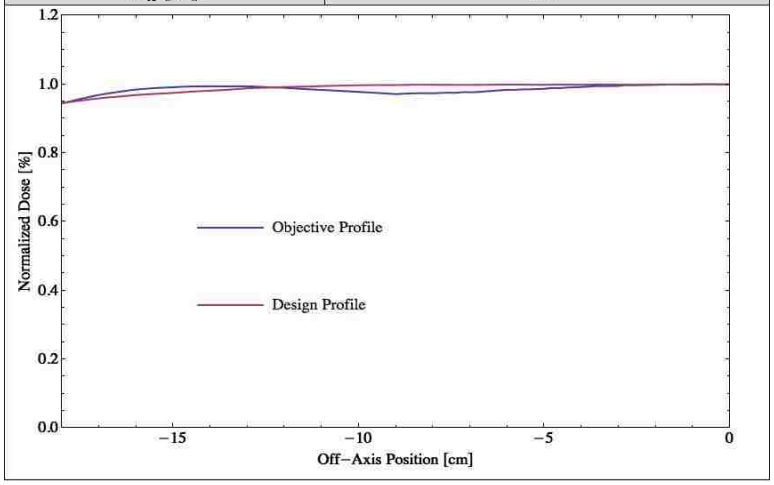

(e)

12 MeV	
Number of Primary Foils	5
Secondary Foil Thickness [cm]	0.12410
Secondary Foil Sigma [cm]	1.52
Δ_{max}^{+}	2.7
Δ_{max}^{-}	−1.4
D_x [%]	2.5

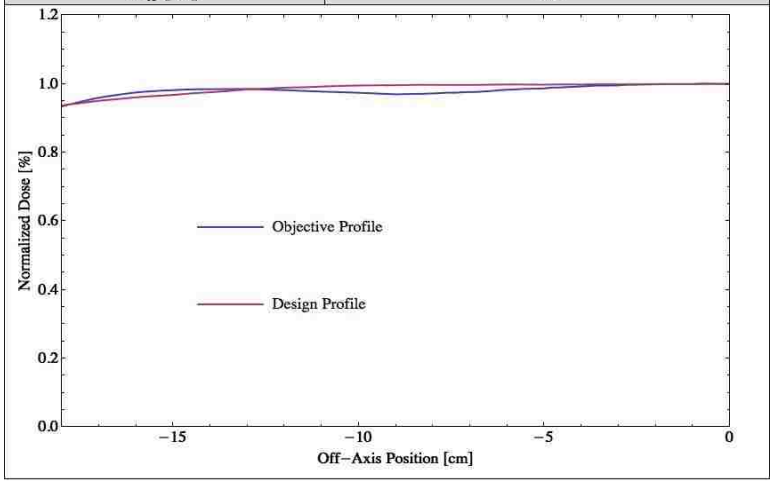

(f)

Figure 26 (continued): Comparison of normalized dose [%] versus off-axis position [cm] for the objective and design profiles for design energies of (a) 7 MeV, (b) 8 MeV, (c) 9 MeV, (d) 10 MeV, (e) 11 MeV, (f) 12 MeV, and (g) 13 MeV. The Al secondary foil parameters are identified; the number of 30μm Ta primary foils varies. The maximum differences above (Δ_{max}^{+}) and below (Δ_{max}^{-}) the objective profile and D_x are indicated.

13 MeV	
Number of Primary Foils	6
Secondary Foil Thickness [cm]	0.12410
Secondary Foil Sigma [cm]	1.52
$\Delta_{max}{}^{+}$	2.6
$\Delta_{max}{}^{-}$	−1.1
D_x [%]	2.8

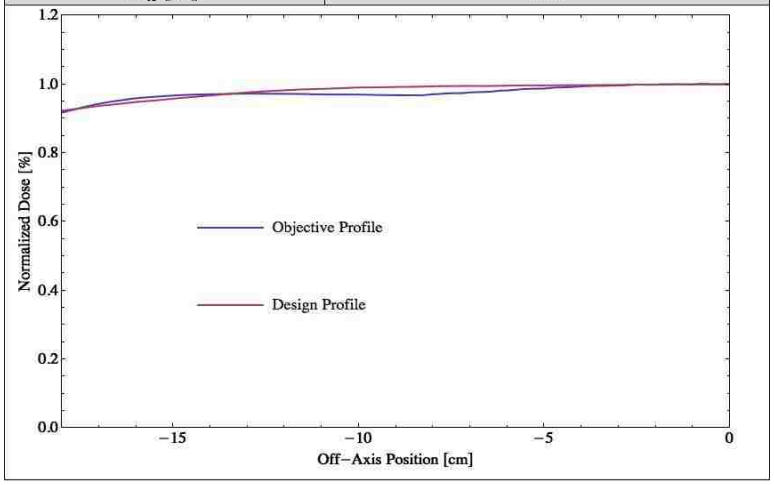

(g)

Figure 26 (continued): Comparison of normalized dose [%] versus off-axis position [cm] for the objective and design profiles for design energies of (a) 7 MeV, (b) 8 MeV, (c) 9 MeV, (d) 10 MeV, (e) 11 MeV, (f) 12 MeV, and (g) 13 MeV. The Al secondary foil parameters are identified; the number of 30μm Ta primary foils varies. The maximum differences above ($\Delta_{max}{}^{+}$) and below ($\Delta_{max}{}^{-}$) the objective profile and D_x are indicated.

Figure 27 shows the agreement between simulation design profiles and objective profiles for the secondary foil designed for most probable energies at the surface of 14 and 15 MeV. The secondary foil is a Gaussian-shaped aluminum pyramid (approximated by 10 stacked disks of equal thickness) having a thickness of 0.2221 cm along central axis and a sigma of 1.22 cm. Both of the design profiles were within the ±3% goal, with the maximum deviation being 2.8% for 15 MeV.

14 MeV	
Number of Primary Foils	3
Secondary Foil Thickness [cm]	0.22210
Secondary Foil Sigma [cm]	1.22
Δ_{max}^{+}	1.6
Δ_{max}^{-}	−1.3
D_x [%]	2.7

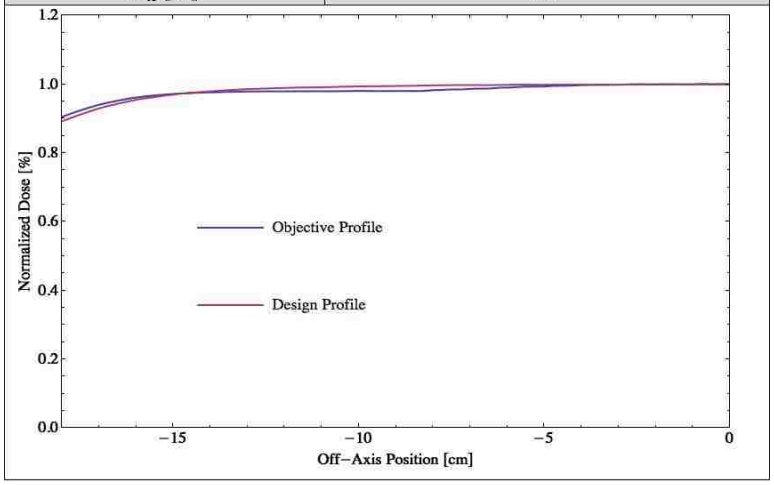

(a)

15 MeV	
Number of Primary Foils	4
Secondary Foil Thickness [cm]	0.22210
Secondary Foil Sigma [cm]	1.22
Δ_{max}^{+}	2.8
Δ_{max}^{-}	−0.3
D_x [%]	3.2

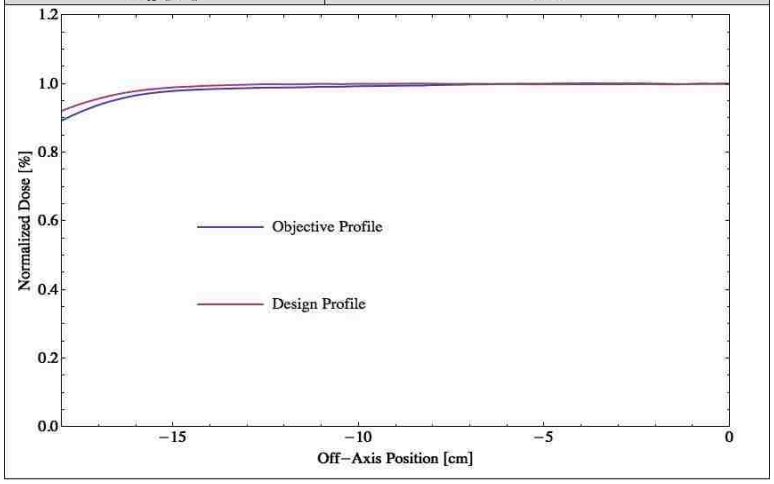

(b)

Figure 27: Comparison of normalized dose [%] versus off-axis position [cm] for the objective and design profiles for design energies of (a) 14 MeV and (b) 15 MeV. The Al secondary foil parameters are identified; the number of 30 μm Ta primary foils varies. The maximum differences above (Δ_{max}^{+}) and below (Δ_{max}^{-}) the objective profile and D_x are indicated.

Table 12: A summary of the primary and secondary foil combination used, as well as maximum deviations and central axis photon dose percentage for each design energy.

$E_{p,0}$ [MeV]	2° σ [cm]	2° Δt [cm]	# 1° Foils	$(\Delta_{max})^-$ [%]	$(\Delta_{max})^+$ [%]	D_x [%]
7	1.52	0.1241	4	2.7	1.5	1.4
8	↓	↓	3	2.4	1.5	1.4
9	↓	↓	3	1.6	1.8	1.6
10	↓	↓	3	1.1	2.3	1.8
11	↓	↓	4	1.7	2.6	2.1
12	↓	↓	5	1.4	2.7	2.5
13	↓	↓	6	1.1	2.6	2.8
14	1.22	0.2221	3	1.3	1.6	2.7
15	↓	↓	4	0.3	2.8	3.2
16	1.12	0.3614	3	2.2	0.6	3.6
17	↓	↓	4	1.2	3.3	4.0
18	↓	↓	4	4.4	0	4.2
19	↓	↓	5	2.9	0	4.7
20	↓	↓	6	2.8	1.0	5.2

Since the design criteria had been met for every other energy, there was not a particular need for the medium-energy (14 and 15 MeV) foil to be any more versatile with energy. As Figure 27 shows, even when the the foil design was tailored specifically for these two design energies, it was barely possible to achieve agreement between the objective and design functions to within the stated goal of ±3%. It was found that attempts to design a foil that spanned a greater range of energies had detrimental effects to the foil's ability to meet design criteria at these two energies. Thus, it was decided to design specfically for these two energies that had yet to be covered.

The lack of versatility for this foil can be attributed in part to the discrete steps of the primary foil thicknesses. For lower energies (e.g., 7-13 MeV) the effect of a 1 MeV

change in the design energy was approximately offset by increasing or decreasing the primary foil by one 30μm thick layer. However, at higher energies (>13 MeV), a 1 MeV change in beam energy caused a pronounced reduction in the effectiveness of the primary foil. Figure 28(a) shows the same secondary foil used for 14 and 15 MeV at a design energy of 13 MeV. The same number of primary foils were used in both instances. Notice that a 1 MeV change in design energy causes an change in the design function of approximately 10%. Figure 28(b) shows the change induced (approximately 15%) in the design profile when a 30μm foil thickness was removed to attempt to compensate for the increased scatter due to the 1 MeV reduction in energy (from 14 MeV). These data indicate that for this particular secondary foil design, the optimal primary foil thickness would consist of approximately 2.5 tantalum primary foil layers.

13 MeV	
Number of Primary Foils	3
Secondary Foil Thickness [cm]	0.22200
Secondary Foil Sigma [cm]	1.22
Δ_{max}^{+}	6.5
Δ_{max}^{-}	−0.1
D_x [%]	2.5

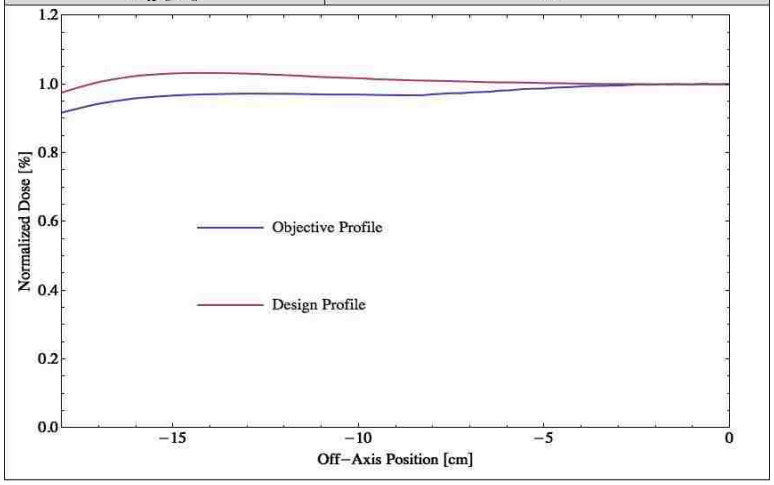

(a)

13 MeV	
Number of Primary Foils	2
Secondary Foil Thickness [cm]	0.22200
Secondary Foil Sigma [cm]	1.22
Δ_{max}^{+}	1.7
Δ_{max}^{-}	−8.3
D_x [%]	2.4

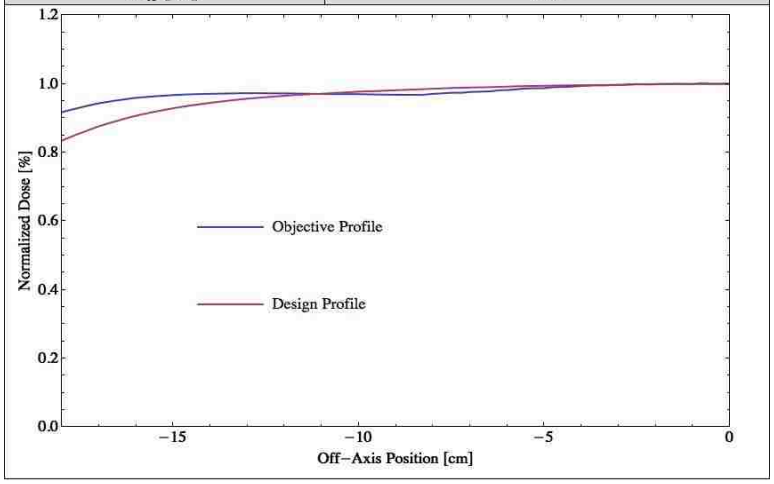

(b)

Figure 28: Comparison of normalized dose [%] versus off-axis position [cm] for the objective and design profiles for the design energy of 13 MeV with (a) 3 and (b) 2 Tantalum primary foils. Aluminum secondary foil parameters are identified. The maximum differences above (Δ_{max}^{+}) and below (Δ_{max}^{-}) the objective profile and D_x are indicated.

Chapter 4 Aim 3—Use of Monte Carlo Dose Calculation for Refinement of Design of Electron Dual Foil Scattering System and Resulting Dose Calculation

Aim 3: The results of Aim 2 will be compared with Monte Carlo dose calculations, after which the objective profiles used in Aim 2 will be modified such that a second optimization should provide more uniform beams. The Monte Carlo dose calculations with the revised design of electron dual scattering foil system will be used to test the hypothesis.

The intention of aim 3 was to use Monte Carlo calculations to verify that the scattering foil system designs produced clinically usable beams. A model of the Mary Bird Perkins Cancer Center's Elekta Infinity, already developed by Harris (2012), was used for Monte Carlo calculations of the existing beams. For the optimization process, which design foils in 1-MeV increments from 7-20 MeV, the model was modified. Specifically, this included modifying input parameters, such as accelerator energy spectra, x-ray jaw positions, backup diaphragm positions, and dual scattering foil system design. The resulting Monte Carlo calculated dose distributions were used to extract major axes profiles, diagonal profiles, and bremsstrahlung dose along central axis. These results were used to modify the initial objective profiles for the analytical electron dual scattering foil simulator, which then re-optimized the dual scattering foil design. The refined dual foil designs were then used by the Monte Carlo for final dose calculations.

4.1 Methods

4.1.1 Monte Carlo Model Modifications

Harris (2012) developed a Monte Carlo model of the Elekta Infinity accelerator at Mary Bird Perkins Cancer Center (MBPCC). This model accounted for every component currently utilized on the accelerator. The source was modeled for all energies as a parallel beam (zero angular spread) having a two-dimensional elliptical Gaussian spatial distribution ($FWHM_x \times FWHM_y$=1mm×2mm) in width. In this study the incident beam at all energies was assumed an elliptical Gaussian (1mm×1mm), parallel beam. In order to use this model to verify the dual foil designs, some modifications and assumptions were made. These changes are addressed in the following subsections.

4.1.1.a Incident Energy Spectra

MBPCC Elekta beam energies, nominally referred to as 7, 9, 10, 11, 13, 16, and 20 MeV, correspond to most probable energies at the surface (isocenter) of 7.15, 8.66, 9.92, 11.28, 13.13, 16.22, and 20.5 MeV, respectively. However, energies exiting the accelerator are considerably greater because of energy loss in the end window, dual scattering foils, monitor ion chamber and air. Harris (2012) determined Gaussian incident energy spectra exiting the accelerator for the current energies available on the MBPCC Elekta Infinity accelerator. These energy spectra were assumed Gaussian and defined by two parameters: most probable incident energy, $E_{p,i}$, and the full-width and half-maximum (FWHM) expressed as a percentage of the most probable energy at the surface, $\frac{FWHM}{E_{p,i}} \times 100\%$. Harris adjusted the parameters so that the Monte Carlo-calculated and measured percent depth

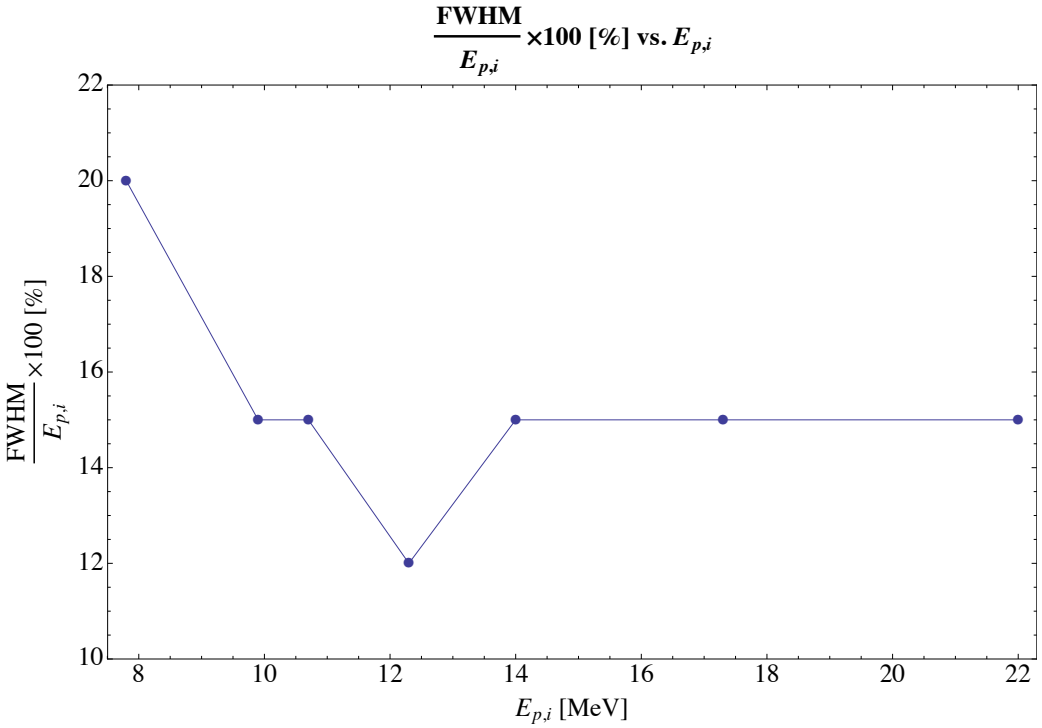

Figure 29: Incident energy width versus energy (from Harris 2012).

Table 13: Table of parameters used in defining incident energy spectra for each of the design energies.

$E_{p,0}$ [MeV]	Analytical Code $E_{p,i}$ [MeV]	$FWHM_{Harris}$ [%]	$FWHM_{Used}$ [%]
7	7.76	22	22
8	8.71	20	20
9	9.66	17	18
10	10.67	15	16
11	11.74	14	14
12	12.8	13	14
13	13.87	13	16
14	14.83	15	16
15	15.89	15	16
16	17.09	15	16
17	18.13	15	16
18	19.15	15	16
19	20.2	15	16
20	21.25	15	16

dose curves agreed. Figure 29 shows a plot of $\frac{FWHM}{E_{p,i}} \times 100\%$ versus $E_{p,i}$ for the spectra developed by Harris.

The scattering foil systems designed in this study were developed for different most probable surface energies ($E_{p,0}$). Thus, it was necessary to determine the appropriate incident energy spectra parameters exiting the accelerator for each of the respective design energies. The most probable incident energy, $E_{p,i}$, for each design energy was known, for this was determined by the design simulator during the design process. The FWHM was determined using linear interpolation in Figure 29, and the results are listed in Table 13. It should be noted that the spectra FWHMs actually used differed slightly from those indicated in Figure 29 due to a systematic interpolation error. These differences, noted in Table 13, have no significant impact on the calculations and study.

4.1.1.b X-ray Jaw and Back-up Diaphragm Positions

Positions currently used on the MBPCC Elekta Infinity accelerator for both the x-ray jaws and the back-up diaphragms were used in the model developed by Harris. Though it had already been found that scatter from these collimators was negligible (see section 3.2.1), positions of x-ray collimators impacts beam uniformity as it impacts side-scatter equilibrium, particularly near the projection of the collimator edges and at low electron energies. As evidenced by Figure 30, the current jaw positions do not follow a smooth, monotonic pattern indicating x-ray collimator position may not be optimal, and there could be needless leakage, particularly at 9 MeV. Until the parallel project to redesign the collimation system at the new energies (7-20 MeV in 1-MeV increments) can provide x-ray collimation settings, it was assumed that these settings should vary smoothly and linearly

with energy. Thus, in order to determine the collimator settings used in the Monte Carlo validation, parallel lines separated 1 cm were drawn to estimate the expected trend the collimators might follow (cf. Figure 30).

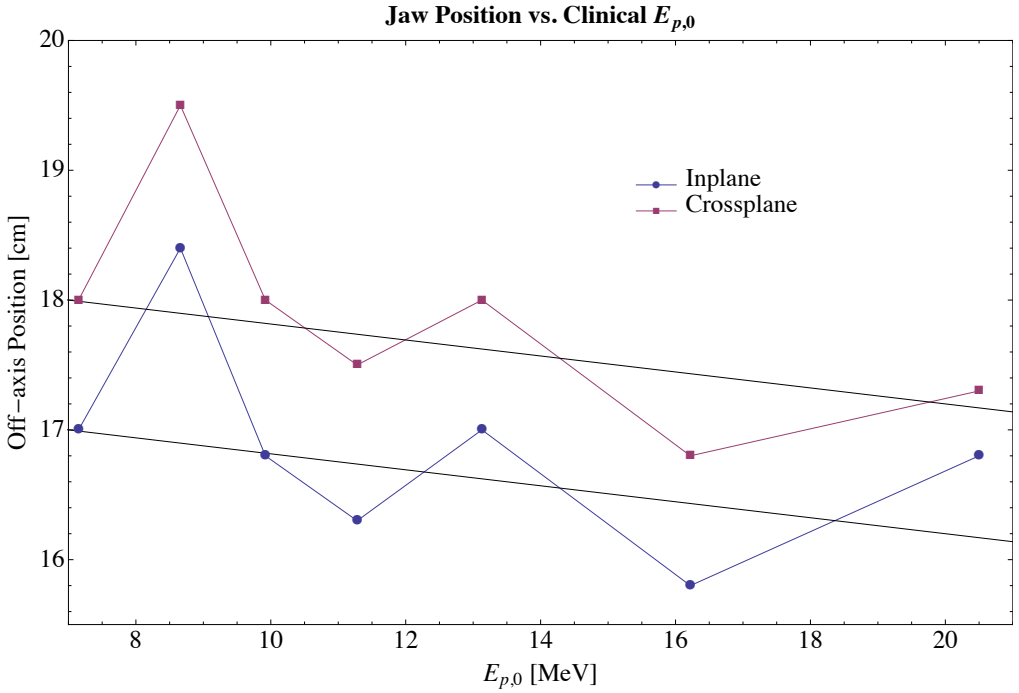

Figure 30: Jaw positions vs. clinical $E_{p,0}$ for 25×25cm² applicator on the MBPCC Elekta Infinity accelerator and the fit lines used to determine jaw positions for Monte Carlo simulations to verify foil designs. Crossplane (backup diaphragms) are red points, and inplane (x-ray jaws) are blue points.

X-raw jaw and back-up diaphragm positions were determined according to the estimated fit lines presented in Figure 30. These lines correspond to:

$$Crossplane\ Jaw\ Positions(E) = -\frac{4}{65}(E-7) + 17$$

$$Inplane\ Jaw\ Positions(E) = -\frac{4}{65}(E-7) + 18.$$

These equations were used to calculate jaw positions at each of the design energies. The field widths were then coded into the appropriate Monte Carlo input files.

4.1.2 Monte Carlo Simulations to Verify Foil Designs

4.1.2.a Monte Carlo Simulations: Profile Analysis

Monte Carlo simulations were performed to verify the calculations of the electron dual foil scattering system simulator, i.e., that the foils designed in this study produced sufficiently broad and flat beams for the case of a $25\times25cm^2$ applicator. BEAMnrc was used to score phasespaces at 100cm from the source for a total of 2 billion initial histories in each simulation. The phasespaces were then passed to DOSXYZ, where 2 billion histories were transported into a water phantom with dimensions $50x50x50cm^3$. Dose deposited by all particles was recorded, and a voxel size of $5x5x5mm^3$ was used were centered about the depth of calculation, i.e., for 1 cm depth the voxel edges were at 0.75cm and 1.25cm depths.All profiles analyzed were at a depth of 2cm, except for 7 MeV, which was at a depth of 1 cm.

Transverse and diagonal profiles were then extracted from the DOSXYZ output files. These profiles were then symmetrized and normalized to an average of the five voxel values ±1cm from central axis. Flatness was evaluated over clinically-relevant off-axis ranges, i.e, for the transverse profiles, 2 cm inside the off-axis positions of the 50% dose points. For the diagonals, flatness was evaluated from $2\sqrt{2}$ cm inside the off-axis positions of the 25% dose points. A designed foil combination was considered "successful" if it produced a profile with dose values within ±3% of 100% dose within these ranges. Monte Carlo statistics were such that relative uncertainties (1σ) within these ranges were approximately 1% (standard error for a typical voxel in the uniform dose region was 1.0%).

4.1.2.b Monte Carlo Simulation: Bremsstrahlung Analysis

The same phases paces were used as sources to verify the photon dose predicted by the foil design simulator. Two billion phasespace particles were transported again into a $50x50x50cm^3$ water phantom. Dose was scored in $5x5mm^2$ voxels with 1mm thickness along central axis to a depth of 13 cm, yielding relative uncertainties of less than 3%.

Bremsstrahlung dose was determined by finding the dose at R_p+2cm as a percentage of the maximum dose along central axis for each of the design energies. Each result was then compared with the bremsstrahlung dose predicted by the design simulator.

4.1.3 Refining of Objective Profiles Based on Monte Carlo Data

Monte Carlo data provided a means by which to refine the objective profiles so as to improve upon the original dual scattering foil designs. This was accomplished by comparing the off-axis dose profiles calculated by the electron dual scattering foil simulator with that of the Monte Carlo calculations. The correction scheme below assumes the Monte Carlo calculations to be accurate, i.e., to agree with measurements (within 1%). This is not the case, as Harris showed differences as great as 3% (cf. Appendix B). If future work cannot improve agreement, such differences could be taken into account by accounting for them in the current scheme or by strictly using measured data. However, the Monte Carlo calculations were assumed 100% accurate in the current work, whose purpose was to demonstrate methodology.

The refinement procedure was as follows: First, the off-axis dose calculations from Monte Carlo were compared with 100%. Second, the magnitude by which the Monte Carlo off-axis dose profile deviated from 100% (over the clinically-relevant range) was subtracted from the off-axis dose calculated by the electron dual scattering foils system

simulator at each point. Third, the resulting curve becomes the new objective profile for the dual foil scattering foil system simulator. Fourth, the simulator is used to re-optimize the dual scattering foil designs, i.e., the refined designs. If the new off-axis profiles reproduced the objective profile, then the Monte Carlo calculation should produce a profile that is closer to 100% (over the entire clinically-relevant range). This process is illustrated in Figure 31.

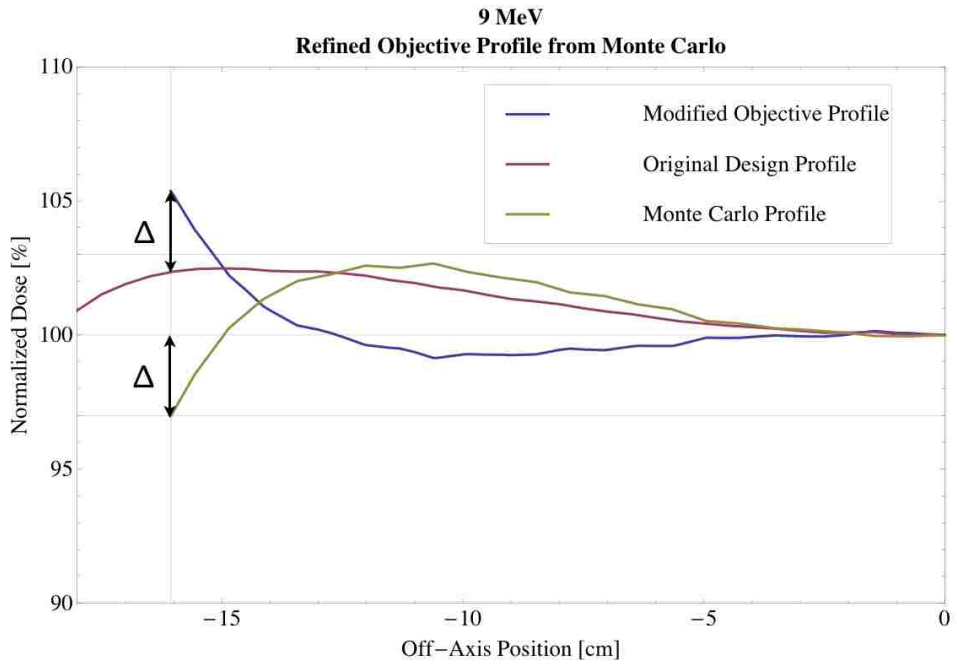

Figure 31: Example plots at 9 MeV illustrating the process of refining the objective profile.

4.2 Results

4.2.1 Foil Design Simulations

4.2.1.a Transverse Profiles

Monte Carlo simulations showed that all energies (7-20 MeV) passed flatness criteria along the major axes (perpendicular to collimator edges) in both transverse directions (inplane and crossplane). Figure 32 shows representative plots of off-axis dose profiles along the major axes from the Monte Carlo simulations for: (a) the best case, 14

MeV; and (b) the worst case, 17 MeV. The remaining transverse profiles are shown in Appendix I. The maximum deviations of dose from 100% within the clinically-relevant range (2 cm inside 50% dose points) above and below 100% are shown in Table 14 for each beam energy. The greatest deviation from 100%, with a deviation of 2.8% was at 17 MeV.

Table 14: Table of maximum deviations from 100% over the clinically relevant ranges (2 cm inside of 50% dose points) for each of the design energies.

Transverse Monte Carlo Results				
$E_{p,0}$ [MeV]	2° Foil	1° Foil	$(\Delta)_{min}$	$(\Delta)_{max}$
7	1	4	−0.3%	2.4%
8	1	3	0%	2.2%
9	1	3	−0.2%	1.8%
10	1	3	−1%	0.9%
11	1	4	−1.2%	0.5%
12	1	5	−0.9%	0.8%
13	1	6	−1.5%	0.3%
14	2	3	−0.3%	0.8%
15	2	4	0%	1.3%
16	3	3	−0.2%	2.2%
17	3	4	−0.5%	2.8%
18	3	4	−1.1%	0%
19	3	5	−1.0%	0.8%
20	3	6	−1.2%	0.7%

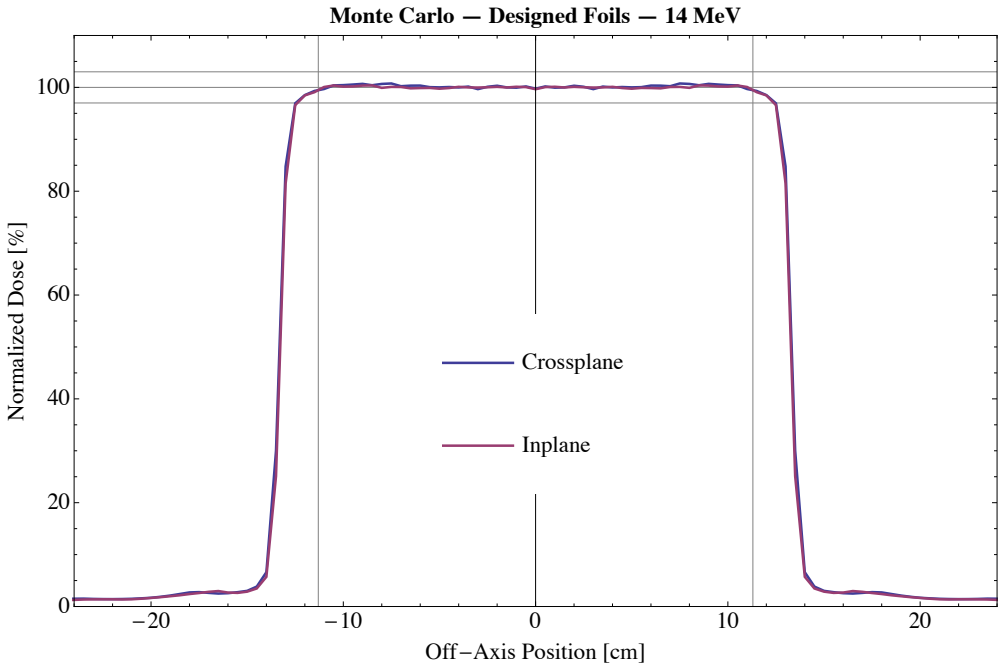

(a)

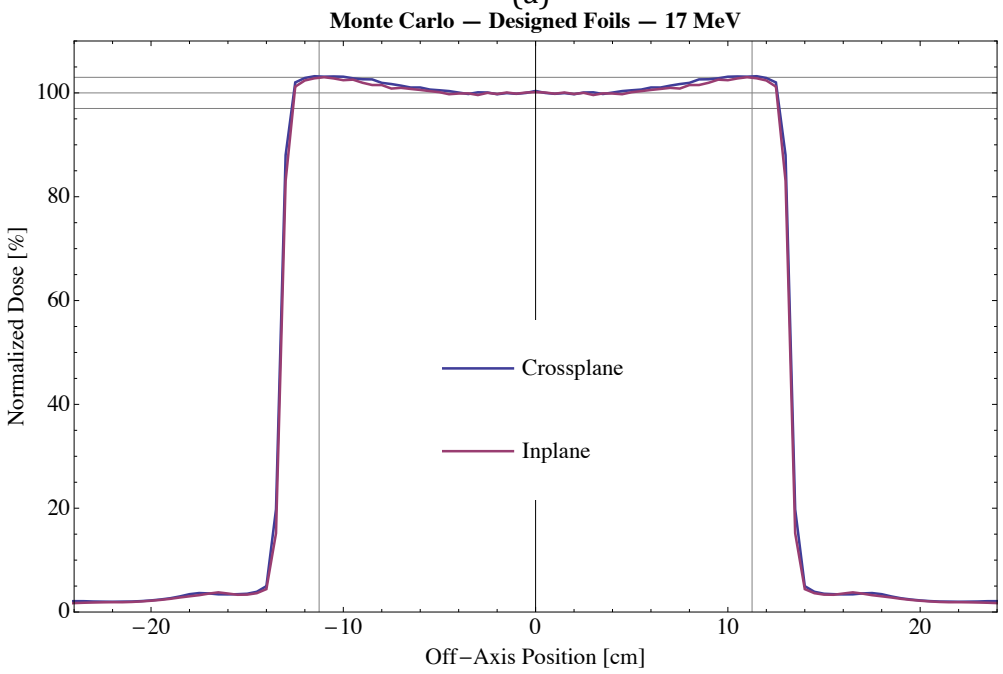

(b)

Figure 32: Plots of crossplane and inplane profiles for Monte Carlo simulations of designed foil systems for (a) 14 MeV and (b) 17 MeV. Horizontal lines at 100±3% and vertical lines 2 cm inside the 50% dose value demarcate the acceptable range for transverse off-axis dose profiles.

4.2.1.b Diagonal Profiles

Monte Carlo simulations showed that all energies did not pass flatness criteria along the diagonals. Figure 33, which shows plots of off-axis dose profiles along the diagonals from the Monte Carlo simulations for (a) the best case, 20 MeV, and (b) the worst case, 18 MeV. The remaining diagonal profiles plots may be found in Appendix J. The maximum deviations of dose from 100% within the clinically-relevant range ($2\sqrt{2}$ cm inside the 25% dose points) above and below 100% are shown in Table 15 for each beam energy. The best agreement was found in the case of 20 MeV, which did not deviate more than 2.3% over the clinically relevant range, whereas 18 MeV had the worst results, being 6.1% below 100% dose at the edge of the clinically relevant range.

Table 15: Table of maximum deviations from 100% dose over the clinically relevant ranges ($2\sqrt{2}$ $2\sqrt{2}$cm inside of 25% dose points) for each of the design energies.

Diagonal Monte Carlo Results				
$E_{p,0}$ [MeV]	1° Foil	2° Foil	$(\Delta)_{min}$	$(\Delta)_{max}$
7	1	4	−2.9%	4%
8	1	3	−2.4%	3.7%
9	1	3	−3.0%	2.7%
10	1	3	−5.0%	1.5%
11	1	4	−4.8%	0.9%
12	1	5	−4.4%	1.5%
13	1	6	−5.1%	0.5%
14	2	3	−3.7%	1.4%
15	2	4	−2.0%	2.4%
16	3	3	−2.0%	3.7%
17	3	4	−0.6%	5.3%
18	3	4	−6.1%	0.1%
19	3	5	−2.2%	2.3%
20	3	6	−1.9%	2.3%

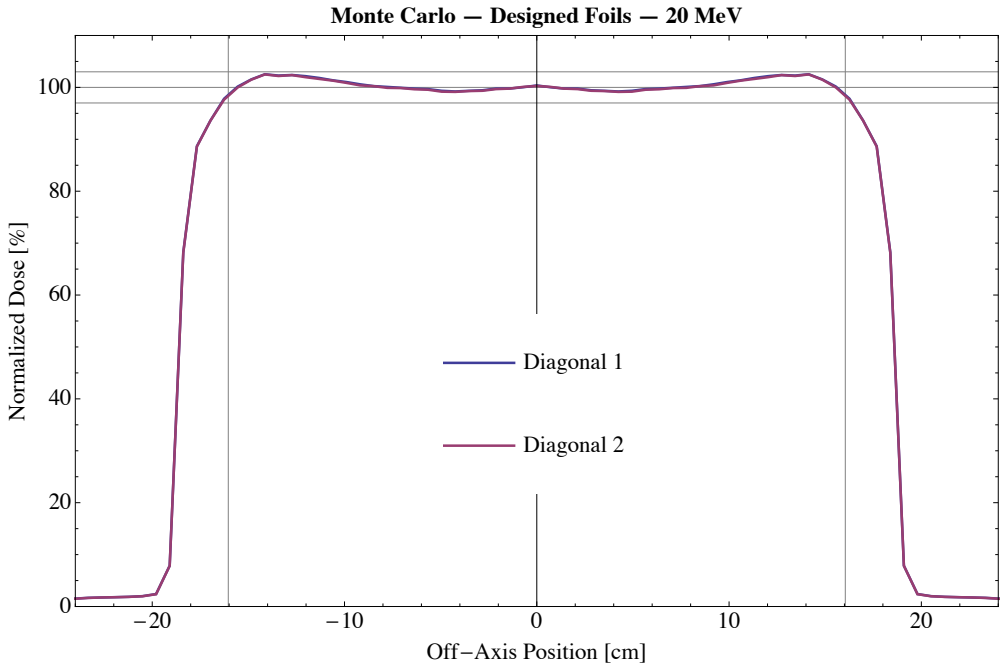

(a)

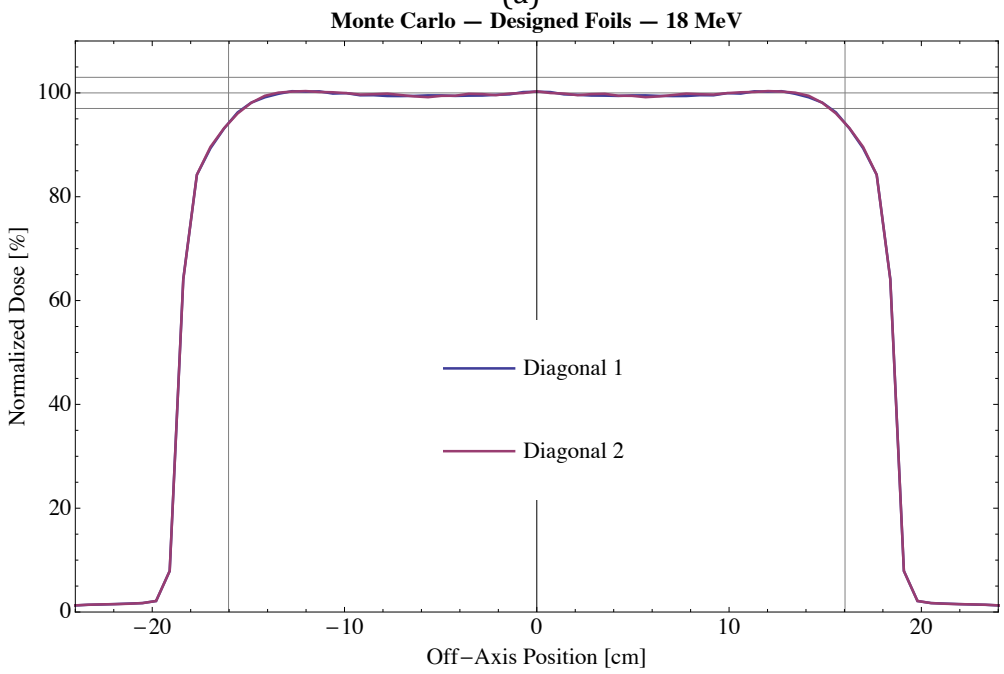

(b)

Figure 33: Plots of crossplane and inplane profiles for Monte Carlo simulations of designed foil systems for (a) 20 MeV and (b) 18 MeV. Horizontal lines at 100±3% and vertical lines at $2\sqrt{2}$ cm inside the 25% dose points demarcate the acceptable range for diagonal off-axis dose profile.

4.2.1.c Bremsstrahlung Dose

Bremsstrahlung doses predicted by Monte Carlo, which ranged from 1.2% at 7 MeV to 5.7% at 20 MeV, were found to agree well with that from the dual foil scattering design simulator. As seen in Table 16, the greatest deviation between the two was 0.5%.

Table 16: Bremsstrahlung dose (percent of maximum central axis dose) calculated by Monte Carlo (MC) simulations compared to that predicted by the design simulator (DS), along with the depth of calculation for each of the design energies.

$E_{p,0}$ [MeV]	R_p+2 [cm]	D_x (MC) [%]	D_x (DS) [%]
7	5.4	1.2	1.5
8	5.9	1.2	1.6
9	6.4	1.4	1.6
10	6.9	1.6	1.8
11	7.4	2.	2.1
12	7.9	2.6	2.5
13	8.4	3.	2.8
14	8.9	2.6	2.7
15	9.4	3.2	3.2
16	9.9	3.4	3.6
17	10.4	3.9	4.
18	10.9	4.4	4.2
19	11.4	4.9	4.7
20	11.9	5.7	5.2

4.2.2 Refined Objective Profiles

After the initial Monte Carlo simulations were performed, the objective profile for each of the design energies was modified according to the Monte Carlo simulation data as described in section 4.1.3. Plots showing the original design function, Monte Carlo dose profiles, and the new objective profile for each of the design energies are shown in Figure 34.

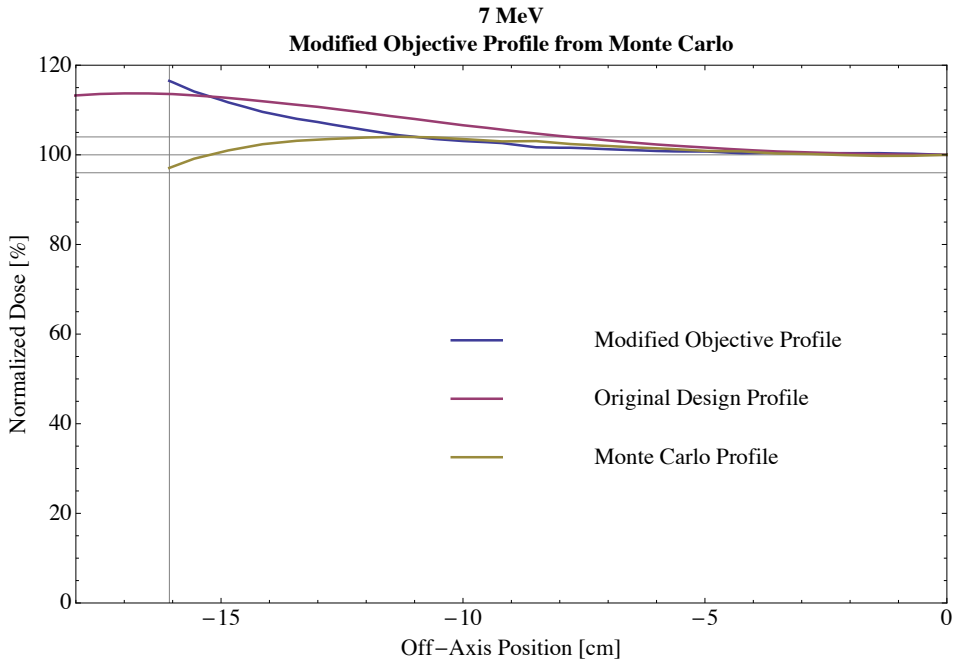

(a)

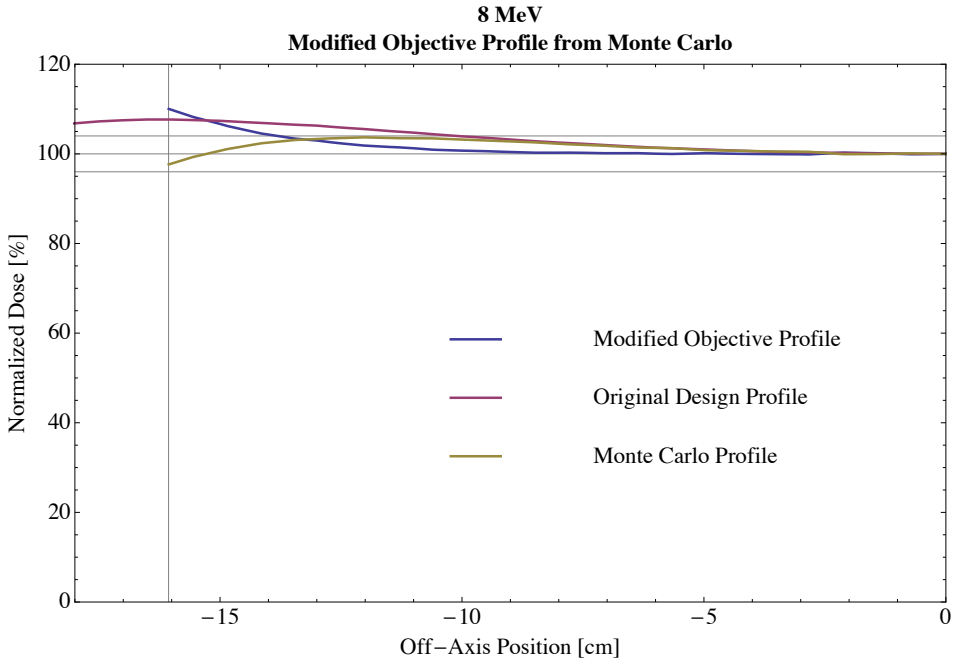

(b)

Figure 34: Plots of the original design profiles, Monte Carlo simulation data, and the modified objective profiles for (a) 7 MeV, (b) 8 MeV, (c) 9 MeV, (d) 10 MeV, (e) 11 MeV, (f) 12 MeV, (g) 13 MeV, (h) 14 MeV, (i) 15 MeV, (j) 16 MeV, (k) 17 MeV, (l) 18 MeV, (m) 19 MeV, and (n) 20 MeV.

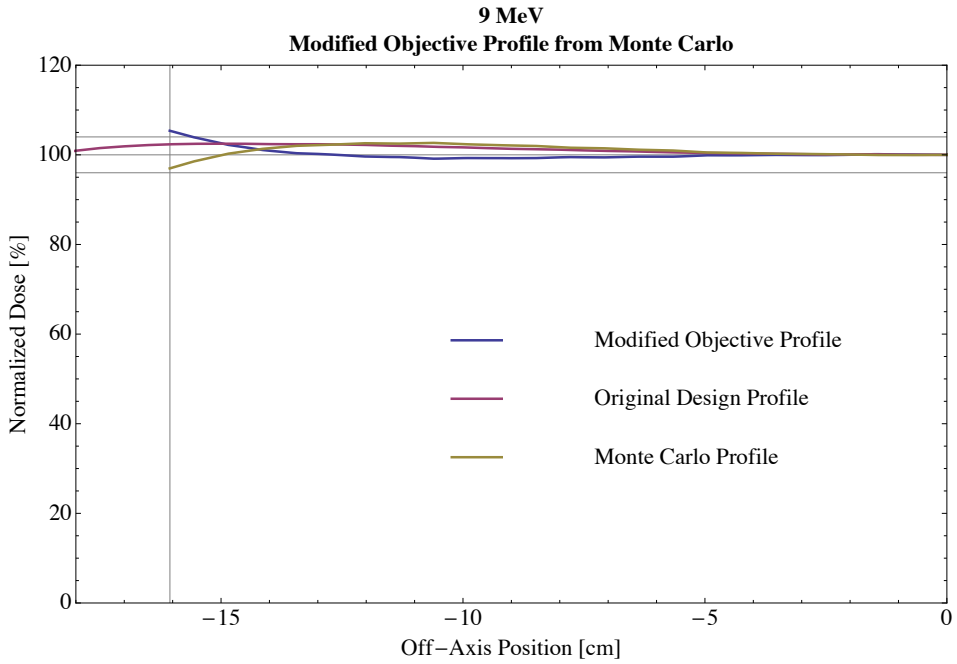

(c)

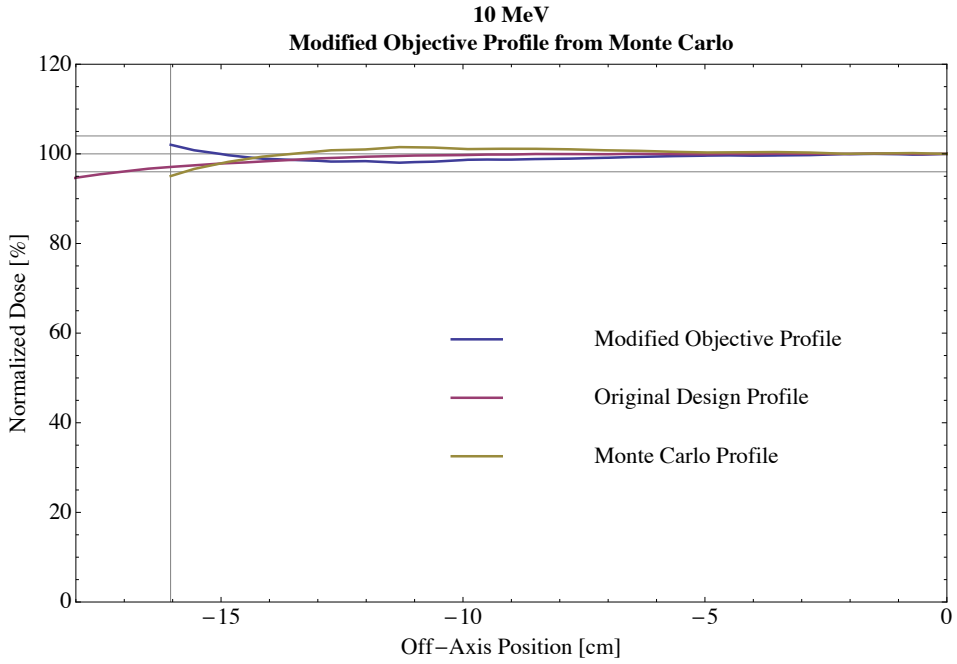

(d)

Figure 34 (continued): Plots of the original design profiles, Monte Carlo simulation data, and the modified objective profiles for (a) 7 MeV, (b) 8 MeV, (c) 9 MeV, (d) 10 MeV, (e) 11 MeV, (f) 12 MeV, (g) 13 MeV, (h) 14 MeV, (i) 15 MeV, (j) 16 MeV, (k) 17 MeV, (l) 18 MeV, (m) 19 MeV, and (n) 20 MeV.

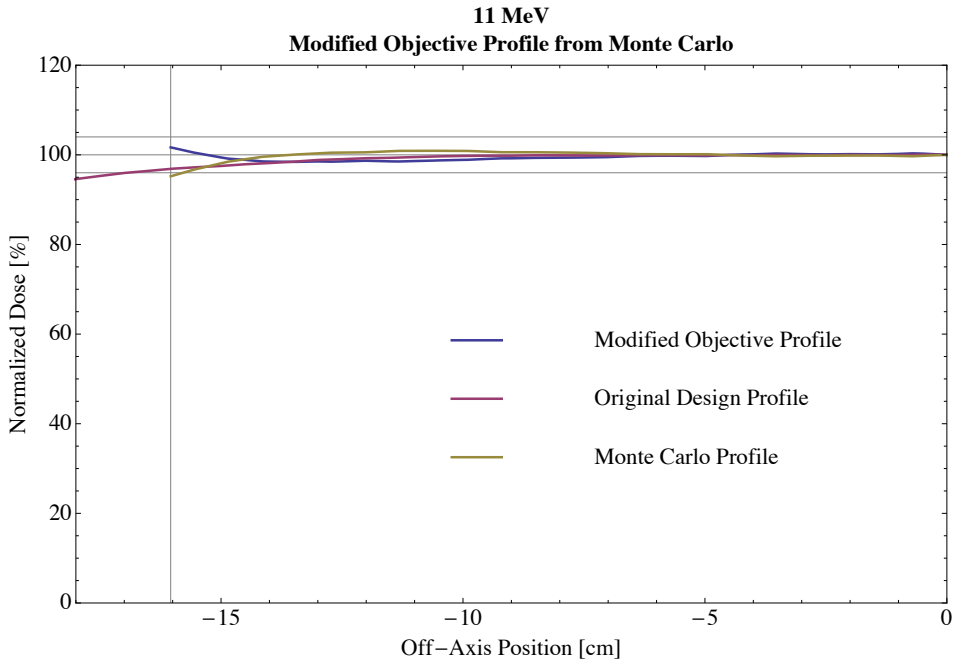

(e)

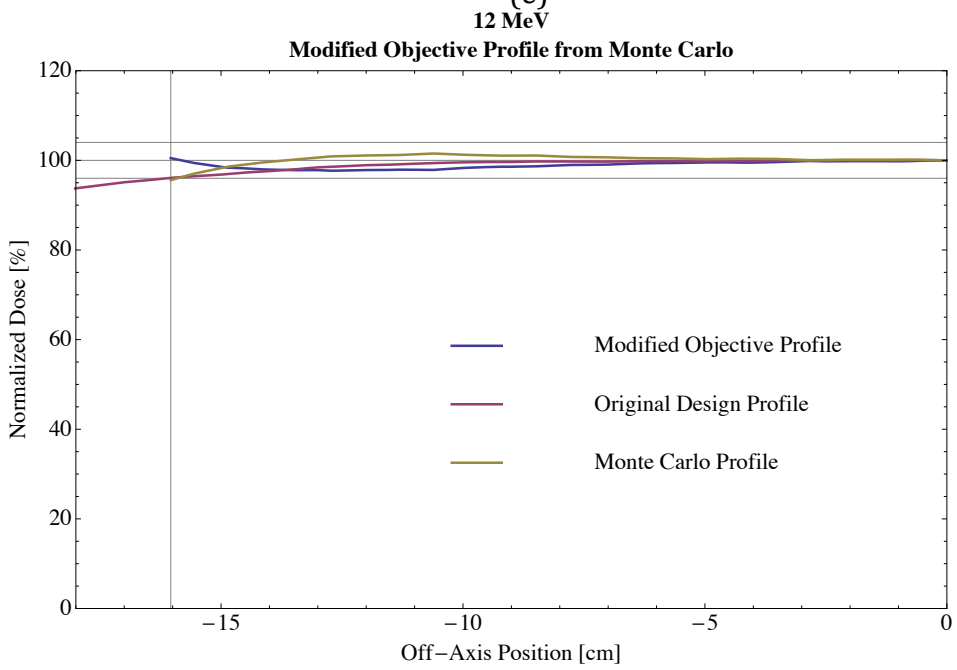

(f)

Figure 34 (continued): Plots of the original design profiles, Monte Carlo simulation data, and the modified objective profiles for (a) 7 MeV, (b) 8 MeV, (c) 9 MeV, (d) 10 MeV, (e) 11 MeV, (f) 12 MeV, (g) 13 MeV, (h) 14 MeV, (i) 15 MeV, (j) 16 MeV, (k) 17 MeV, (l) 18 MeV, (m) 19 MeV, and (n) 20 MeV.

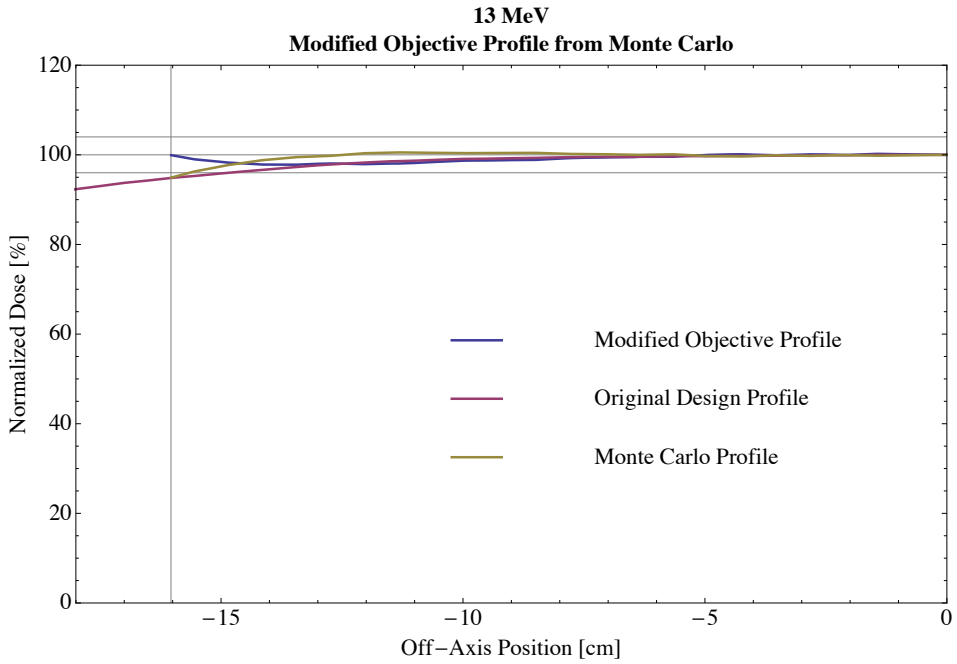

(g)

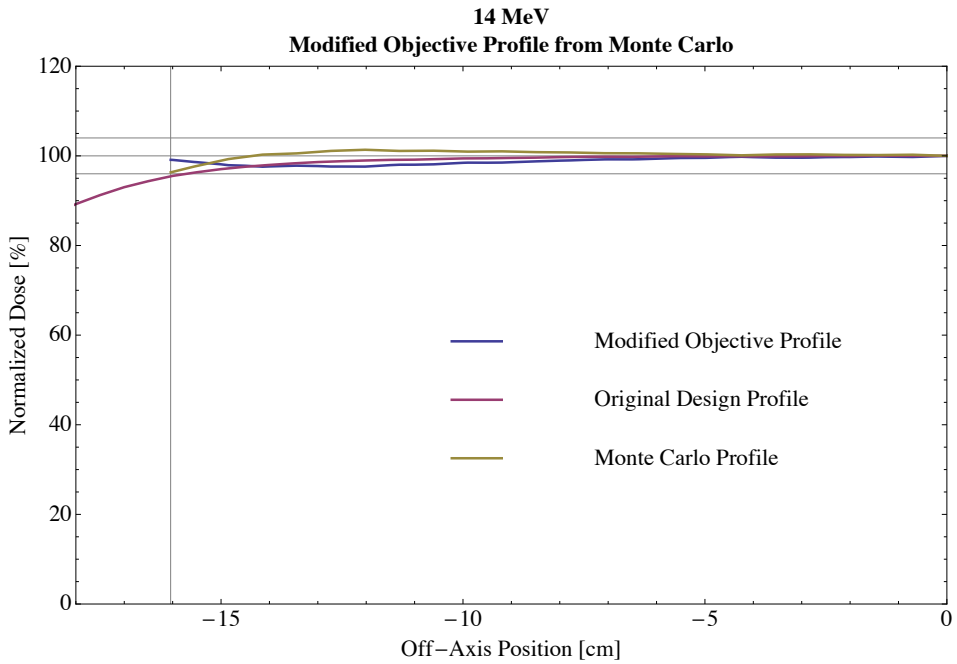

(h)

Figure 34 (continued): Plots of the original design profiles, Monte Carlo simulation data, and the modified objective profiles for (a) 7 MeV, (b) 8 MeV, (c) 9 MeV, (d) 10 MeV, (e) 11 MeV, (f) 12 MeV, (g) 13 MeV, (h) 14 MeV, (i) 15 MeV, (j) 16 MeV, (k) 17 MeV, (l) 18 MeV, (m) 19 MeV, and (n) 20 MeV.

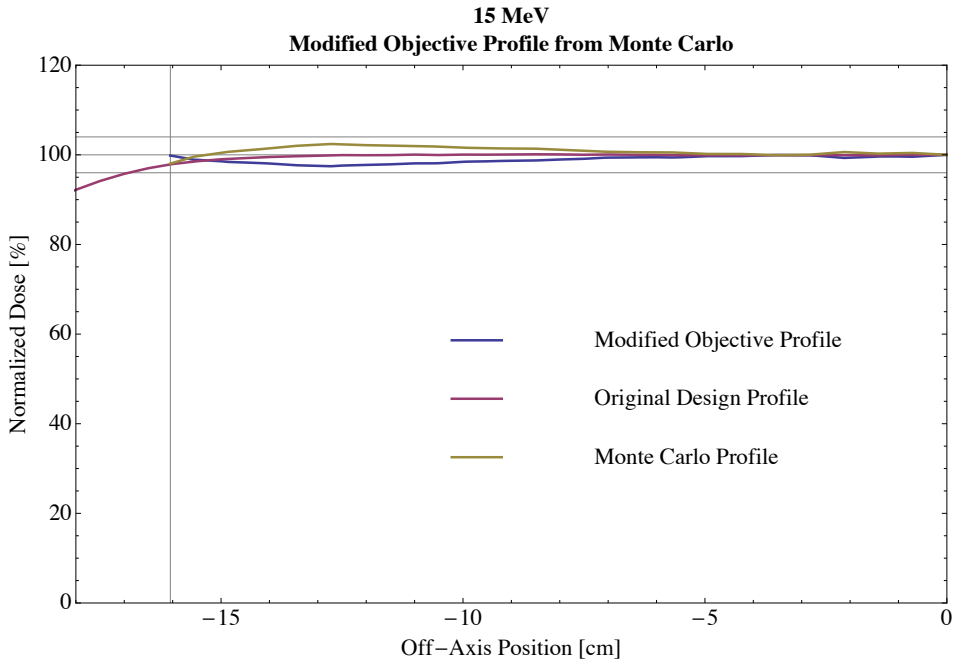

(i)

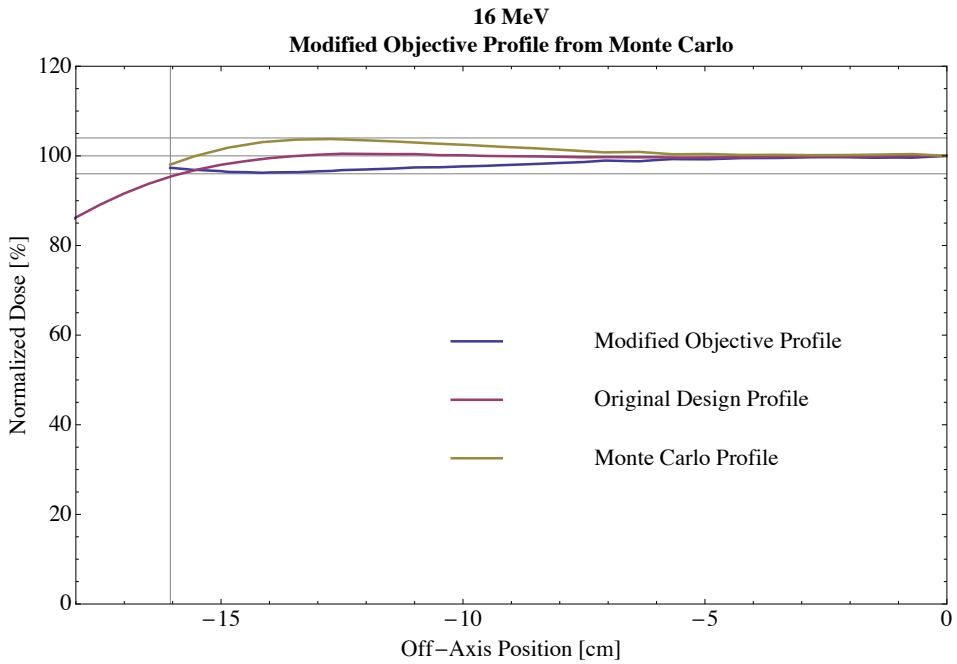

(j)

Figure 34 (continued): Plots of the original design profiles, Monte Carlo simulation data, and the modified objective profiles for (a) 7 MeV, (b) 8 MeV, (c) 9 MeV, (d) 10 MeV, (e) 11 MeV, (f) 12 MeV, (g) 13 MeV, (h) 14 MeV, (i) 15 MeV, (j) 16 MeV, (k) 17 MeV, (l) 18 MeV, (m) 19 MeV, and (n) 20 MeV.

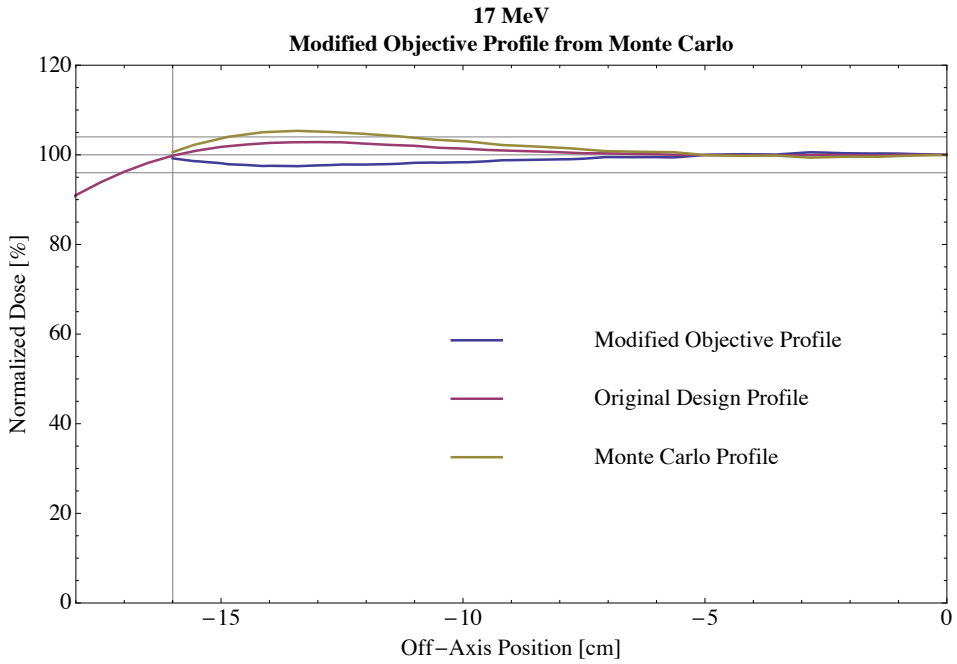

(k)

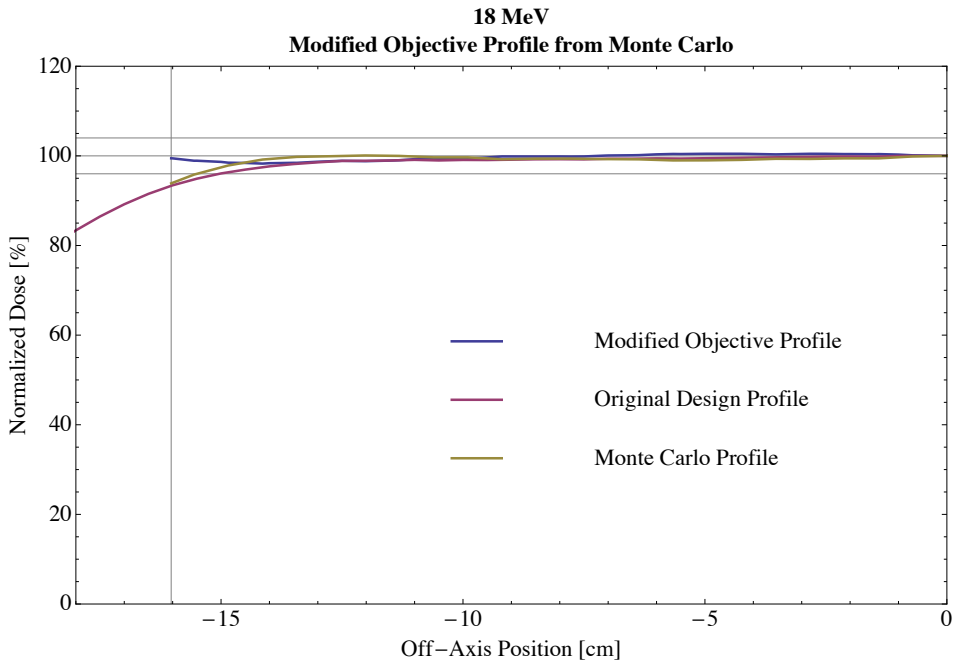

(l)

Figure 34 (continued): Plots of the original design profiles, Monte Carlo simulation data, and the modified objective profiles for (a) 7 MeV, (b) 8 MeV, (c) 9 MeV, (d) 10 MeV, (e) 11 MeV, (f) 12 MeV, (g) 13 MeV, (h) 14 MeV, (i) 15 MeV, (j) 16 MeV, (k) 17 MeV, (l) 18 MeV, (m) 19 MeV, and (n) 20 MeV.

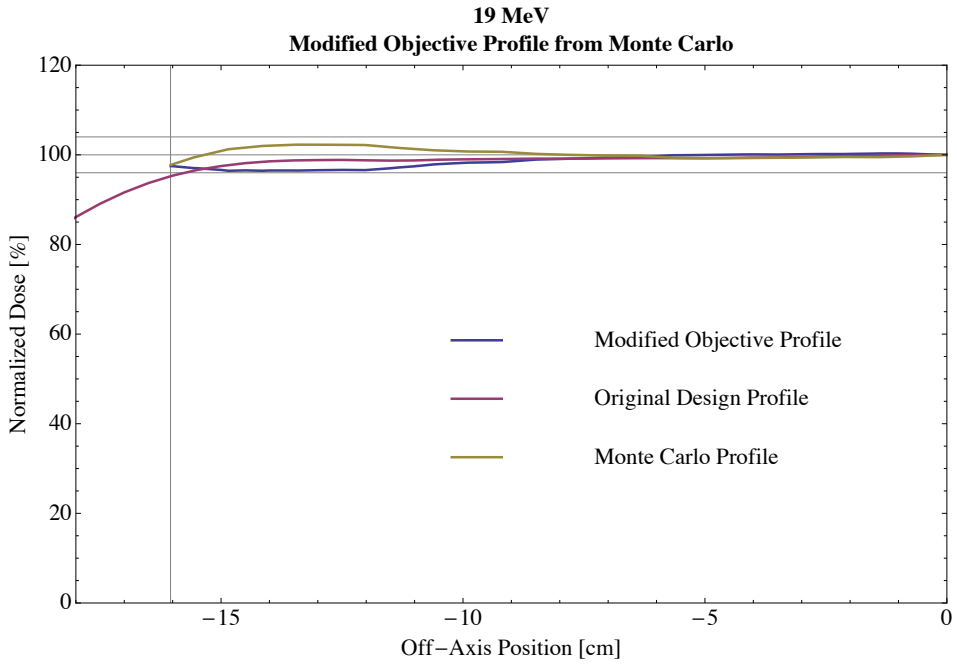

(m)

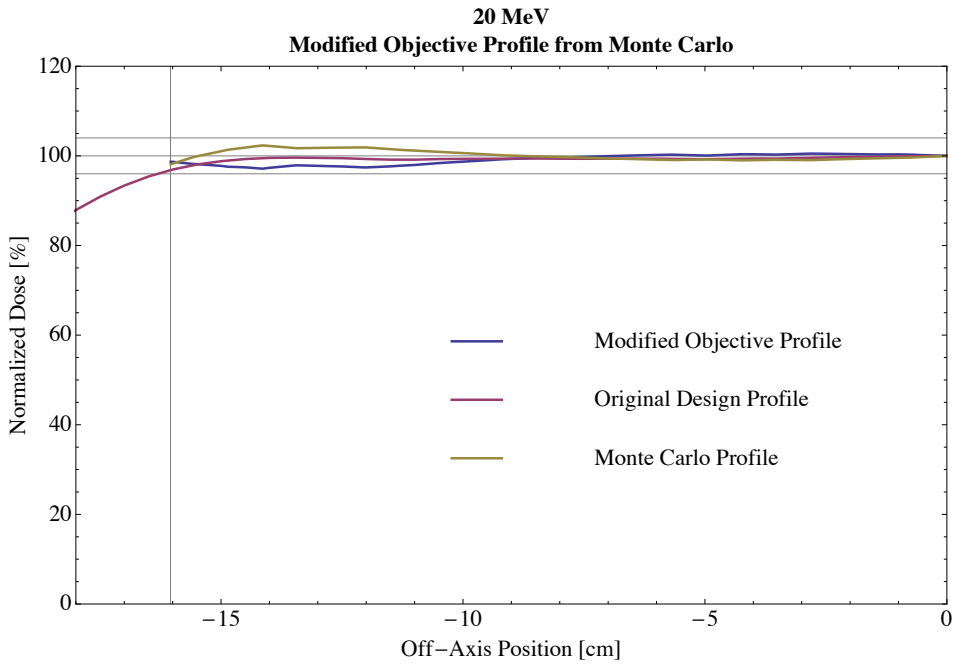

(n)

Figure 34 (continued): Plots of the original design profiles, Monte Carlo simulation data, and the modified objective profiles for (a) 7 MeV, (b) 8 MeV, (c) 9 MeV, (d) 10 MeV, (e) 11 MeV, (f) 12 MeV, (g) 13 MeV, (h) 14 MeV, (i) 15 MeV, (j) 16 MeV, (k) 17 MeV, (l) 18 MeV, (m) 19 MeV, and (n) 20 MeV.

4.2.3 Re-optimization of Foil Designs

The dual scattering foils systems were re-optimized according to the modified objective profiles shown in Figure 34. Table 17 shows a summary of all of the pertinent design data. Figure 35 shows the agreement between simulation design profiles and modified objective profiles for the refined secondary foil design for most probable energies at the surface 7-13 MeV. The secondary foil is a Gaussian-shaped Al pyramid (again approximated by 10 stacked disks of equal thickness) having a thickness of 0.1241 cm along central axis and a sigma of 1.46 cm. Each design profile was not within the ±3% goal, with the maximum deviation reaching only 4.3% for 9 MeV.

7 MeV	
Number of Primary Foils	3
Secondary Foil Thickness [cm]	0.12410
Secondary Foil Sigma [cm]	1.46
$\Delta_{max}{}^{+}$	3.9
$\Delta_{max}{}^{-}$	−3.7
D_x [%]	1.3

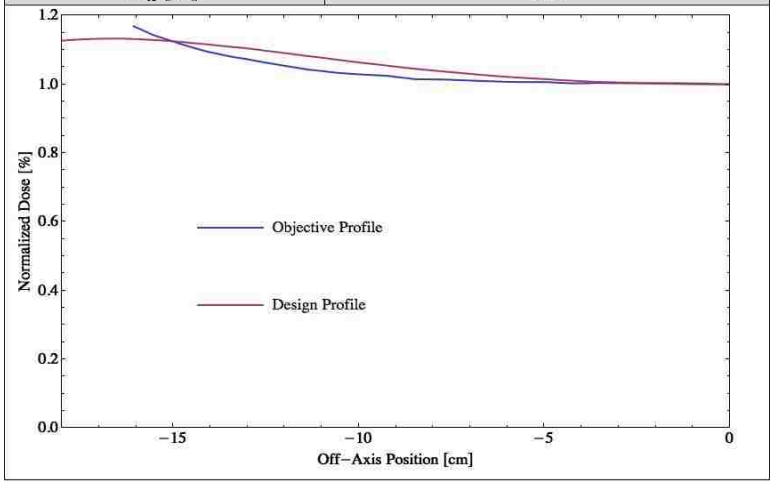

(a)

Figure 35: Comparison of normalized dose [%] versus off-axis position [cm] for the objective and design profiles at energies of (a) 7 MeV, (b) 8 MeV, (c) 9 MeV, (d) 10 MeV, (e) 11 MeV, (f) 12 Mev, and (g) 13 MeV. The Al secondary foil parameters and the number of 30 μm Ta primary foils are identified. The maximum differences above ($\Delta_{max}{}^{+}$) and below ($\Delta_{max}{}^{-}$) the objective profile and D_x are indicated.

8 MeV	
Number of Primary Foils	3
Secondary Foil Thickness [cm]	0.12410
Secondary Foil Sigma [cm]	1.46
Δ_{max}^{+}	3.9
Δ_{max}^{-}	−2.4
D_x [%]	1.4

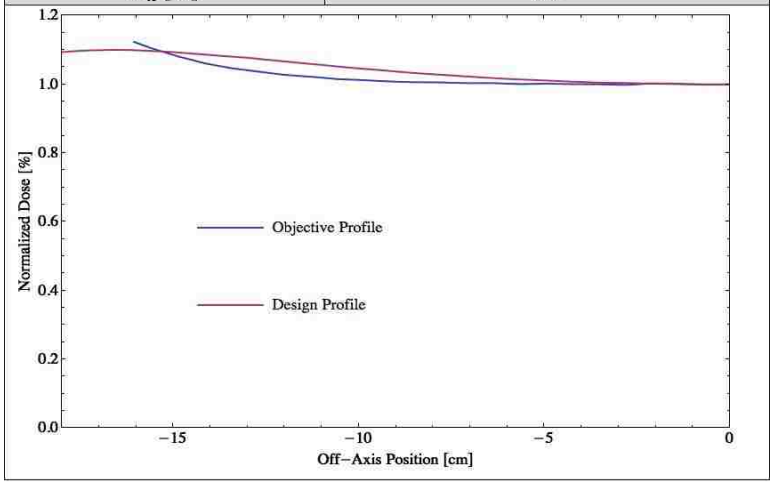

(b)

9 MeV	
Number of Primary Foils	3
Secondary Foil Thickness [cm]	0.12410
Secondary Foil Sigma [cm]	1.46
Δ_{max}^{+}	4.3
Δ_{max}^{-}	−0.1
D_x [%]	1.6

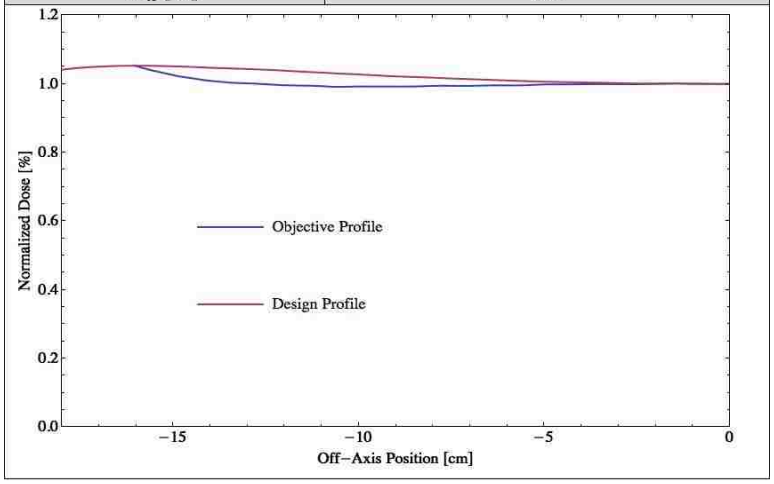

(c)

Figure 35 (continued): Comparison of normalized dose [%] versus off-axis position [cm] for the objective and design profiles at energies of (a) 7 MeV, (b) 8 MeV, (c) 9 MeV, (d) 10 MeV, (e) 11 MeV, (f) 12 Mev, and (g) 13 MeV. The Al secondary foil parameters and the number of 30 μm Ta primary foils are identified. The maximum differences above (Δ_{max}^{+}) and below (Δ_{max}^{-}) the objective profile and D_x are indicated.

10 MeV	
Number of Primary Foils	3
Secondary Foil Thickness [cm]	0.12410
Secondary Foil Sigma [cm]	1.46
Δ_{max}^{+}	2.8
Δ_{max}^{-}	−2.3
D_x [%]	1.8

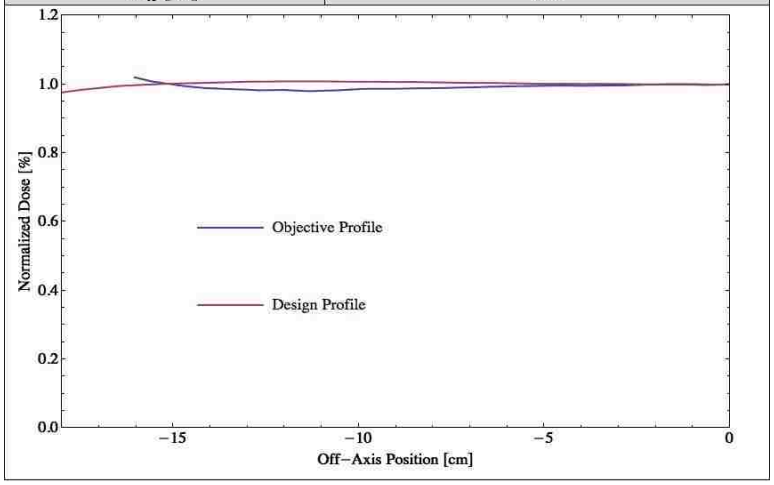

(d)

11 MeV	
Number of Primary Foils	4
Secondary Foil Thickness [cm]	0.12410
Secondary Foil Sigma [cm]	1.46
Δ_{max}^{+}	2.2
Δ_{max}^{-}	−2.1
D_x [%]	2.1

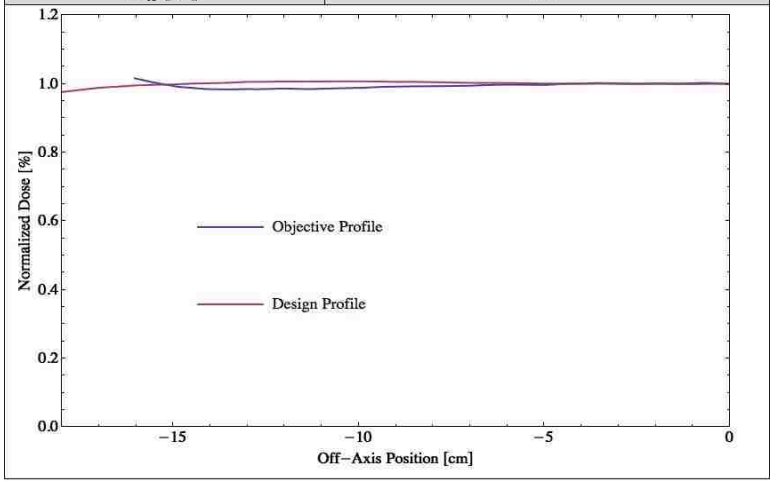

(e)

Figure 35 (continued): Comparison of normalized dose [%] versus off-axis position [cm] for the objective and design profiles at energies of (a) 7 MeV, (b) 8 MeV, (c) 9 MeV, (d) 10 MeV, (e) 11 MeV, (f) 12 Mev, and (g) 13 MeV. The Al secondary foil parameters and the number of 30 μm Ta primary foils are identified. The maximum differences above (Δ_{max}^{+}) and below (Δ_{max}^{-}) the objective profile and D_x are indicated.

12 MeV	
Number of Primary Foils	5
Secondary Foil Thickness [cm]	0.12410
Secondary Foil Sigma [cm]	1.46
Δ_{max}^{+}	2.5
Δ_{max}^{-}	−1.9
D_x [%]	2.5

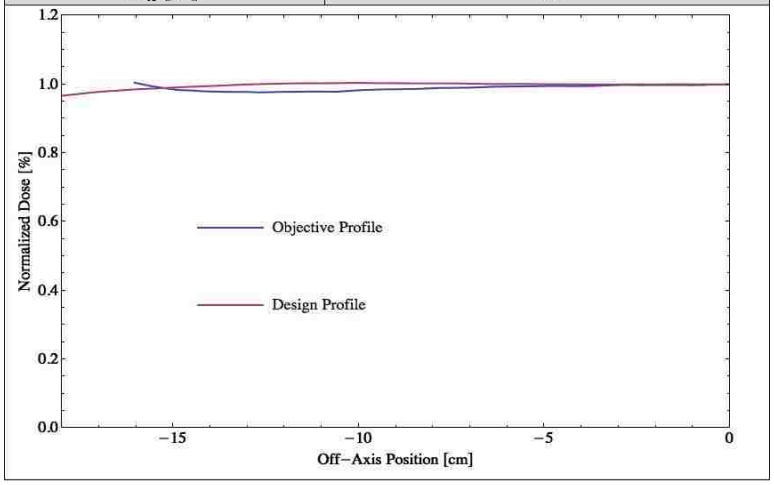

(f)

13 MeV	
Number of Primary Foils	6
Secondary Foil Thickness [cm]	0.12410
Secondary Foil Sigma [cm]	1.46
Δ_{max}^{+}	1.7
Δ_{max}^{-}	−2.9
D_x [%]	2.8

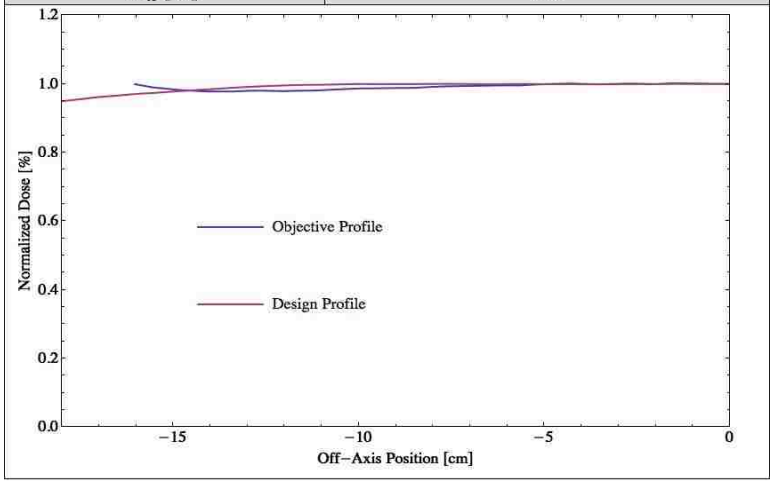

(g)

Figure 35 (continued): Comparison of normalized dose [%] versus off-axis position [cm] for the objective and design profiles at energies of (a) 7 MeV, (b) 8 MeV, (c) 9 MeV, (d) 10 MeV, (e) 11 MeV, (f) 12 Mev, and (g) 13 MeV. The Al secondary foil parameters and the number of 30 μm Ta primary foils are identified. The maximum differences above (Δ_{max}^{+}) and below (Δ_{max}^{-}) the objective profile and D_x are indicated.

Figure 36 shows the agreement between simulation design profiles and refined objective profiles for the refined secondary foil design for most probable energies at the surface of 14 and 15 MeV. The secondary foil is a Gaussian-shaped Al pyramid (again approximated by 10 stacked disks of equal thickness) having a thickness of 0.220 cm along central axis and a sigma of 1.20 cm. Both of the design profiles were within the ±3% goal, with the maximum deviation being 3.0% for 15 MeV.

Figure 37 shows the agreement between simulation design profiles and refined objective profiles for the refined secondary foil design for most probable energies at the surface of 16-20 MeV. The secondary foil is a Gaussian-shaped Al pyramid (again approximated by 10 stacked disks of equal thickness) having a thickness of 0.371 cm and a sigma of 1.15. All but two of the design profiles were within the ±3% goal, but the maximum deviation was only 4.3% in the case of 17 MeV.

14 MeV	
Number of Primary Foils	3
Secondary Foil Thickness [cm]	0.22000
Secondary Foil Sigma [cm]	1.20
Δ_{max}^{+}	1.7
Δ_{max}^{-}	−2.7
D_x [%]	2.7

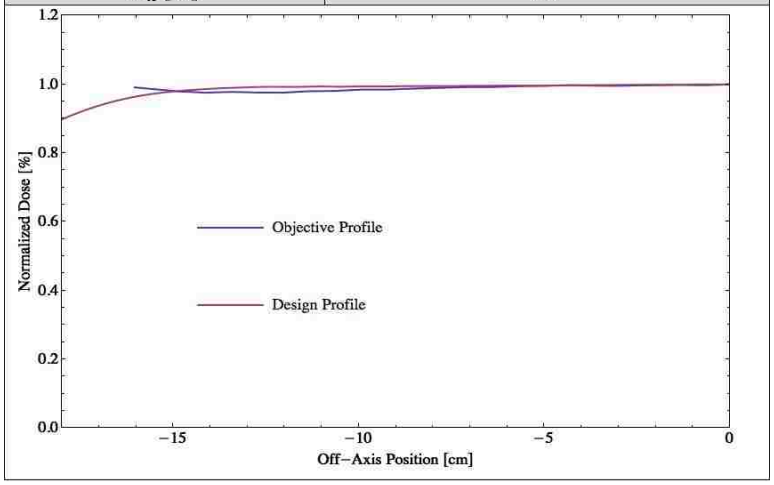

(a)

15 MeV	
Number of Primary Foils	4
Secondary Foil Thickness [cm]	0.22000
Secondary Foil Sigma [cm]	1.20
Δ_{max}^{+}	3.
Δ_{max}^{-}	−0.9
D_x [%]	3.1

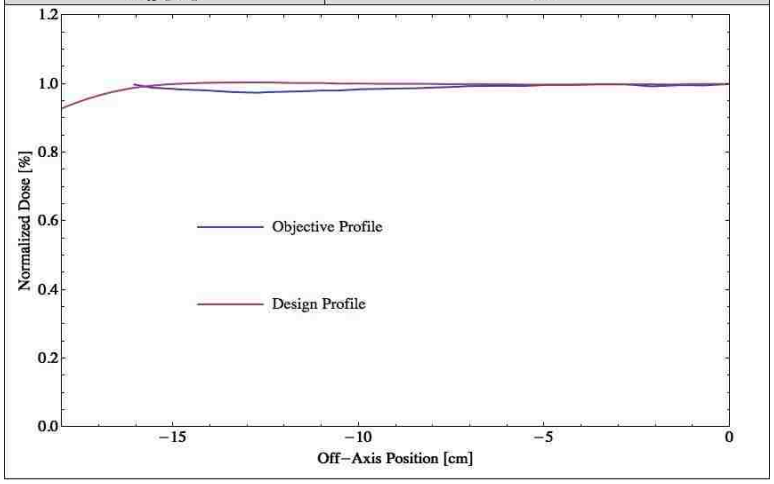

(b)

Figure 36: Comparison of normalized dose [%] versus off-axis position [cm] for the objective and design profiles at energies of (a) 14 MeV and (b) 15 MeV. The Al secondary foil parameters and the number of 30 μm Ta primary foils are identified. The maximum differences above (Δ_{max}^{+}) and below (Δ_{max}^{-}) the objective profile and D_x are indicated.

16 MeV	
Number of Primary Foils	3
Secondary Foil Thickness [cm]	0.37100
Secondary Foil Sigma [cm]	1.15
Δ_{max}^{+}	2.7
Δ_{max}^{-}	−2.7
D_x [%]	3.6

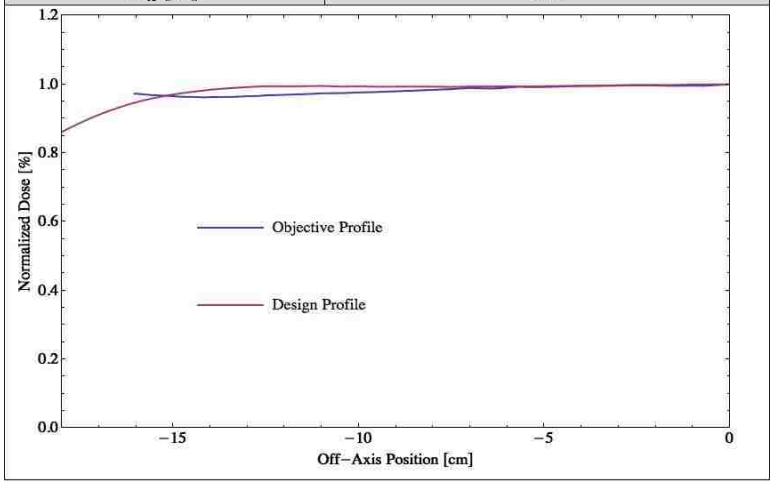

(a)

17 MeV	
Number of Primary Foils	4
Secondary Foil Thickness [cm]	0.37100
Secondary Foil Sigma [cm]	1.15
Δ_{max}^{+}	4.3
Δ_{max}^{-}	−0.7
D_x [%]	4.0

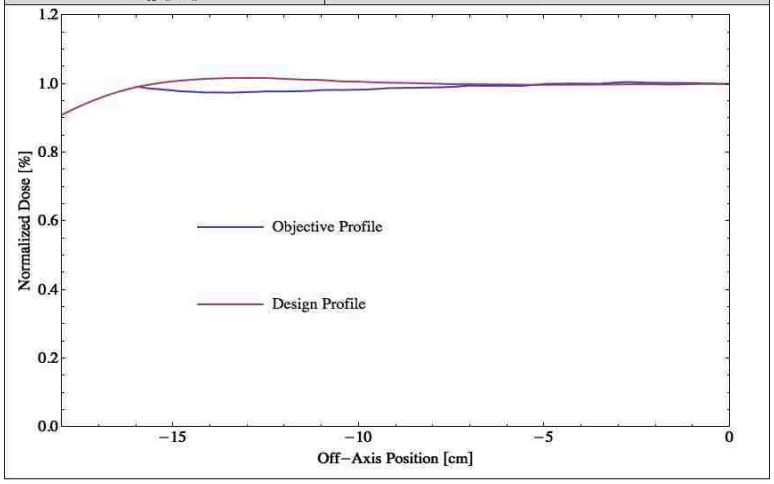

(b)

Figure 37: Comparison of normalized dose [%] versus off-axis position [cm] for the objective and design profiles at energies of (a) 16 MeV, (b) 17 MeV, (c) 18 MeV, (d) 19 MeV, and (e) 20 MeV. The Al secondary foil parameters and the number of 30 μm Ta primary foils are identified. The maximum differences above (Δ_{max}^{+}) and below (Δ_{max}^{-}) the objective profile and D_x are indicated.

18 MeV	
Number of Primary Foils	5
Secondary Foil Thickness [cm]	0.37100
Secondary Foil Sigma [cm]	1.15
Δ_{max}^{+}	3.9
Δ_{max}^{-}	−1.
D_x [%]	4.5

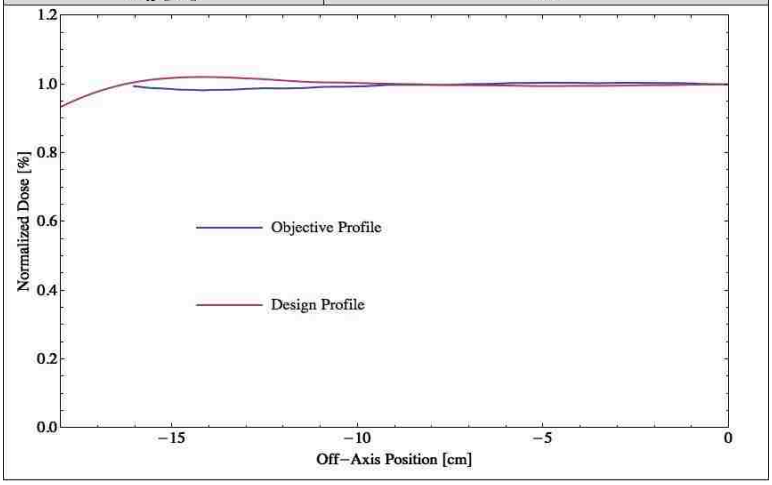

(c)

19 MeV	
Number of Primary Foils	5
Secondary Foil Thickness [cm]	0.37100
Secondary Foil Sigma [cm]	1.15
Δ_{max}^{+}	1.3
Δ_{max}^{-}	−2.9
D_x [%]	4.7

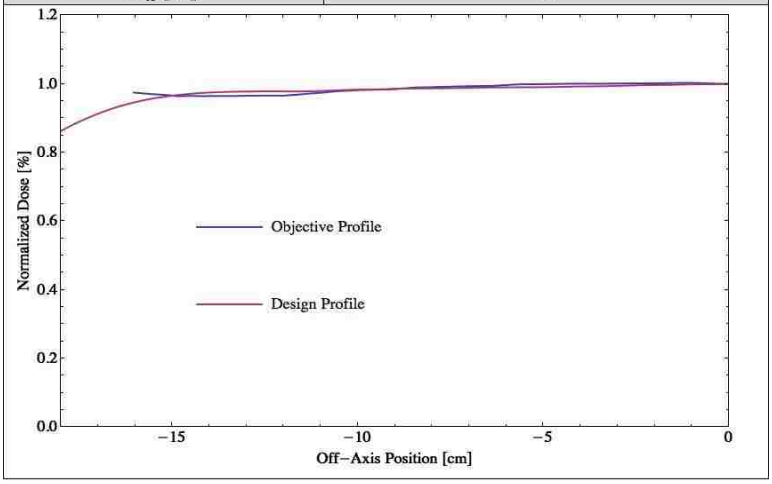

(d)

Figure 37 (continued): Comparison of normalized dose [%] versus off-axis position [cm] for the objective and design profiles at energies of (a) 16 MeV, (b) 17 MeV, (c) 18 MeV, (d) 19 MeV, and (e) 20 MeV. The Al secondary foil parameters and the number of 30 μm Ta primary foils are identified. The maximum differences above (Δ_{max}^{+}) and below (Δ_{max}^{-}) the objective profile and D_x are indicated.

20 MeV	
Number of Primary Foils	6
Secondary Foil Thickness [cm]	0.37100
Secondary Foil Sigma [cm]	1.15
Δ_{max}^{+}	1.2
Δ_{max}^{-}	−2.6
D_x [%]	5.2

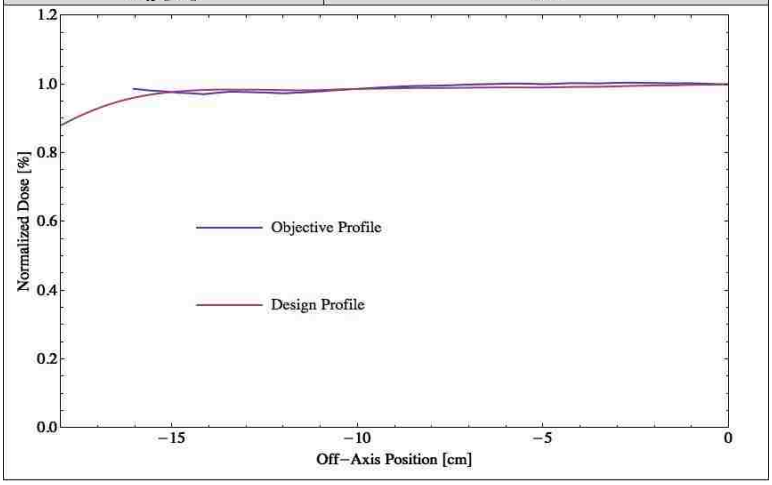

(e)

Figure 37 (continued): Comparison of normalized dose [%] versus off-axis position [cm] for the objective and design profiles at energies of (a) 16 MeV, (b) 17 MeV, (c) 18 MeV, (d) 19 MeV, and (e) 20 MeV. The Al secondary foil parameters and the number of 30 μm Ta primary foils are identified. The maximum differences above (Δ_{max}^{+}) and below (Δ_{max}^{-}) the objective profile and D_x are indicated.

Table 17: A summary of the primary and secondary foil combination used in the final design, as well as maximum deviations and central axis photon dose percentage for each design energy.

$E_{p,0}$ [MeV]	2° σ [cm]	2° Δt [cm]	# 1° Foils	$(\Delta_{max})^-$ [%]	$(\Delta_{max})^+$ [%]	D_x [%]
7	1.46	0.1241	3	3.7	3.9	1.3
8	↓	↓	3	2.4	3.9	1.4
9	↓	↓	3	0.1	4.3	1.6
10	↓	↓	3	2.3	2.8	1.8
11	↓	↓	4	2.1	2.2	2.1
12	↓	↓	5	1.9	2.5	2.5
13	↓	↓	6	2.9	1.7	2.8
14	1.20	0.220	3	2.7	1.7	2.7
15	↓	↓	4	0.9	3.0	3.1
16	1.15	0.3710	3	2.7	2.7	3.6
17	↓	↓	4	0.7	4.3	4.0
18	↓	↓	5	1.0	3.9	4.5
19	↓	↓	5	2.9	1.3	4.7
20	↓	↓	6	2.6	1.2	5.2

4.2.4 Final Monte Carlo Dose Calculations

4.2.4.a Transverse Profiles

Final Monte Carlo dose calculations showed that all energies except one passed flatness criteria along the major axes (perpendicular to collimator edges) in both transverse directions (inplane and crossplane). Figure 38 shows plots of off-axis dose profiles along the major axes (crossplane and inplane) from the final Monte Carlo dose calculations. The maximum deviations of dose from 100% within the clinically-relevant range (2 cm inside the 50% dose points) above and below 100% are shown in Table 18. The best agreement was found in the case of 14 MeV, which did not deviate more than

1.0% over the clinically relevant range, whereas 8 MeV had the worst results, reaching as much as 3.2% above 100% dose.

Table 18: Table of maximum deviations from 100% over the clinically relevant ranges (2 cm inside of 50% dose points) for each of the design energies.

Transverse Monte Carlo Results				
$E_{p,0}$ [MeV]	2° Foil	1° Foil	$(\overline{\Delta})_{min}$	$(\overline{\Delta})_{max}$
7	1	4	0%	2.9%
8	1	3	0%	3.2%
9	1	3	–0.1%	2.6%
10	1	3	–0.3%	1.5%
11	1	4	–0.5%	1.2%
12	1	5	–0%	1.5%
13	1	6	–0.8%	0.7%
14	2	3	–0.2%	1.0%
15	2	4	–0.5%	1.2%
16	3	3	–0.4%	1.4%
17	3	4	–0.3%	2.2%
18	3	4	–0.6%	1.8%
19	3	5	–0.6%	0.8%
20	3	6	–0.9%	0.6%

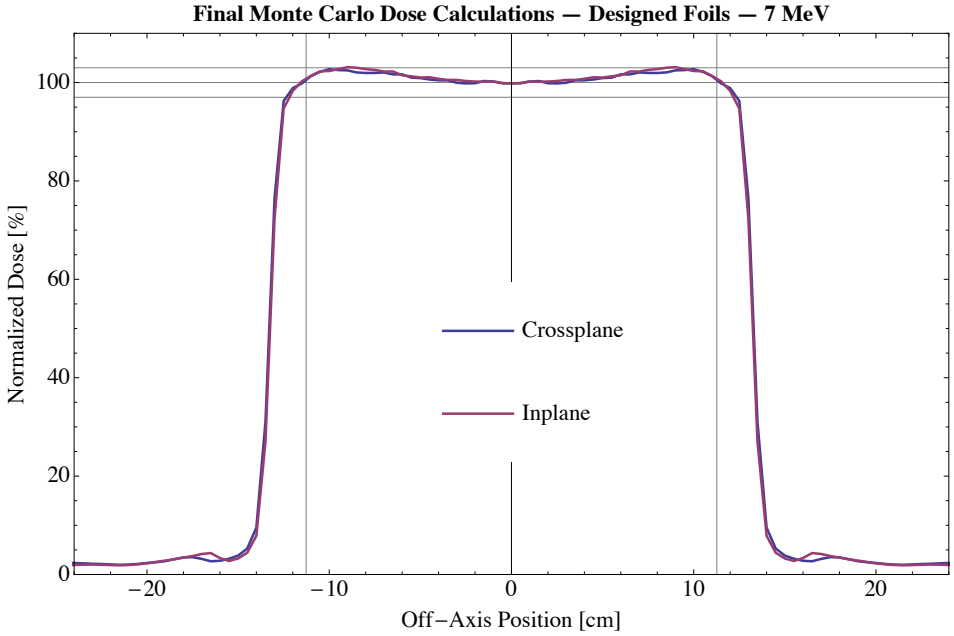

(a)

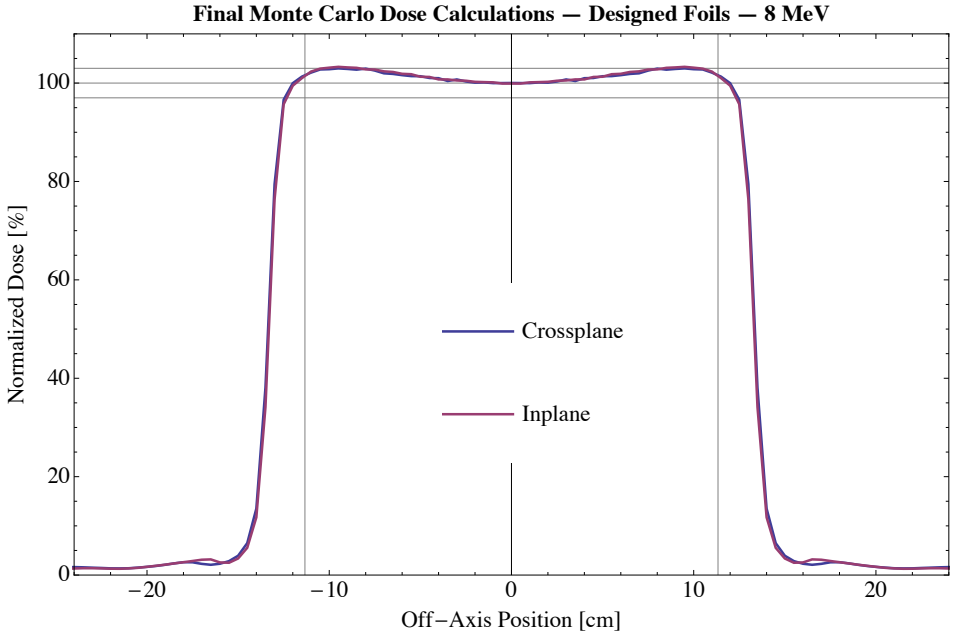

(b)

Figure 38: Plots of crossplane and inplane profiles (relative dose vs. off-axis position) for final Monte Carlo dose calculations of re-designed foil system for (a) 7, (b) 8, (c) 9, (d) 10, (e) 11, (f) 12, (g) 13, (h) 14, (i) 15, (j) 16, (k) 17, (l) 18, (m) 19, and (n) 20 MeV. Horizonal lines at 100±3% and vertical lines 2 cm inside the 50% dose value demarcate the acceptable range for transverse off-axis dose profile.

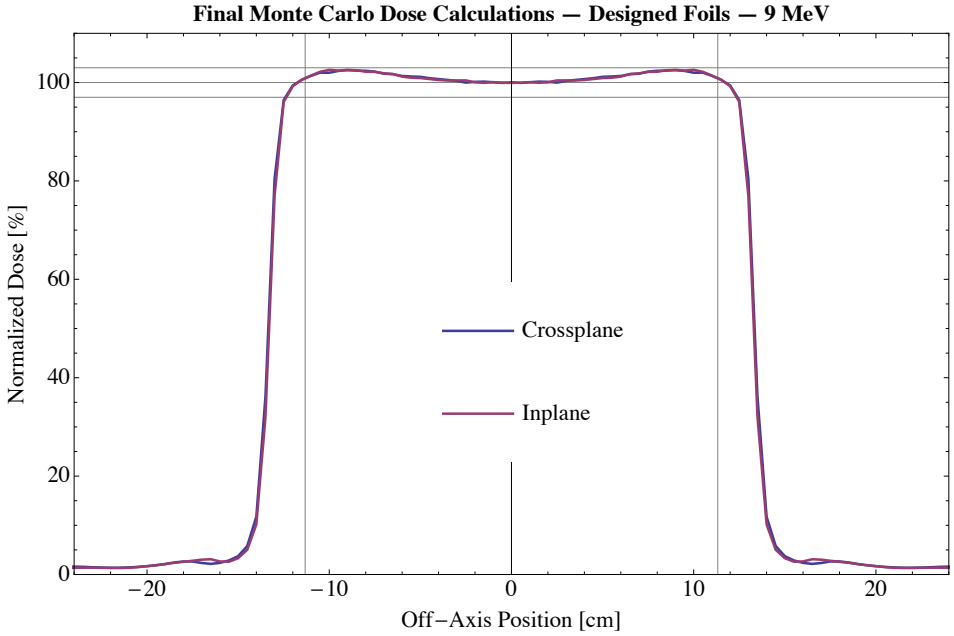

(c)

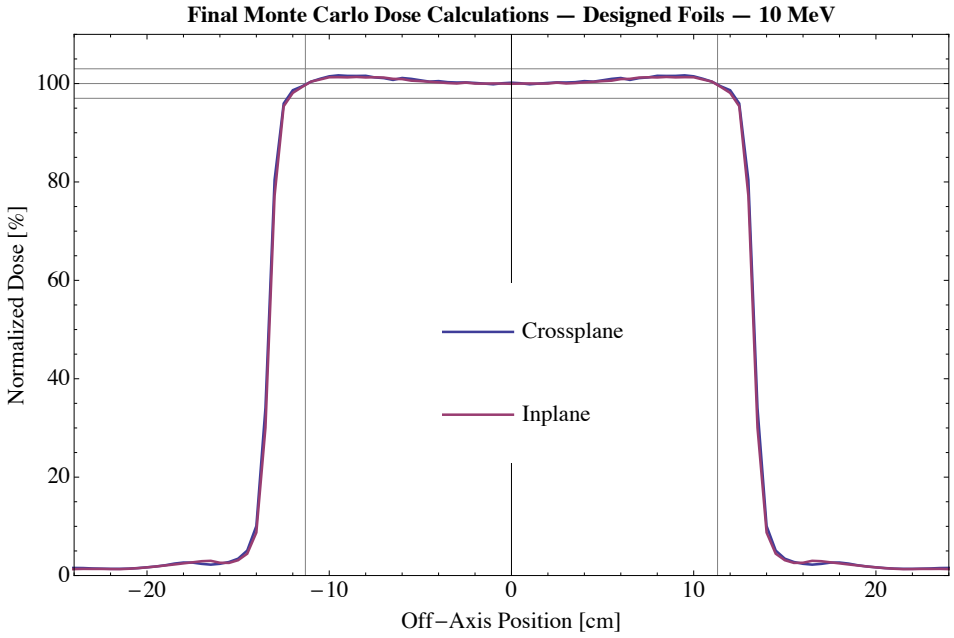

(d)

Figure 38 (continued): Plots of crossplane and inplane profiles (relative dose vs. off-axis position) for final Monte Carlo dose calculations of re-designed foil system for (a) 7, (b) 8, (c) 9, (d) 10, (e) 11, (f) 12, (g) 13, (h) 14, (i) 15, (j) 16, (k) 17, (l) 18, (m) 19, and (n) 20 MeV. Horizonal lines at 100±3% and vertical lines 2 cm inside the 50% dose value demarcate the acceptable range for transverse off-axis dose profile.

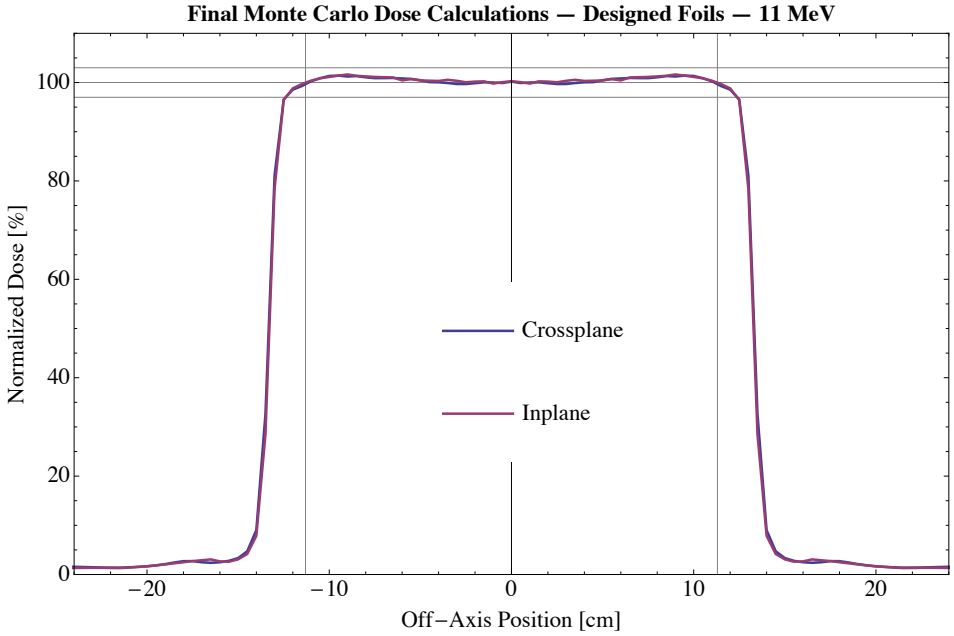

(e)

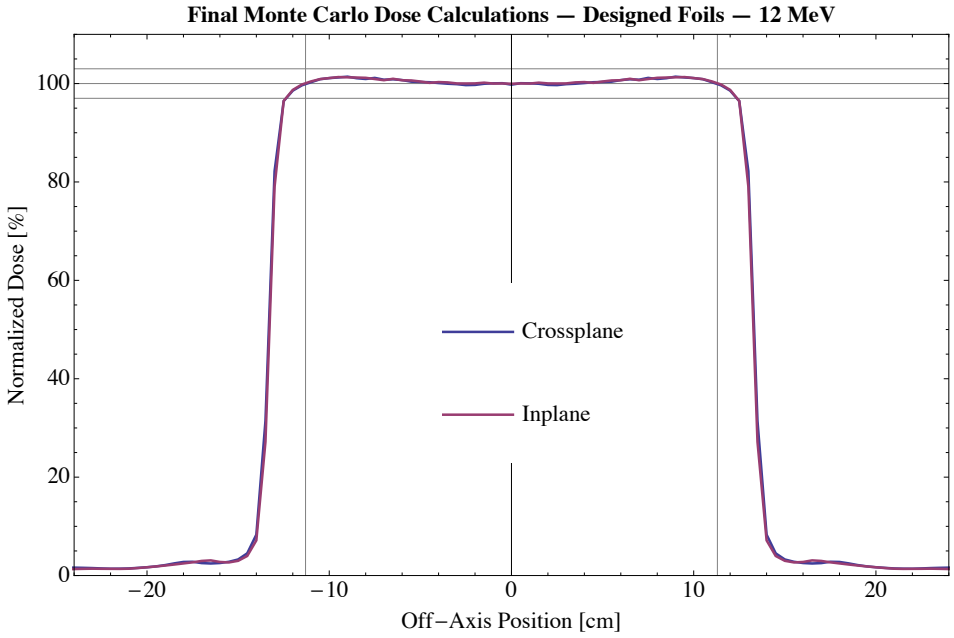

(f)

Figure 38 (continued): Plots of crossplane and inplane profiles (relative dose vs. off-axis position) for final Monte Carlo dose calculations of re-designed foil system for (a) 7, (b) 8, (c) 9, (d) 10, (e) 11, (f) 12, (g) 13, (h) 14, (i) 15, (j) 16, (k) 17, (l) 18, (m) 19, and (n) 20 MeV. Horizonal lines at 100±3% and vertical lines 2 cm inside the 50% dose value demarcate the acceptable range for transverse off-axis dose profile.

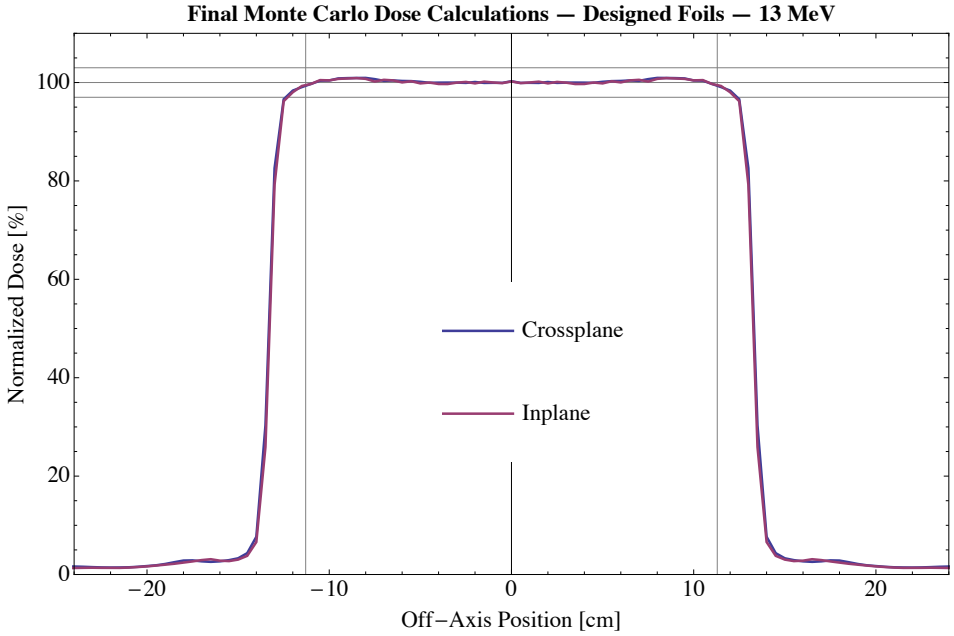

(g)

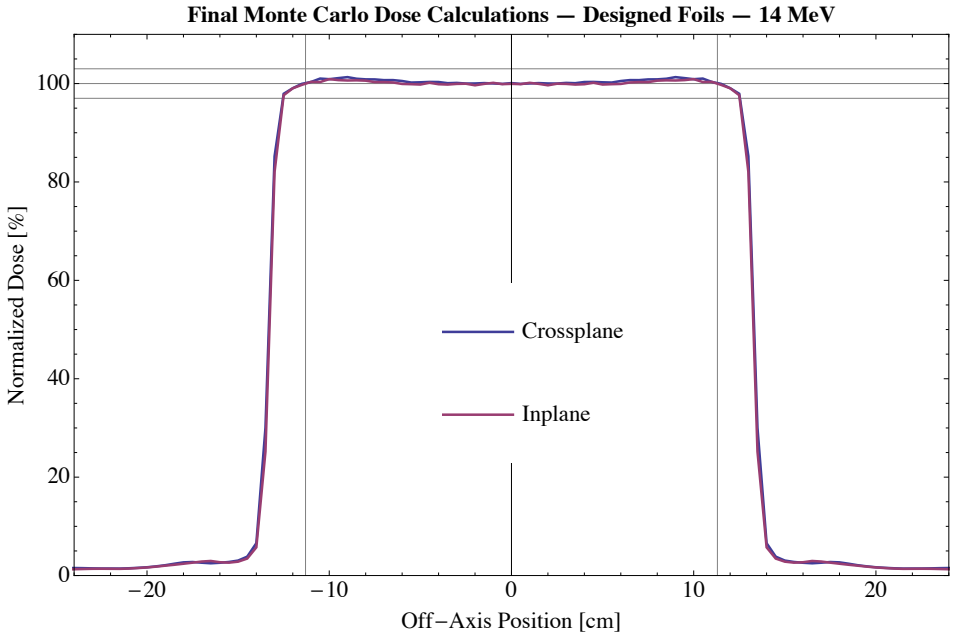

(h)

Figure 38 (continued): Plots of crossplane and inplane profiles (relative dose vs. off-axis position) for final Monte Carlo dose calculations of re-designed foil system for (a) 7, (b) 8, (c) 9, (d) 10, (e) 11, (f) 12, (g) 13, (h) 14, (i) 15, (j) 16, (k) 17, (l) 18, (m) 19, and (n) 20 MeV. Horizonal lines at 100±3% and vertical lines 2 cm inside the 50% dose value demarcate the acceptable range for transverse off-axis dose profile.

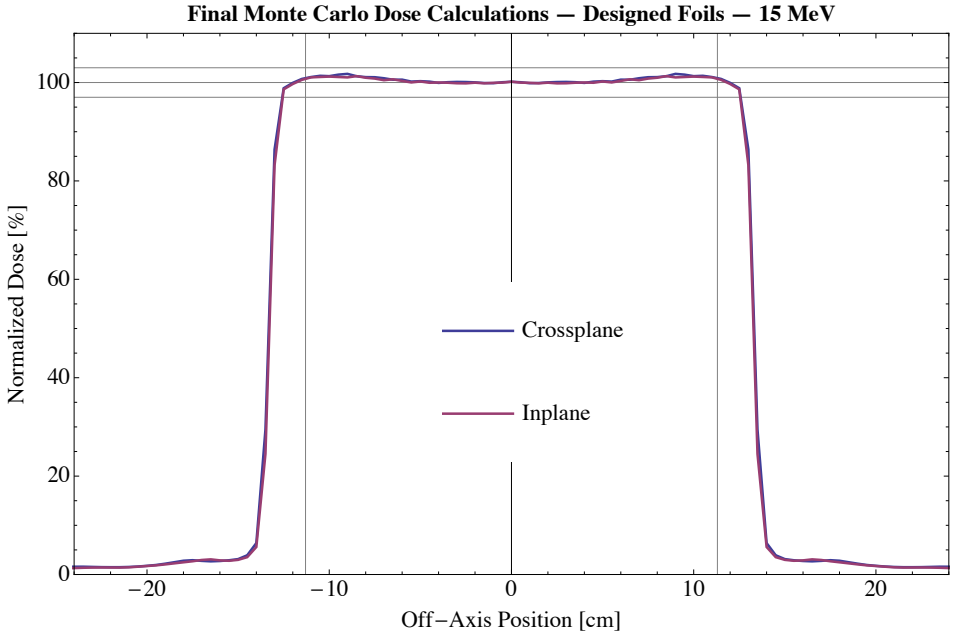

(i)

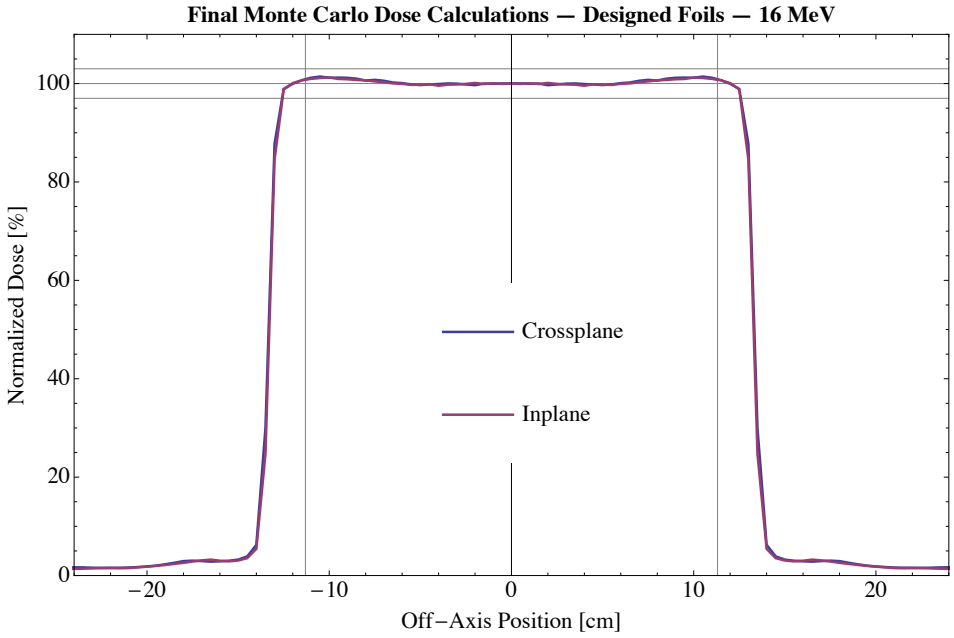

(j)

Figure 38 (continued): Plots of crossplane and inplane profiles (relative dose vs. off-axis position) for final Monte Carlo dose calculations of re-designed foil system for (a) 7, (b) 8, (c) 9, (d) 10, (e) 11, (f) 12, (g) 13, (h) 14, (i) 15, (j) 16, (k) 17, (l) 18, (m) 19, and (n) 20 MeV. Horizonal lines at 100±3% and vertical lines 2 cm inside the 50% dose value demarcate the acceptable range for transverse off-axis dose profile.

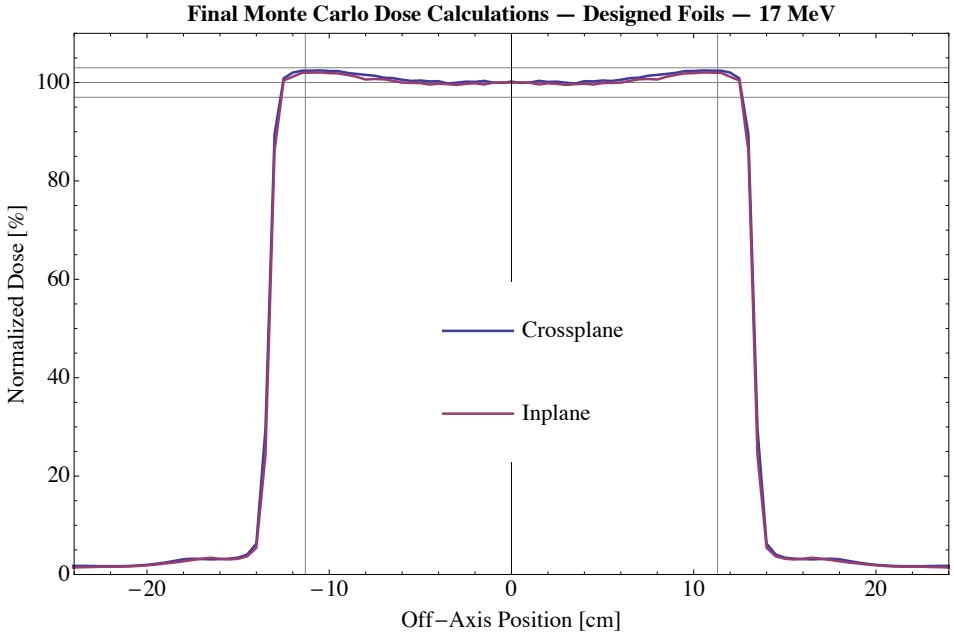

(k)

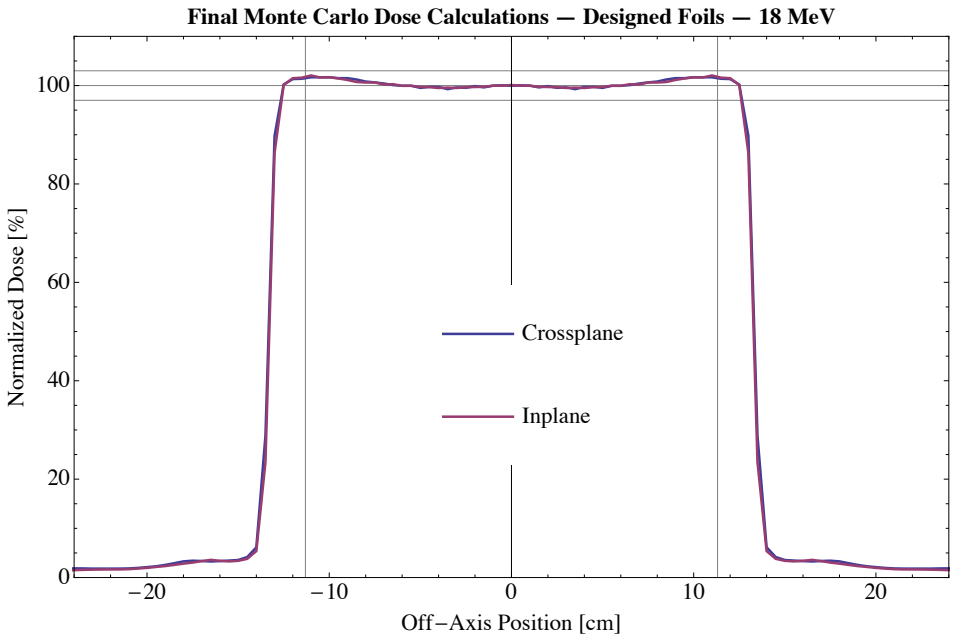

(l)

Figure 38 (continued): Plots of crossplane and inplane profiles (relative dose vs. off-axis position) for final Monte Carlo dose calculations of re-designed foil system for (a) 7, (b) 8, (c) 9, (d) 10, (e) 11, (f) 12, (g) 13, (h) 14, (i) 15, (j) 16, (k) 17, (l) 18, (m) 19, and (n) 20 MeV. Horizonal lines at 100±3% and vertical lines 2 cm inside the 50% dose value demarcate the acceptable range for transverse off-axis dose profile.

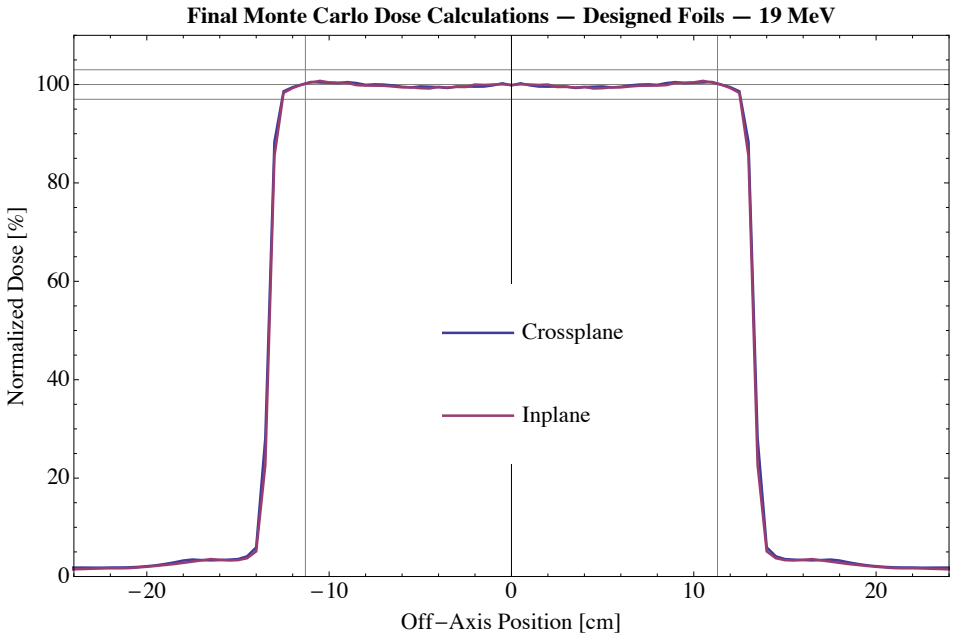

(m)

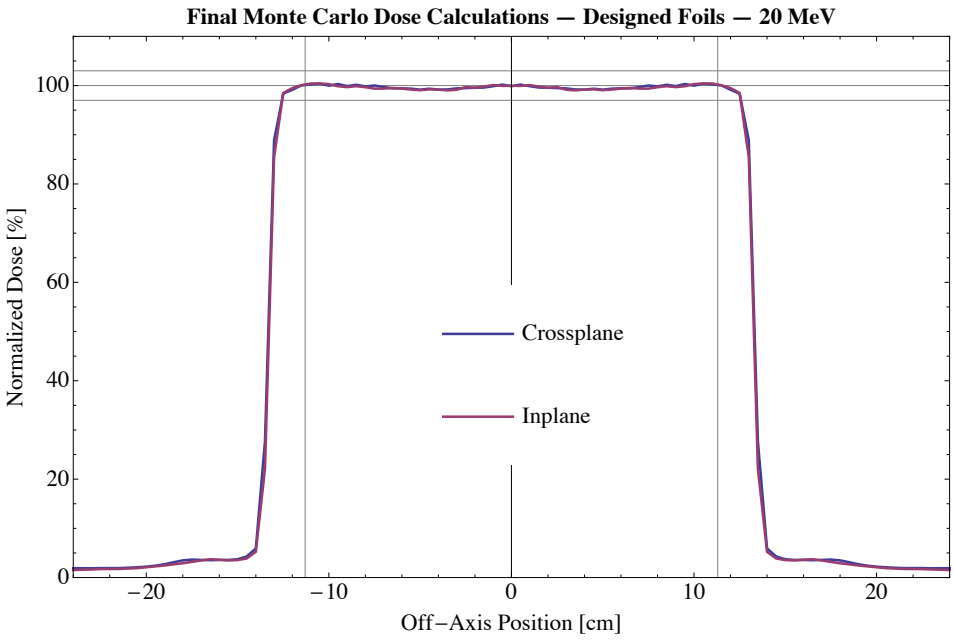

(n)

Figure 38 (continued): Plots of crossplane and inplane profiles (relative dose vs. off-axis position) for final Monte Carlo dose calculations of re-designed foil system for (a) 7, (b) 8, (c) 9, (d) 10, (e)11, (f) 12, (g) 13, (h) 14, (i) 15, (j) 16, (k) 17, (l) 18, (m) 19, and (n) 20 MeV. Horizonal lines at 100±3% and vertical lines 2 cm inside the 50% dose value demarcate the acceptable range for transverse off-axis dose profile.

4.2.4.b Diagonal Profiles

Monte Carlo simulations showed that all energies did not pass flatness criteria along the diagonals. Figure 39 shows plots of off-axis dose profiles along the diagonals from the final Monte Carlo dose calculations. The maximum deviations of dose from 100% within the clinically-relevant range ($2\sqrt{2}$ cm inside the 25% dose points) above and below 100% are shown in Table 19 for each beam energy. The best agreement was found in the case of 15 MeV, which did not deviate more than 2.5% over the clinically relevant range, whereas 8 MeV had the worst results, reaching as much as 5.1% above 100% dose.

Table 19: Table of maximum deviations from 100% over the clinically relevant ranges ($2\sqrt{2}$ cm inside of 25% dose points) for each of the design energies.

Diagonal Monte Carlo Results				
$E_{p,0}$ [MeV]	1° Foil	2° Foil	$(\overline{\Delta})_{min}$	$(\overline{\Delta})_{max}$
7	1	4	−1.6%	4.7%
8	1	3	−0.3%	5.1%
9	1	3	−1.1%	4.0%
10	1	3	−3.2%	2.1%
11	1	4	−3.0%	2.1%
12	1	5	−2.8%	2.4%
13	1	6	−3.9%	1.5%
14	2	3	−3.3%	1.6%
15	2	4	−1.5%	2.5%
16	3	3	−2.7%	2.6%
17	3	4	−0.6%	4.3%
18	3	4	−0.6%	4.0%
19	3	5	−2.6%	2.0%
20	3	6	−2.2%	1.9%

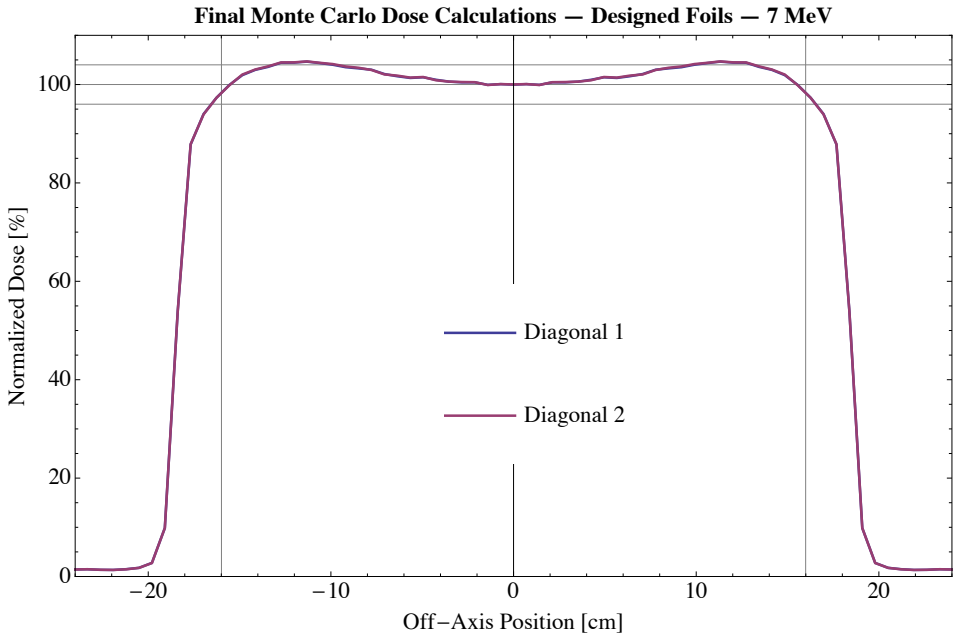

(a)

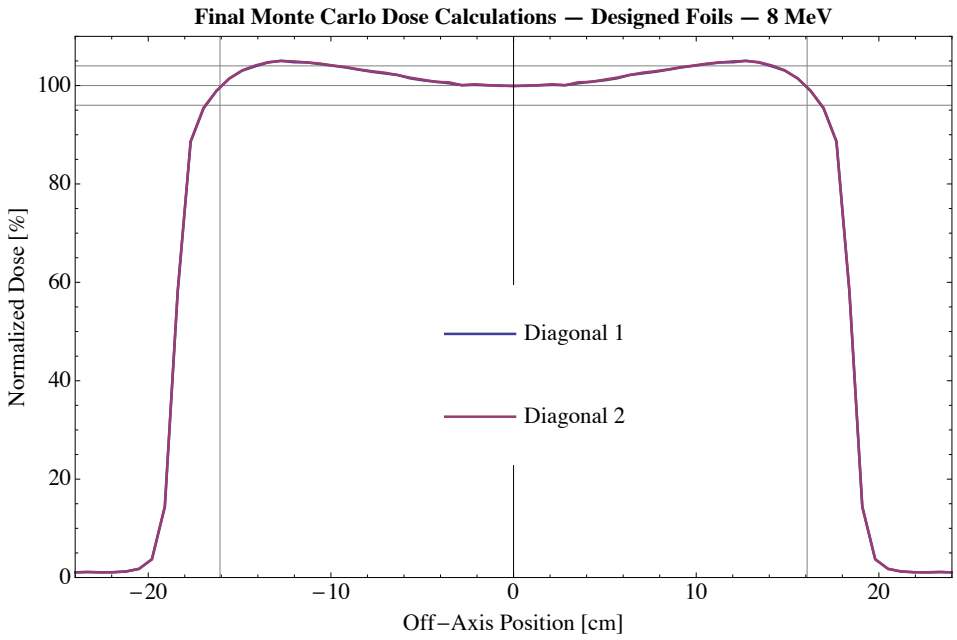

(b)

Figure 39: Plots of diagonal profiles (relative dose vs. off-axis position) for final Monte Carlo dose calculations for redesigned foil systems for (a) 7, (b) 8, (c) 9, (d) 10, (e) 11, (f) 12, (g) 13, (h) 14, (i) 15, (j) 16, (k) 17, (l) 18, (m) 19, and (n) 20 MeV. Horizontal lines at 100±4% and vertical lines $2\sqrt{2}$ cm inside 50% dose values demarcate the acceptable range for diagonal off-axis dose profiles.

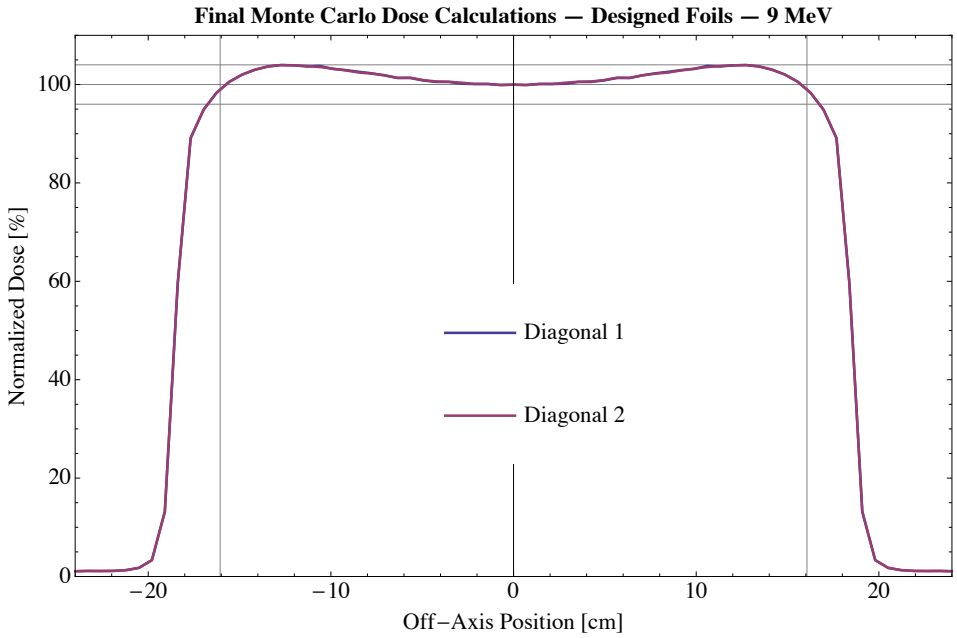

(c)

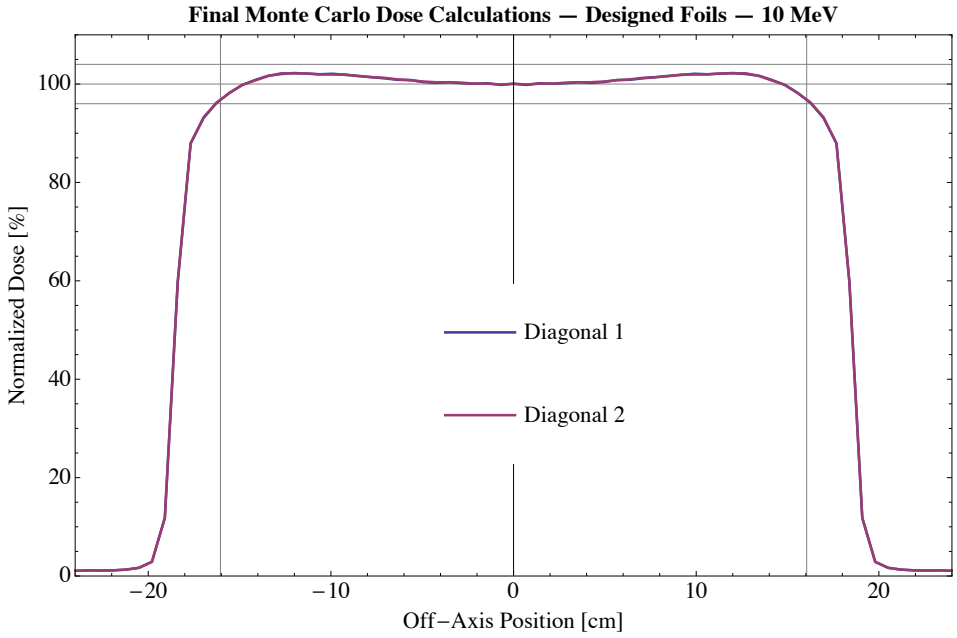

(d)

Figure 39 (continued): Plots of diagonal profiles (relative dose vs. off-axis position) for final Monte Carlo dose calculations for redesigned foil systems for (a) 7, (b) 8, (c) 9, (d) 10, (e) 11, (f) 12, (g) 13, (h) 14, (i) 15, (j) 16, (k) 17, (l) 18, (m) 19, and (n) 20 MeV. Horizontal lines at 100±4% and vertical lines $2\sqrt{2}$ cm inside 50% dose values demarcate the acceptable range for diagonal off-axis dose profiles.

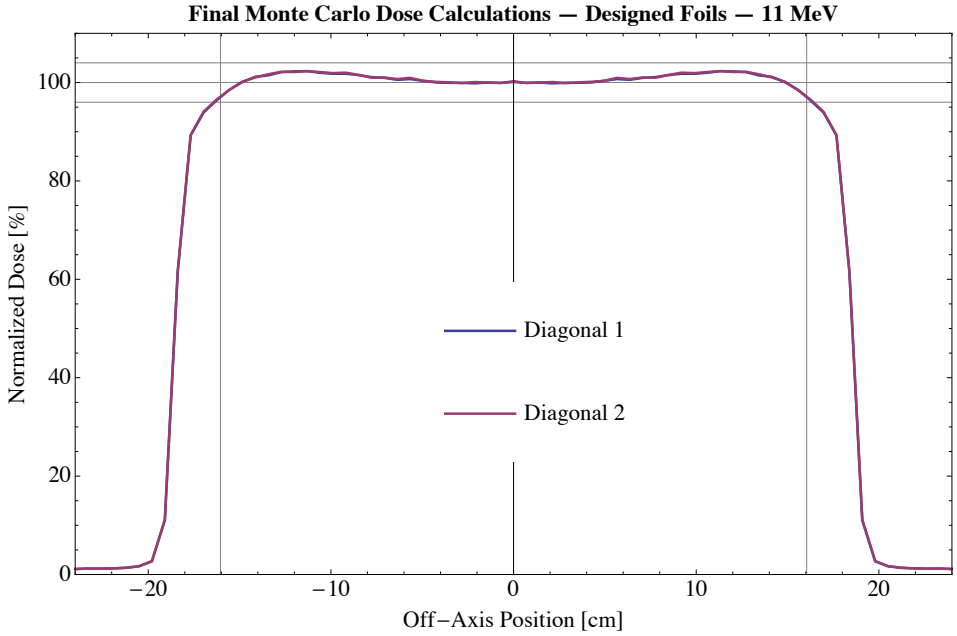

(e)

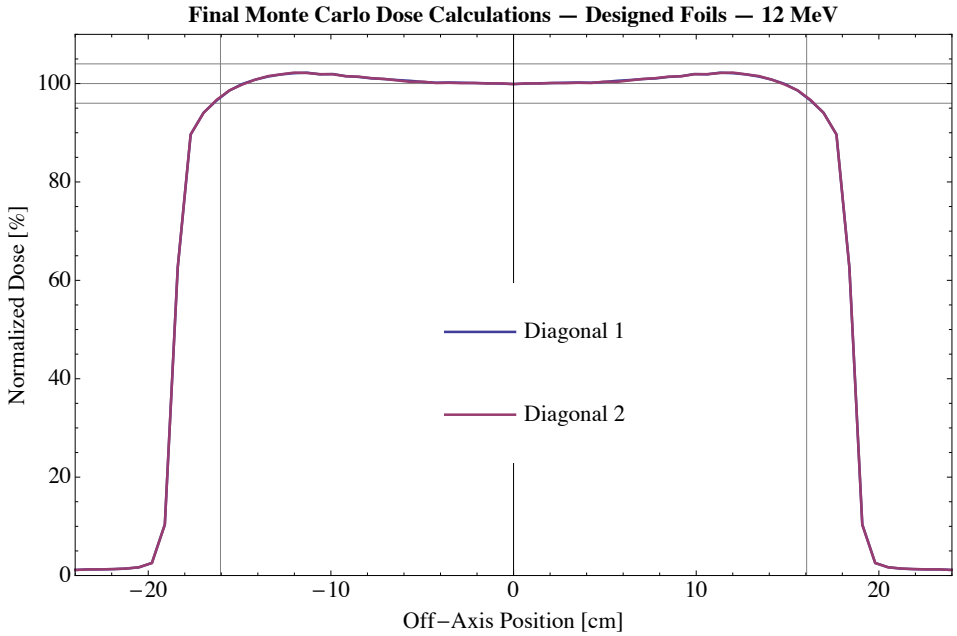

(f)

Figure 39 (continued): Plots of diagonal profiles (relative dose vs. off-axis position) for final Monte Carlo dose calculations for redesigned foil systems for (a) 7, (b) 8, (c) 9, (d) 10, (e) 11, (f) 12, (g) 13, (h) 14, (i) 15, (j) 16, (k) 17, (l) 18, (m) 19, and (n) 20 MeV. Horizontal lines at 100±4% and vertical lines $2\sqrt{2}$ cm inside 50% dose values demarcate the acceptable range for diagonal off-axis dose profiles.

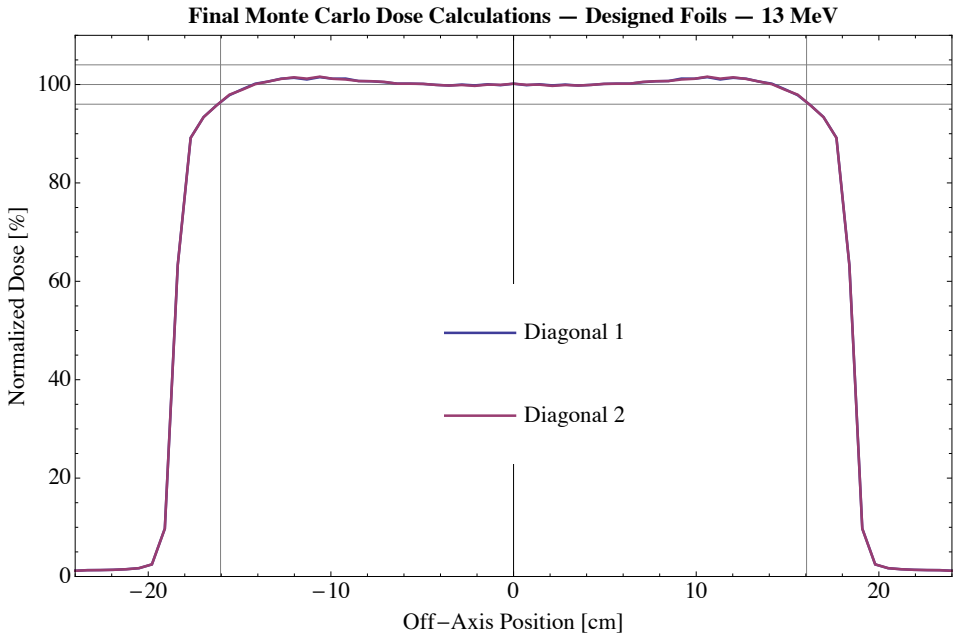

(g)

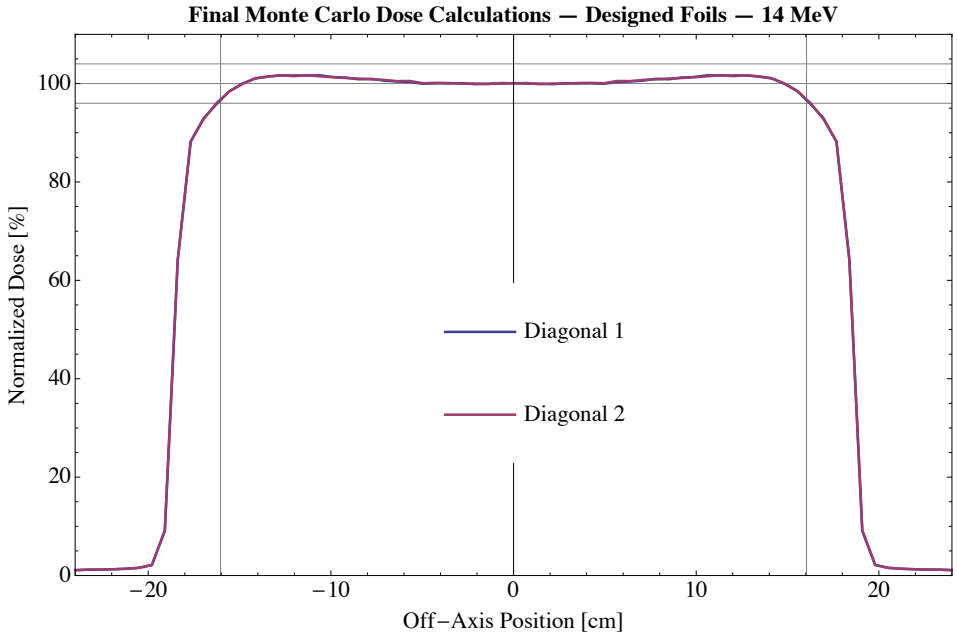

(h)

Figure 39 (continued): Plots of diagonal profiles (relative dose vs. off-axis position) for final Monte Carlo dose calculations for redesigned foil systems for (a) 7, (b) 8, (c) 9, (d) 10, (e) 11, (f) 12, (g) 13, (h) 14, (i) 15, (j) 16, (k) 17, (l) 18, (m) 19, and (n) 20 MeV. Horizontal lines at 100±4% and vertical lines $2\sqrt{2}$ cm inside 50% dose values demarcate the acceptable range for diagonal off-axis dose profiles.

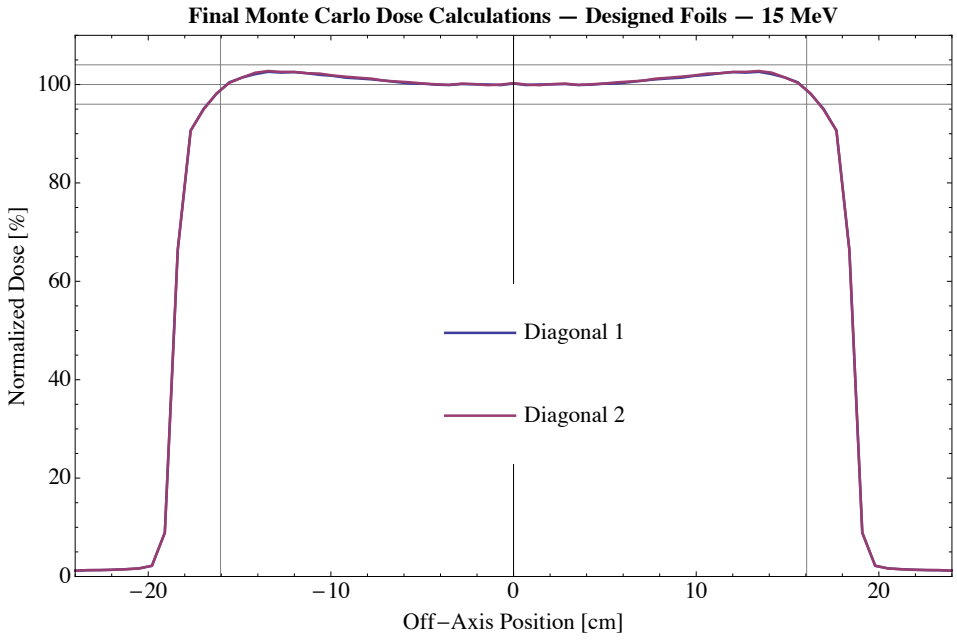

(i)

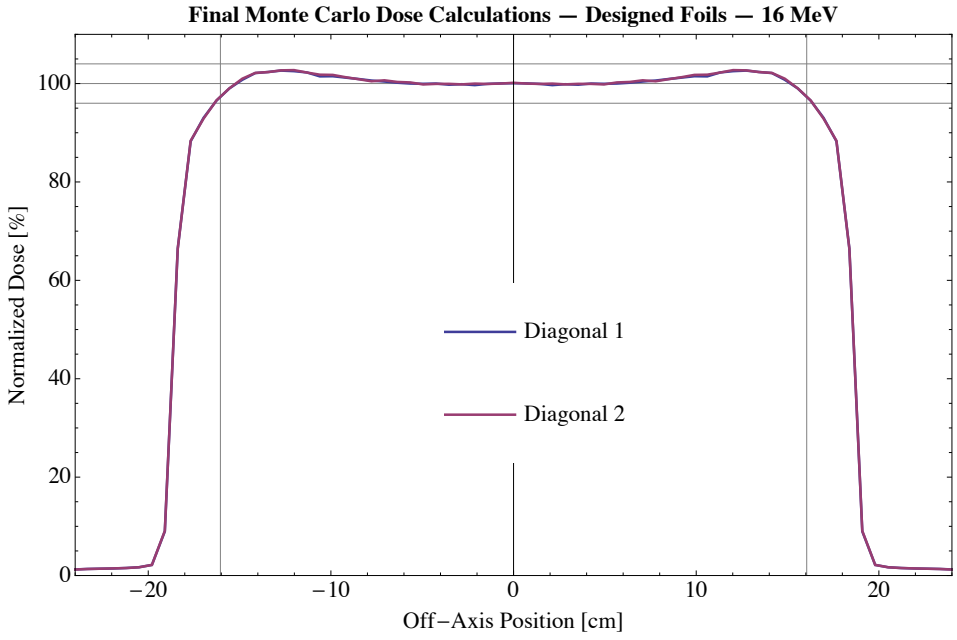

(j)

Figure 39 (continued): Plots of diagonal profiles (relative dose vs. off-axis position) for final Monte Carlo dose calculations for redesigned foil systems for (a) 7, (b) 8, (c) 9, (d) 10, (e) 11, (f) 12, (g) 13, (h) 14, (i) 15, (j) 16, (k) 17, (l) 18, (m) 19, and (n) 20 MeV. Horizontal lines at 100±4% and vertical lines $2\sqrt{2}$ cm inside 50% dose values demarcate the acceptable range for diagonal off-axis dose profiles.

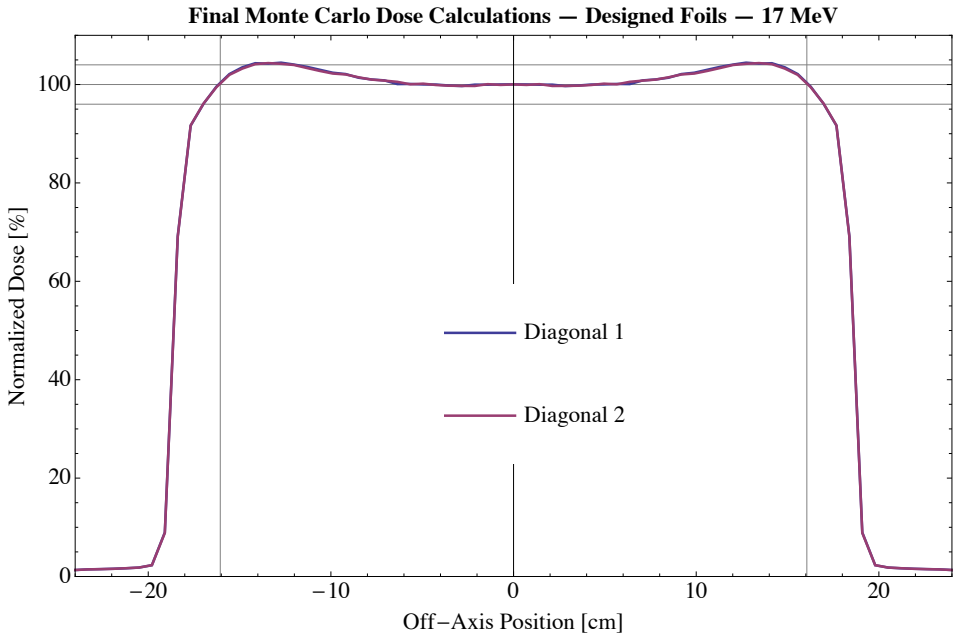

(k)

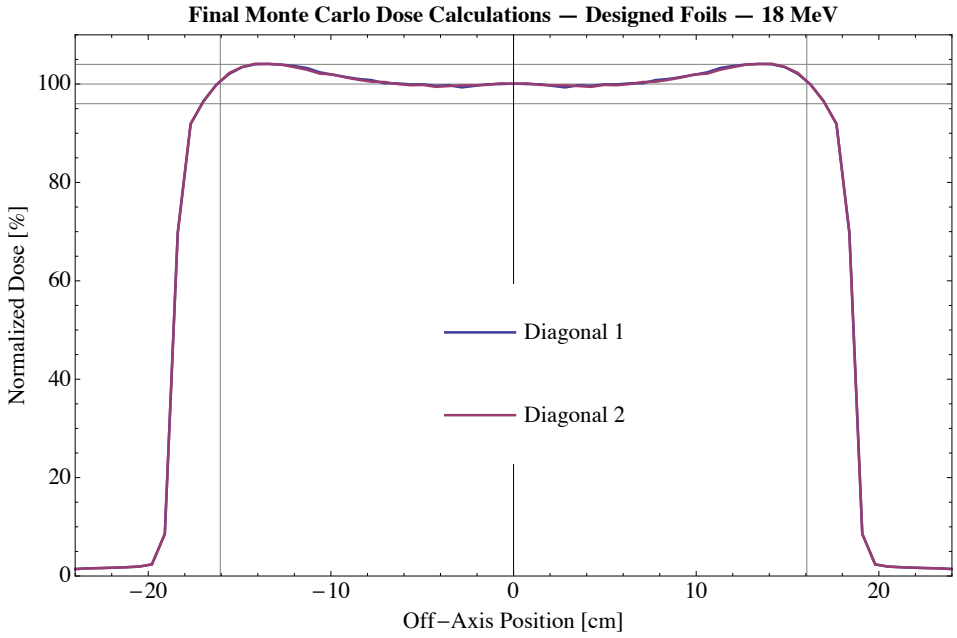

(l)

Figure 39 (continued): Plots of diagonal profiles (relative dose vs. off-axis position) for final Monte Carlo dose calculations for redesigned foil systems for (a) 7, (b) 8, (c) 9, (d) 10, (e) 11, (f) 12, (g) 13, (h) 14, (i) 15, (j) 16, (k) 17, (l) 18, (m) 19, and (n) 20 MeV. Horizontal lines at 100±4% and vertical lines $2\sqrt{2}$ cm inside 50% dose values demarcate the acceptable range for diagonal off-axis dose profiles.

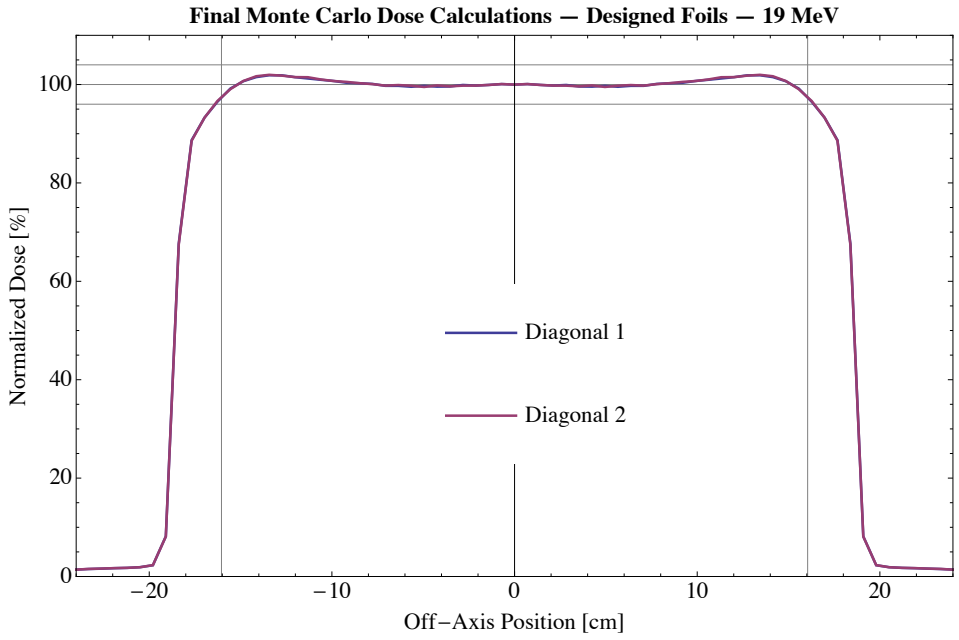

(m)

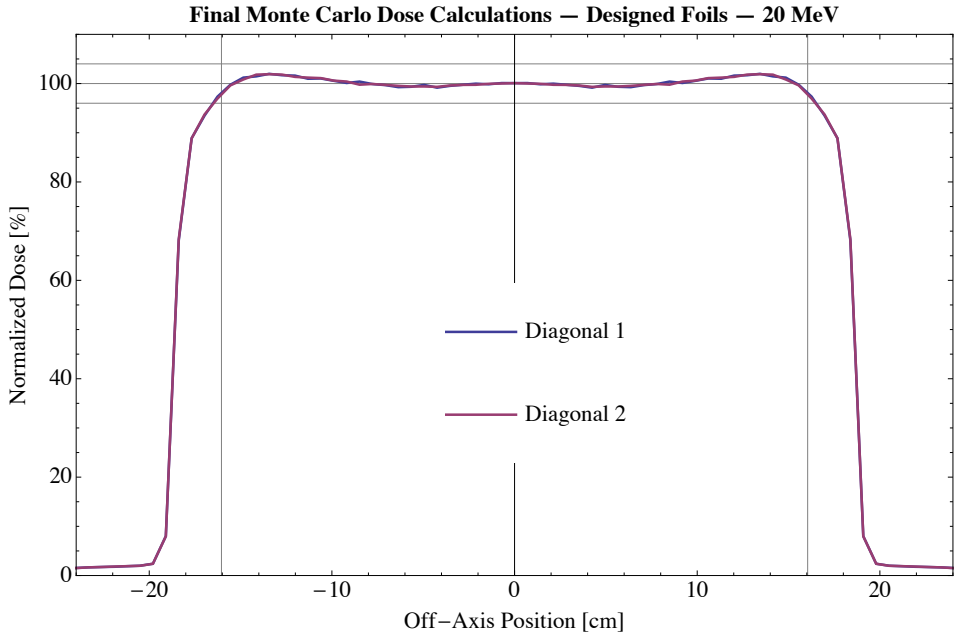

(n)

Figure 39 (continued): Plots of diagonal profiles (relative dose vs. off-axis position) for final Monte Carlo dose calculations for redesigned foil systems for (a) 7, (b) 8, (c) 9, (d) 10, (e) 11, (f) 12, (g) 13, (h) 14, (i) 15, (j) 16, (k) 17, (l) 18, (m) 19, and (n) 20 MeV. Horizontal lines at 100±4% and vertical lines $2\sqrt{2}$ cm inside 50% dose values demarcate the acceptable range for diagonal off-axis dose profiles.

For the modified designs, the case of 18 MeV was one of the worst-performing cases. Figure 40 shows that reducing the primary foil thickness by one primary foil layer results in far worse agreement (Δ_{max}=8%) between the design and objective profiles. The figure also shows that the disagreement can be remedied if the primary foil is allowed to vary. The green line shows the resulting design profile when the primary foil thickness is optimized (x4.7 primary foils), which reduces the Δ_{max} from 3.9% with 5 primary foil layers to 1.7%.

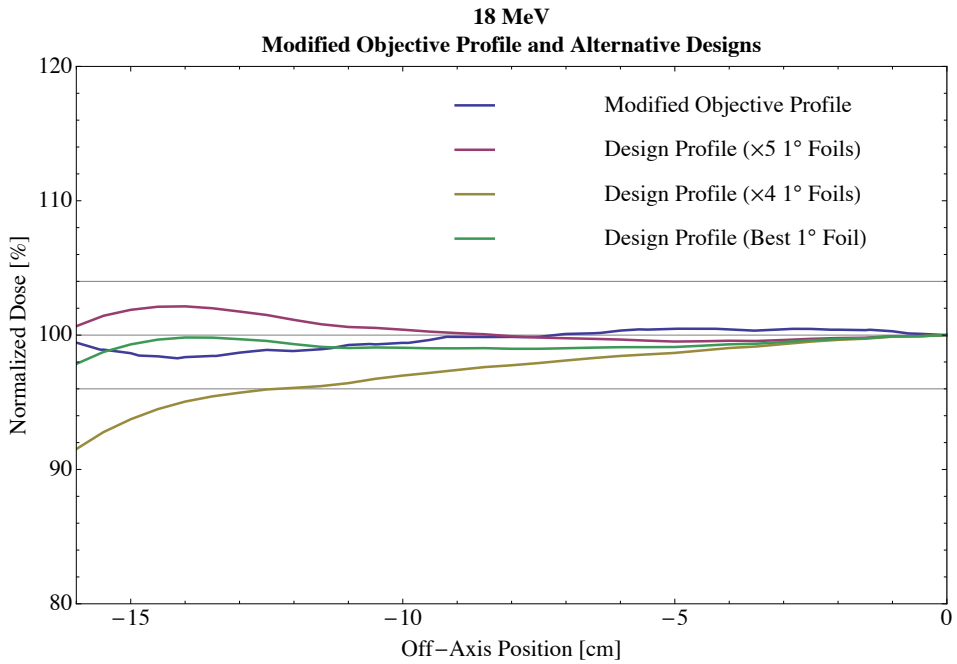

Figure 40: Plots comparing the modified objective profile for 18 MeV with design profiles with 5 primary foil layers (red line), 4 primary foil layers (gold line), and optimized primary foil thickness (green line).

For the case of 8 MeV, which is the worst case of all the energies, agreement cannot be achieved by merely changing the primary foil. Figure 41 shows that if a primary foil layer is removed from the design, the results is an increase in the Δ_{max} from 3.9% to 7.8%. If the primary foil is allowed to vary in non-discrete steps, however, a Δ_{max} smaller than 3.9%

cannot be achieved. Thus, in order to improve the agreement for the 8 MeV beam, a change in the secondary foil would be required.

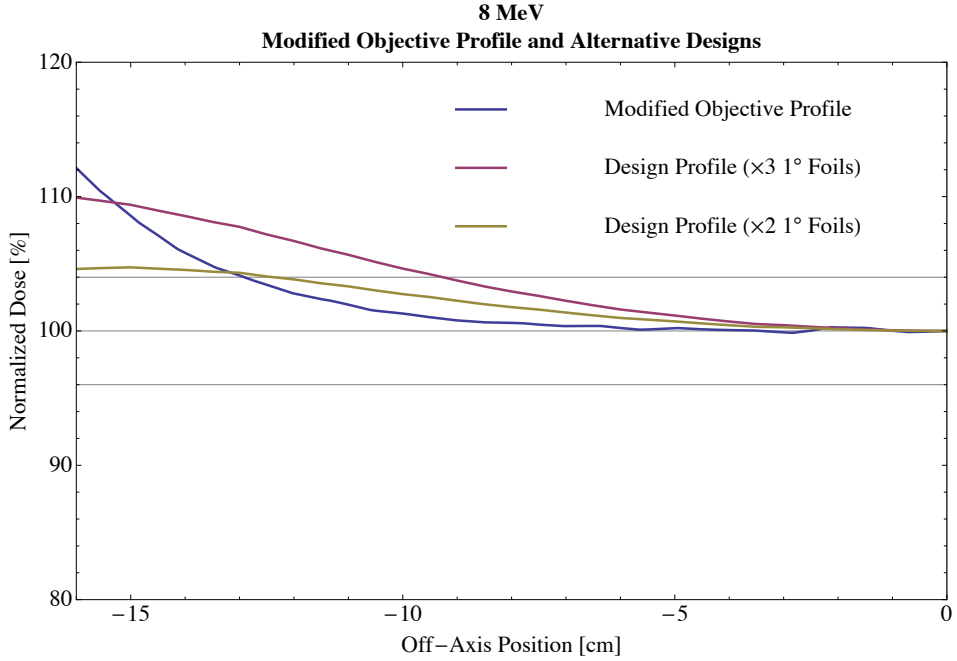

Figure 41: Plots comparing the modified objective profile for 8 MeV with design profiles with 3 primary foil layers (red line) and 2 primary foil layers (gold line).

4.2.4.c X-ray Dose

For the final designs, x-ray dose had no significant change from the initial designs. Every design resulted in the same D_x except for three cases, none of which changed by more than 0.2%. Because the foil parameters were not substantially changed in the re-design process and the design simulator had already been shown to predict x-ray dose with sufficient accuracy (cf. Table 16), it was decided that Monte Carlo dose calculations were unnecessary for the x-ray dose for the re-designed foils.

4.2.5 Comparison with MBPCC Elekta Electron Beam Commissioning Data

Comparisons between final Monte Carlo dose calculations and clinical acceptance data for MBPCC Elekta electron beams show that the newly designed foils yield beams nearly as good as, or superior to, what is currently clinically available. Table 20 shows design data at the beam energies nearest what is currently available on MBPCC Elekta electron beams.

Table 20: Table comparing final Monte Carlo dose calculations for modified designed foils with the commissioning data for the current MBPCC Elekta electron beams.

	Monte Carlo		**Clinical**	
$E_{nominal}$ [MeV]	$(\Delta)_{min}$	$(\Delta)_{max}$	$(\Delta)_{min}$	$(\Delta)_{max}$
7	−1.6%	4.7%	−5.4%	1.9%
9	−1.1%	4.0%	−3.1%	1.7%
10	−3.2%	2.1%	−5.4%	1.3%
11	−3.0%	2.1%	−5.1%	1.9%
13	−3.9%	1.5%	−5.2%	1.5%
16	−2.7%	2.6%	−3.6%	0.%
20	−2.2%	1.9%	−6.9%	0.1%

Chapter 5 Conclusions

5.1 Summary of Results

Hypothesis: A dual foil scattering system within the constraints of the Elekta Infinity radiotherapy linear accelerator can be designed such that clinical beams meet flatness criteria of ±3% (±4%) along its principal axes (diagonal axes) for 25x25cm^2 applicator and most probable surface energies of 7-20 MeV.

The hypothesis was tested through the completion of three specific aims. Aim 1 consisted of commissioning the dual foil scattering system design simulator by validating it against Monte Carlo simulations. Results showed that for the dual foils used for 7 and 9 MeV, the design simulator deviated from Monte Carlo simulations by no more than 4.2% and 4.4%, respectively, within ±17.6 cm of central axis. For the dual foils used for 10, 11, and 13 MeV, the greatest deviations between the two methods within ±17.6 cm of central axis were 1.3%, 1.6%, and 1.4% respectively. Finally, for the secondary foil used for the two highest energies, 16 and 20 MeV, deviations within ±12 cm of central axis were no more than 1.1% and 1.3% respectively. Outside of the range of ±12 cm, agreement between the two methods deteriorated, being 10.7% and 6.4% at ±17.6cm respectively

Aim 2 was to design a new dual foil scattering system for the Elekta Infinity linear accelerator. First measurements of clinical profiles were taken to determine the effect of collimation on scatter, particularly loss of side-scatter equilibrium from the x-ray collimators at low energies and scatter from the applicators at all energies. Once this was known, it was then possible to develop objective profiles that correlated the design simulator's calculated profile to measurements. Objective profiles for most probable

surface energies ranging from 7-20 MeV in 1-MeV increments were interpolated using the objective profiles already developed for the clinical beams. The design constraints selected for this study were that combinations of any of three aluminum secondary foils and five equally spaced (0.003 cm) primary tantalum foil thicknesses could be used. Results showed that it was possible to design profiles that agreed with the objective profiles within the goal of ±3% for each of the design energies except 18 MeV. Also, for the energies currently available on the Mary Bird Perkins Cancer Center's Elekta Infinity, bremsstrahlung contamination for the newly design foils only increased in three cases, one of which was 0.2% and the other two were 0.1%. In one case bremsstrahlung dose was reduced by 0.4%, and in the remaining three it was unchanged.

Aim 3 was to verify that the designs from Aim 2 produce clinically usable beams. This was accomplished by running Monte Carlo simulations with the new foil designs in place. The appropriate incident energy spectra and reasonable x-ray jaw positions, and backup diaphragm positions were selected for each of the design energies with a $25\times25 cm^2$ applicator. Results from Monte Carlo simulations showed that using the dual foil design from Aim 2 that for each of the energies, transverse profiles met flatness requirements, with the greatest flatness deviation over the clinically relevant range being 2.8%. Results from diagonal profiles showed that all cases did not meet flatness requirements. The worst case had a maximum deviation of 6.1% over the clinically relevant range, whereas the best case had a maximum deviation of only 2.3%. Bremsstrahlung dose predictions from the Monte Carlo simulations were within 0.5% of the results found by the design simulator. Refined objective profiles were then generated based on the Monte Carlo data and the original design profiles. The modified objective profiles allowed for a more accurate

prediction of flatness based on analytically derived profiles. Thus, a flatter dual scattering foil system was designed. The modified designs resulted in beams that all passed flatness criteria along the principal axes except for one, failing in the case of 8 MeV with a 3.2% maximum deviation. Along the diagonal axes, beams at every energy passed flatness criteria except for three cases: 7, 8, and 17 MeV, which had maximum deviations of 4.7%, 5.1%, and 4.3%, respectively. The modified designs reduced the number of beams failing flatness criteria from six in the initial designs to three after one iteration; the maximum deviation was also reduced from 6.1% to 5.1%.

5.2 Conclusions

1. Dual Foil Scattering System Simulator: The dual foil scattering system simulator can predict relative off-axis primary dose with sufficient accuracy to be used for the design of dual foil scattering systems. Also, the dual foil scattering system simulator can be used to accurately predict photon contamination dose to within 0.5%. The beams created by the refined designs created beams as good as, or superior to, the current Elekta electron beams used at MBPCC.
2. Hypothesis: Assuming the Monte Carlo is accurate, the iterative design process outlined in this study was unable to produce off-axis profiles for Elekta electron beams (7-20 MeV) that met flatness specifications (±3% transverse, ±4% diagonals). Hence, using the design procedure and one iteration, the hypothesis was not proven. However, it is likely that future work will allow the hypothesis to be proven.

5.3 Future Work

1. In order to further improve the dual scattering foil system design and meet the hypothesis, three possible future strategies are:
    a. Increase the number of iterations from one;
    b. Include collimator effects in the design simulator, particularly their effect on side-scatter equilibrium at the lower energies; and
    c. Add more flexibility in primary foil thicknesses or make smarter selection of spacing of five foils (i.e., not necessarily equally spaced).
2. Improvement in tools:
    a. Improve the electron dual foil scattering system simulator to allow simultaneous optimization and viewing of multiple energies and
    b. Improve the Monte Carlo beam model to agree with measurements within 1% or modify optimization method to account for its inaccuracy

References

Bjarngard B E, Piontek R W, and Svensson G K 1976 Electron scattering and collimation system for a 12 MeV linear accelerator *Med. Phys.* 3 153–58

Carver R, Hogstrom K R, Price M, LeBlanc J D, and Harris G M 2012 SU-E-T-25: Real time simulator for designing electron dual scattering foil systems *Med. Phys.* 39

Green A D 1991 Modeling of dual foil scattering systems for clinical electron beams *MS Thesis* The University of Texas Health Science Center at Houston, Houston, TX

Grusell E, Montelius A, Brahme A, Rikner G and Russell K 1994 A general solution to charged particle beam flattening using an optimized dual-scattering-foil technique, with application to proton therapy beams *Phys. Med. Biol.* 39 2201–16

Harris G M 2012 Development and validation of an electron Monte Carlo model for the Elekta Infinity linear accelerator *MS Thesis* Louisiana State University and Agricultural and Mechanical College, Baton Rouge, LA

Hogstrom K R 2004 Electron beam therapy: dosimetry, planning, and techniques *Principles and Practice of Radiation Oncology* ed C Perez *et al* (Baltimore, MD: Lippincott, Williams & Wilkins pp 252-8

ICRU 1984 Radiation Dosimetry: Electron Beams with Energies Between 1 and 50 MeV *ICRU Report 35* (Bethesda, MD: ICRU)

Kainz K K, Hogstrom K R, Antolak J A, Almond P R, Bloch C D, Chiu C, Fomytskyi M, Raischel F, Downer M and Tajima T 2004 Dose properties of a laser accelerated electron beam and prospects for clinical application *Med. Phys.* 31 2053–67

Kainz K K, Antolak J A, Almond P R, Bloch C D, and K R Hogstrom 2005 Dual scattering foil design for poly-energetic electron beams *Phys. Med. Biol.* 50 755–767

Karzmark C J, Nunan C S, and Tanabe E 1993 *Medical Electron Accelerators* (McGraw-Hill, Inc., New York).

Keys R A and Purdy J A 1984 Radiation leakage from linac electron applicator assembly *Radiat Oncol Biol Phys* 10 713-21

Khan F M, Doppke K P, Hogstrom K R, Kutcher G J, Nath R, Prasad S C, Purdy J A, Rozenfeld M and Werner B L 1991 Clinical electron-beam dosimetry: report of AAPM Radiation Therapy Committee Task Group No. 25 *Med. Phys.* 18 73–109

Klein E E, Low D A and Purdy J A 1995 Changes in electron beam dosimetry with a new scattering foil-applicator system on a CL2100C *Int. J. Radiat. Oncol. Biol. Phys.* 32 483–90

Kawrakow I, Mainegra-Hin E, Rogers D W O, Tessier F, and Walters B R B 2011 The EGSnrc code system: Monte Carlo simulation of electron and photon transport *Technical Report PIRS-701*, National Research Council of Canada (NRCC)

Lax I, and Brahme A 1980 Collimation of high energy electron beams *Acta Radiol. Oncology* 19 199–207

Shiu A S 1988 Three-dimensional electron beam dose calculations *MS Thesis* The University of Texas Health Science Center at Houston, Houston, TX

Shiu A S, Tung S S, Nyerick C E, Ochran T G, Otte V A, Boyer A L and Hogstrom K R 1994 Comprehensive analysis of electron beam central axis dose for a radiotherapy linear accelerator *Med. Phys.* 21 559–66

Tapley N 1976 *Clinical Application of the Electron Beam* New York: Wiley Biomedical

Vaeth J M and Meyer J L 1991 The Role of High Energy Electrons in the Treatment of Cancer *Frontiers of Radiation Therapy and Oncology*, eds. Vaeth J M and Meyer J L San Francisco: Karger

Appendix A: Monte Carlo calculations quantifying off-axis collimator scatter and the impact thereon when one of the collimators (inplane or crossplane as indicated) is removed from the field.

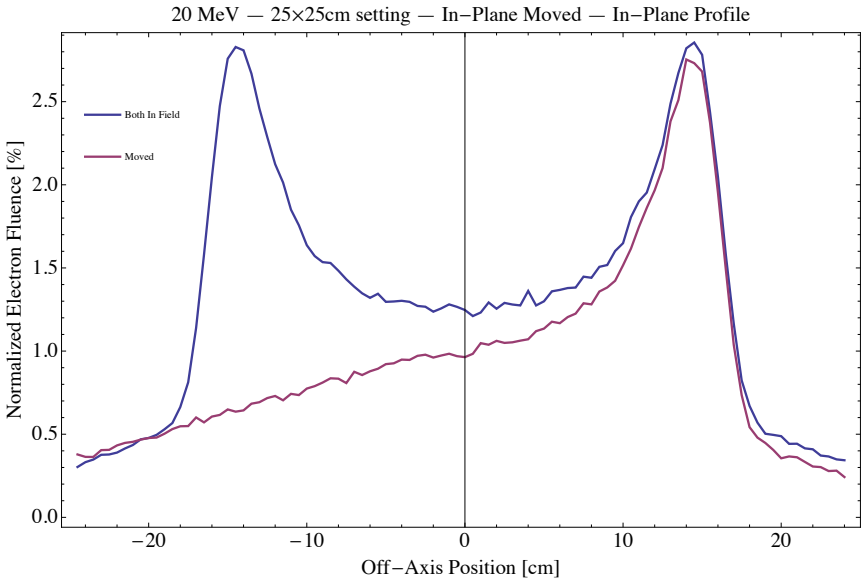

(a)

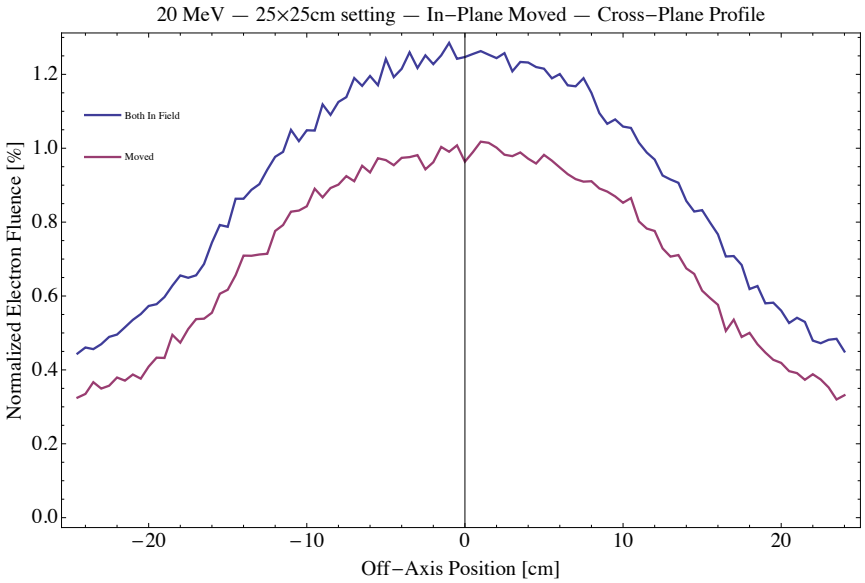

(b)

Figure A.1: Plots comparing electron fluence profiles due to scatter off the x-ray collimation system for 20 MeV in the (a) inplane and (b) crossplane directions calculated when the x-ray jaws are set to the 25x25cm^2 applicator settings (blue) and one is moved entirely from the field as indicated (red).

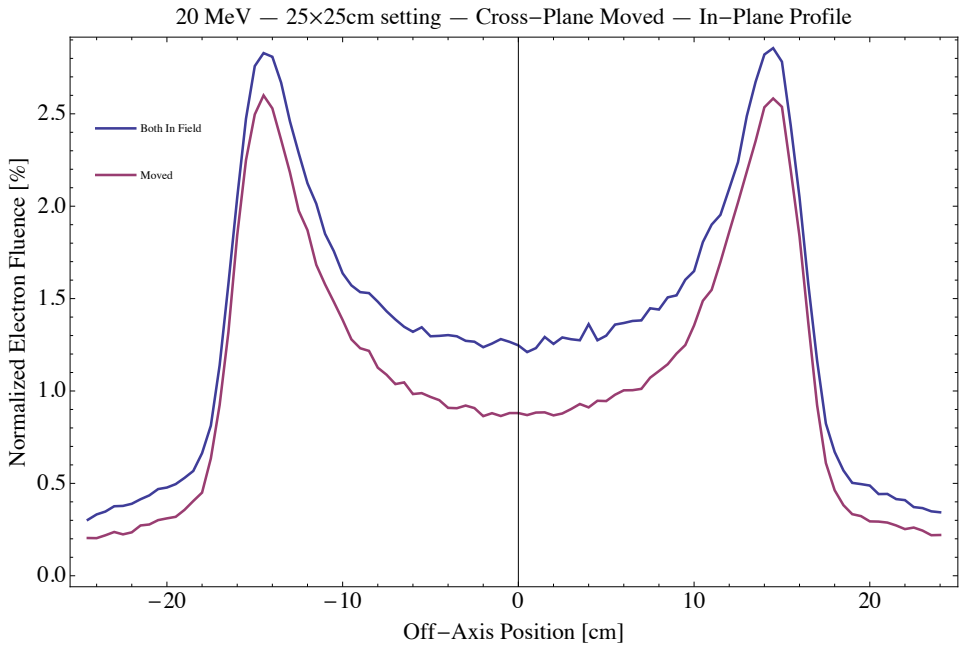

(a)

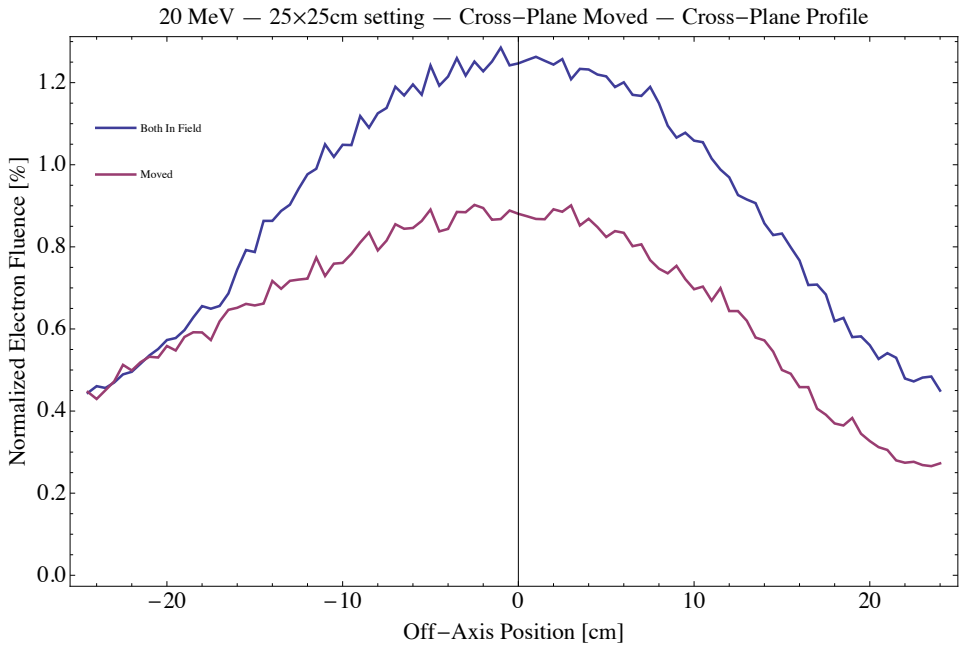

(b)

Figure A.2: Plots comparing electron fluence profiles due to scatter off the x-ray collimation system for 20 MeV in the (a) inplane and (b) crossplane directions calculated when the x-ray jaws are set to the 25x25cm^2 applicator settings (blue) and one is moved entirely from the field as indicated (red).

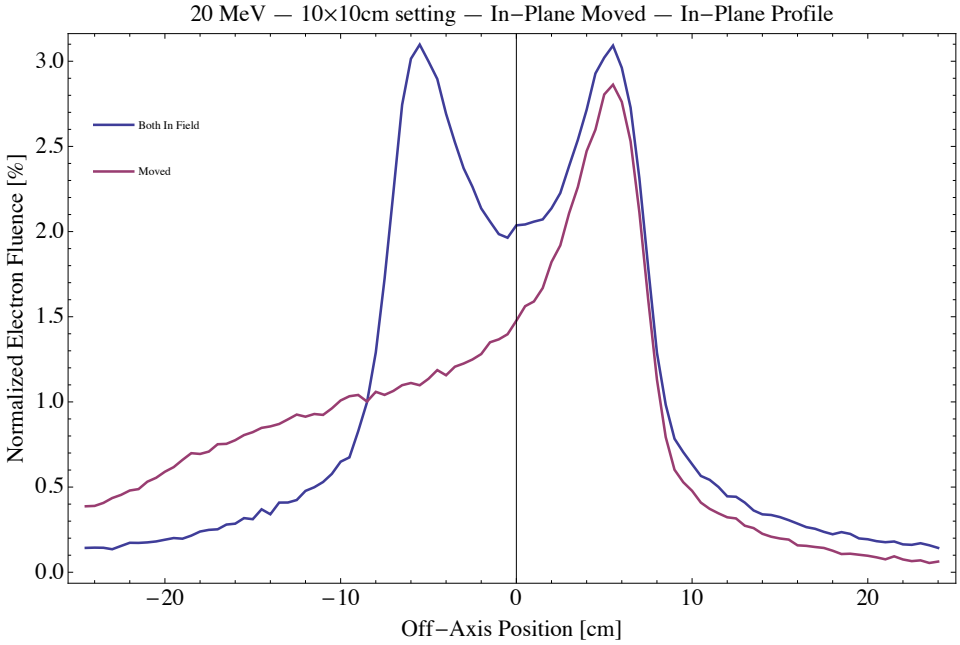

(a)

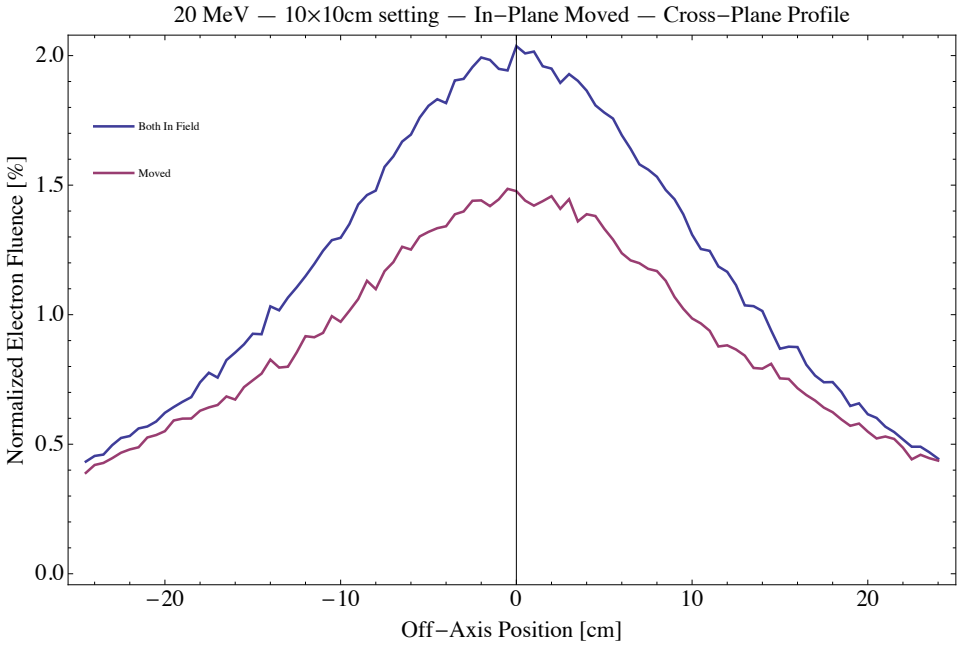

(b)

Figure A.3: Plots comparing electron fluence profiles due to scatter off the x-ray collimation system for 20 MeV in the (a) inplane and (b) crossplane directions calculated when the x-ray jaws are set to the 10x10cm^2 applicator settings (blue) and one is moved entirely from the field as indicated (red).

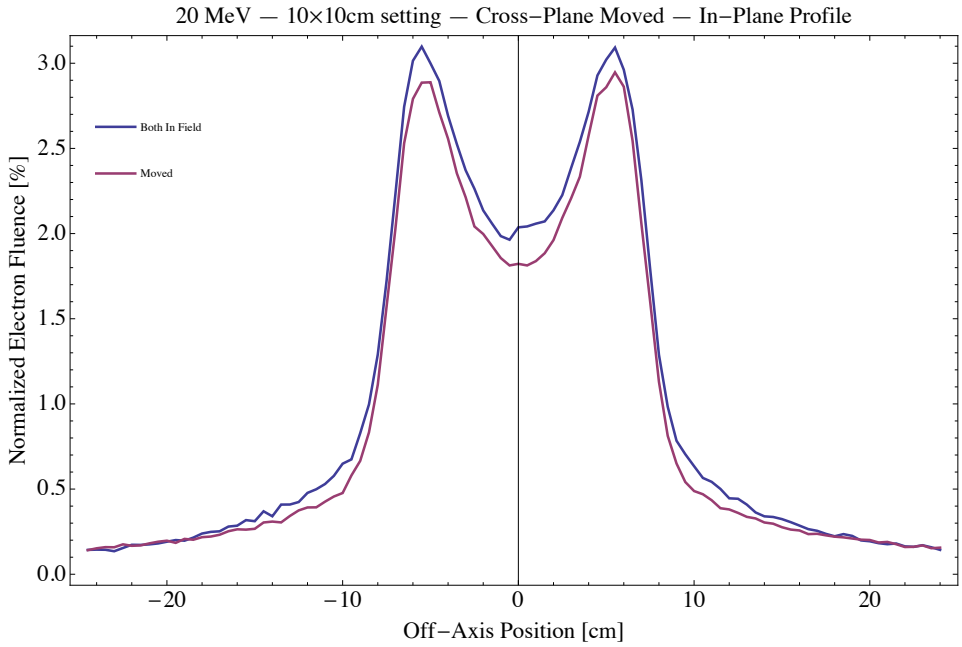

(a)

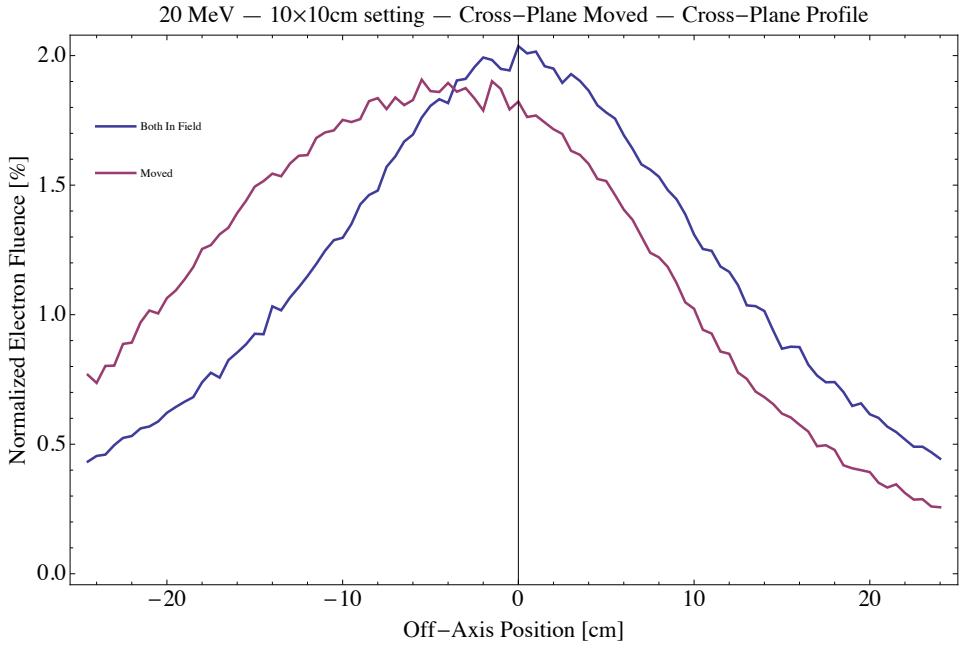

(b)

Figure A.4: Plots comparing electron fluence profiles due to scatter off the x-ray collimation system for 20 MeV in the (a) inplane and (b) crossplane directions calculated when the x-ray jaws are set to the 10x10cm^2 applicator settings (blue) and one is moved entirely from the field as indicated (red).

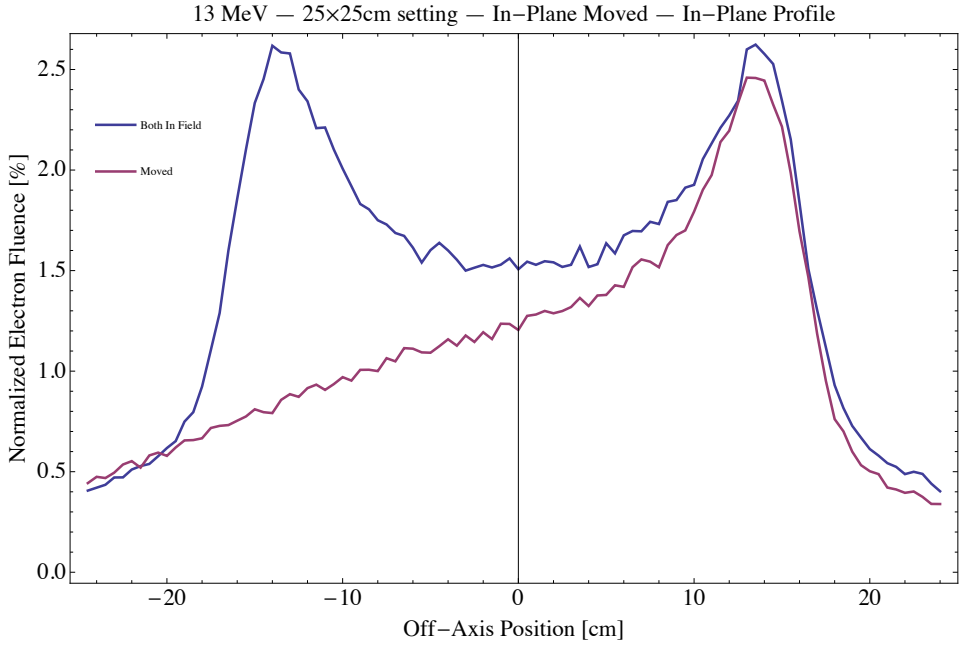

(a)

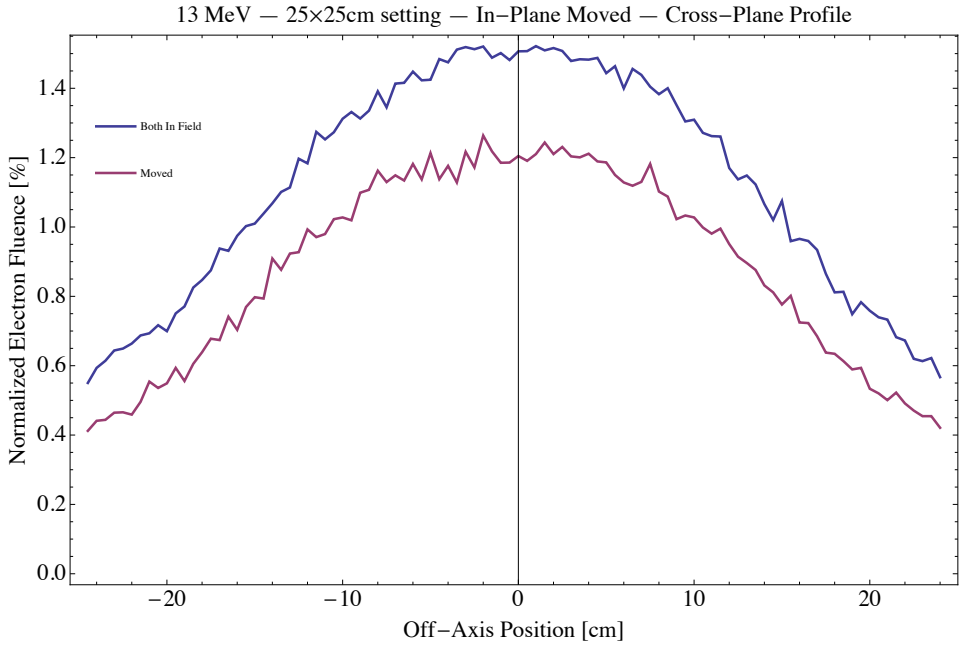

(b)

Figure A.5: Plots comparing electron fluence profiles due to scatter off the x-ray collimation system for 13 MeV in the (a) inplane and (b) crossplane directions calculated when the x-ray jaws are set to the 25x25cm^2 applicator settings (blue) and one is moved entirely from the field as indicated (red).

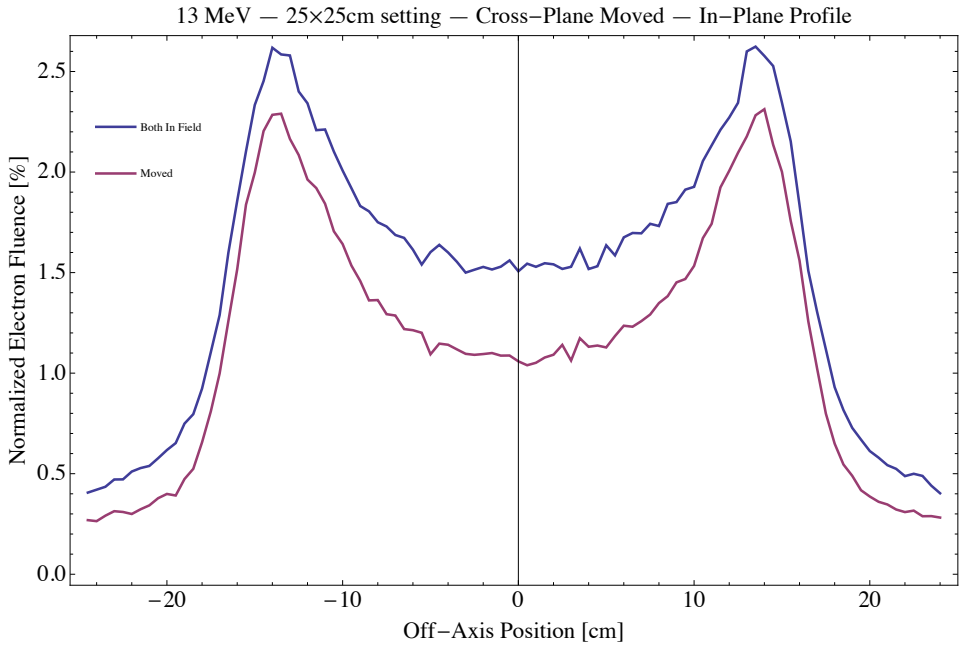

(a)

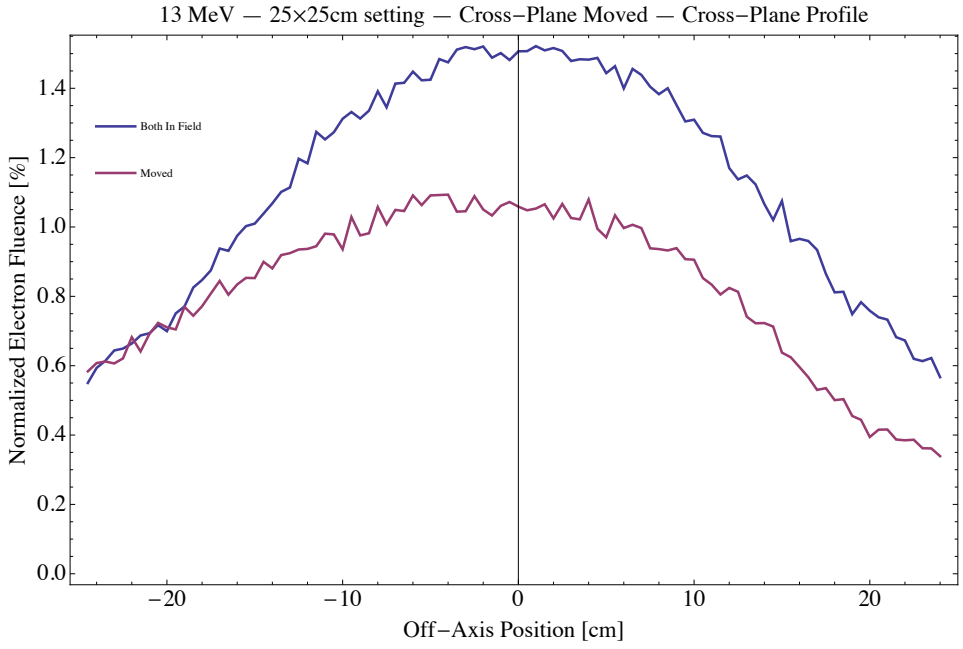

(b)

Figure A.6: Plots comparing electron fluence profiles due to scatter off the x-ray collimation system for 13 MeV in the (a) inplane and (b) crossplane directions calculated when the x-ray jaws are set to the 25x25cm^2 applicator settings (blue) and one is moved entirely from the field as indicated (red).

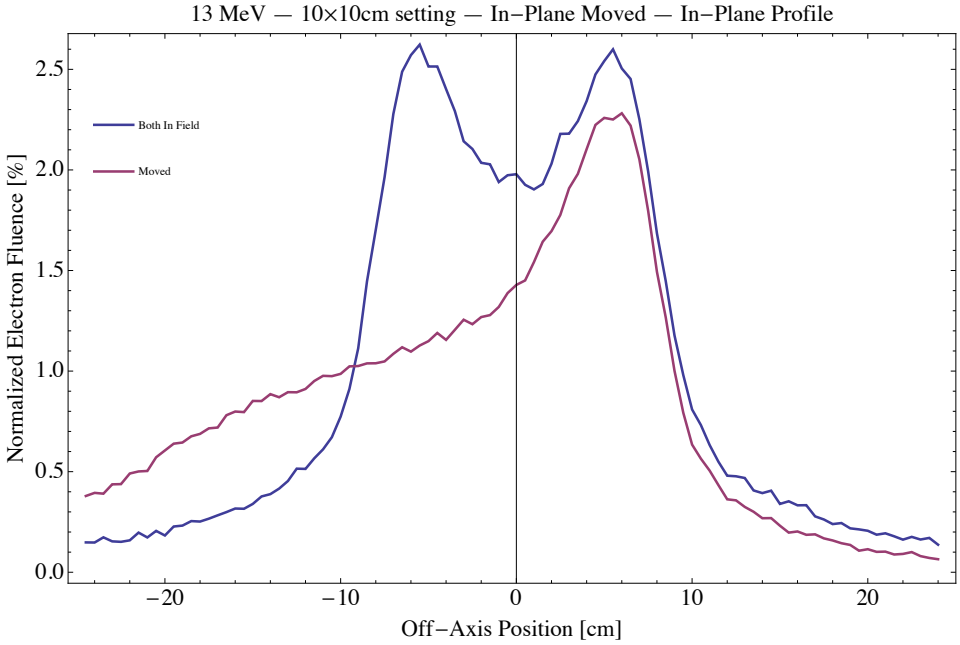

(a)

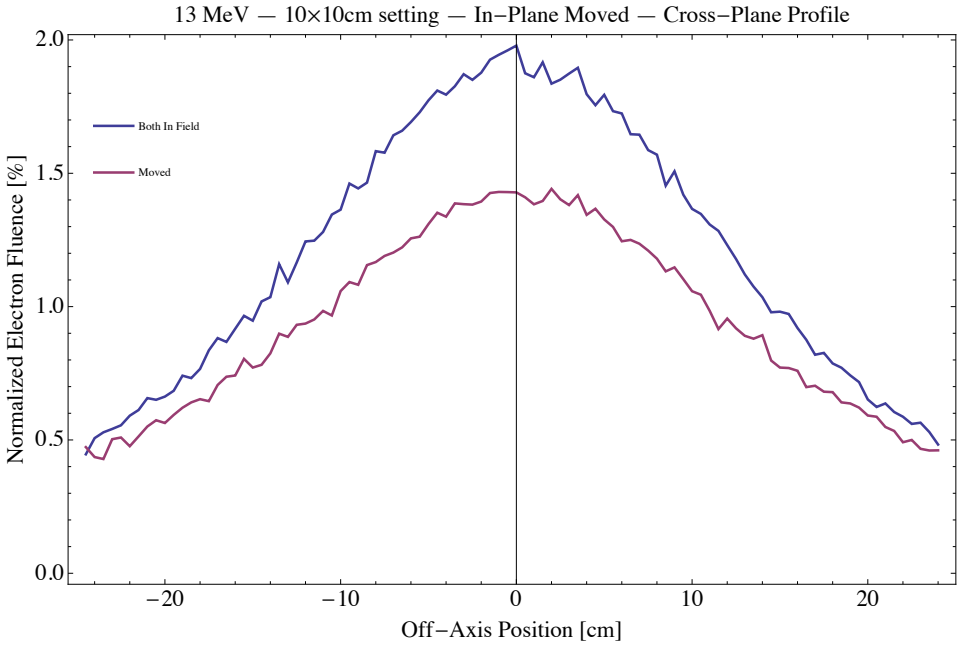

(b)

Figure A.7: Plots comparing electron fluence profiles due to scatter off the x-ray collimation system for 13 MeV in the (a) inplane and (b) crossplane directions calculated when the x-ray jaws are set to the 10x10cm^2 applicator settings (blue) and one is moved entirely from the field as indicated (red).

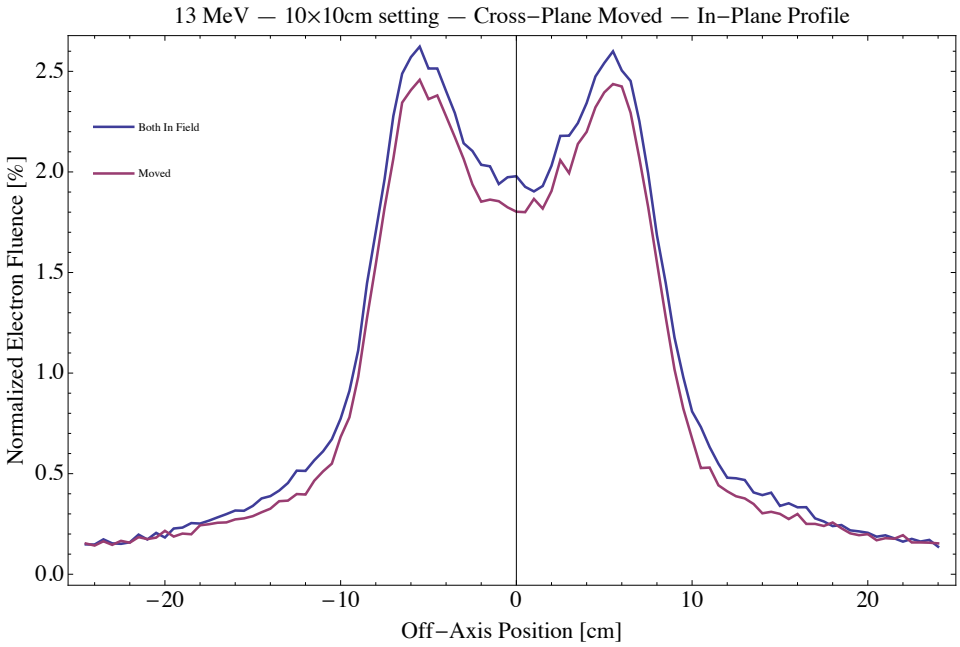

(a)

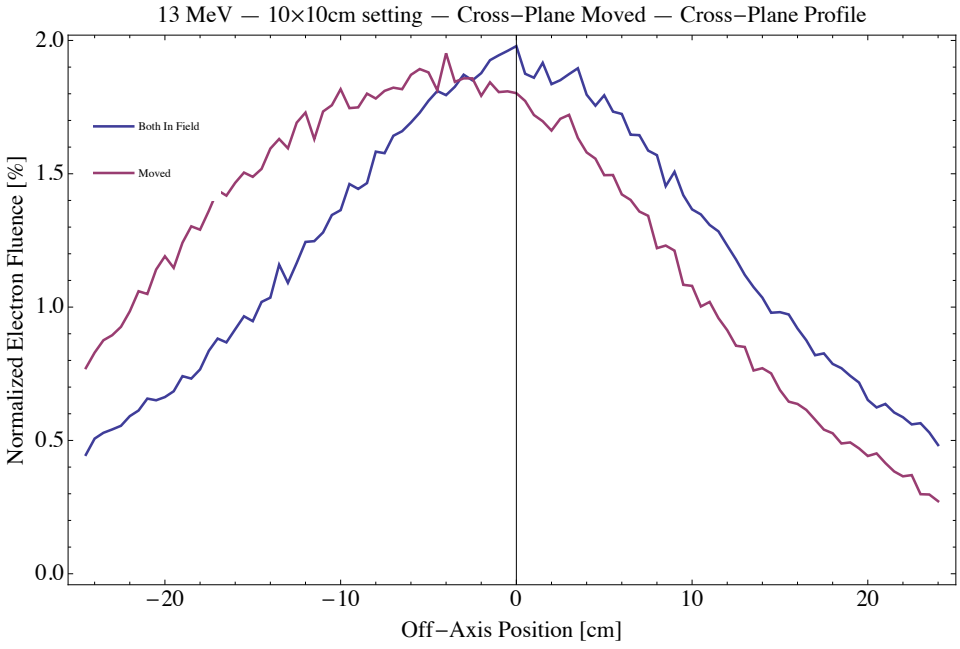

(b)

Figure A.8: Plots comparing electron fluence profiles due to scatter off the x-ray collimation system for 13 MeV in the (a) inplane and (b) crossplane directions calculated when the x-ray jaws are set to the 10x10cm^2 applicator settings (blue) and one is moved entirely from the field as indicated (red).

Appendix B: Measured profiles vs. Harris (2012) Monte Carlo Calculation

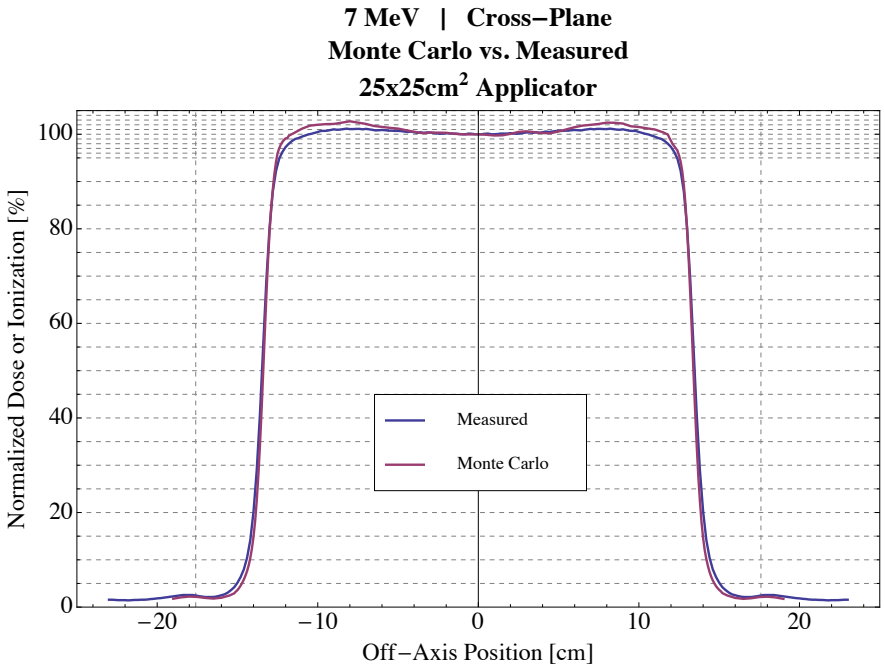

(a)

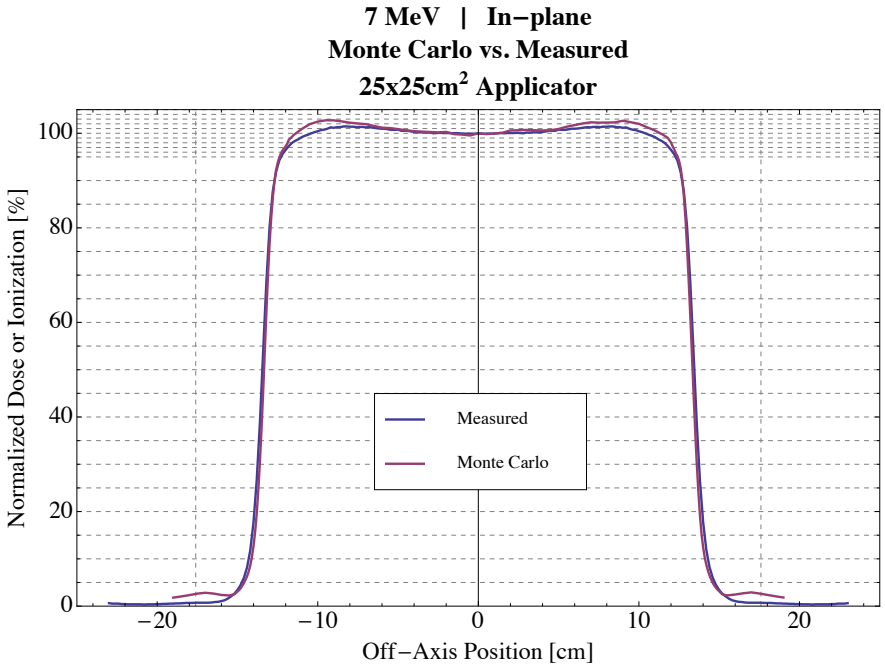

(b)

Figure B.1: Measured vs. Monte Carlo profiles for 7 MeV (a) crossplane and (b) inplane.

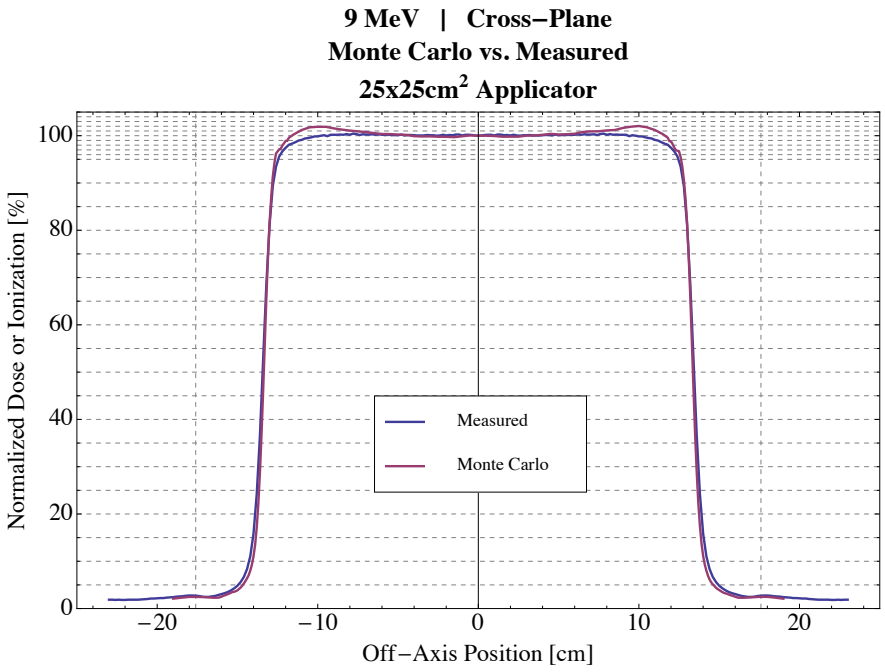

(a)

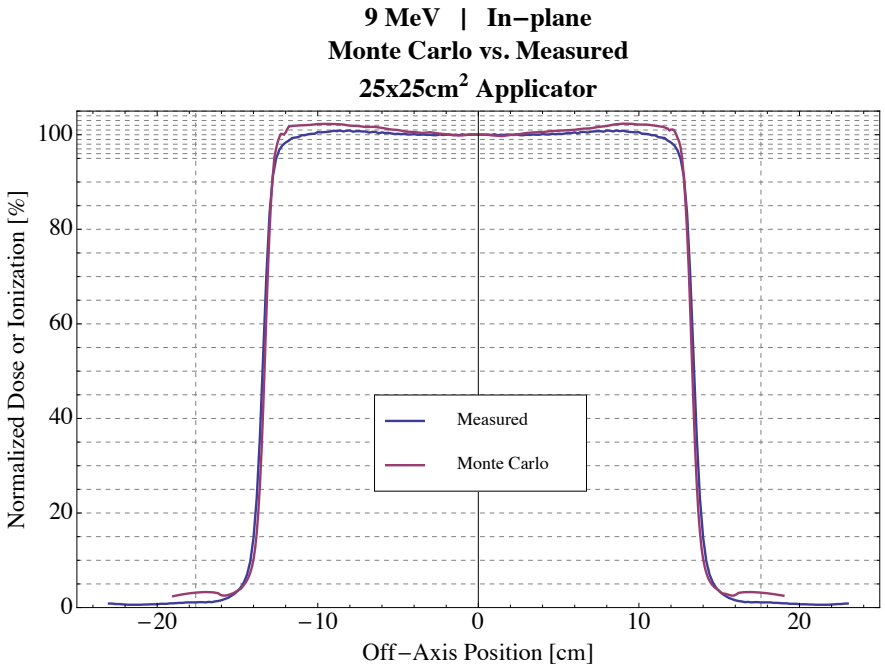

(b)

Figure B.2: Measured vs. Monte Carlo profiles for 9 MeV (a) crossplane and (b) inplane.

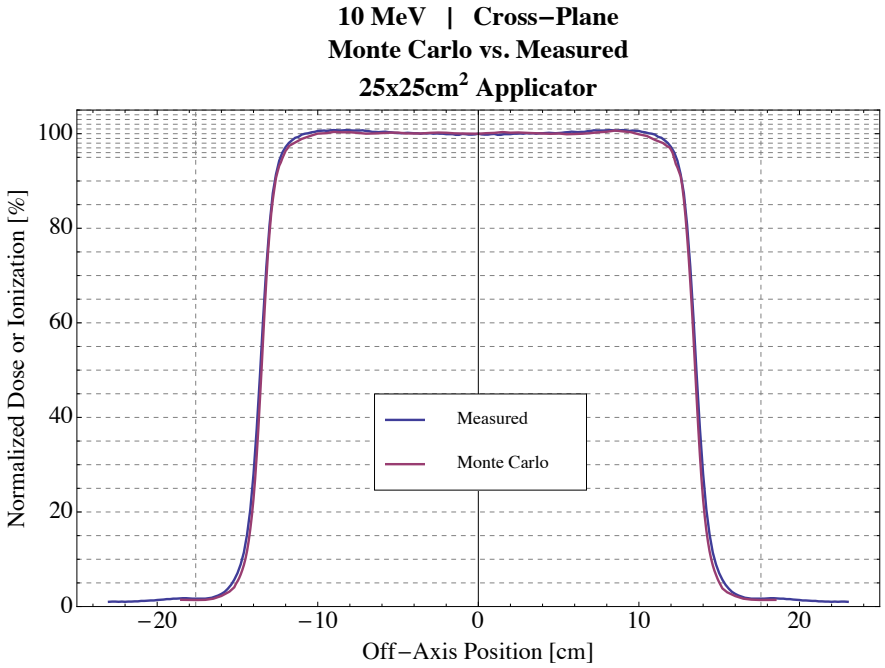

(a)

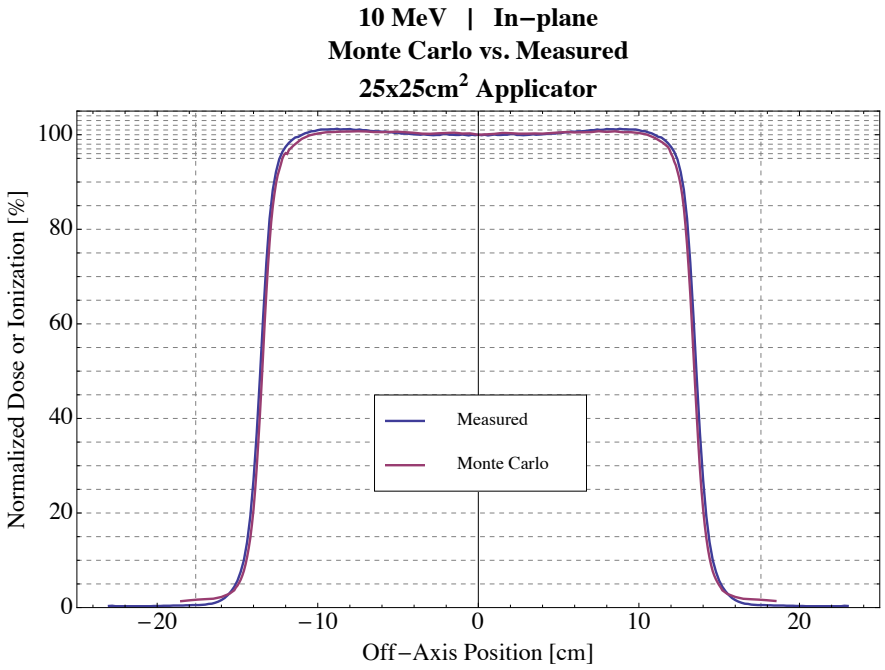

(b)

Figure B.3: Measured vs. Monte Carlo profiles for 10 MeV (a) crossplane and (b) inplane.

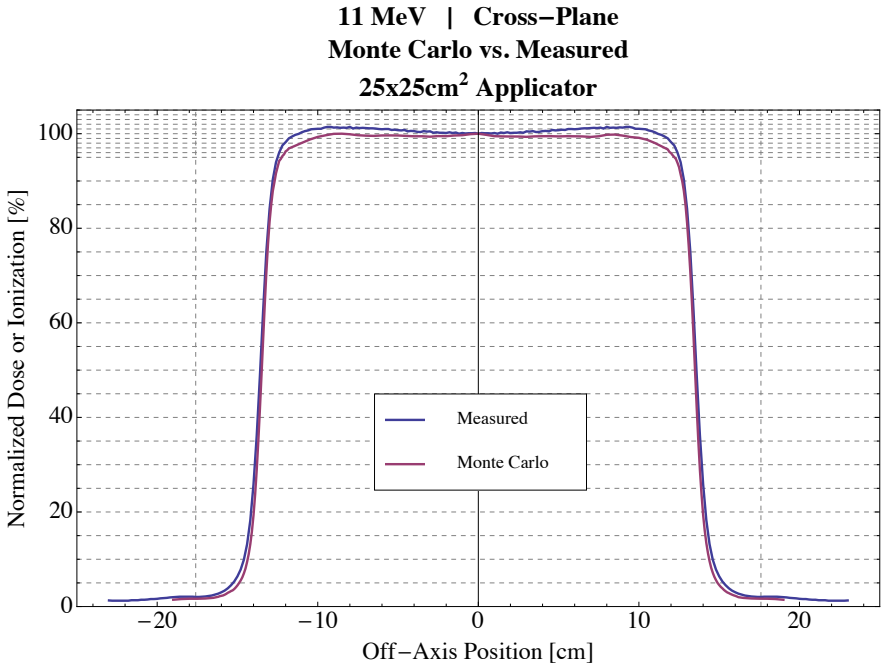

(a)

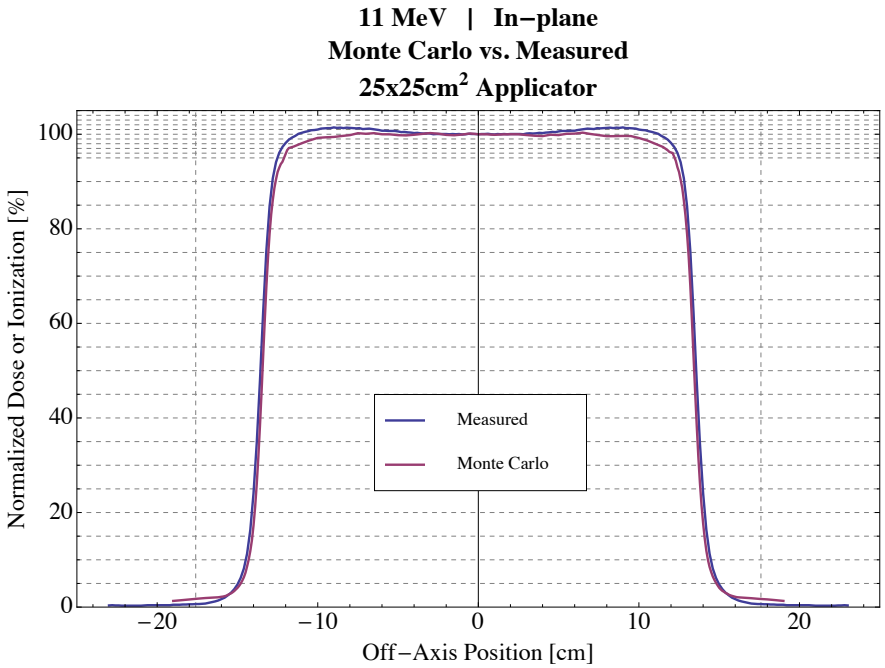

(b)

Figure B.4: Measured vs. Monte Carlo profiles for 11 MeV (a) crossplane and (b) inplane.

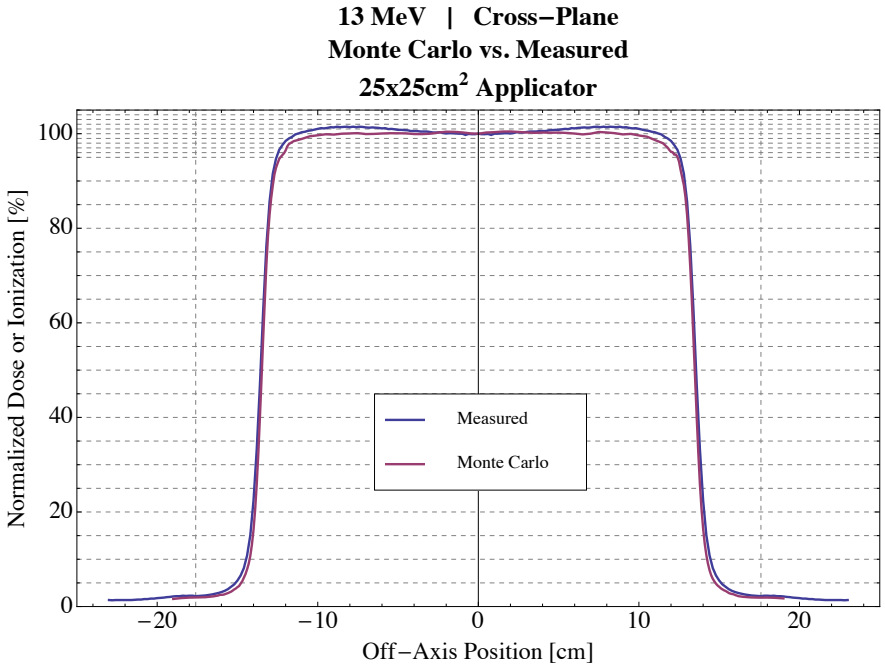

(a)

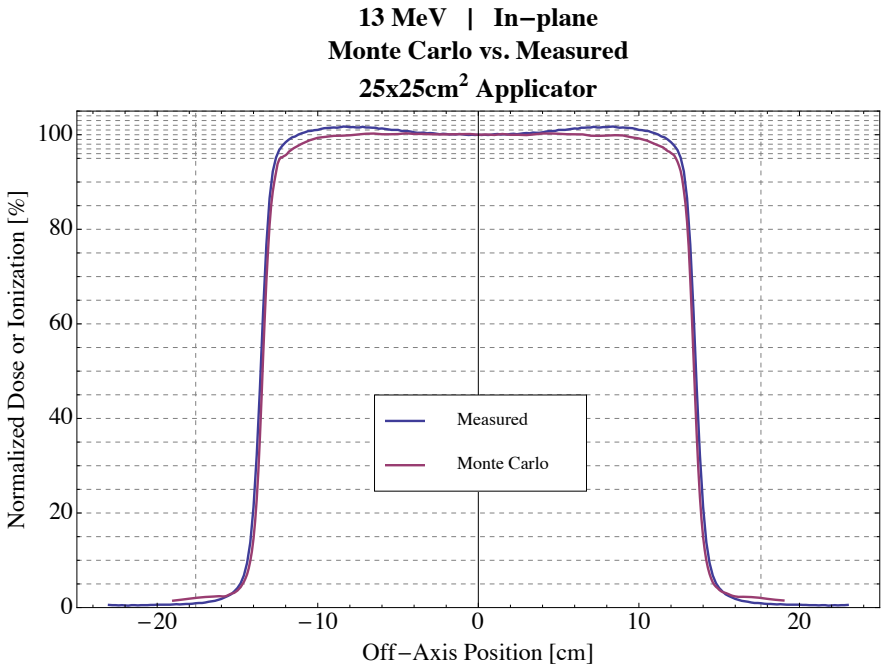

(b)

Figure B.5: Measured vs. Monte Carlo profiles for 13 MeV (a) crossplane and (b) inplane.

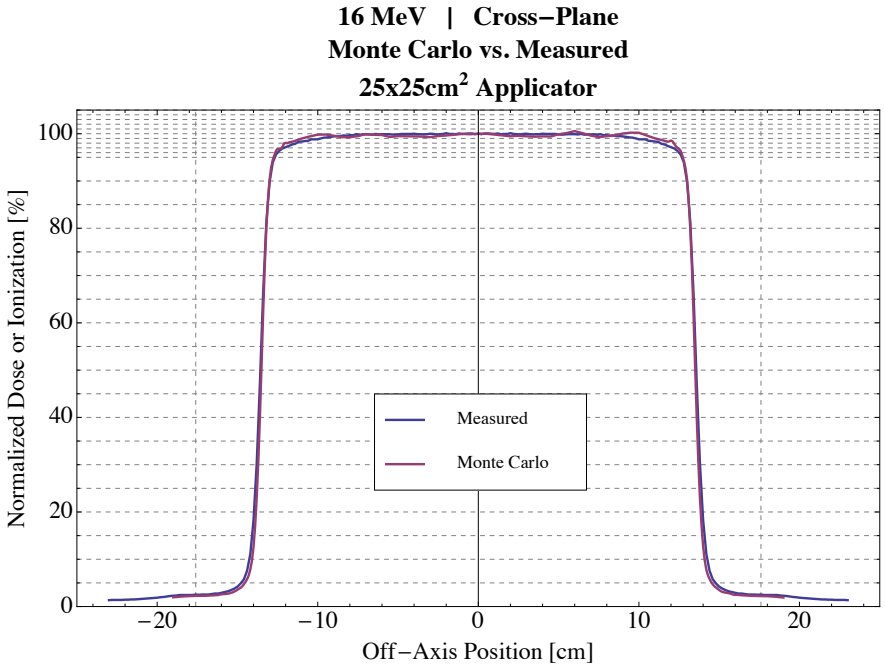

(a)

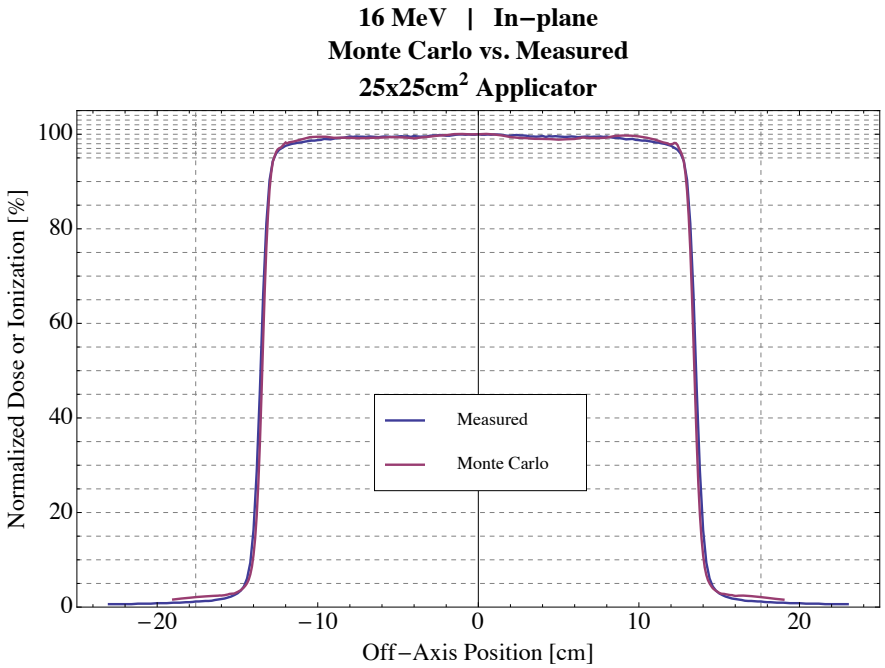

(b)

Figure B.6: Measured vs. Monte Carlo profiles for 16 MeV (a) crossplane and (b) inplane.

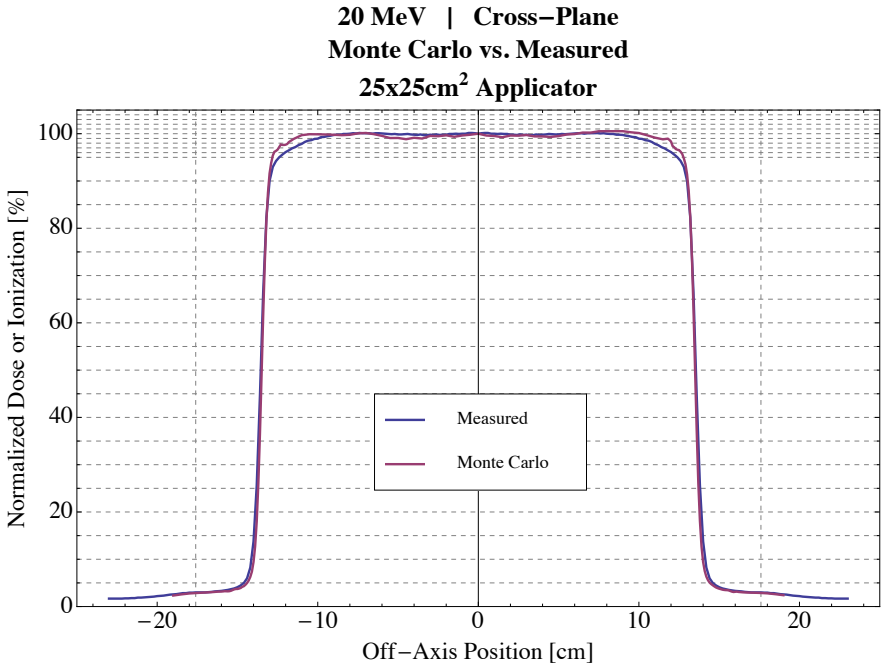

(a)

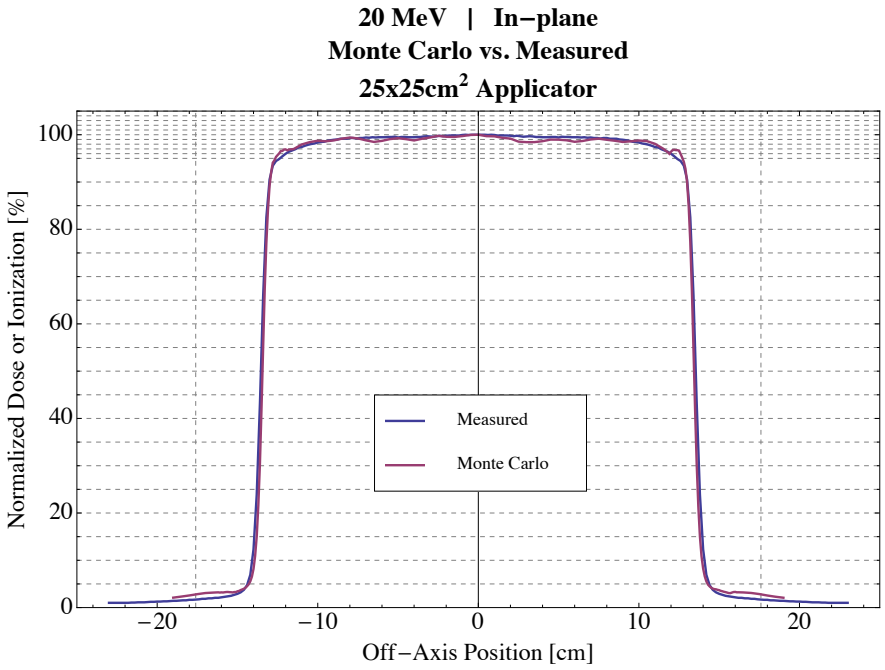

(b)

Figure B.7: Measured vs. Monte Carlo profiles for 20 MeV (a) crossplane and (b) inplane.

Appendix C: Comparison of measured profiles: (1) x-ray jaws at 40x40cm^2 with (2) x-ray jaws at energy dependent settings for 25x25cm^2 (both with no applicator).

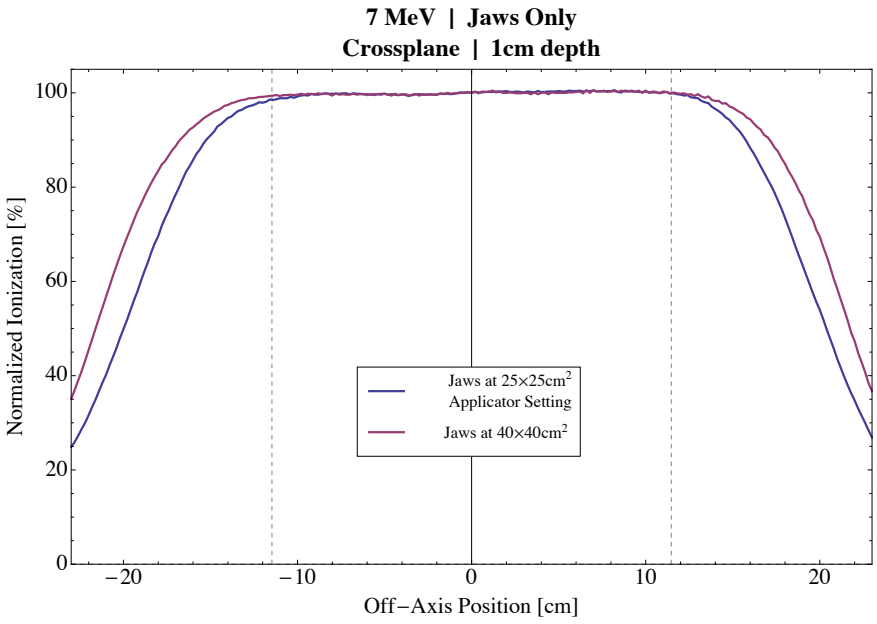

(a)

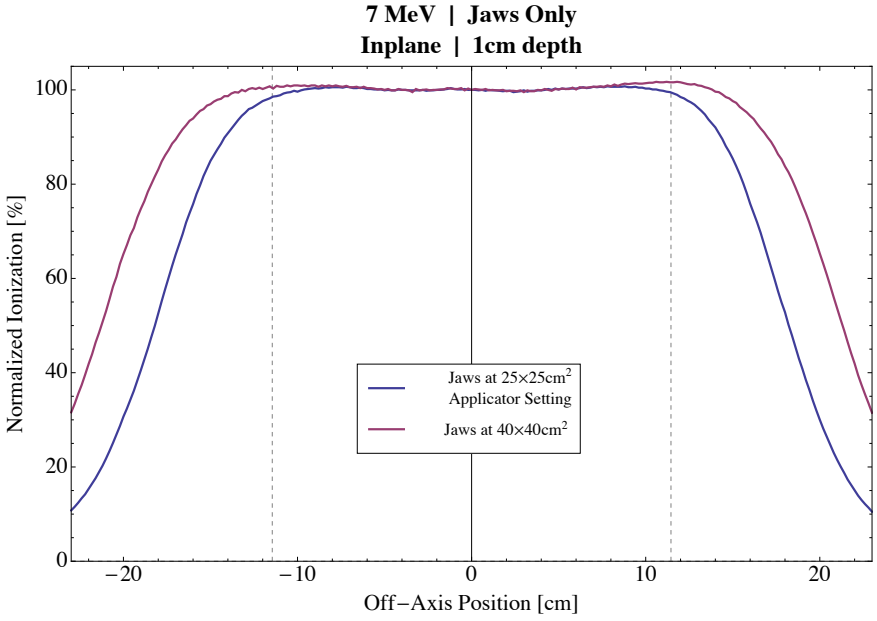

(b)

Figure C.1: Measured profiles for jaws at 40x40cm^2 and at 25×25cm^2 applicator settings for 7 MeV (a) crossplane and (b) inplane.

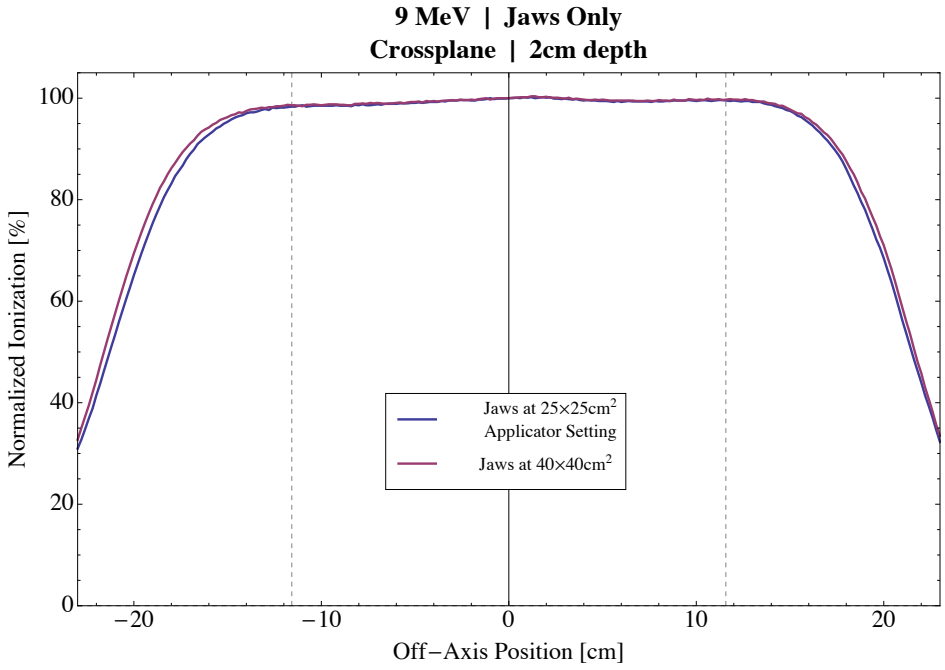

(a)

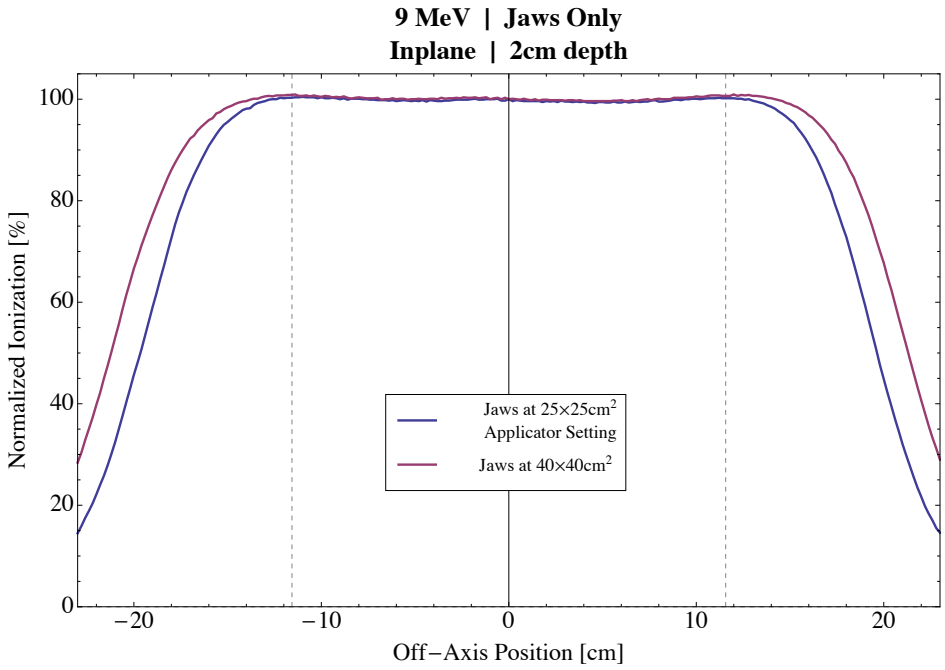

(b)

Figure C.2: Measured profiles for jaws at 40x40cm² and at 25×25cm² applicator settings for 9 MeV (a) crossplane and (b) inplane.

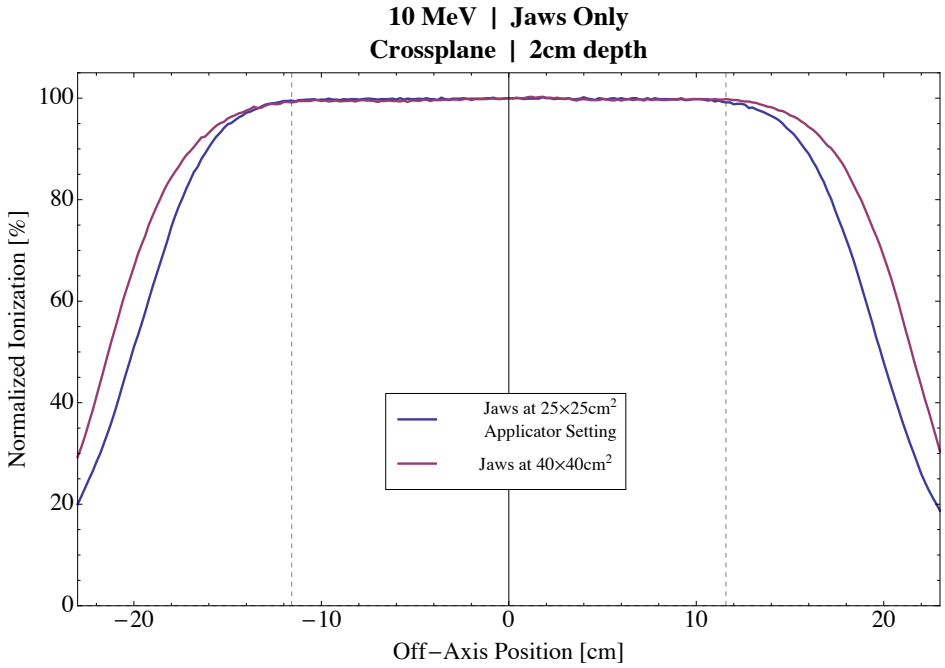

(a)

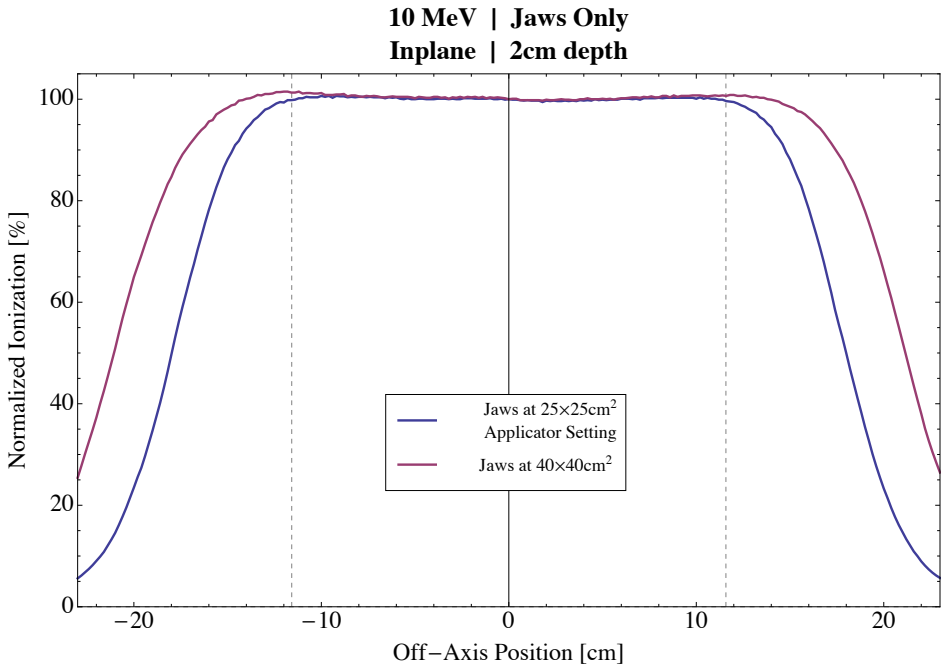

(b)

Figure C.3: Measured profiles for jaws at 40x40cm² and at 25×25cm² applicator settings for 10 MeV (a) crossplane and (b) inplane.

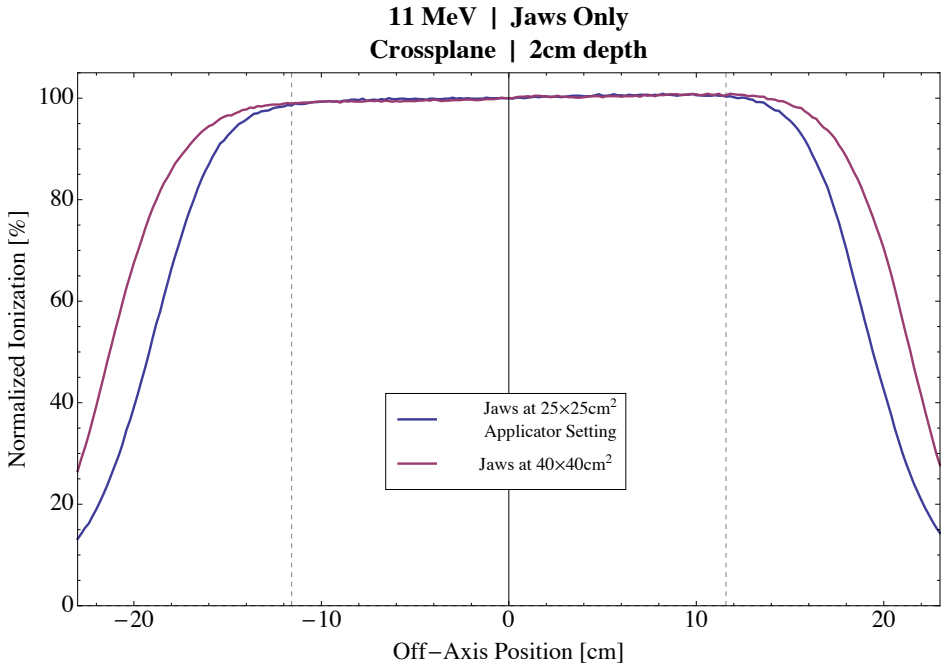

(a)

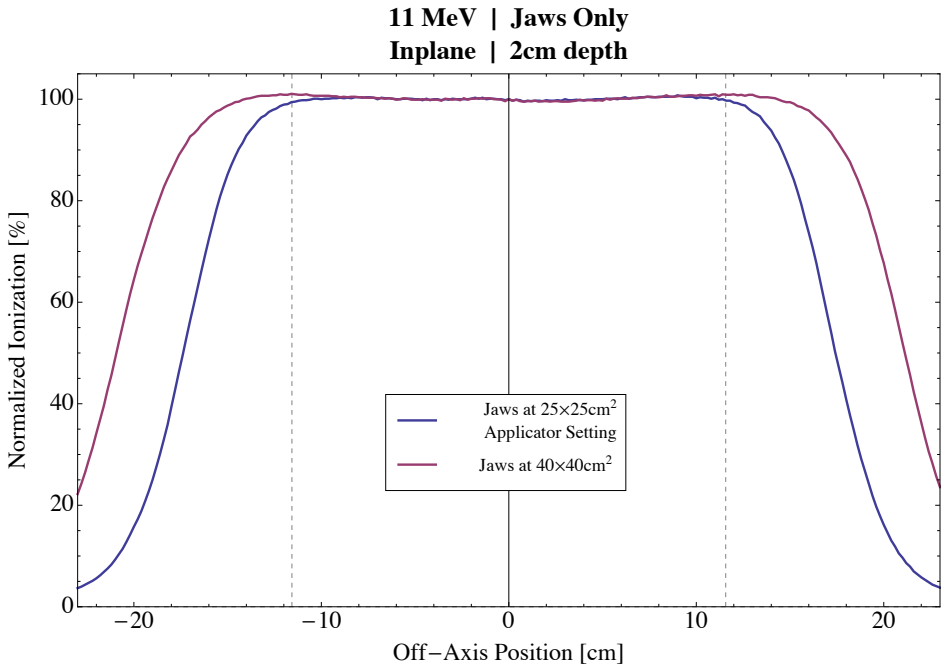

(b)

Figure C.4: Measured profiles for jaws at 40x40cm² and at 25×25cm² applicator settings for 11 MeV (a) crossplane and (b) inplane.

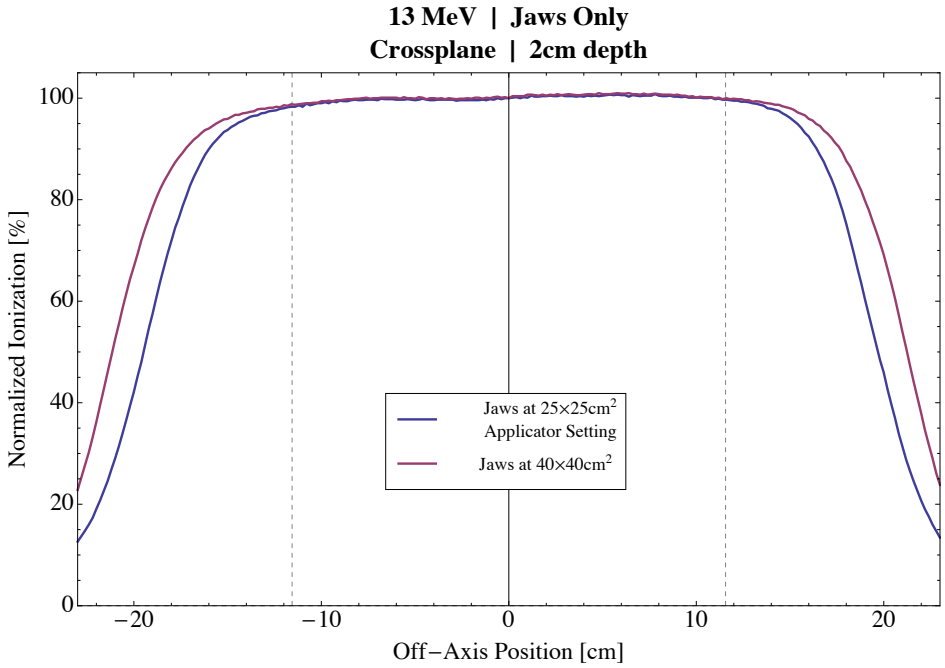

(a)

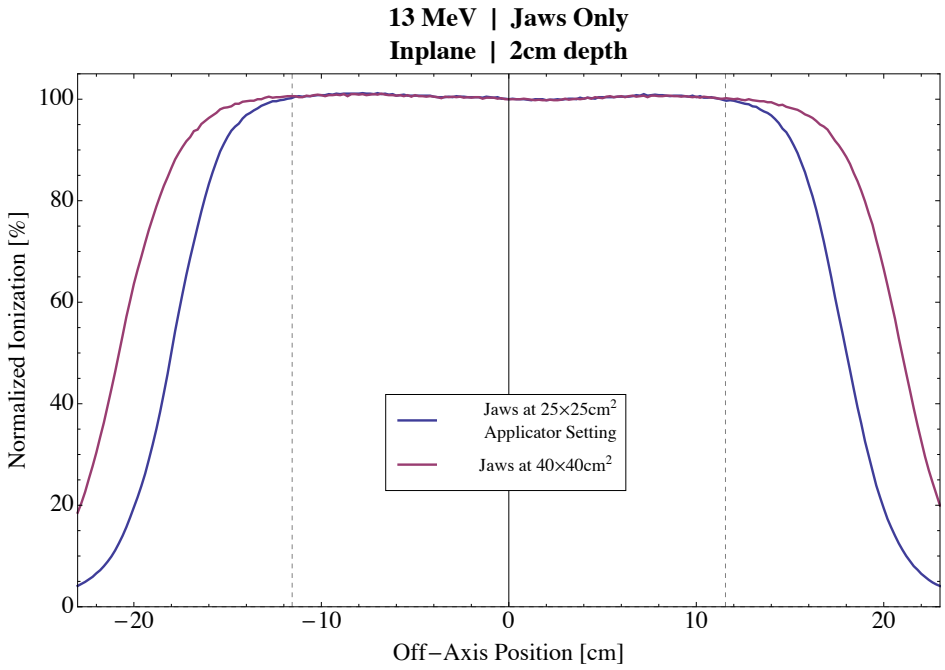

(b)

Figure C.5: Measured profiles for jaws at 40x40cm² and at 25×25cm² applicator settings for 13 MeV (a) crossplane and (b) inplane.

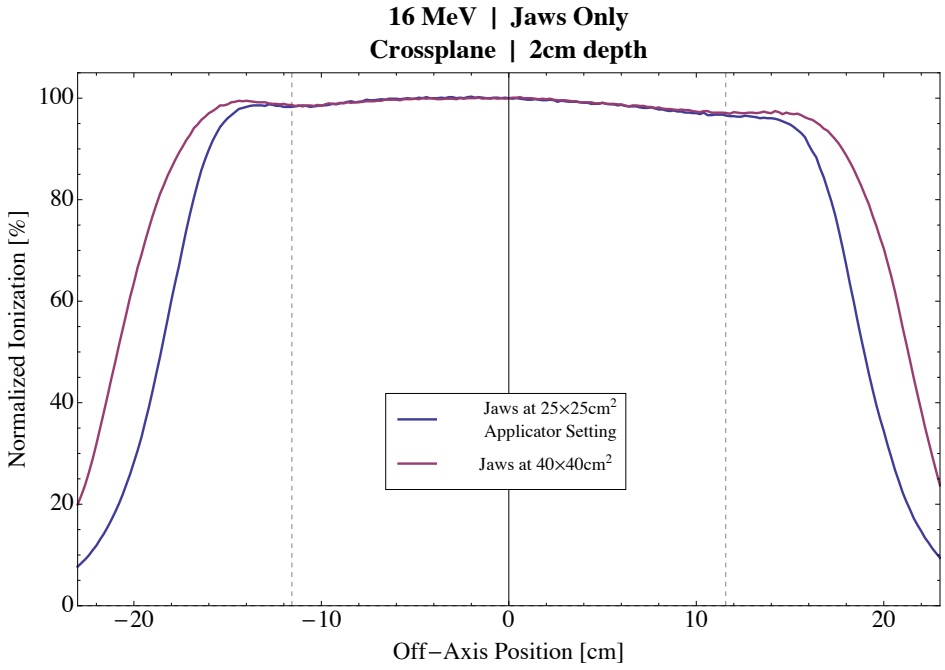

(a)

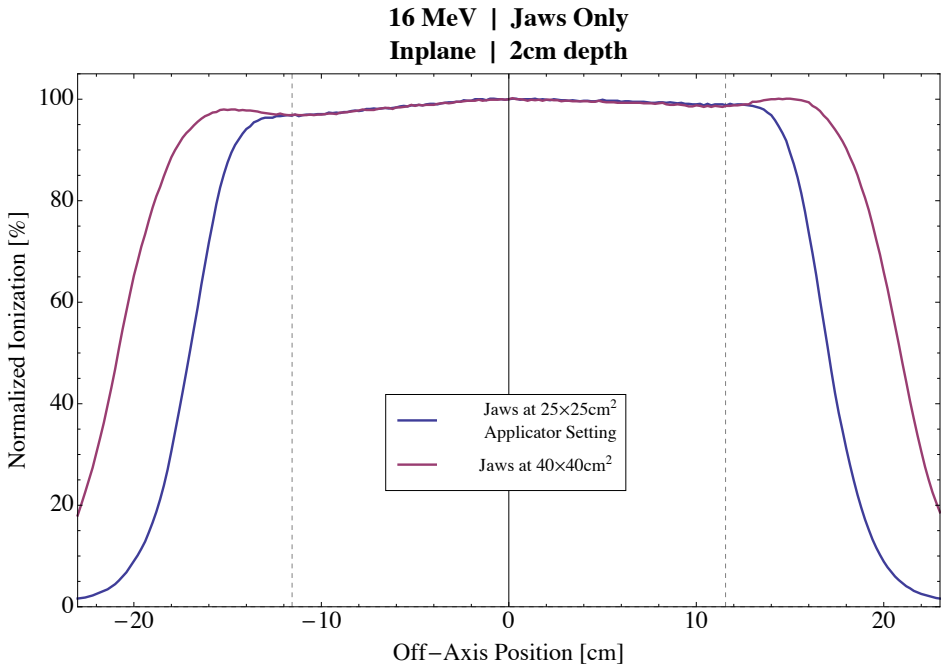

(b)

Figure C.6: Measured profiles for jaws at 40x40cm² and at 25×25cm² applicator settings for 16 MeV (a) crossplane and (b) inplane.

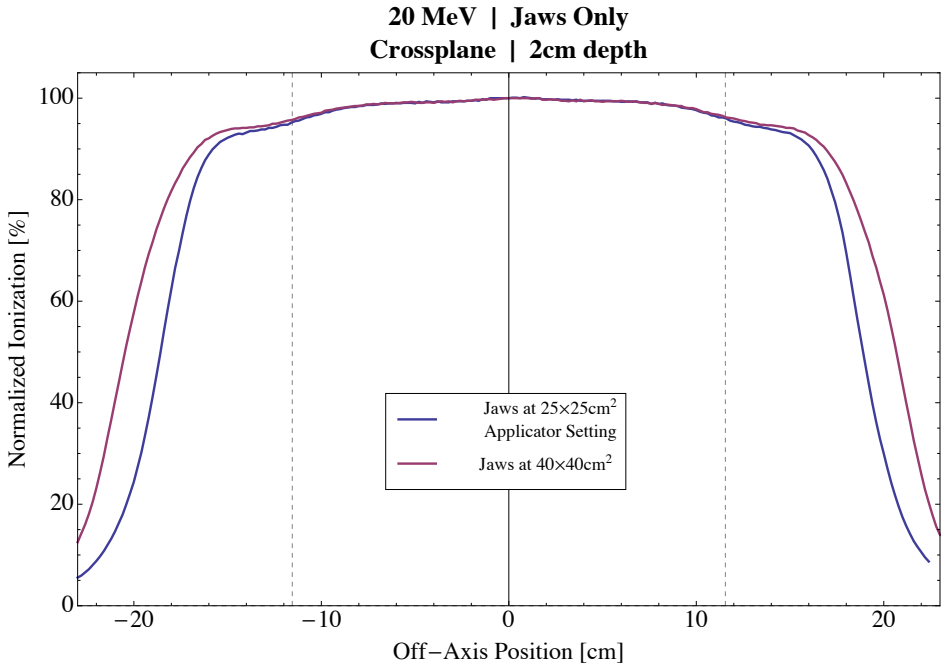

(a)

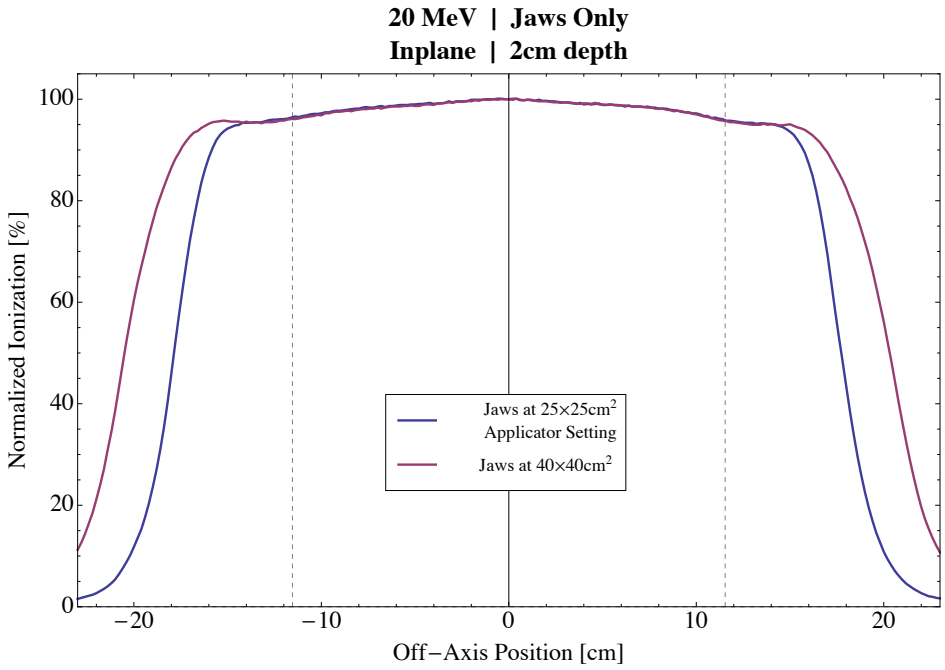

(b)

Figure C.7: Measured profiles for jaws at 40x40cm² and at 25×25cm² applicator settings for 20 MeV (a) crossplane and (b) inplane.

Appendix D: Comparison of measured profiles: (1) x-ray jaws at 40x40cm^2 with (2) x-ray jaws at energy dependent settings for 20x20cm^2 (both with no applicator).

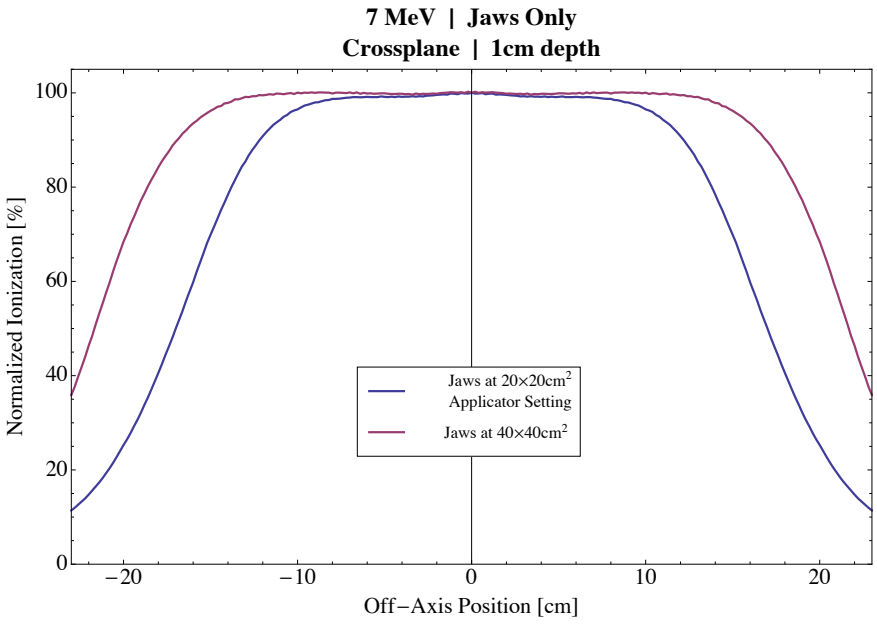

(a)

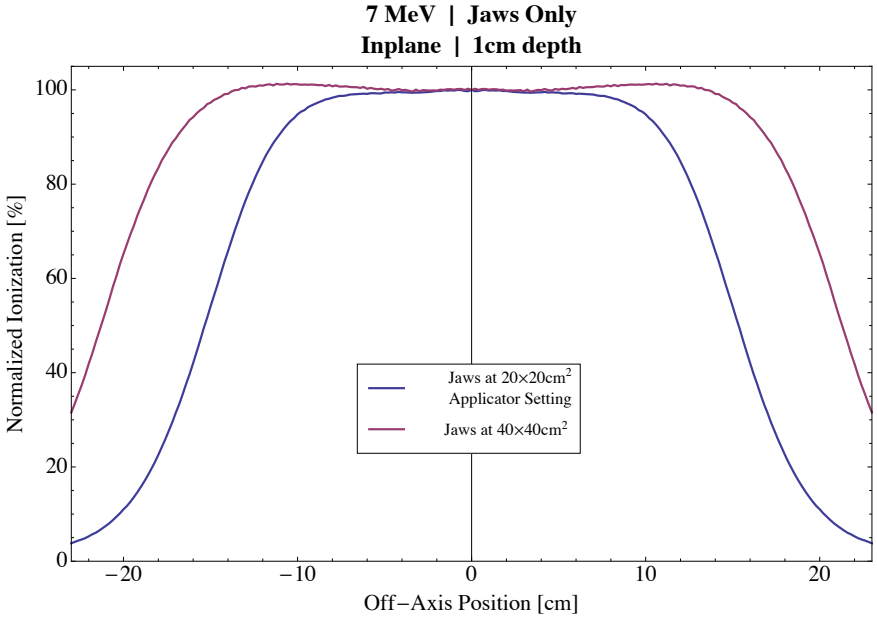

(b)

Figure D.1: Measured profiles for jaws at 40x40cm^2 and at 20x20cm^2 applicator settings for 7 MeV (a) crossplane and (b) inplane.

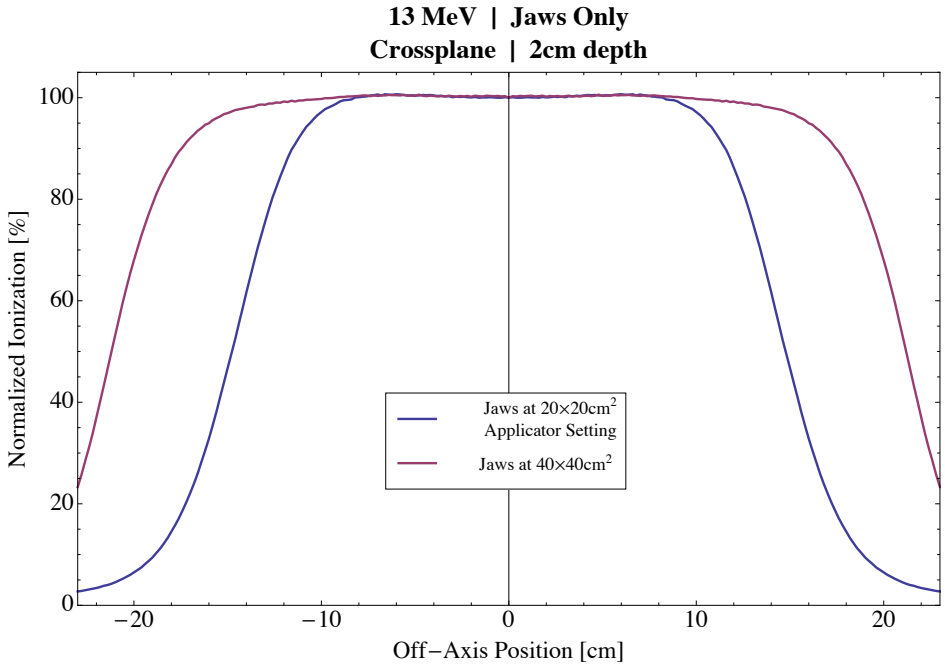

(a)

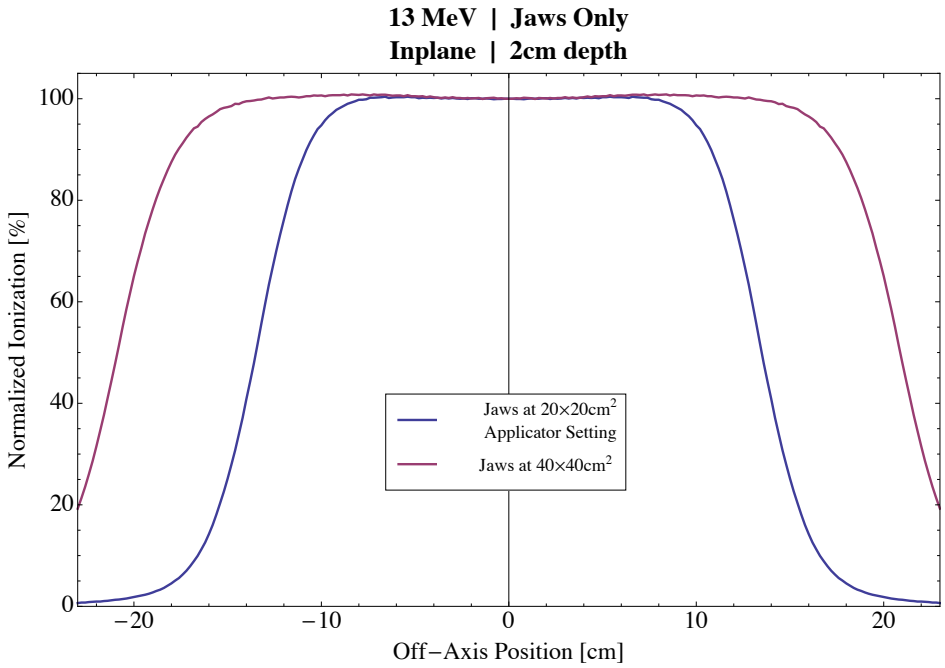

(b)

Figure D.2: Measured profiles for jaws at 40x40cm^2 and at 20x20cm^2 applicator settings for 13 MeV (a) crossplane and (b) inplane.

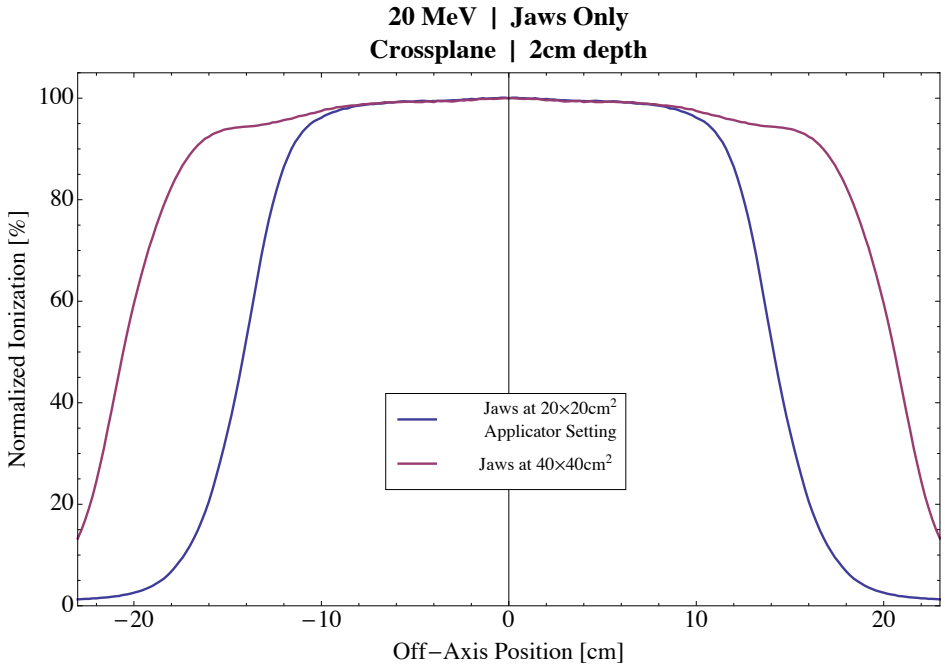

(a)

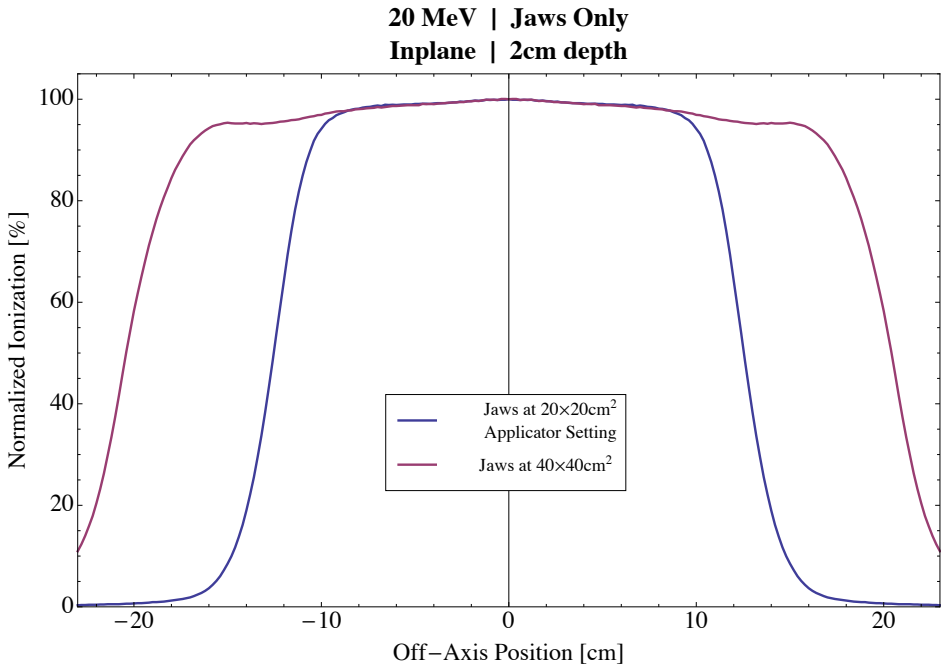

(b)

Figure D.3: Measured profiles for jaws at 40x40cm^2 and at 20x20cm^2 applicator settings for 20 MeV (a) crossplane and (b) inplane.

Appendix E: Comparison of measured profiles: (1) x-ray jaws at 40x40cm^2 with (2) x-ray jaws at energy dependent settings for 10x10cm^2 (both with no applicator).

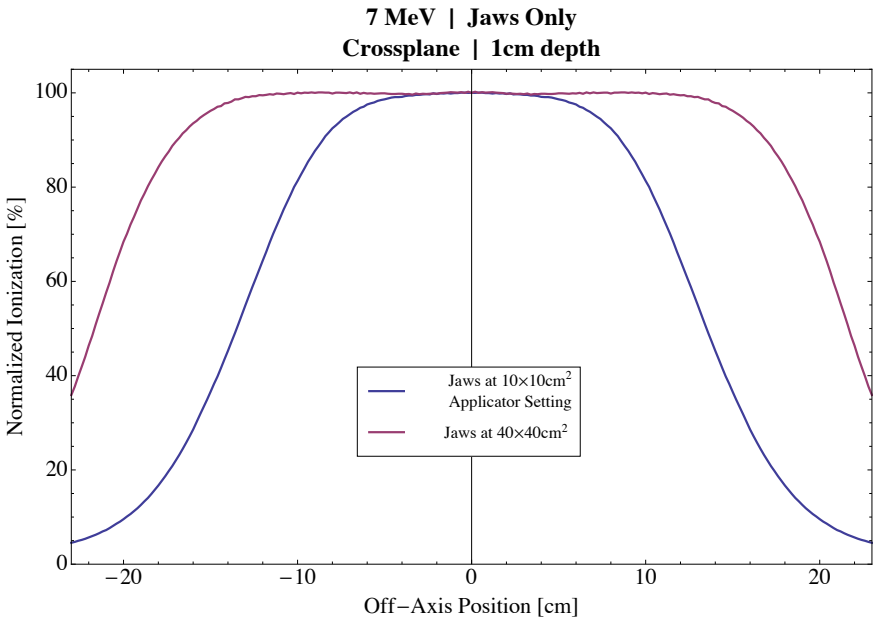

(a)

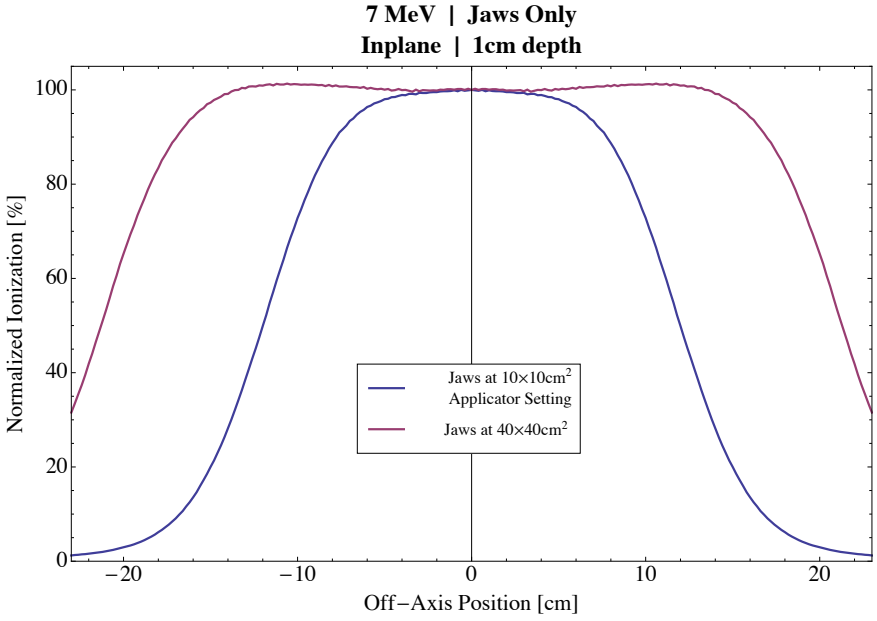

(b)

Figure E.1: Measured profiles for jaws at 40x40cm^2 and at 10x10cm^2 applicator settings for 7 MeV (a) crossplane and (b) inplane.

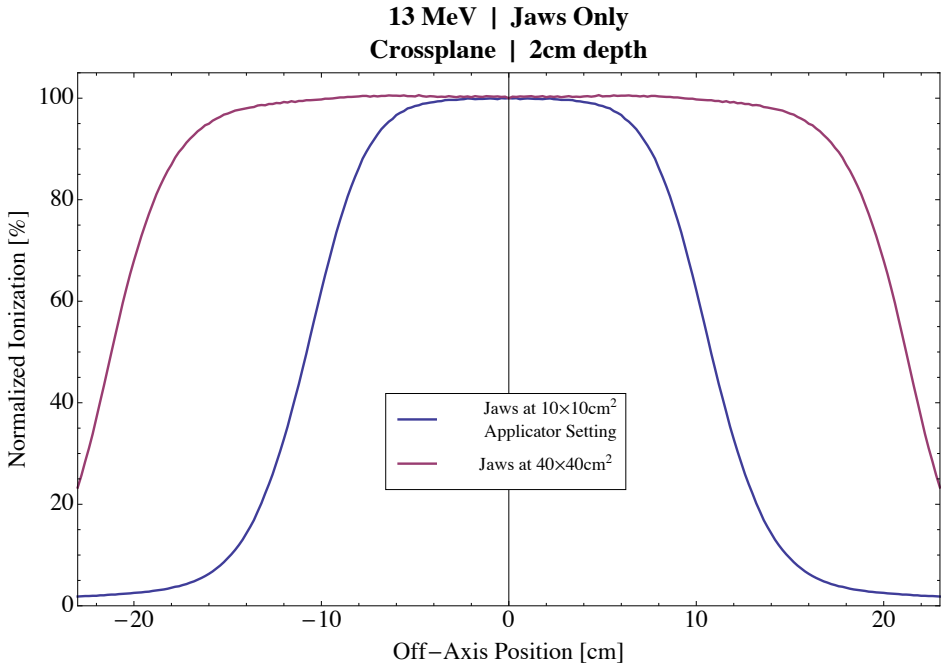

(a)

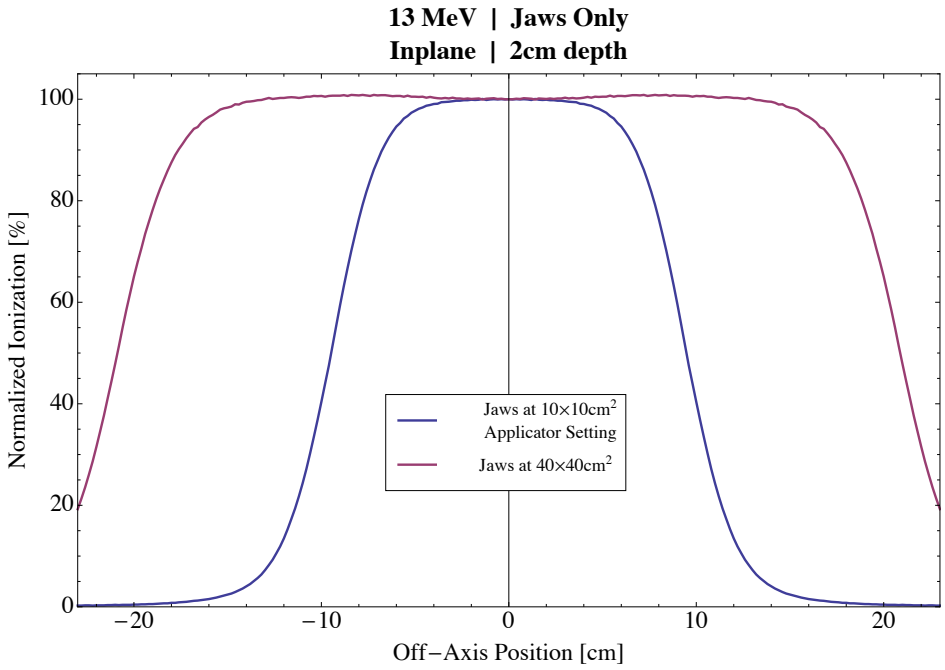

(b)

Figure E.2: Measured profiles for jaws at 40x40cm^2 and at 10x10cm^2 applicator settings for 13 MeV (a) crossplane and (b) inplane.

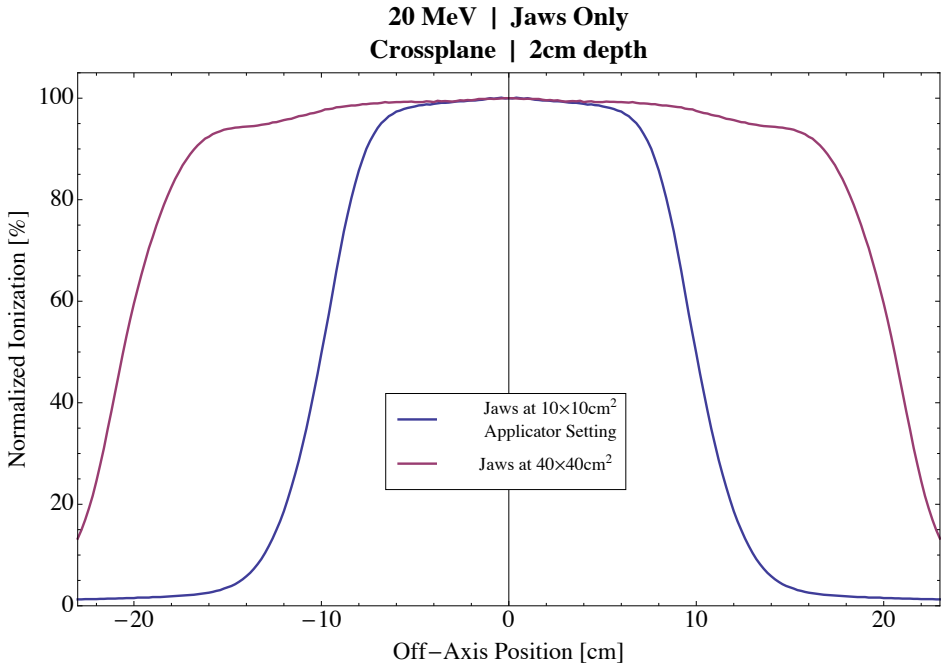

(a)

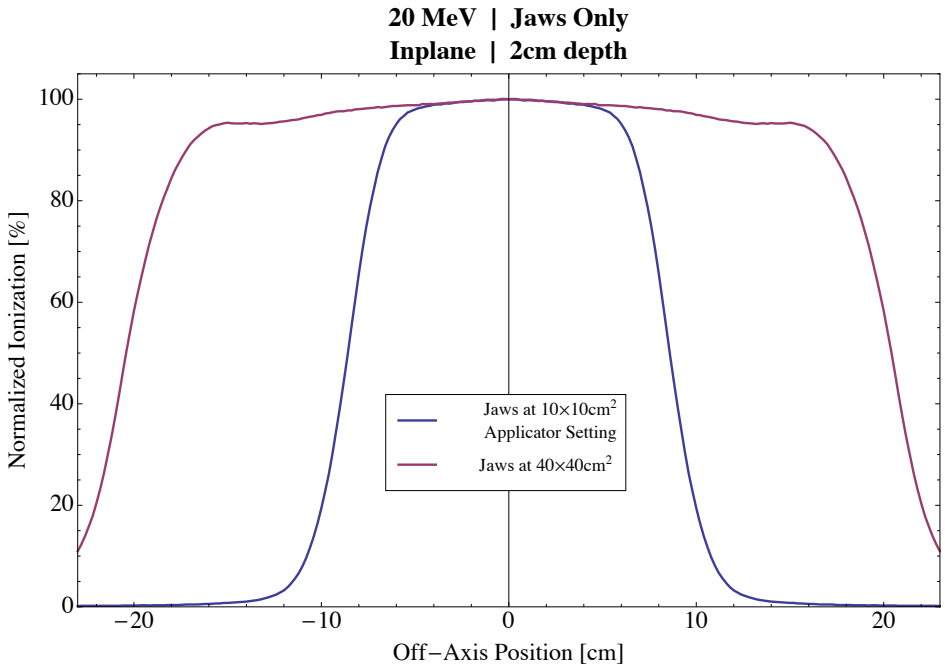

(b)

Figure E.3: Measured profiles for jaws at 40x40cm^2 and at 10x10cm^2 applicator settings for 20 MeV (a) crossplane and (b) inplane.

Appendix F: Measured profiles with jaws at 40x40cm^2 and with 25x25cm^2 applicator.

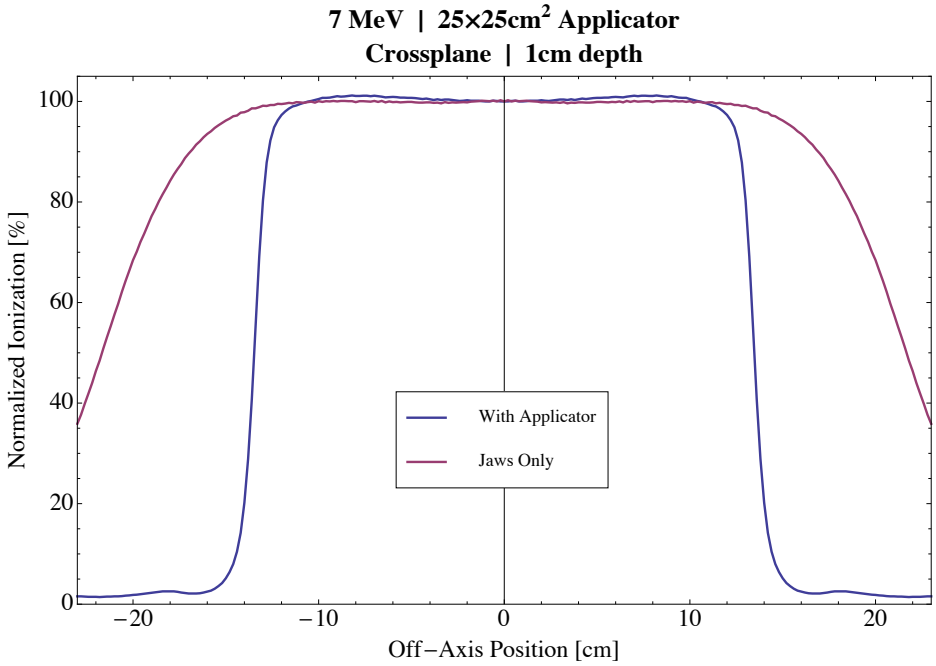

(a)

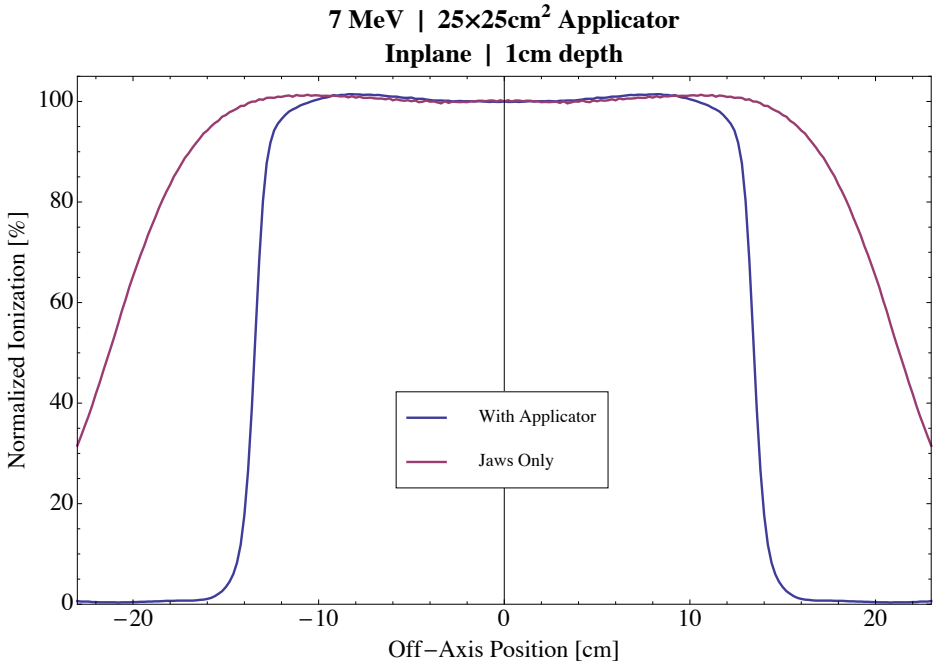

(b)

Figure F.1: Measured profiles for jaws at 40x40cm^2 and with 25×25cm^2 applicator for 7 MeV (a) crossplane and (b) inplane.

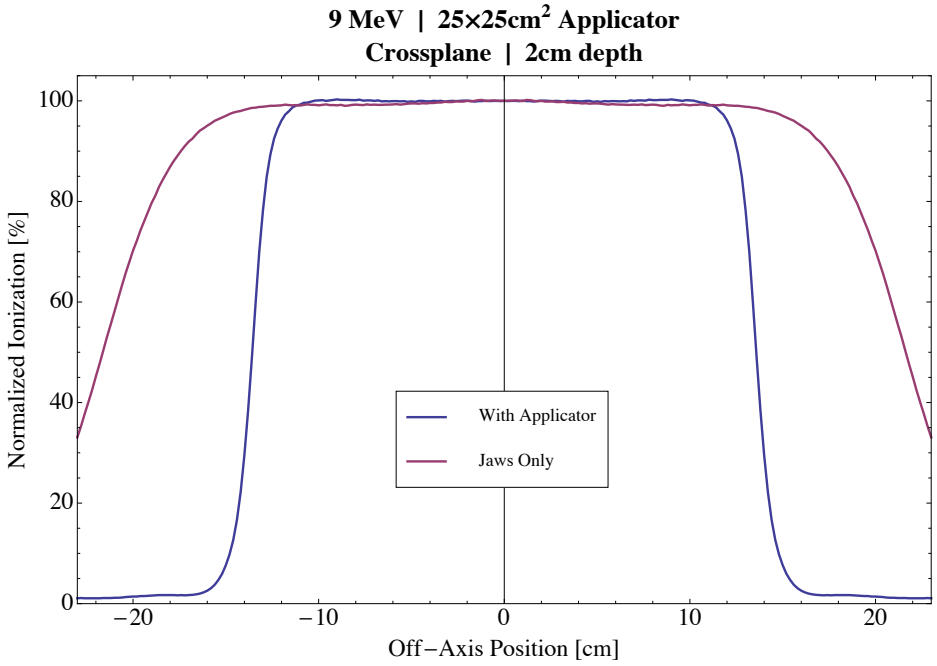

(a)

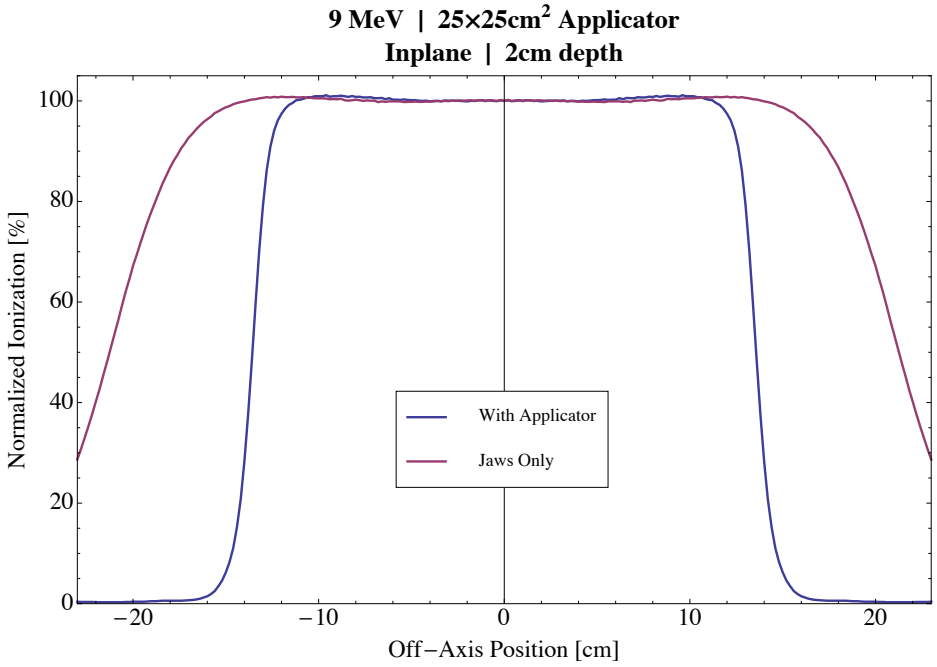

(b)

Figure F.2: Measured profiles for jaws at 40x40cm² and with 25x25cm² applicator for 9 MeV (a) crossplane and (b) inplane.

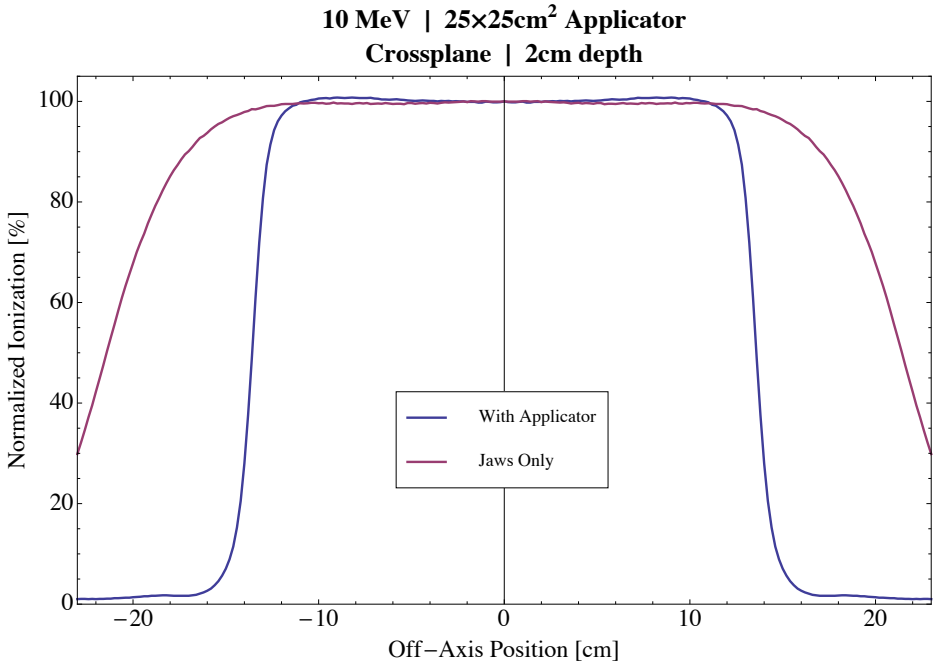

(a)

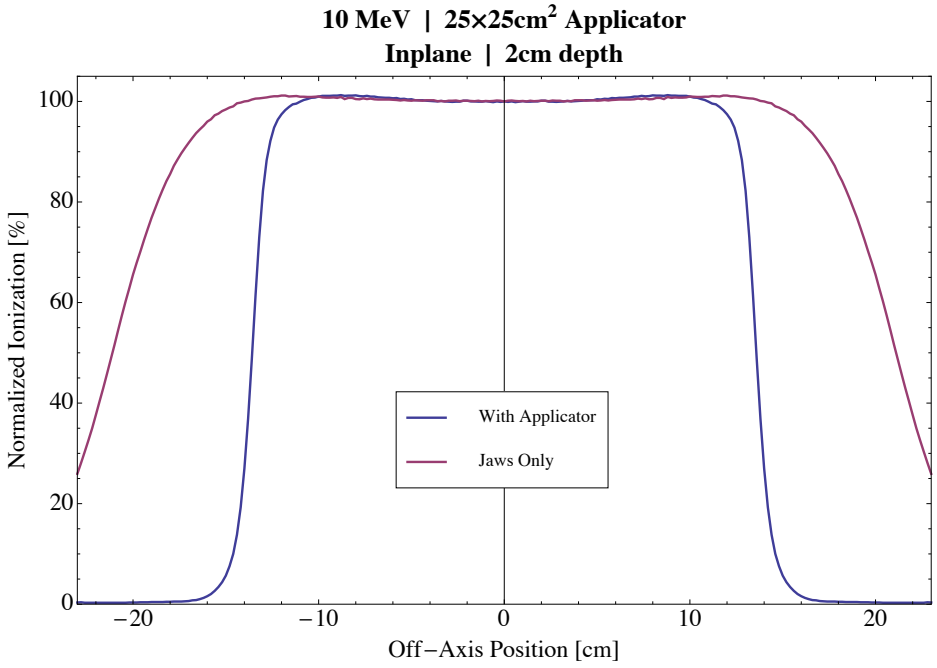

(b)

Figure F.3: Measured profiles for jaws at 40x40cm^2 and with 25x25cm^2 applicator for 10 MeV (a) crossplane and (b) inplane.

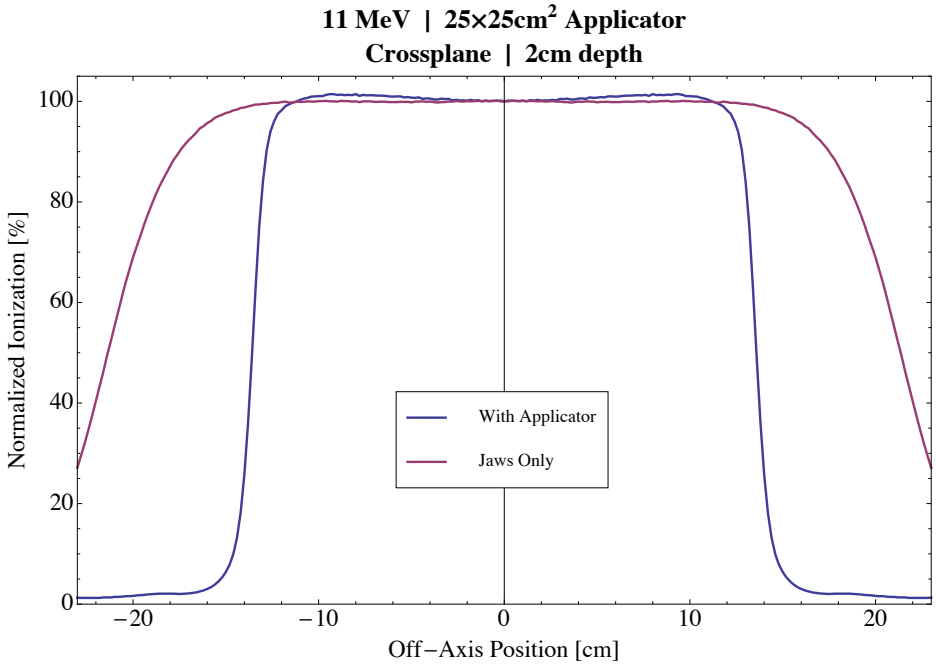

(a)

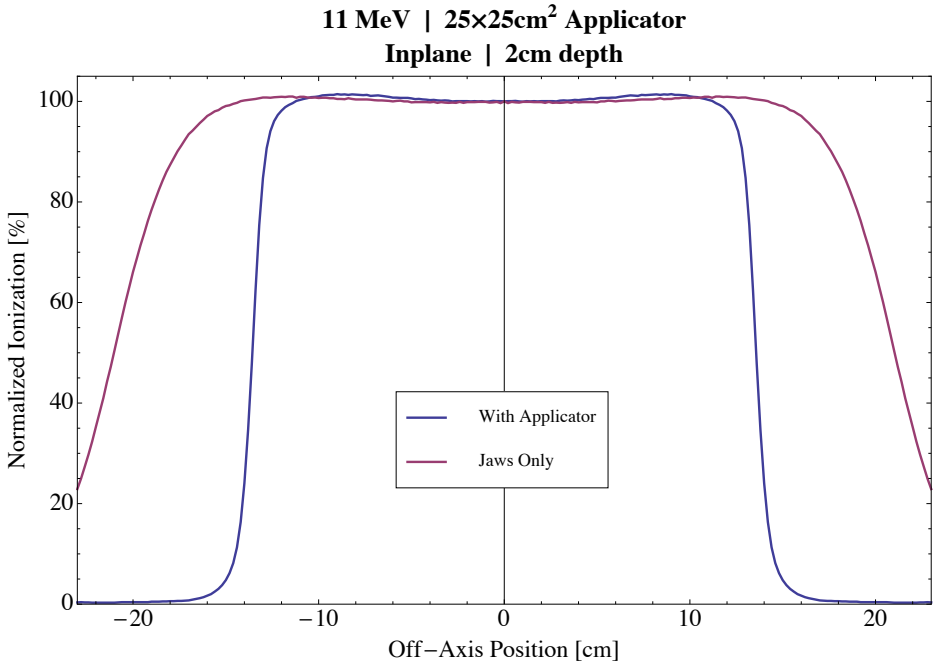

(b)

Figure F.4: Measured profiles for jaws at 40x40cm^2 and with 25x25cm^2 applicator for 11 MeV (a) crossplane and (b) inplane.

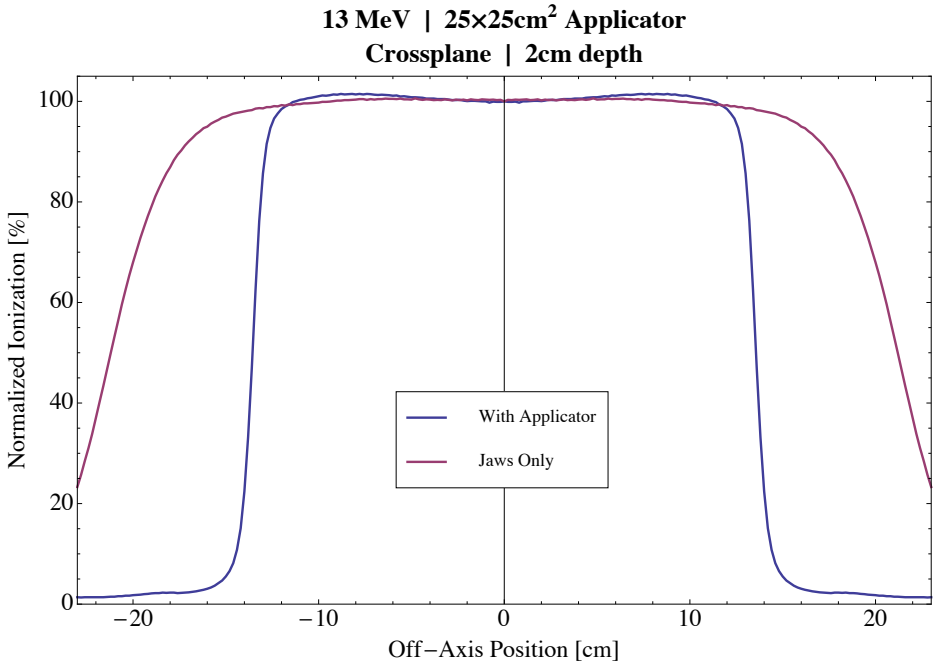

(a)

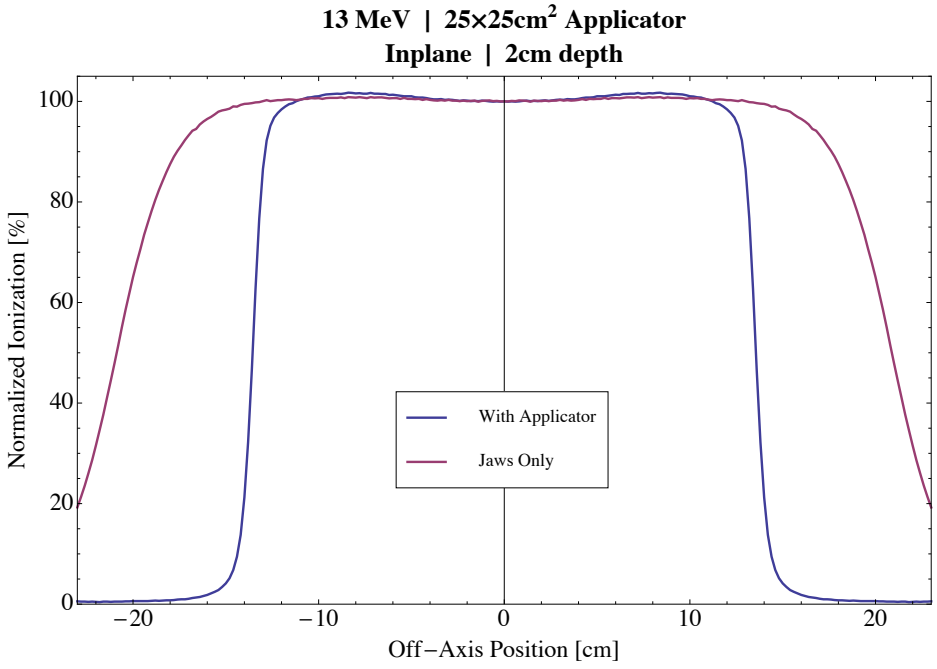

(b)

Figure F.5: Measured profiles for jaws at 40x40cm^2 and with 25x25cm^2 applicator for 13 MeV (a) crossplane and (b) inplane.

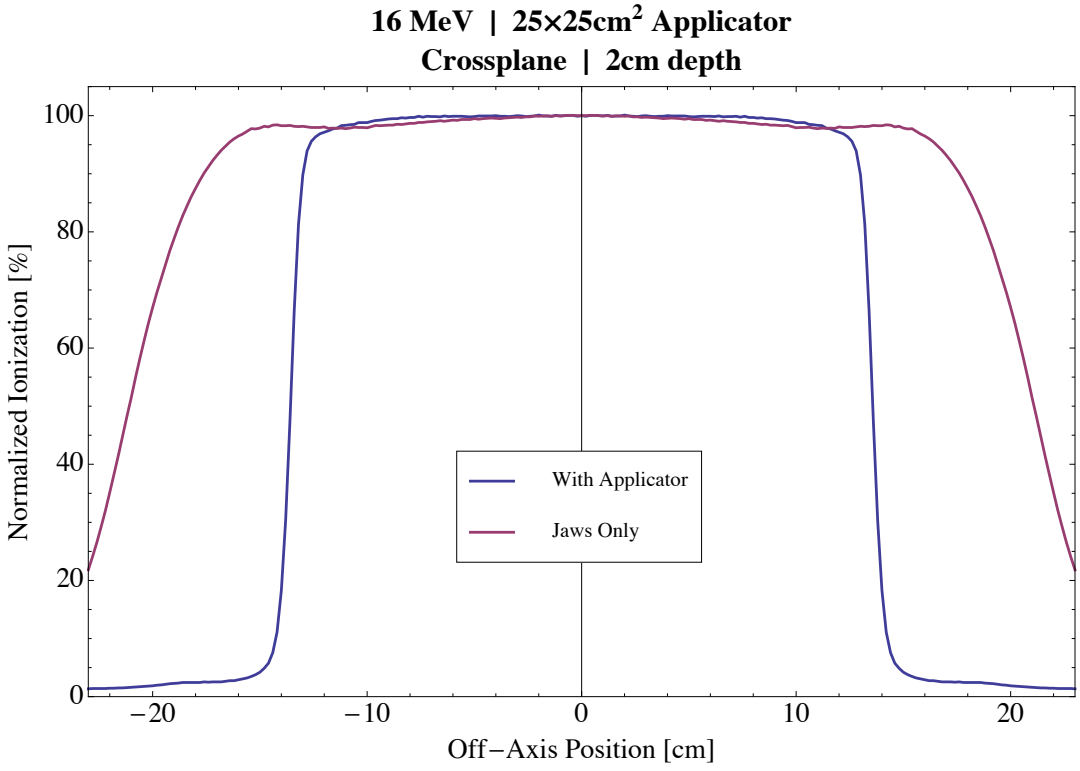

(a)

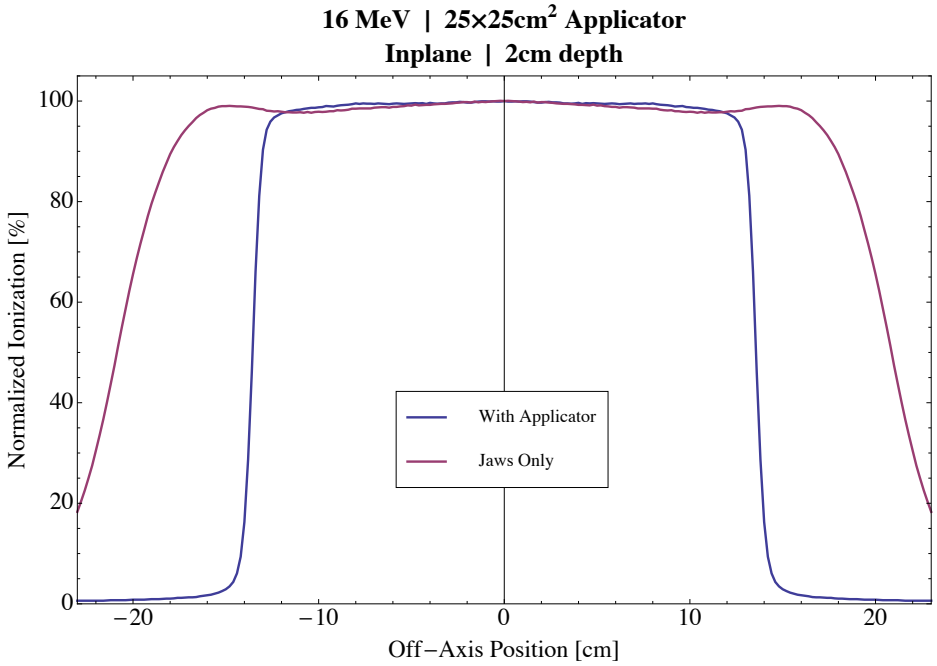

(b)

Figure F.6: Measured profiles for jaws at 40x40cm² and with 25x25cm² applicator for 16 MeV (a) crossplane and (b) inplane.

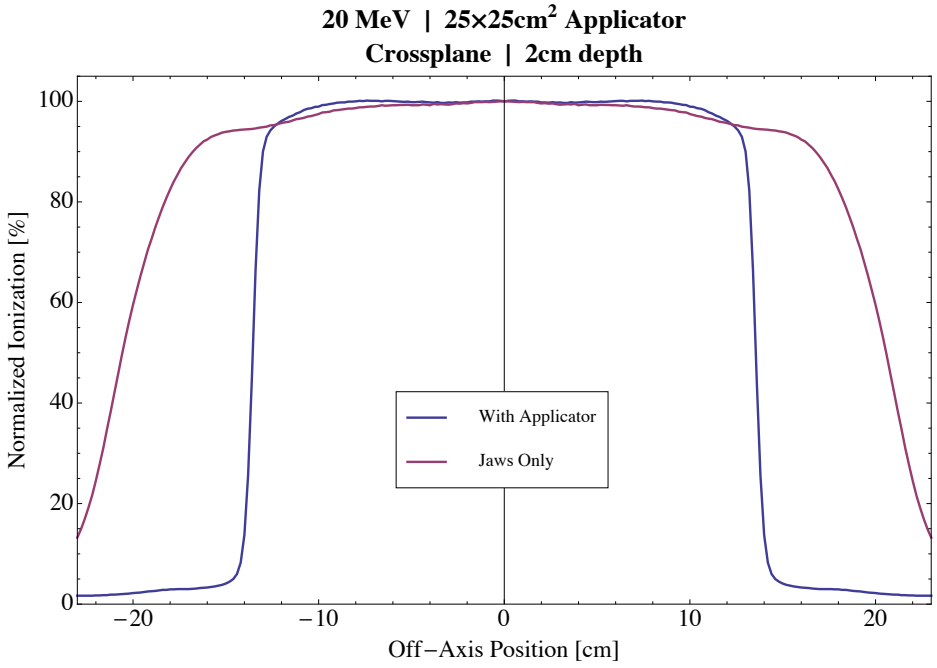

(a)

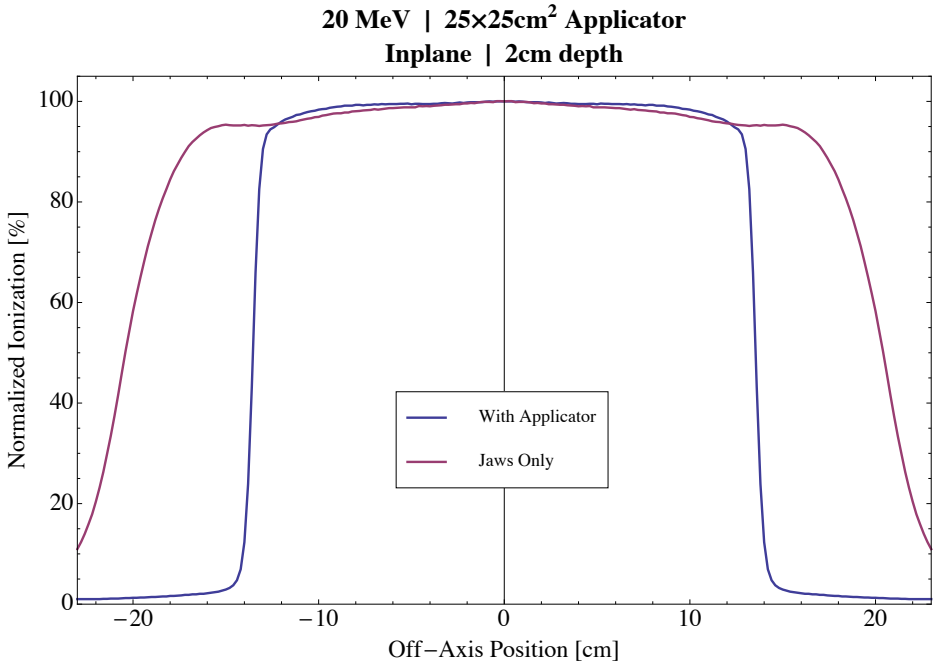

(b)

Figure F.7: Measured profiles for jaws at 40x40cm^2 and with 25×25cm^2 applicator for 20 MeV (a) crossplane and (b) inplane.

Appendix G: Measured profiles with jaws at 40x40cm^2 and with 20x20cm^2 applicator.

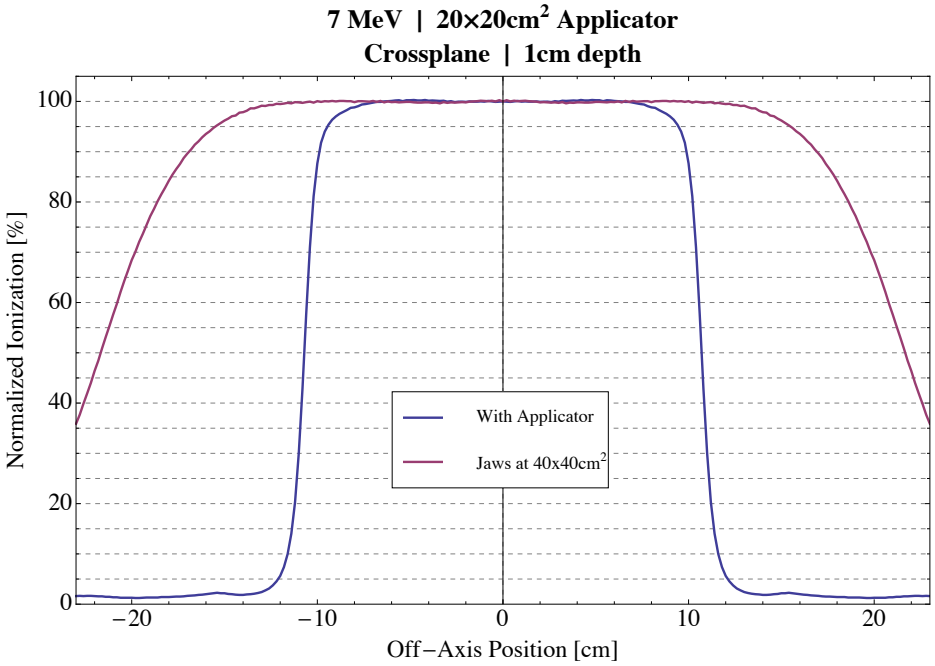

(a)

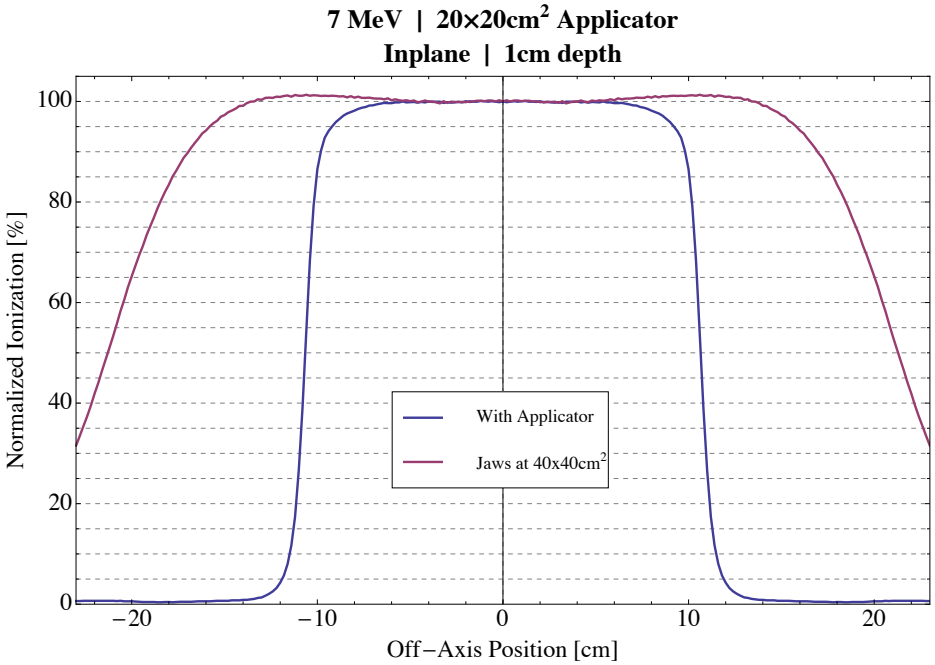

(b)

Figure G.1: Measured profiles for jaws at 40x40cm^2 and with 20x20cm^2 applicator for 7 MeV (a) crossplane and (b) inplane.

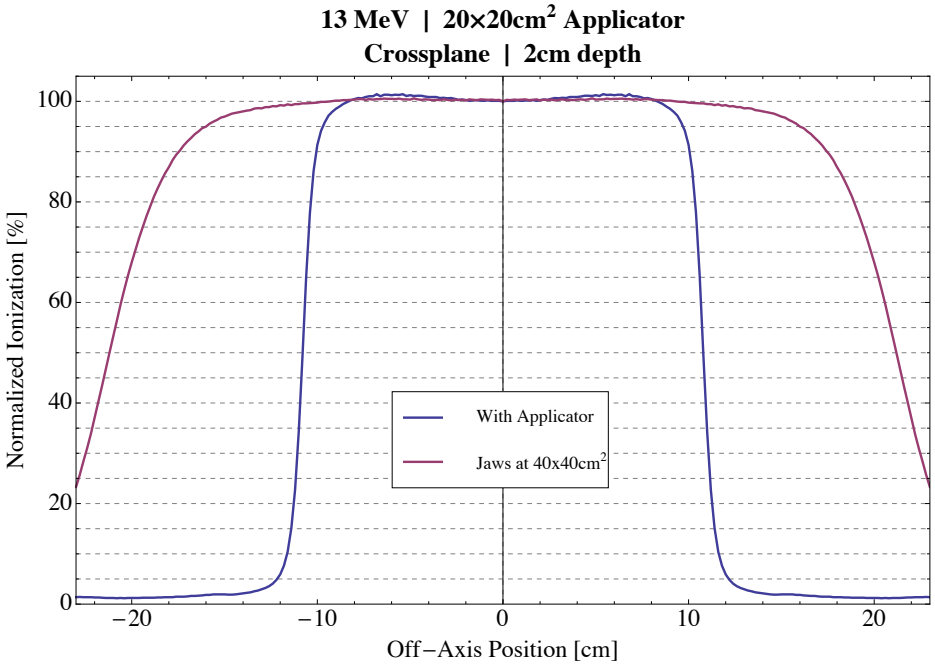

(a)

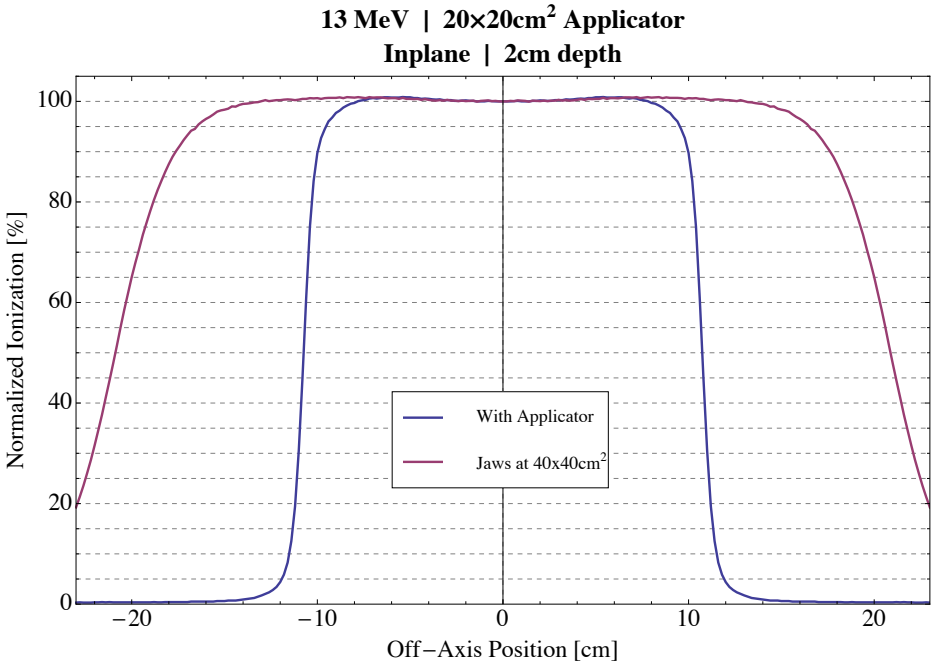

(b)

Figure G.2: Measured profiles for jaws at 40x40cm^2 and with 20x20cm^2 applicator for 13 MeV (a) crossplane and (b) inplane.

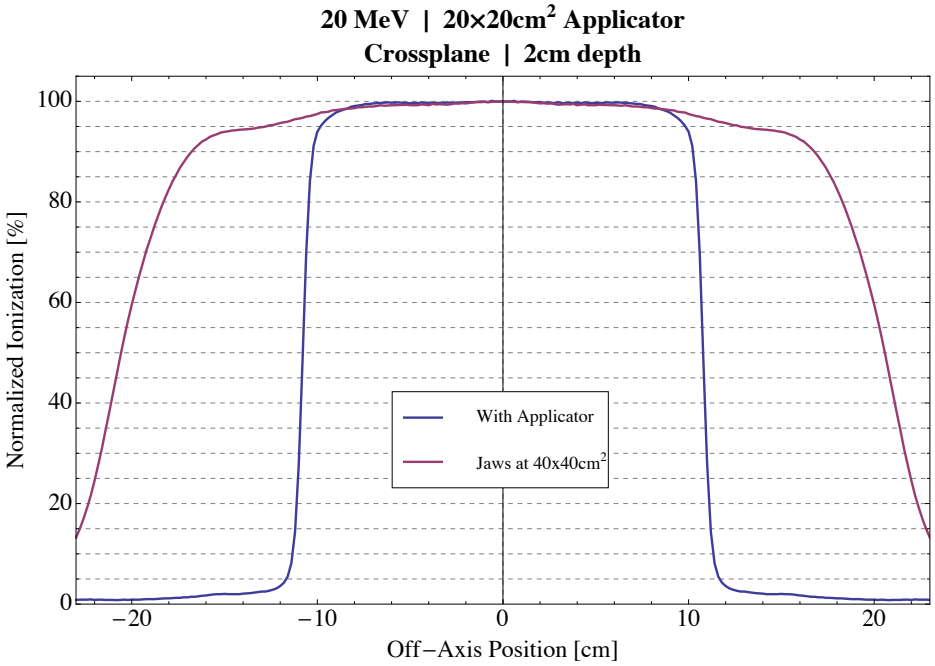

(a)

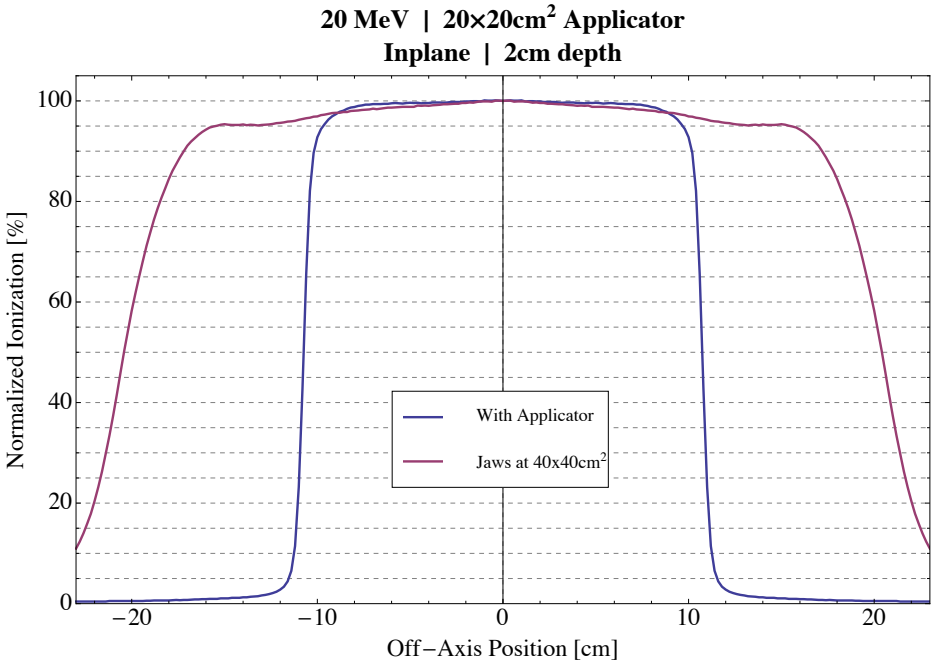

(b)

Figure G.3: Measured profiles for jaws at 40x40cm² and with 20x20cm² applicator for 20 MeV (a) crossplane and (b) inplane.

Appendix H: Measured profiles with jaws at 40x40cm^2 and with 10x10cm^2 applicator.

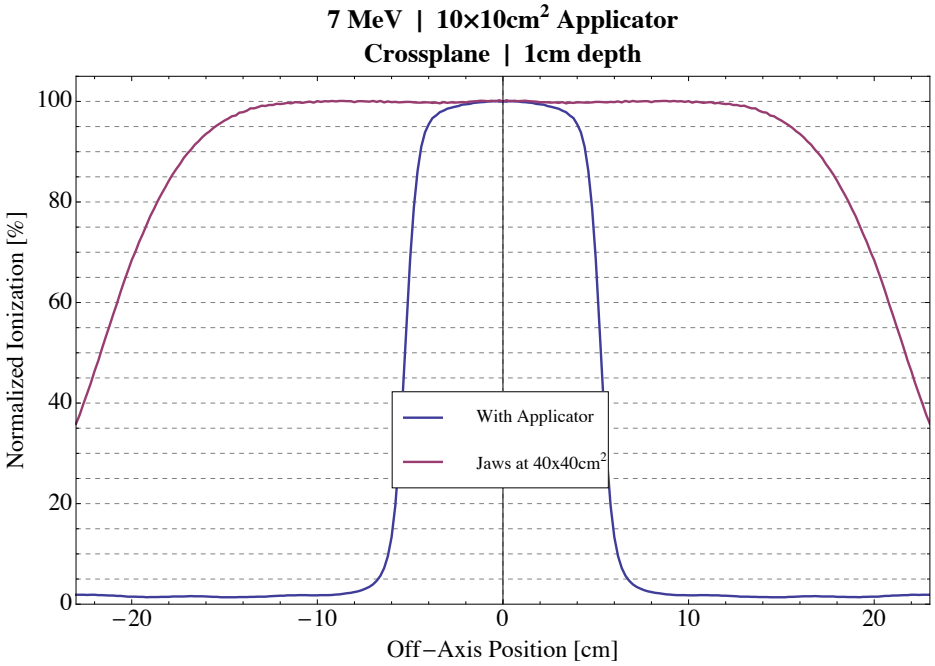

(a)

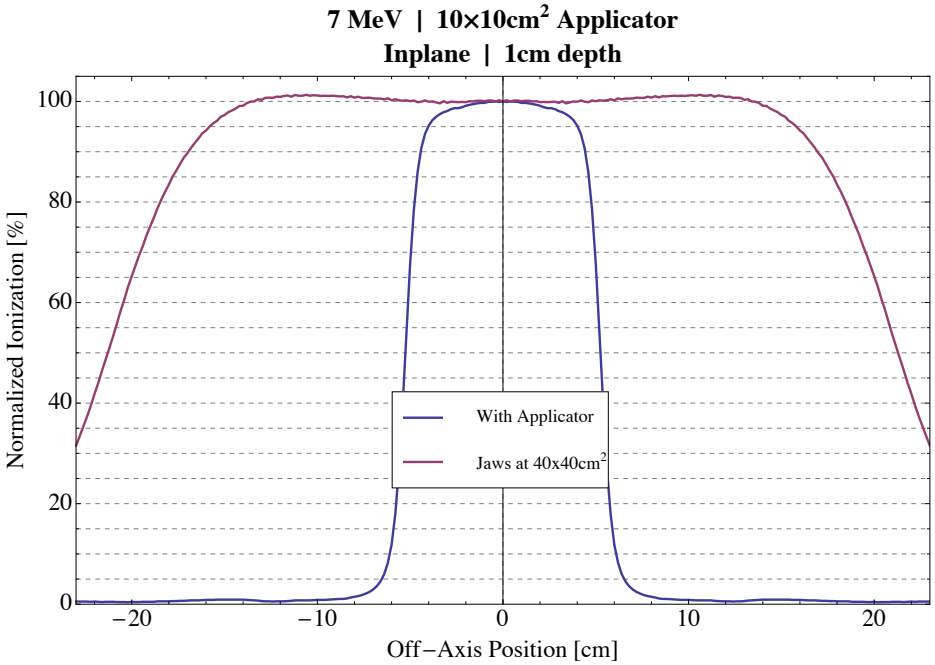

(b)

Figure H.1: Measured profiles for jaws at 40x40cm^2 and with 10x10cm^2 applicator for 7 MeV (a) crossplane and (b) inplane.

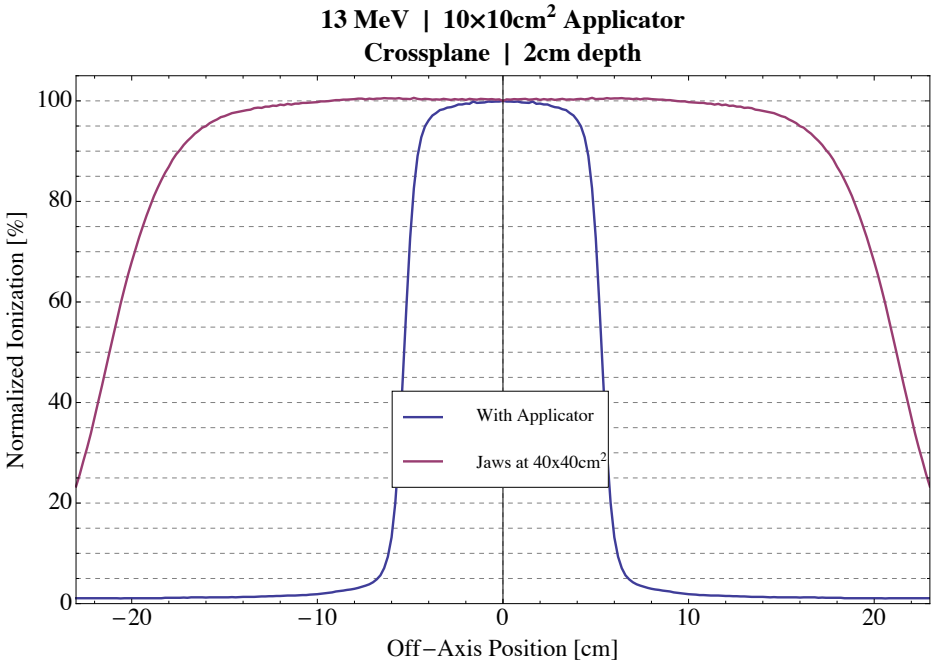

(a)

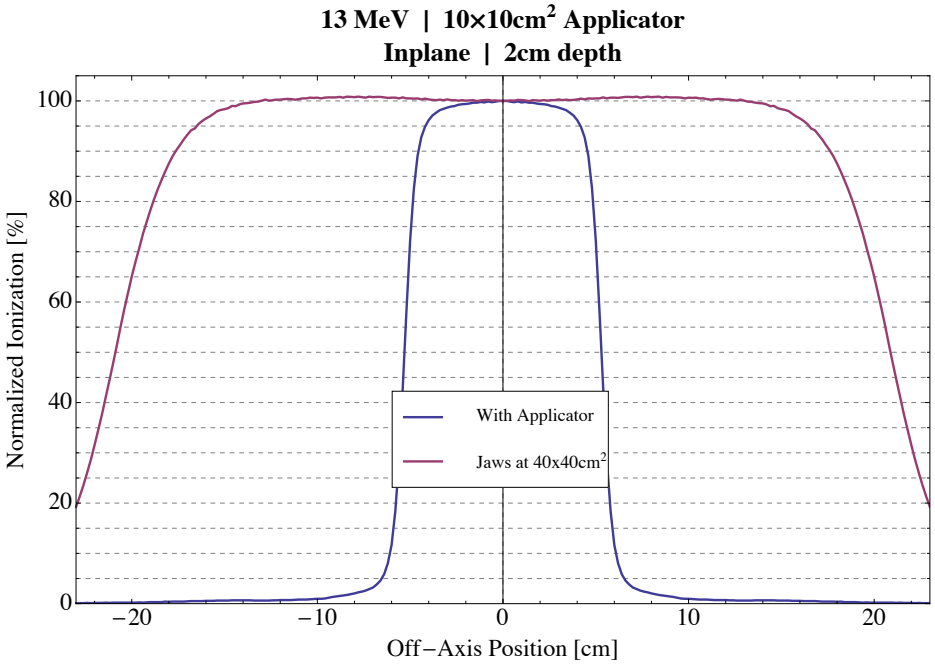

(b)

Figure H.2: Measured profiles for jaws at 40x40cm² and with 10x10cm² applicator for 13 MeV (a) crossplane and (b) inplane.

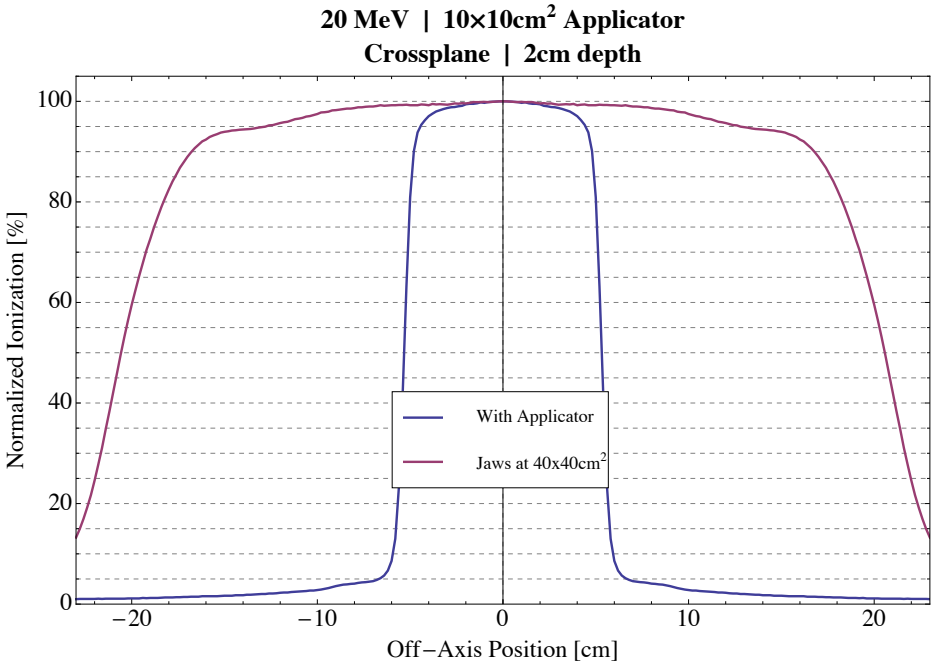

(a)

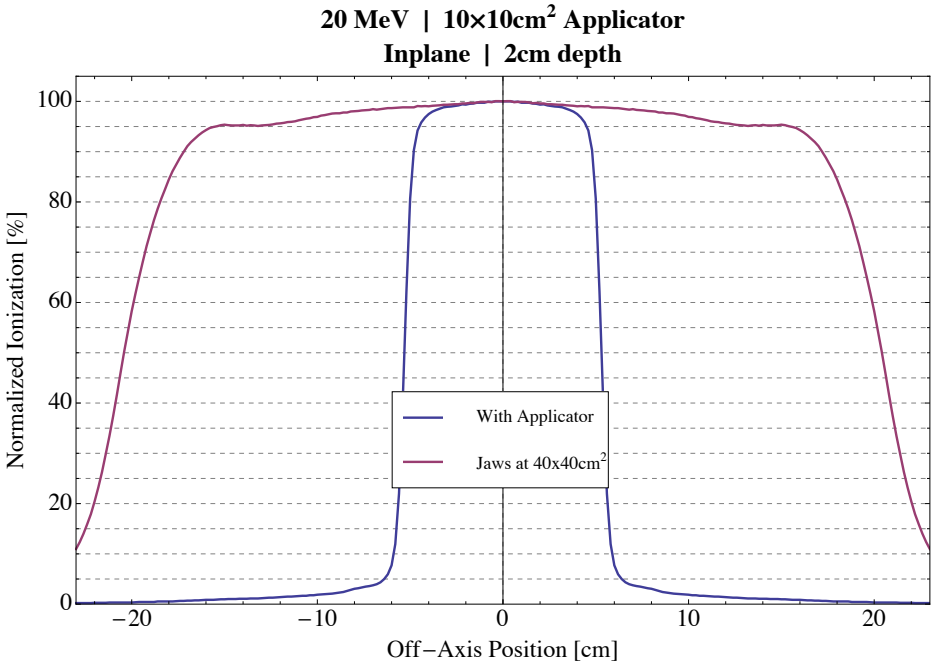

(b)

Figure H.3: Measured profiles for jaws at 40x40cm² and with 10x10cm² applicator for 20 MeV (a) crossplane and (b) inplane.

Appendix I: Transverse profiles of Monte Carlo dose calculations for objective profile refinement.

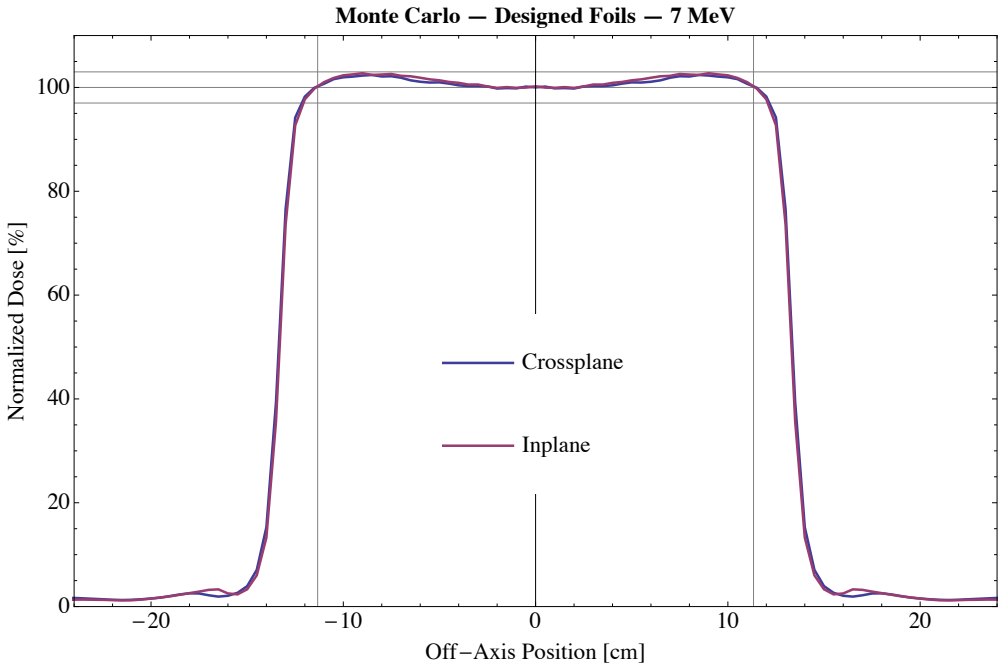

Figure I.1: Transverse profiles for 7 MeV.

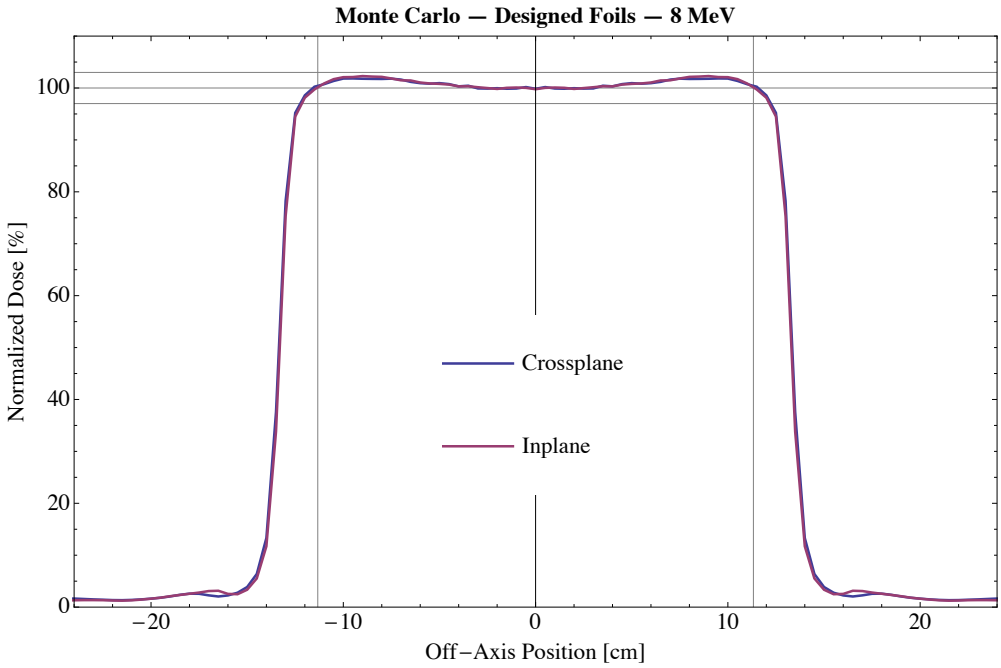

Figure I.2: Transverse profiles for 8 MeV.

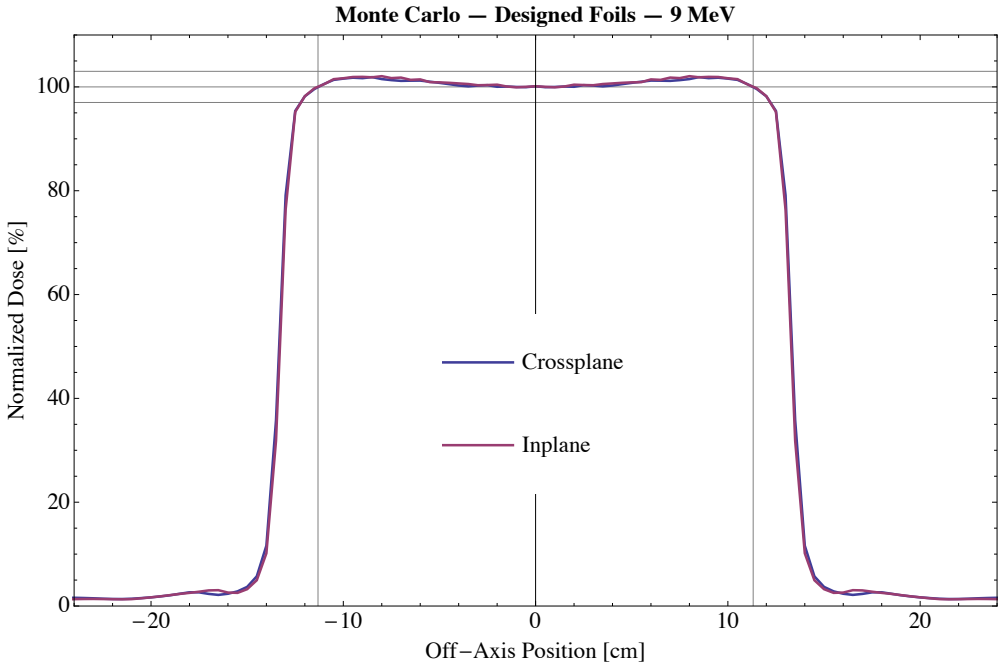

Figure I.3: Transverse profiles for 9 MeV.

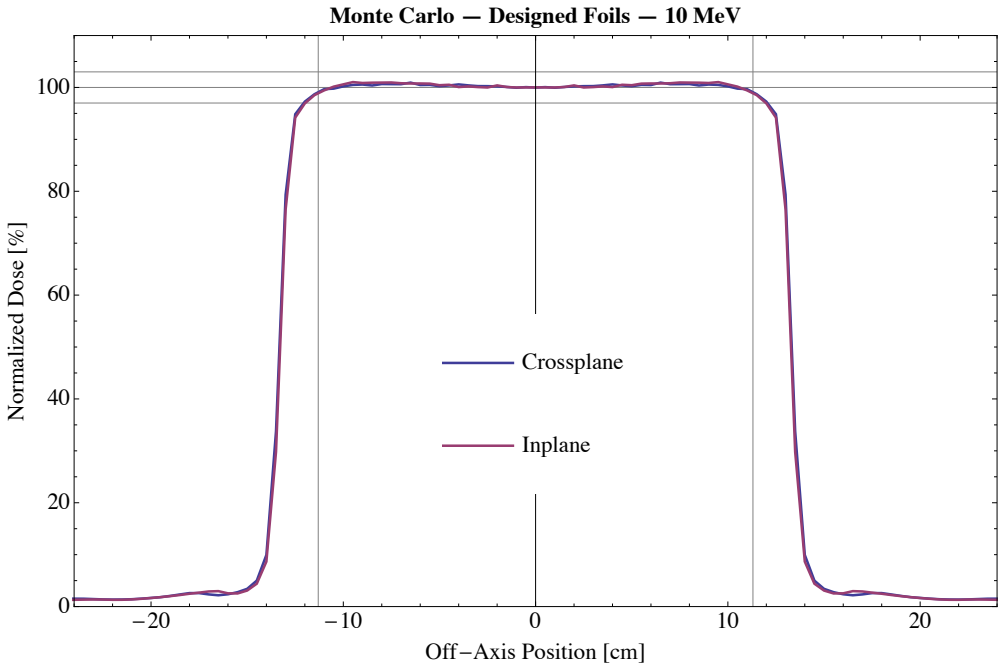

Figure I.4: Transverse profiles for 10MeV.

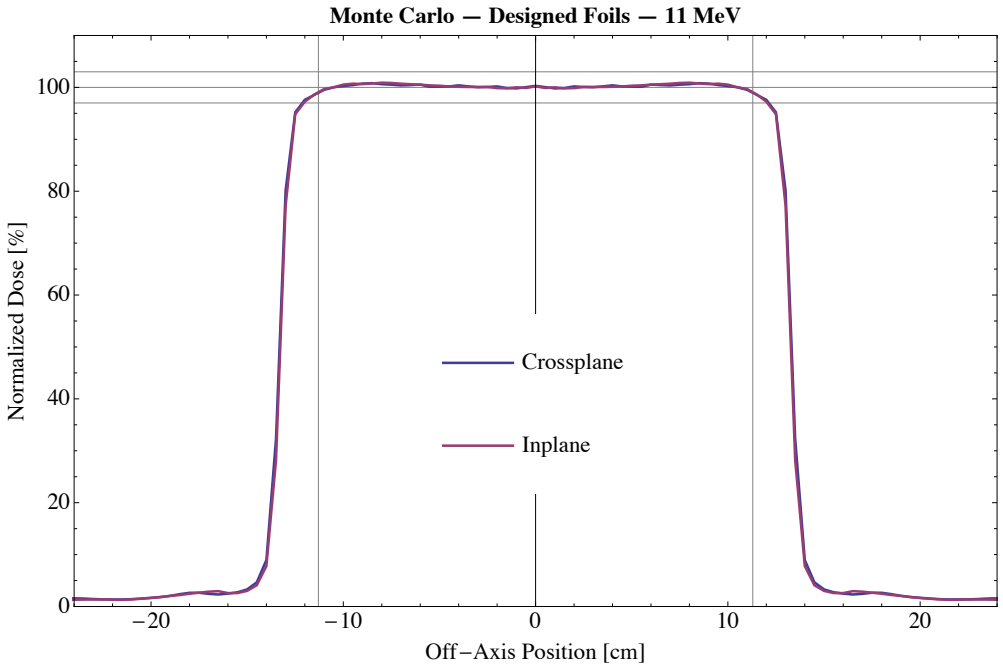

Figure I.5: Transverse profiles for 11 MeV.

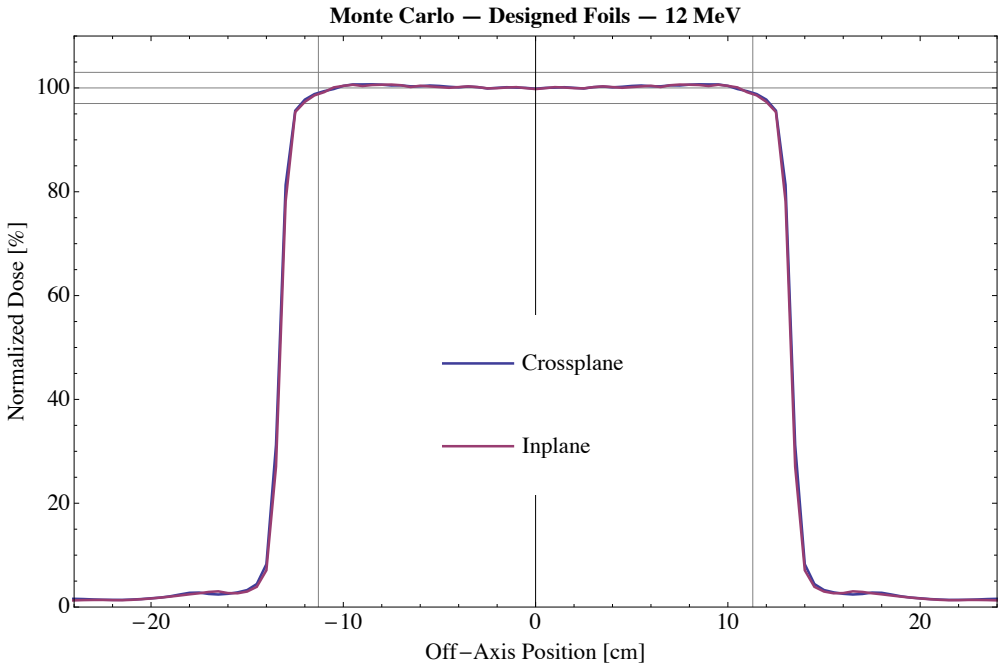

Figure I.6: Transverse profiles for 12 MeV.

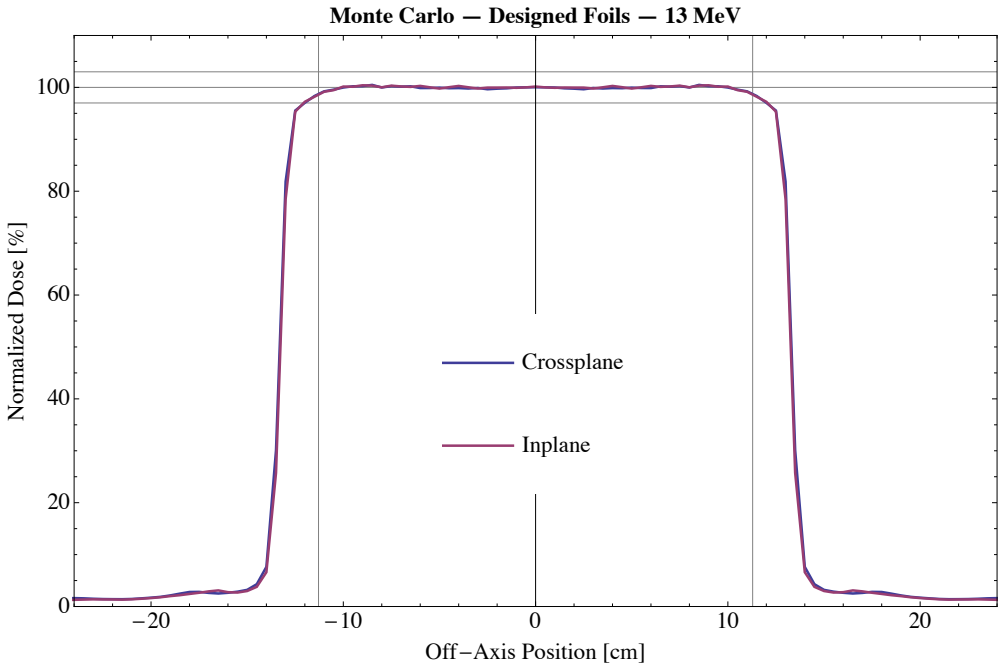

Figure I.7: Transverse profiles for 13 MeV.

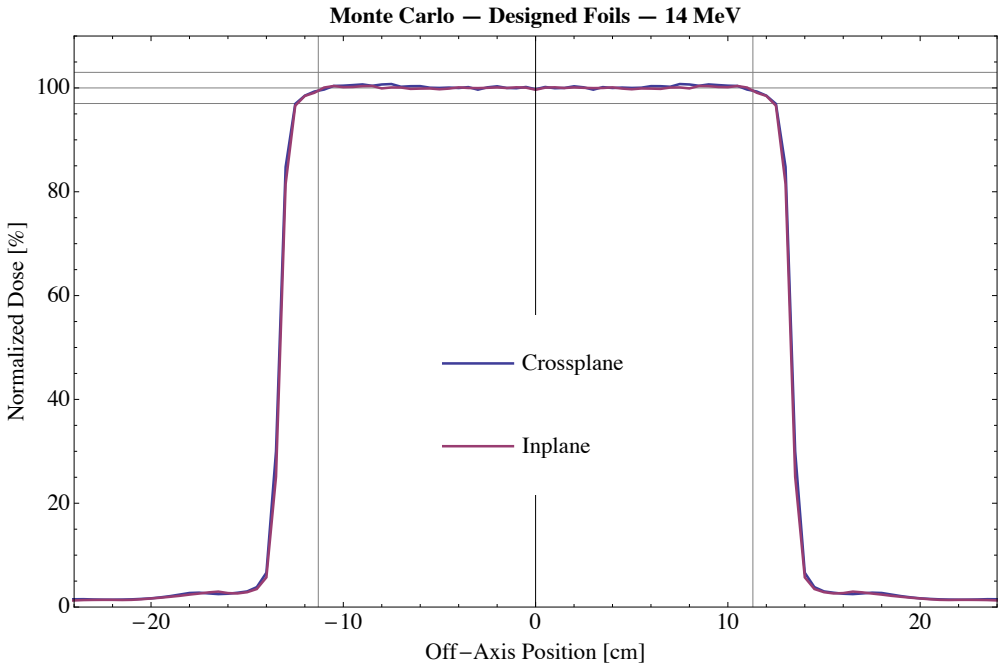

Figure I.8: Transverse profiles for 14 MeV.

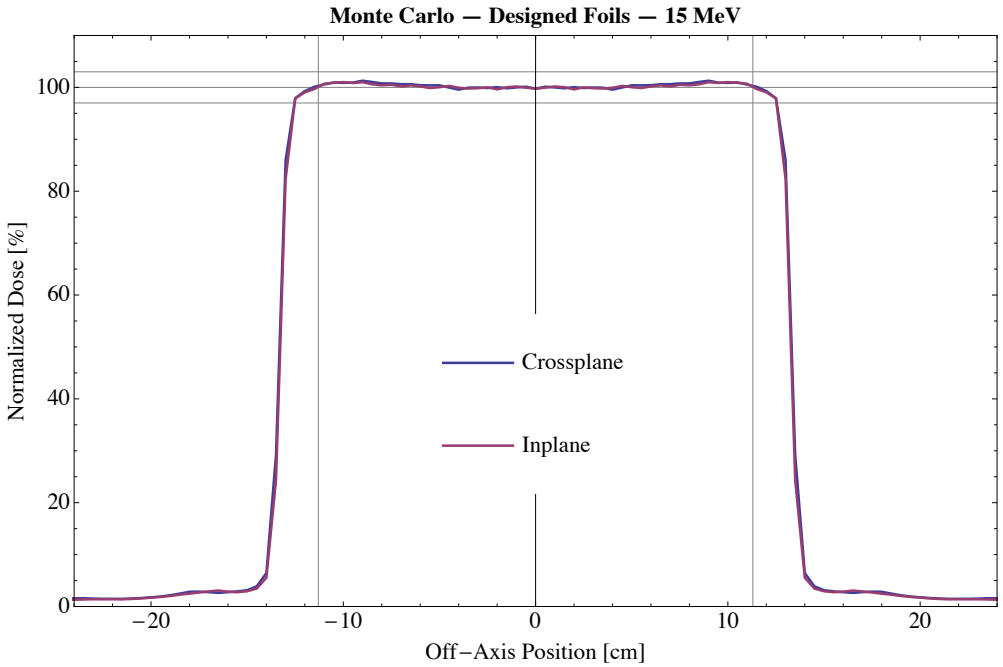

Figure I.9: Transverse profiles for 15 MeV.

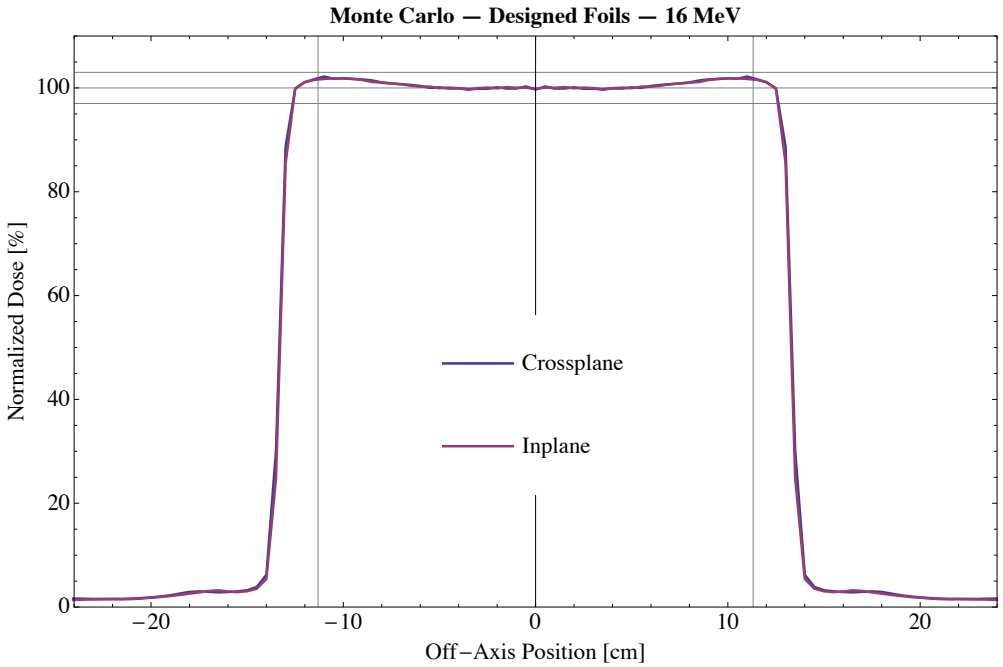

Figure I.10: Transverse profiles for 16 MeV.

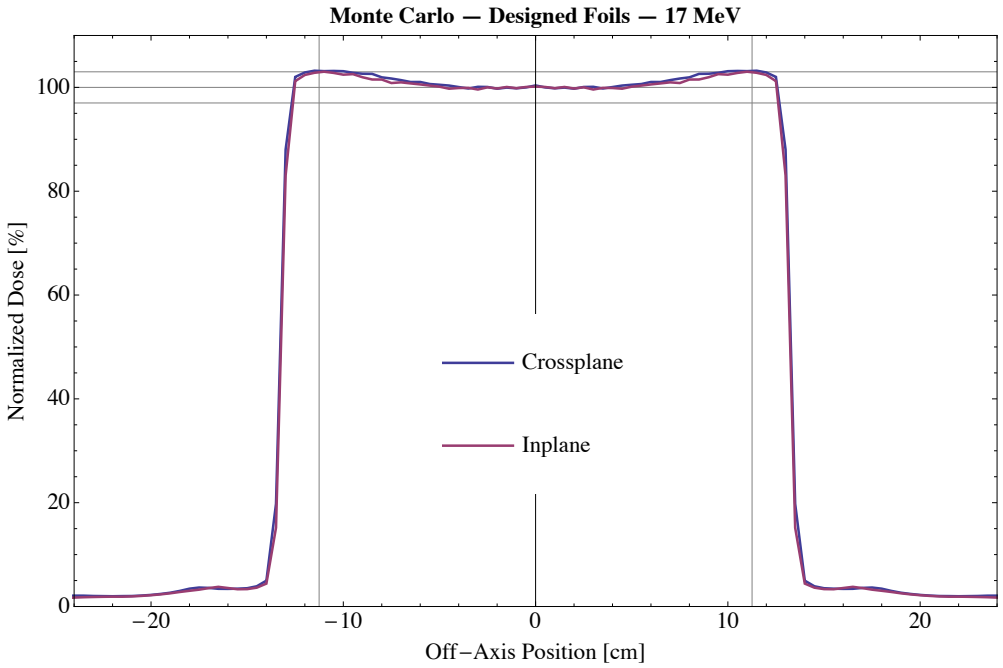

Figure I.11: Transverse profiles for 17 MeV.

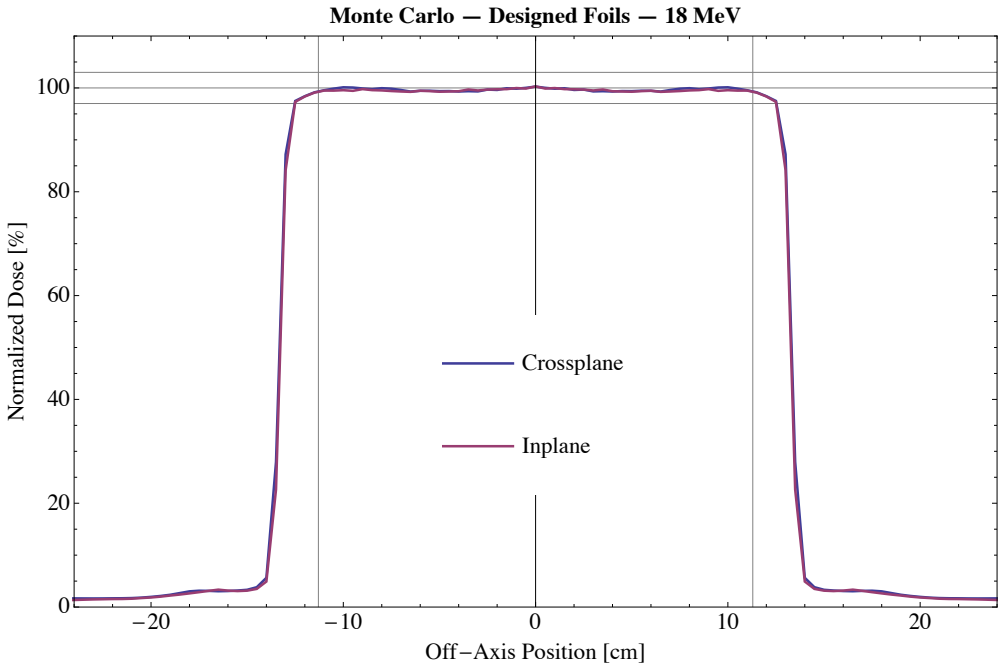

Figure I.12: Transverse profiles for 18 MeV.

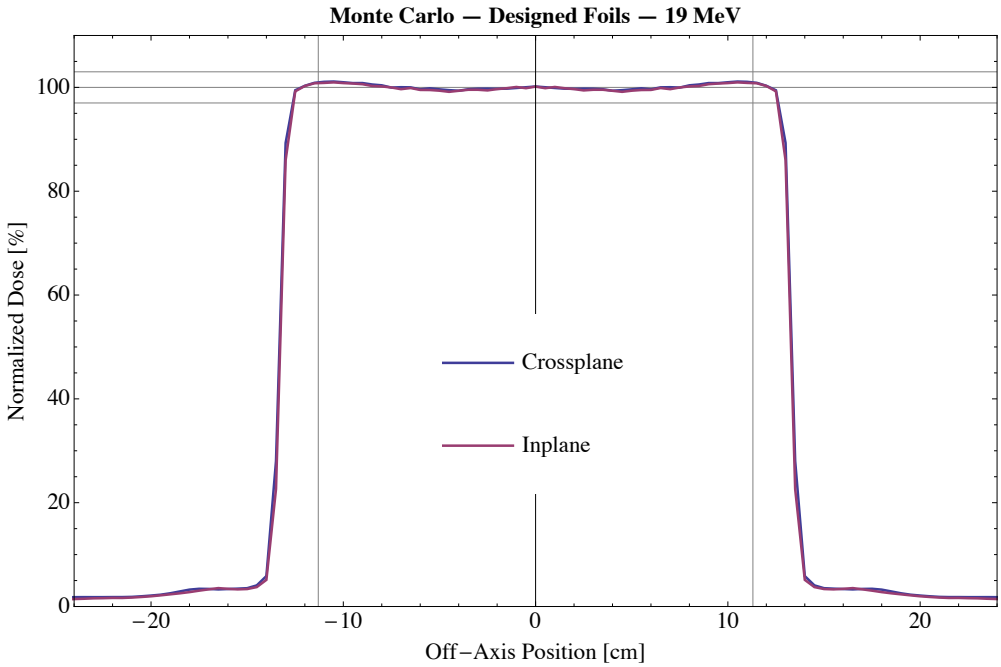

Figure I.13: Transverse profiles for 19 MeV.

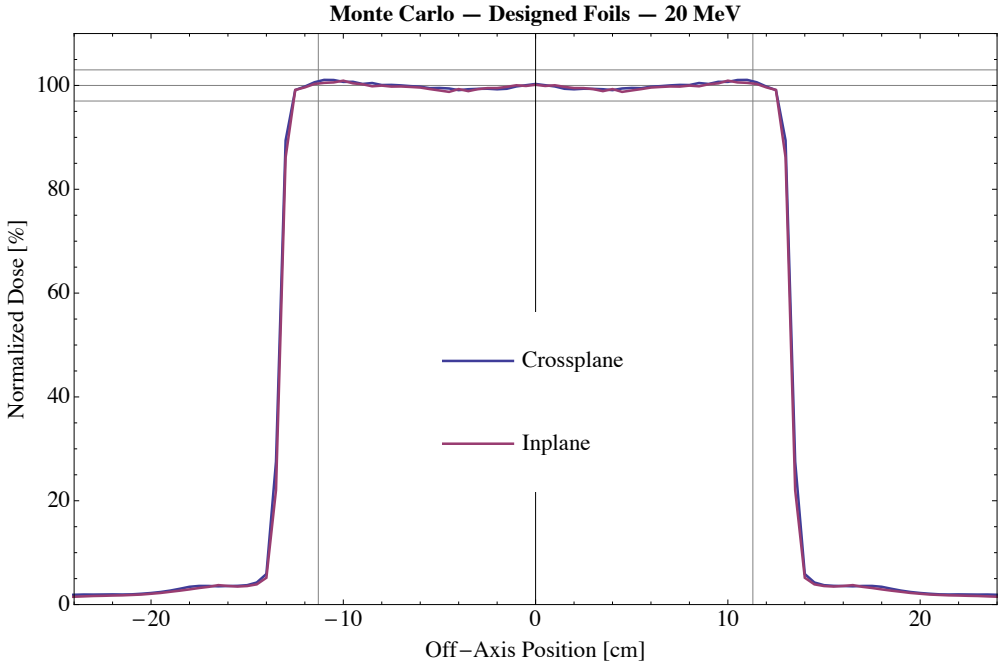

Figure I.14: Transverse profiles for 20 MeV.

Appendix J: Diagonal profiles of Monte Carlo dose calculations for objective profile refinement.

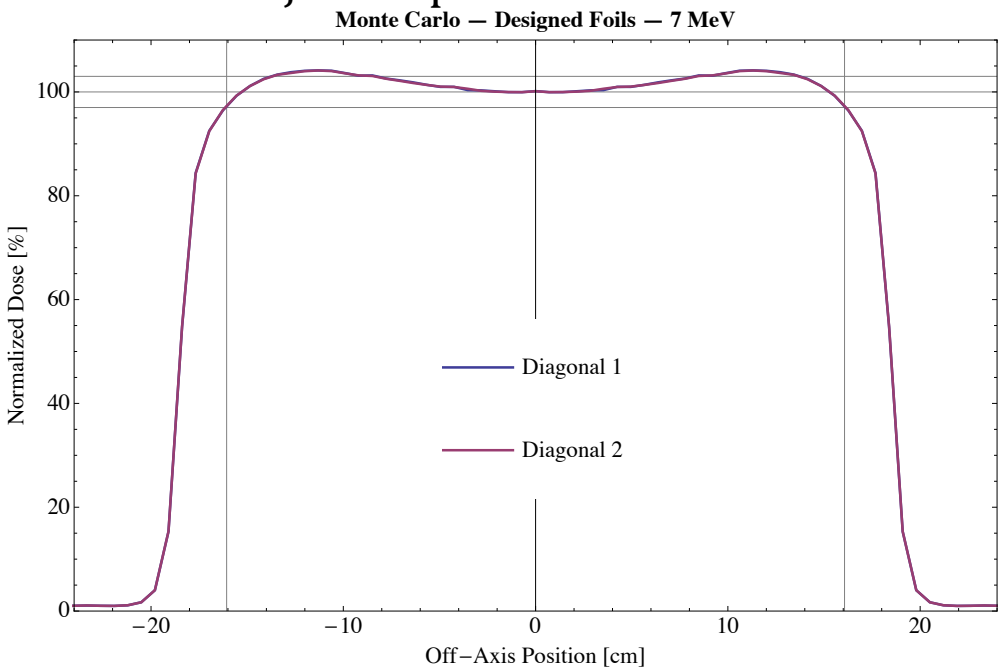

Figure J.1: Diagonal profiles for 7 MeV.

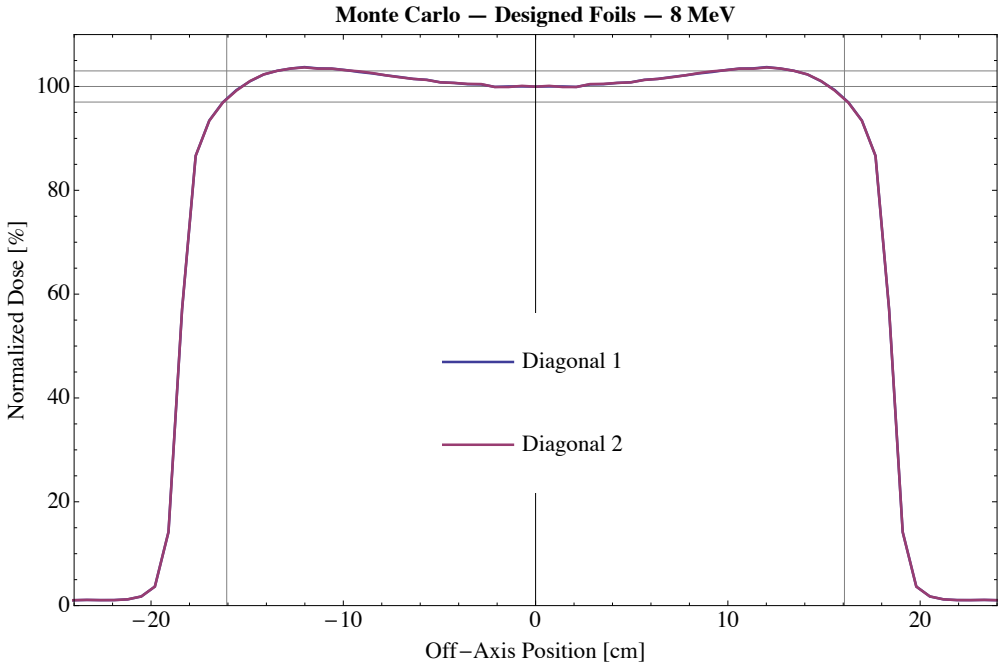

Figure J.2: Diagonal profiles for 8 MeV.

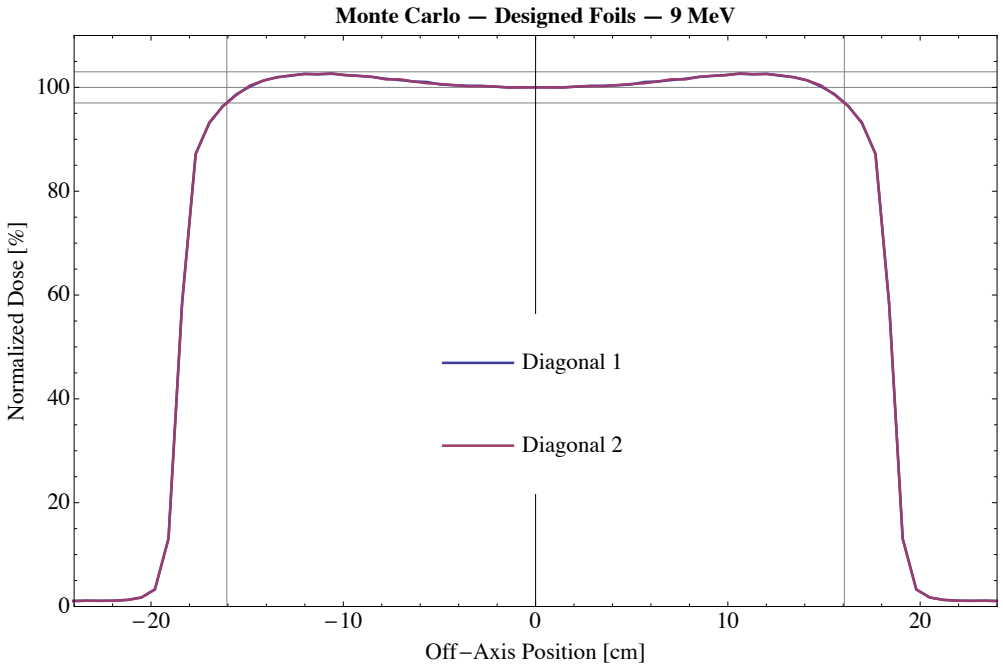

Figure J.3: Diagonal profiles for 9 MeV.

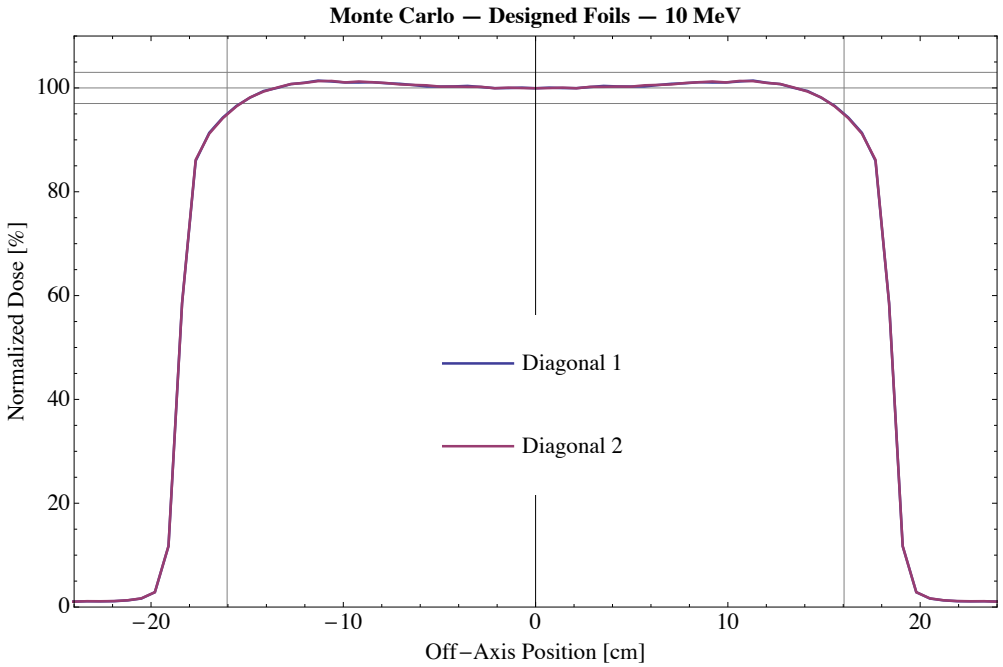

Figure J.4: Diagonal profiles for 10 MeV.

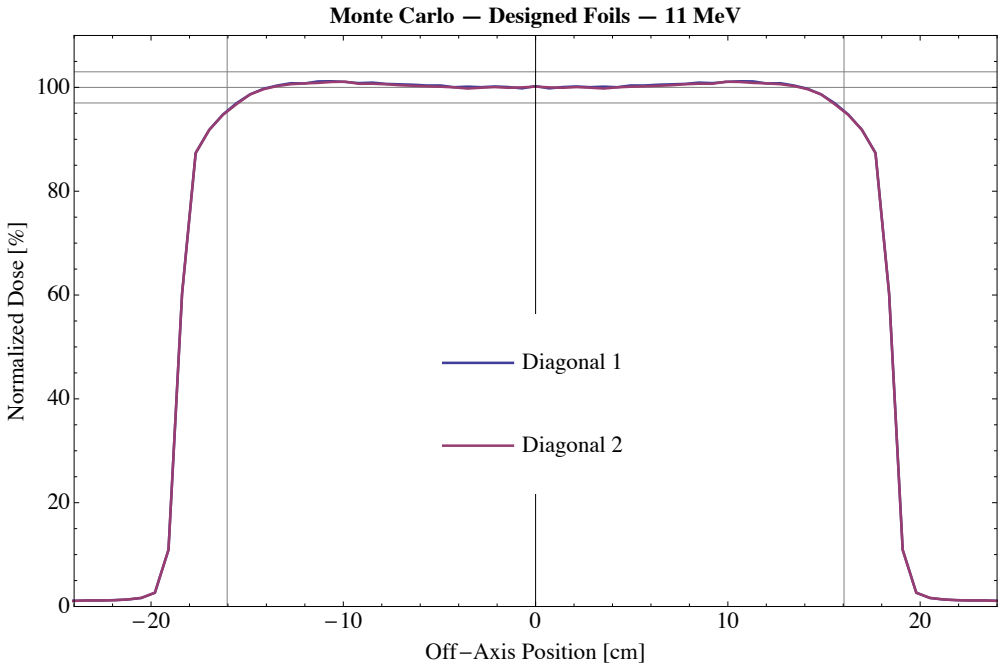

Figure J.5: Diagonal profiles for 11 MeV.

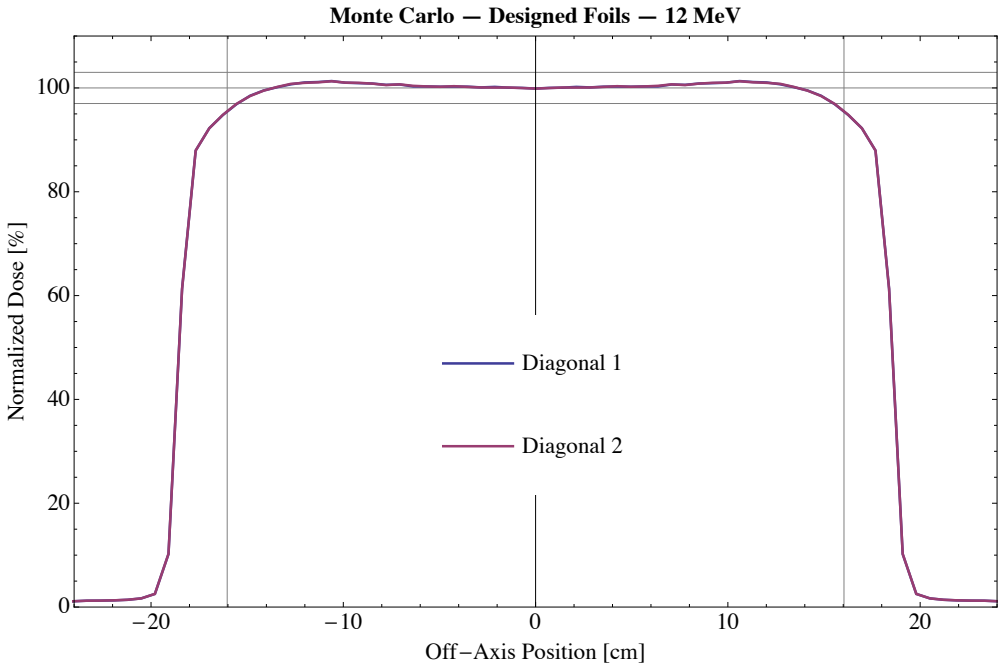

Figure J.6: Diagonal profiles for 12 MeV.

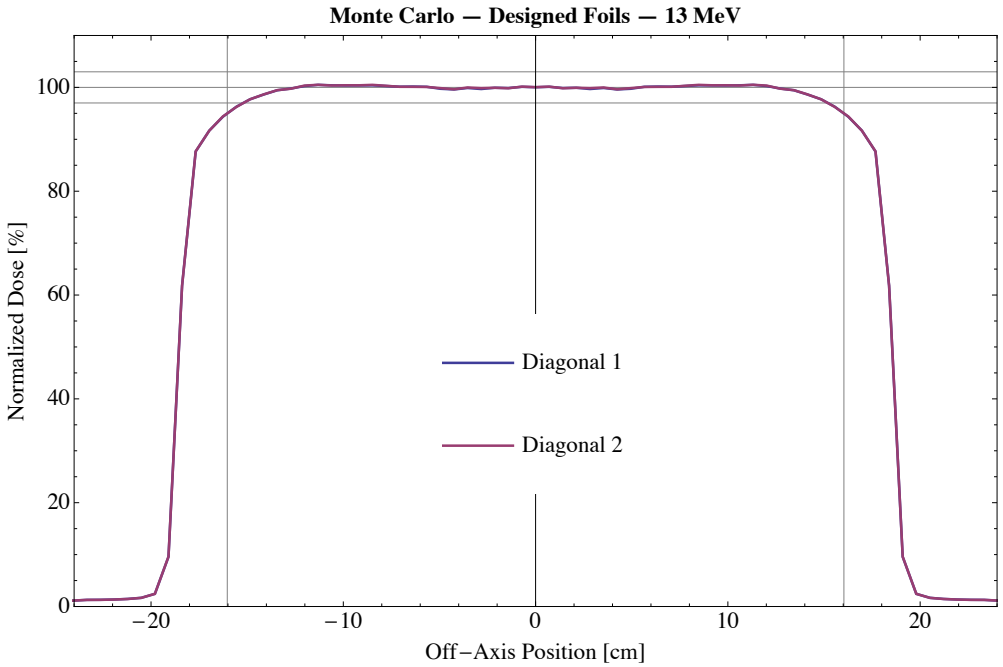

Figure J.7: Diagonal profiles for 13 MeV.

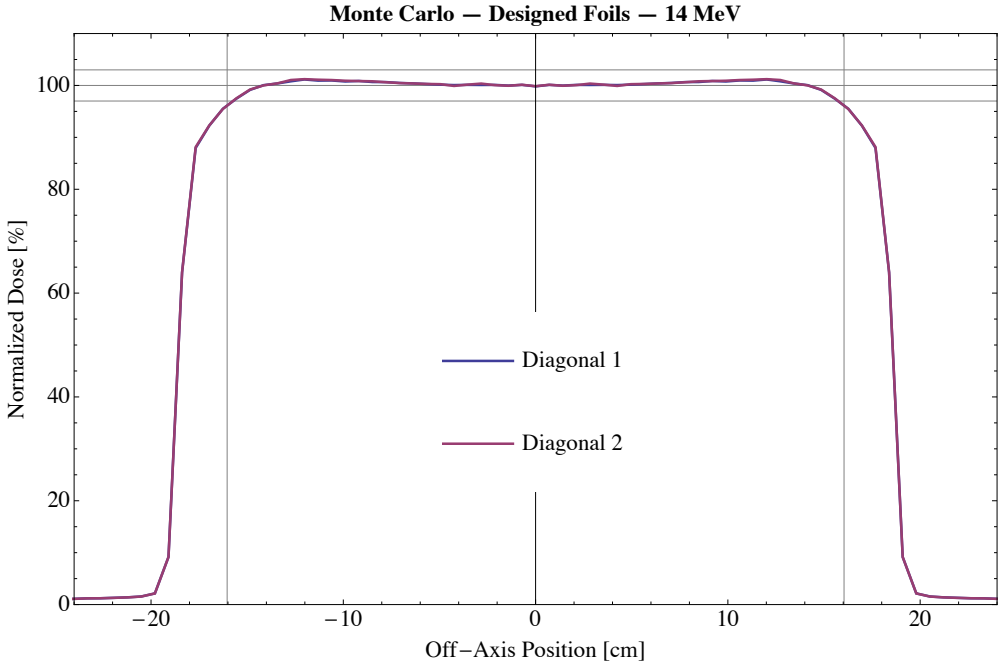

Figure J.8: Diagonal profiles for 14 MeV.

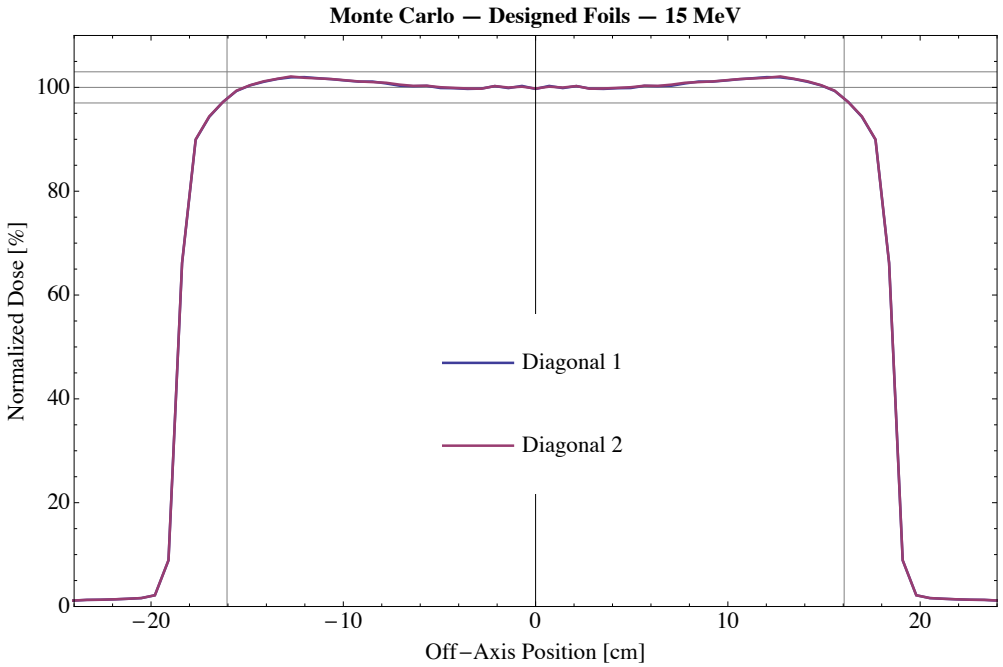

Figure J.9: Diagonal profiles for 15 MeV.

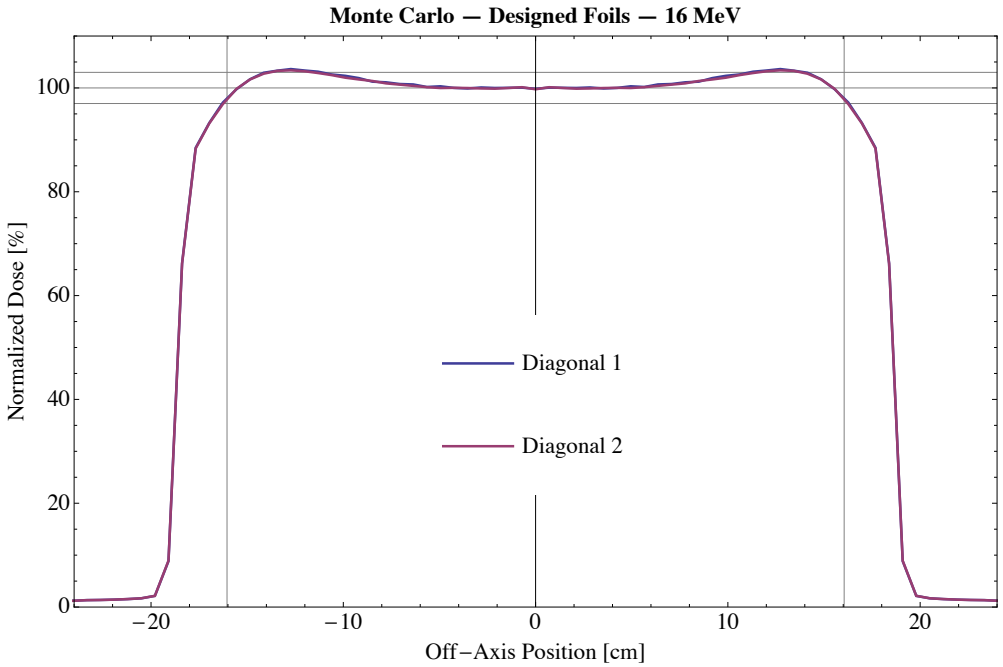

Figure J.10: Diagonal profiles for 16 MeV.

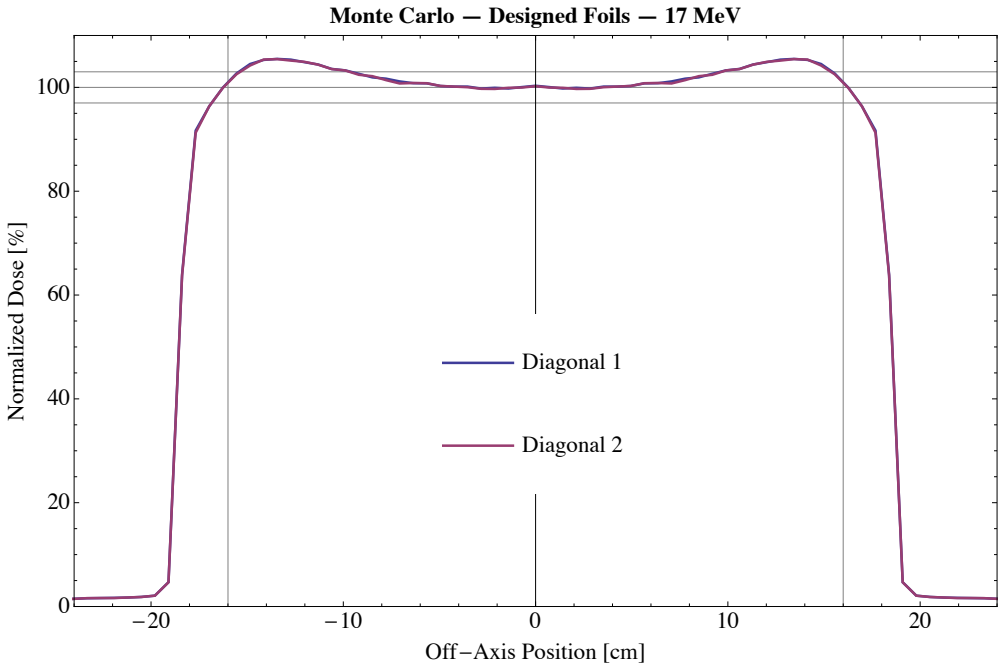

Figure J.11: Diagonal profiles for 17 MeV.

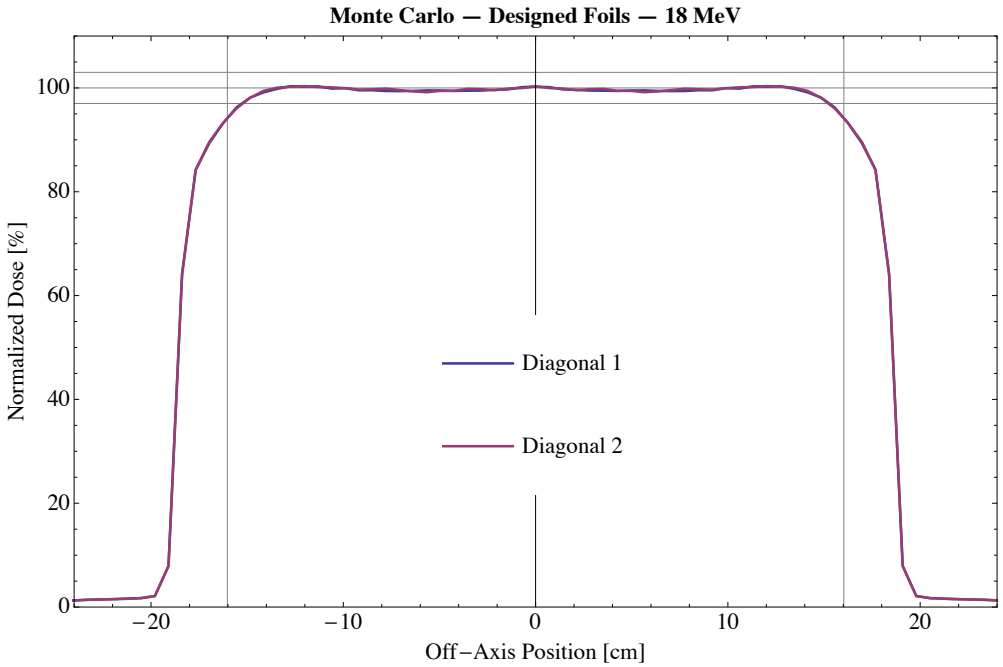

Figure J.12: Diagonal profiles for 18 MeV.

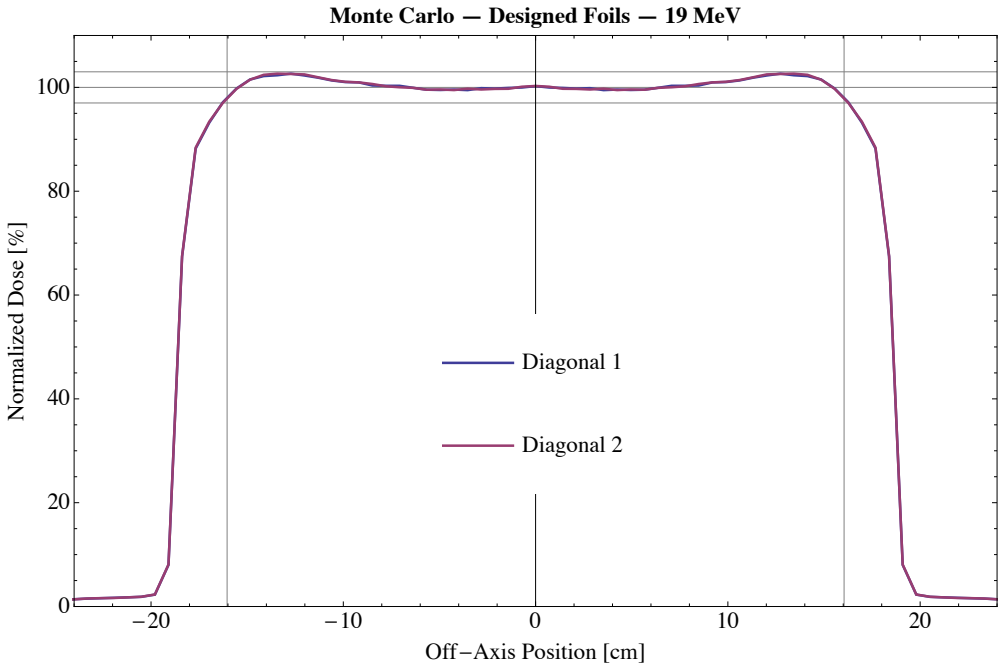

Figure J.13: Diagonal profiles for 19 MeV.

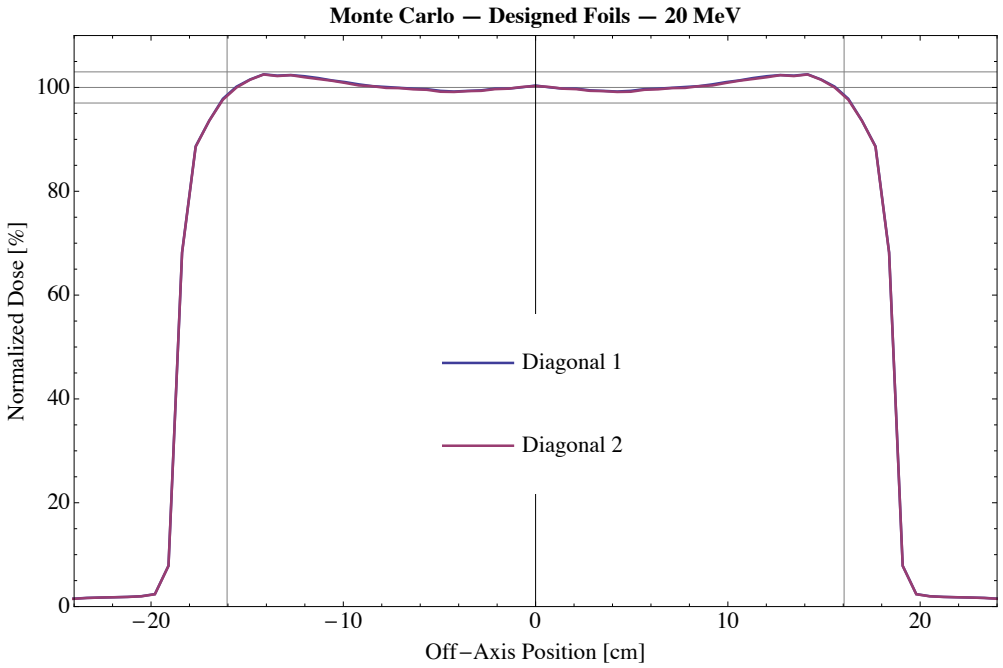

Figure J.14: Diagonal profiles for 20 MeV.

Vita

Justin LeBlanc was born and raised in Harrison, Arkansas. He graduated from Harrison Senior High School in 2005, and subsequently attended Rhodes College in Memphis, Tennessee. While pursing his degree in Physics, he also devoted a great deal of time to studying both theology and philosophy, two disciplines that had a profound effect on Justin's intellectual development. Justin graduated from Rhodes with honors in 2009, receiving a Bachelor of Science degree in Physics. He then went on to pursue his Master of Science degree in Medical Physics at Louisiana State University.

It was during his first year at LSU that Justin discovered the great minds of the Austrian School of Economics: Ludwig von Mises, F.A. Hayek, Murray Rothbard, Hans-Hermann Hoppe, Lew Rockwell, and many others. More than economists, these intellectual giants have laid the philosophical groundwork for the most morally consistent and logically cohesive theories regarding property rights and social order. It is no exaggeration to say these authors' works utterly changed the course of Justin's life, igniting within him a passion for the study and promulgation of the ideas of freedom and peace.

Justin intends to receive his Master of Science degree in Medical Physics in the Summer of 2012. He will then be going on to attend the University of Arkansas, where he has accepted a position as Distinguished Doctoral Fellow in the Department of Economics at the Sam M. Walton Graduate School of Business.